MATHEMATICAL STUDY FOR TWO EQUAL COLLINEAR CRACKS WEAKENING A PIEZOELECTRIC PLATE

Ph. D. THESIS

by

KAMLESH JANGID

DEPARTMENT OF MATHEMATICS
INDIAN INSTITUTE OF TECHNOLOGY ROORKEE
ROORKEE- 247 667 (INDIA)
JUNE, 2014

MATHEMATICAL STUDY FOR TWO EQUAL COLLINEAR CRACKS WEAKENING A PIEZOELECTRIC PLATE

A THESIS

Submitted in partial fulfillment of the

requirements for the award of the degree

of

DOCTOR OF PHILOSOPHY

in

MATHEMATICS

by

KAMLESH JANGID

DEPARTMENT OF MATHEMATICS
INDIAN INSTITUTE OF TECHNOLOGY ROORKEE
ROORKEE- 247 667 (INDIA)
JUNE, 2014

INDIAN INSTITUTE OF TECHNOLOGY ROORKEE
ROORKEE

CANDIDATE'S DECLARATION

I hereby certify that the work which is being presented in the thesis entitled "**MATHEMATICAL STUDY FOR TWO EQUAL COLLINEAR CRACKS WEAKENING A PIEZOELECTRIC PLATE**" in partial fulfilment of the requirements for the award of the Degree of Doctor of Philosophy and submitted in the Department of Mathematics of the Indian Institute of Technology Roorkee, Roorkee is an authentic record of my own work carried out during a period from July, 2010 to June, 2014 under the supervision of Dr. R. R. Bhargava, Professor, Department of Mathematics, Indian Institute of Technology Roorkee, Roorkee.

The matter presented in the thesis has not been submitted by me for the award of any other degree of this or any other Institute.

(**KAMLESH JANGID)**

This is to certify that the above statement made by the candidate is correct to the best of my knowledge.

Date : June , 2014

(R. R. Bhargava)
Supervisor

The Ph. D. Viva-Voce Examination of **Mr. Kamlesh Jangid**, Research Scholar, has been held on…….

Signature of Supervisor Chairman, SRC External Examiner

Head of the Department/Chairman, ODC

Acknowledgements

I must express my heartiest thanks to the God Almighty, for His blessings to write and complete this Thesis. It gives me immense pleasure to express my deep sense of gratitude and sincere thanks to my supervisor Prof. R. R. Bhargava, Department of Mathematics, Indian Institute of Technology Roorkee, Roorkee for her perspicacious guidance, support and patience throughout this study. She has encouraged me to work in the new promising and interesting research area and has fostered both my technical and professional development. Her unique way of tackling problems from strong fundamentals and clear ideas about the subject helped me in smooth progress of this research work. I can never repay the valuable time that she devoted to me during this entire period. It was indeed a fantastic, fruitful and unforgettable experience of my life.

I express my deep sense of gratitude to Prof. R. C. Mittal, Head of Department, Department of Mathematics, Indian Institute of Technology Roorkee, Roorkee for providing me necessary facilities and priceless support to carry out the research work to the completion of thesis.

I am thankful to Prof. P. N. Agrawal (Chairman, SRC) Department of Mathematics, Indian Institute of Technology Roorkee, Roorkee, Prof. B. K. Mishra, Department of Mechanical and Industrial Engineering, Indian Institute of Technology Roorkee, Roorkee and Prof. Kusum Deep, Department of Mathematics, Indian Institute of Technology Roorkee, Roorkee, who are the experts of my Student Research Committee (SRC) and sparing their valuable time in reviewing and critically examining the whole work.

I am deeply grateful and indebted to the family of my supervisor, Late Mrs. Sneh Lata Bhargava (mother) for unconditional love and care during the course of

this research work. I am also indebted to say my heartily thanks to my supervisor's father Prof. R. D. Bhargava Senior Prof. (Retd.), Indian Institute of Technology Bombay, Mumbai for providing me his kind expertise and constructive suggestions to accomplish this work.

The financial support from Ministry of Human Resource Development (MHRD), New Delhi during the course of this work is thankfully acknowledged.

I thankfully appreciate and acknowledge my indebtedness to my seniors Dr. Shehzad Hasan, Dr. Kuldeep Shrama, Manish Khandelwal, Shailesh Kumar and Pooja. I am also thankful to my friends and fellow research scholars, Late Ms. Priyanka, Aakansha, Sunita, Nirmal, Minakshi, Alka, Deepak, Rajendra, Divyesh, Ravi, Yogesh, Aditya, Ankit and Himanshu for fruitful suggestions and shared their knowledge with me.

I make an effort to record my affectionate thanks to my parents Mr. Mohan Lal Jangid and Mrs. Prem Devi Jangid for having faith in me, their unconditional support and love during all my studies. Their encouragement has always given me strength to move ahead in my life. Without their care and support, this Thesis work would not have been possible.

At last but not the least, I wish my sincere gratitude to all my family members and thanks to my younger sister and brother Shimla and Suresh for being my best friends and always providing me positive environment and strength to move ahead in my life.

Finally, I would like to thank everybody who was important to the successful realization of Thesis, as well as expressing my apology that I could not mention personally one by one.

Roorkee (**KAMLESH JANGID**)

June, 2014

Abstract

The concept of "smart" or intelligent materials, systems and structures has been around for many years. A great deal of progress has been made recently in the development of structures that continuously and actively monitor and optimize themselves and their performance through emulating biological systems with their adaptive capabilities and integrated designs.

Piezoelectric materials are the most widely used smart materials as sensors/actuators and transducers in smart structures, automotives, aerospace, and other industries to measure vibration and shock. These materials have some unique properties and functions such as improved dynamic response, high sensitivity to weak hydrostatic waves, damage resistance and control, which can be used to tailor or tune the overall performance of a smart structural system.

However, defects (e.g. voids, inclusions, faults and cracks) have the disadvantages because they often induce the failure of materials and structures. Failure phenomenon naturally arises from their inherent brittle characteristics in piezoelectric materials. Consequently, a better understanding of cracking behavior of piezoelectric materials may provide some fundamental knowledge to improve the performance of piezoelectric devices.

To study their electromechanical behaviors, suitable mathematical modeling becomes important. Since the expanded Stroh formalism for piezoelectric materials preserves most essential features of Stroh formalism, it becomes a popular tool for the study of piezoelectric anisotropic elasticity.

In this thesis, the Stroh formalism and complex variable technique are applied for the mathematical modeling of crack problems in 2D infinite piezoelectric plate.

The effect of permittivity of crack gap media is observed for two equal collinear

cracks cuts in an infinite piezoelectric plate under applied electromechanical loading. For this numerical case study is also presented on various fracture parameters such as intensity factors and energy release rate.

A strip-saturation model is proposed for an infinite piezoelectric plate weakened by two equal collinear cracks. The saturation zones developed are arrested by distributing over them the cohesive saturation limit electric displacement. A qualitative analysis is carried out to find the behavior of load required to close the saturation zones.

A strip-saturation model with coalesced interior saturation zones for a piezoelectric plate is proposed. The other rims of two saturation zones, each developed at the remaining tip of the two cracks, and the coalesced saturation zone are subjected to saturation limit electric displacement to arrest crack opening.

A strip-electro-mechanical yield model is proposed for an infinite piezoelectric plate weakened by two equal collinear cracks. Developed mechanical and electric strip zones are arrested by prescribing over their rims uniform, normal, cohesive yield point stress and saturation limit electric displacement. Three different situations are investigated when developed electrical saturation zone is bigger/smaller or equal to the developed mechanical yield zone. It has been found that for all the three cases the energy release rate is higher at the inner tip as compare to that at outer tip. This is because of the mutual influences of two cracks when they are closely located.

The effect of permittivity of crack gap media is observed for a strip-electro-mechanical yield model for an infinite piezoelectric plate weakened by two equal collinear cracks. Developed mechanical and electric strip zones are arrested by prescribing over their rims uniform, normal, cohesive yield point stress and saturation limit electric displacement. Three different situations are investigated when developed electrical saturation zone is bigger/smaller or equal to the developed mechanical yield zone. It is observed that opening of cracks is maximum for case when developed zones are equal and little less for the case when saturation zone is smaller and least for the case when saturation zone is biggest.

The effect of change in poling direction on a strip-electro-mechanical yield model is observed for an infinite piezoelectric plate weakened by two equal collinear cracks

with semi-permeable crack face electric boundary conditions prevailing on crack faces. The study shows that poling direction perpendicular to crack length opens the crack maximum. And when poling direction axis moved towards the length of the crack, the crack opening is reduced. Consequently the poling direction may also assist in crack arrest.

Table of Contents

List of Figures

List of Tables

Nomenclature and Acronyms

NOMENCLATURE

Symbol	Notation
$C_i (i = 1, 2)$	Cracks
C_{ijks}	Elastic constants
D	Electric flux
D_s	Saturation limit electric displacement
D_i	Electric displacement vector
D_2^{∞}	Electric displacement prescribed at infinity
E	Modulus of elasticity
E_i	Electric field vector
$E(k)$	Complete elliptic integral of second kind
$F(z)$	Holomorphic function
$F(k)$	Complete elliptic integral of first kind
$E(\psi, k)$	Elliptic integral of second kind
$F(\psi, k)$	Elliptic integral of first kind
G	Energy release rate
G_c	Critical energy release rate
G_M	Mechanical energy release rate
G_T	Total energy release rate
$\mathbf{H}^R$	Irwin's matrix
J	Local energy release rate
J_a	Global energy release rate
K_I	Open mode stress intensity factor
K_{IV}	Electric displacement intensity factor
$L_i (i = 1, 2)$	Cracks length
N_1, N_2	Principal stresses

$P_n(z)$	Polynomial of n^{th} degree in z
T_c	Curie temperature
T_i	Traction vector
W	Strain energy density
$Z_1(z)$, $Z_2(z)$	Westergaard functions
a_o	Half crack length
d, c	End points of C_2
$-c$, $-d$	End points of C_1
e_{ij}	Piezoelectric coefficient
k	Modulus of Jacobian elliptic functions and integrals
u_i	Mechanical displacement vector
x_1, x_2	Rectangular co-ordinates
z	Complex variable

ACRONYMS

Symbol	**Notation**
COD	Crack opening displacement
COP	Crack opening potential drop
CTOD	Crack tip opening displacement
EDIF	Electric displacement intensity factor
ER	Electrorhelogical
ERR	Energy release rate
GERR	Global energy release rate
IFs	Field intensity factors
LEFM	Linear elastic fracture mechanics
LERR	Local energy release rate
MEE	Magneto-electro-elastic
MERR	Mechanical energy release rate
MR	Magnetorheological
PSP	Pressure sensitive paint
PZT	Lead zirconium titanate
Re	Real part of complex quantity
SIF	Stress intensity factor

SMA	Shape memory alloys
TERR	Total energy release rate
UV	Ultraviolet radiation

GREEK SYMBOLS

Symbol	**Notation**
$\Psi(z)$, $\chi(z)$	Complex potentials
$\mathbf{\Lambda}$	Inverse of Irwin's matrix
Λ_{ij}	Components of Irwin's matrix
$\mathbf{\Omega(z)}$	Generalized stress function
$\Omega_2(z)$	Stress function
$\Omega_4(z)$	Electric displacement function
Γ_i	Saturation zone
Γ_i'	Yield zone
Υ	Continuous curve enclosing crack-tip in a counter clockwise sense
β	Angle between N_1 and x_1-axis
θ	Polarization angle with crack length
ε_{ij}	Mechanical strain tensor
κ_a	Relative permittivity
κ_{ij}	Dielectric permittivity
σ	Stress
σ_c	Critical stress
σ_f	Failure stress
σ_s	Yield stress
σ_{ij}	Mechanical stress tensor
σ_{22}^{∞}	Normal stress prescribed at infinity
ϕ	Electric potential

List of Publications

List of papers published/accepted in International Refereed Journals

1. Bhargava, R. R. and Jangid, K. (2013), Strip-saturation model for piezoelectric plane weakened by two collinear cracks with coalesced interior zones, *Applied Mathematical Modelling*, Vol 37, 4093-4102.

2. Bhargava, R. R. and Jangid, K. (2014), A mathematical strip-saturation model for piezoelectric plate weakened by two collinear equal cracks, *Mathematics and Mechanics of Solids*, Vol 19, 714-725.

3. Bhargava, R. R. and Jangid, K. (2013), Strip electro-mechanical yielding model for piezoelectric plate cut along two equal collinear cracks, *Applied Mathematical Modelling*, Vol 37, 9101-9116.

4. Bhargava, R. R. and Jangid, K. (2013), Strip-electromechanical model solution for piezoelectric plate cut along two semi-permeable collinear cracks, *Archive of Applied Mechanics*, Vol 83, 1469-1491.

5. Bhargava, R. R. and Jangid, K. (2013), A study on influence of poling direction on piezoelectric plate weakened by two collinear semi-permeable cracks, *Acta Mechanica*, Vol 225, 109-129.

6. Bhargava, R. R., Jangid, K. and Verma, P.R. (2013), Two semi-permeable equal collinear cracks weakening a piezoelectric plate $\sim$ A study using complex variable technique, *ZAMM-Journal of Applied Mathematics and Mechanics*, Wiley (Accepted).

7. Bhargava, R. R. and Jangid, K. (2014), Closed form solution for two unequal

collinear semi-permeable straight cracks in a piezoelectric media, *Archive of Applied Mechanics*, Vol 84, 833-849.

8. Bhargava, R. R. and Jangid, K. (2014), Strip-coalesced interior zone model for two unequal collinear cracks weakening a piezoelectric media, *Applied Mathematics and Mechanics (English Edition)*, Vol 35, 1249-1260.

Research papers presented/published in International Conferences

1. Bhargava, R. R., Jangid, K. (2012), Strip-electromechanical model for two collinear cracks in piezoelectric plate, ICCMS-2012, *International Congress on Computational Mechanics and Simulation*, Hyderabad, India.

2. Bhargava, R. R., Jangid, K. (2013), A study on influence of changing in poling direction on piezoelectric plate cut along two unequal cracks, ECM-2013, *The Second International Conference on Engineering and Computational Mathematics*, Hong Kong.

3. Bhargava, R. R., Jangid, K. (2014), Effect of change in poling direction for two equal collinear semi-permeable cracks in a piezoelectric media, USNCTAM-2014, *17th U.S. National Congress on Theoretical and Applied Mechanics*, Michigan, USA.

Chapter 1

Introduction to Smart Materials and Fracture Mechanics

1.1 Smart Materials

Smart materials are materials having extra ordinary characteristics in comparison to the traditional materials. Such materials are defined as materials whose properties are altered inevitably in response to external stimuli viz. stress, temperature, moisture, pH and electric field etc.

There are many group of smart materials, each offer different properties that can be changed. Smart materials have widespread applications in materials science, sensors/actuator, microelectronics, medical treatment, safety engineering and military engineering etc. Some of them are described below.

(i). Piezoelectric Materials

The materials which generate voltage when mechanical stress is applied are known as piezoelectric materials and the phenomenon is known as direct piezoelectric effect. The phenomenon of direct piezoelectric effect is reversible i.e. when voltage is applied, then deformation takes place. This reverse effect is known as converse piezoelectric effect or electrostriction. The piezoelectric materials are widely used as sensors, transducers and actutators. Piezoelectric generator as an example is shown in Fig. 1.1, which generates electricity from force. This electricity can be stored and used to power street lights, traffic signals etc.

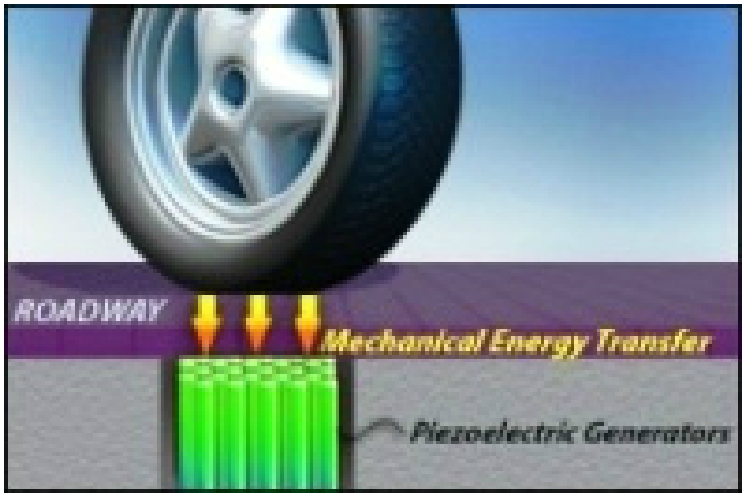

Figure 1.1: Electricity generated from force

(ii). Shape Memory Alloys (SMA)

A shape memory alloy (SMA) possesess the property to "remember" its original shape and that when deformed returns to its pre-deformed shape when heated above their transition temperature. These materials show two unique properties: superelasticity and shape memory effect, which ordinary metals and alloys do not have. Superelasticity allows SMAs to undergo large deformation upon loading at high temperatures and to recover their original shape when unloaded. Shape memory effect is the ability to maintain a deformed shape up to heat induced recovery of the original shape.

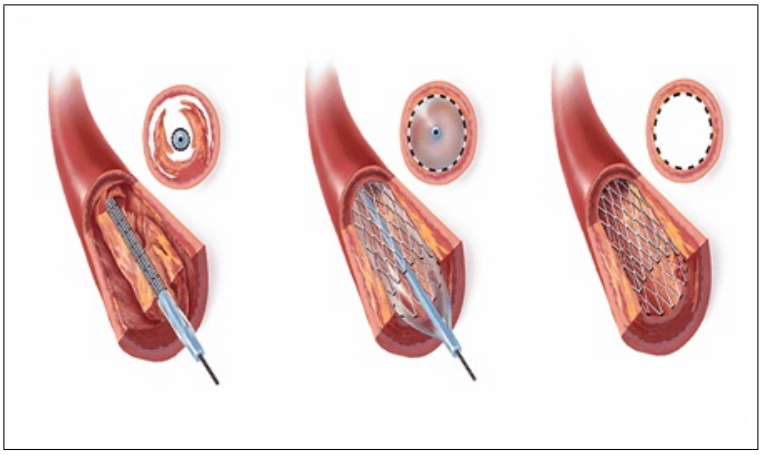

Figure 1.2: A stent made by Nitinol wire

Shape memory have found a large number of applications in aerospace, medicine

and the leisure industry. The shape memory alloys are Ni-Ti, CU-Zn-S, Cu-Al-Ni, Cu-Zn etc.

Fig. 1.2 shows the medical use of Nitinol (Ni-Ti) stents in which rings of SMA wire hold open a polymer tube to open up a blocked vein blood filter.

(iii). Electrochromics

Figure 1.3: Electrochromic glass

The materials which change color when electric voltage is applied are known as electrochromic materials. As an example of these materials, electrochromic glass is shown in Fig. 1.3.

(iv). Chemochromics

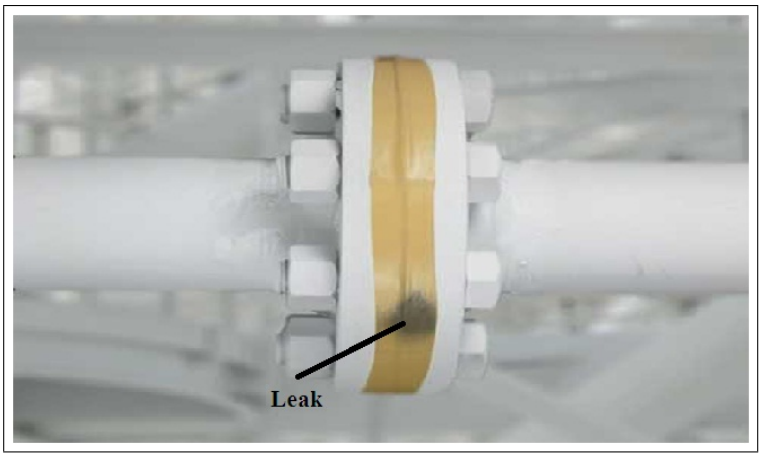

Figure 1.4: Chemochromic tape for Hydrogen leak detection

The materials which change color when exposed to specific environment are known as chemochromics materials.

As an example chemochromic tape is shown in Fig. 1.4. Chemochromic tape is conveniently used for leak detection of Hydrogen at unions, valves, or outlets.

(v). Photochromics

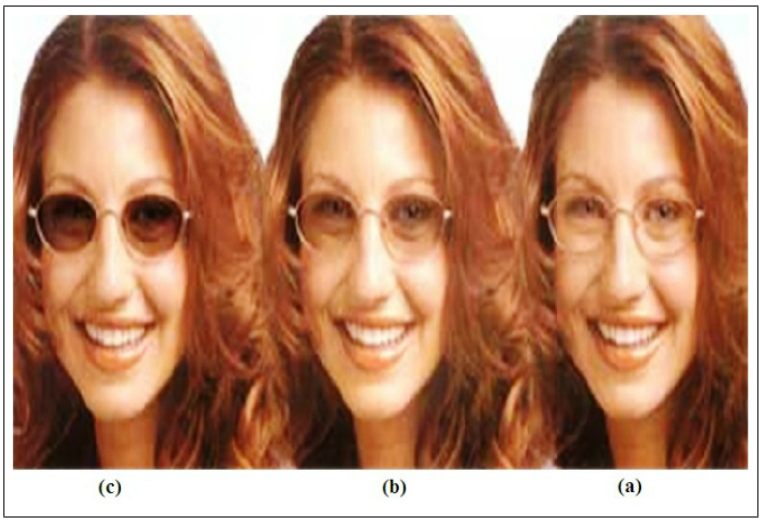

Figure 1.5: Photochromic glasses

The materials which change color when exposed to light are known as photochromic materials.

Example of photochromic glasses is shown in Fig. 1.5, which get darken on exposure to UV radiation. Once the UV is removed, the glasses will gradually return to their clear state as could be noted from Figs. 1.5(a, b, c).

(vi). Mechanochromics

The materials which change color when exposed to stresses and/or strains are known as mechanochromic materials. Pressure-sensitive paint (PSP) is an example of these materials. PSP is a method for measuring local oxygen concentration, usually in aerodynamic settings. PSP is paint-like coating as shown in Fig. 1.6, which fluoresces under a specific illumination wavelength in differing intensities depending on the local Oxygen concentration being applied to its surface.

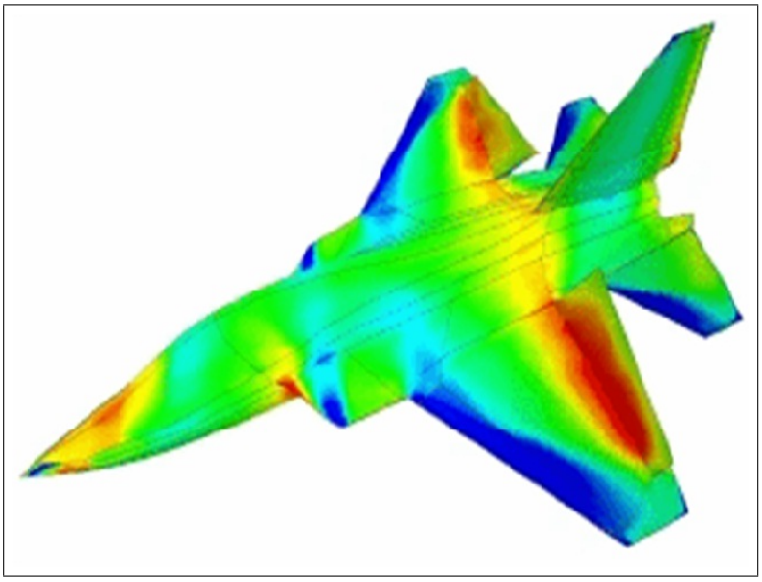

Figure 1.6: Pressure sensitive paint on aeroplane model

(vii). Thermochromics

Figure 1.7: Thermochromic ink

The materials which change color due to temperature change are called thermochromic materials.

Thermochromic ink as an example of these materials is shown in Fig. 1.7. When the wall papers impregnated with thermochromic ink is touched by a person the wallpaper changes color due to body heat. It changes back to the original color after it is no longer touched.

(viii). Electrorheological (ER)

Figure 1.8: Future force warrior infantry combat suite using ER fluid

The materials which change stiffness/viscosity when electric voltage is applied are known as electrorheological materials.

Future Force Warrior Infantry Combat Suite made of ER fluids is shown in Fig. 1.8. US army's made Future Force Warrior Infantry Combat Suite to create bulletproof vests using an ER fluid. ER fluid has the ability to soak the fluid into cloth. Thus creates the potential for a very light vest that can change from a normal cloth into a hard covering almost instantaneously.

(ix). Magnetorheological (MR)

The materials which change stiffness/viscosity when exposed to magnetic field are known as magnetorheological materials.

As shown in Fig. 1.9, the mixture remains liquid (a) until a magnet is brought close to it. The material reverts back to its original liquid state once the magnetic field is removed.

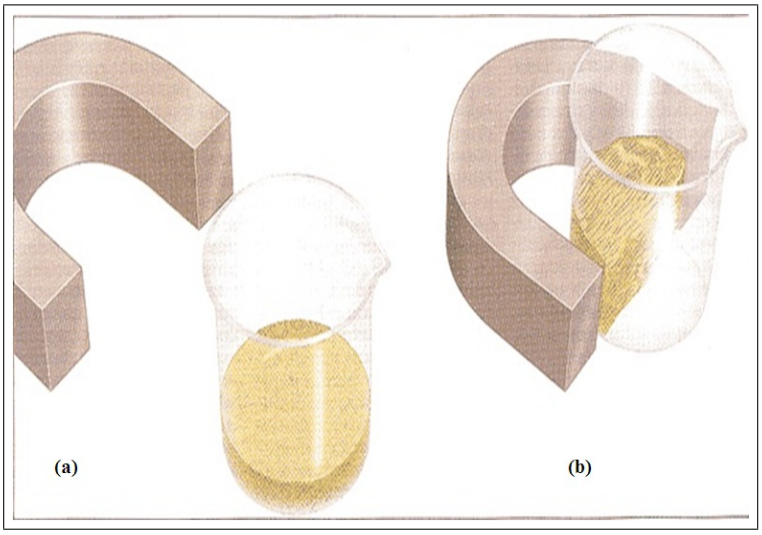

Figure 1.9: MR fluid (a) without magnetic field (b) under magnetic field

(x). Biomimetics

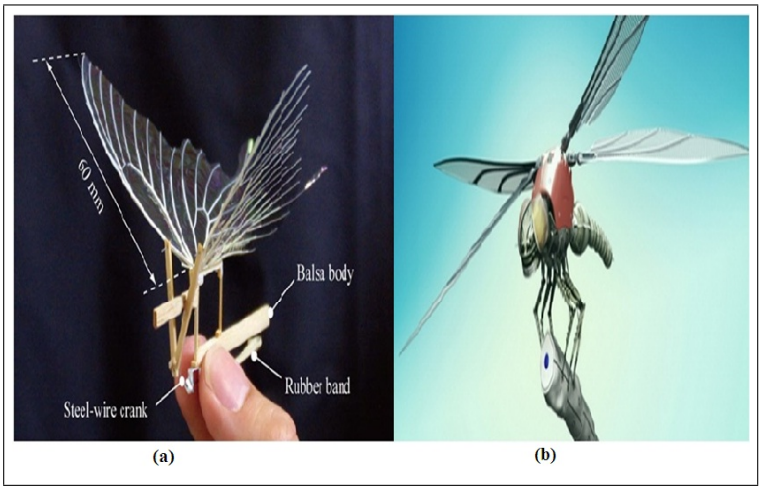

Figure 1.10: Biomimetic robot of butterfly

Biomimetic is the human-made processes, substances, devices that imitate nature. The art and science of designing and building biomimetic apparatus is called biomimetics.

The goal of biomimetic is to develop a new class of biological inspired robots to perform in unstructured environment, able to respond to change in environmental factors. Shown above is a biomimetic robot mimicking the butterfly movements, Fig. 1.10(a) shows the biomimetic robot of butterfly while Fig. 1.10(b) shows the real butterfly.

1.2 Fracture Mechanics

Fracture mechanics is the field of solid mechanics concerned with the study of mechanical behavior of cracked materials subjected to the applied load. It uses methods of analytical mechanics to calculate the driving force for crack propagation and those of experimental mechanics to characterize the resistance of materials to crack extension.

In modern materials science, fracture mechanics is an importnant tool in improving the mechanical performance of mechanical components.

Griffith [48] proposed the first fracture problem in 1920. He proposed an energy balance approach for brittle materials and found that crack will propagate if the potential energy of the system is decreased with crack propagation. Griffith's model correctly gave the relationship between srtength and flaw size in glass. Griffith approach only applied to ideally brittle solids. A modification to Griffith's model that made it applicable to metals did not came until 1948.

The first milestone as a modification to Griffith's model came for ductile materials in 1950s, when Irwin [55, 56] included the energy dissipation by local plastic flow, after studying the work of Inglis [54], Griffith [48]. Orowan [91] independently proposed a similar modification to the Griffith theory. Later, Irwin [57] replaced the concept of the energy release rate by the stress intensity factor.

After the fundamentals of linear elastic fracture mechanics (LEFM) were established around 1960, researchers and scientists turned their attention to the crack tip plasticity. Irwin [58], Dugdale [24], Barenblatt [1] and Wells [129] developed analyses to correct for yielding at the crack tip.

Wells [129] proposed the crack tip opening displacement (CTOD) as an alternative fracture criterion when significant plasticity precedes failure. In 1968, Rice [105] modeled the plastic deformation as nonlinear elastic behavior and extended the method of energy release rate to nonlinear materials. He showed that the energy release rate can be expressed as a path-independent line integral, called the J-integral.

Thereafter, many experiments were conducted to verify the accuracy of the models of fracture mechanics [44, 62, 86–88, 96, 97, 100, 113].

1.2.1 Crack

A crack may be defined as an inner material surface split into two unconnected faces. Fig. 1.11 shows crack occurring in the wall.

Figure 1.11: Crack in the wall

1.2.2 Modes of Crack Deformation

Crack opening is categorised in three different modes as follows:

Mode I (Opening mode)

A tensile stress applied normal to the plane of the crack which opens the crack rims perpendicular to each other is called Mode I or Opening mode.

Mode II (Sliding mode)

A shear stress acting parallel to the plane of the crack and perpendicular to the crack front is applied which slides the crack rims on each other. This is called Mode II or Sliding mode.

Mode III (Tearing mode)

A shear stress acting parallel to the plane of the crack and parallel to the crack front opens the crack rims out of plane sliding is known as Mode III or Tearing mode.

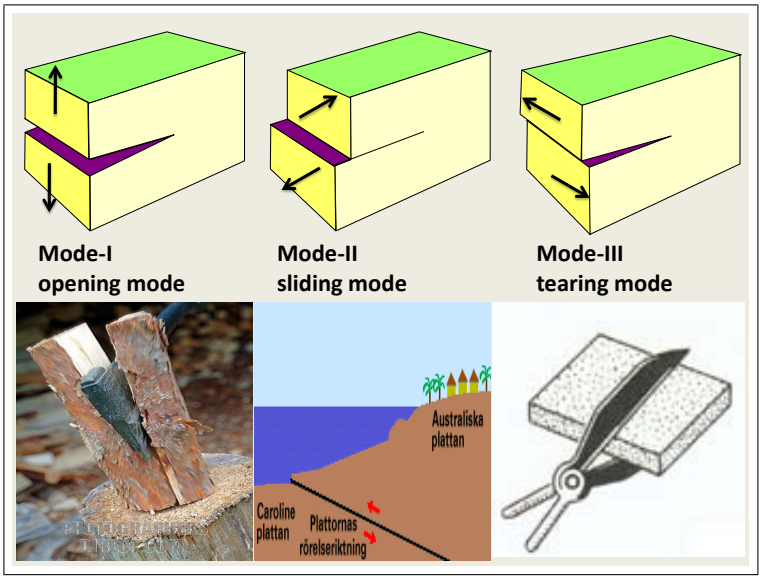

Figure 1.12: Modes of crack deformation

1.2.3 Fracture

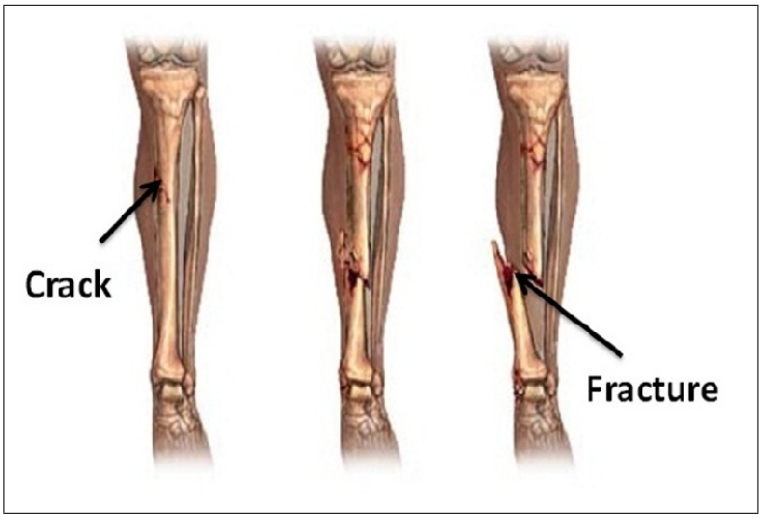

Figure 1.13: Bone crack leading to fracture

Separation of material in two or more parts under the action of stresses is known as fracture. Fig. 1.13 shows the fracture in bone.

Fractures are categoried in following two categories:

Ductile Fracture

Ductile fracture is defined as the fracture which takes place by a slow propagation of crack with considerable amount of plastic deformation. Ductile fractures are

associated with overload of the structure or large discontinuities. Fig. 1.14 shows the ductile fracture of Copper metal.

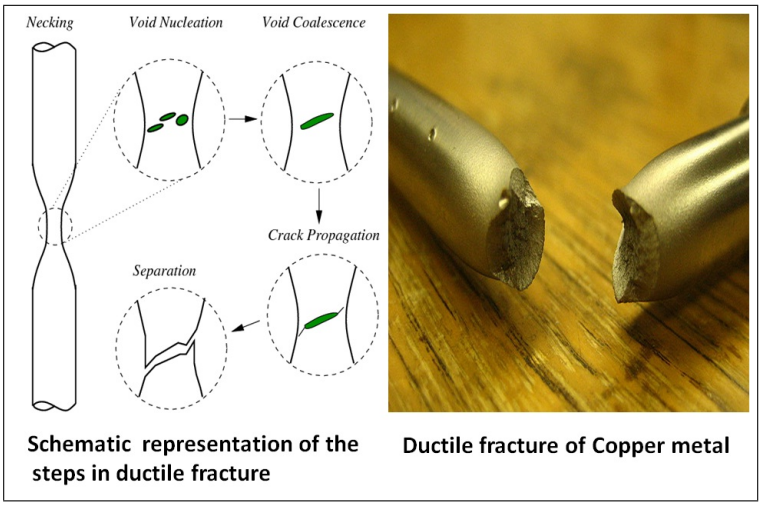

Figure 1.14: Ductile fracture of Copper metal

Brittle Fracture

Brittle fracture takes place by a rapid propagation of crack with low energy release and without significant plastic deformation. Fig. 1.15 depicts brittle fracture in Aluminum crank arm.

Figure 1.15: Brittle fracture in Aluminum crank arm

1.2.4 Different Fracture Criterion

There are various approaches for fracture analysis for fracture parameters and are explained below:

1.2.4.1 Energy release rate (ERR), G

The energy release rate, G, is the rate of change in potential energy with crack area for a linear elastic material. At the moment of fracture, $G = G_{cr}$, the critical energy release rate, which is a measure of fracture toughness.

For a crack of length $2a$ in an infinite plate subjected to a remote tensile stress σ the energy release rate is given by

$$G = \frac{\pi\sigma^2 a}{E}. \tag{1.2.1}$$

At fracture, $G = G_{cr}$, so the critical energy release rate for the fracture is

$$G_{cr} = \frac{\pi\sigma_f^2 a_c}{E}, \tag{1.2.2}$$

where σ_f is failure stress and a_c is critical crack size at which crack propagates.

1.2.4.2 Stress intensity factor (SIF)

In an elastic material, near the tip of the crack, each stress component is proportional to a constant K. And if this constant is known then the state of stress at the tip of crack can be determined. This constant is known as stress intensity factor. The magnitude of K depends on sample geometry, the size and location of the crack.

For a crack of length $2a$ in an infinite plate subjected to a uniform tensile stress σ, the stress intensity is given by

$$K_I = \sigma\sqrt{\pi a}. \tag{1.2.3}$$

At the moment of fracture, $K_I = K_c$, which implies $K_c = \sigma_f\sqrt{\pi a_c}$.
Comparing Equations (1.2.1 and 1.2.3), one can obtain the relationship

$$G = \frac{K_I^2}{E}. \tag{1.2.4}$$

Thus both the above approaches are equivalent for linear elastic materials.

1.2.4.3 J-integral

J-integral is applicable to elastic, non-linear elastic and materials exhibiting elastic-plastic behavior near the crack-tip. J-integral was first applied to fracture mechanics

by Rice [105] in 1968 for plane problems. It is defined as

$$J = \int_{\Upsilon} \left(W dx_2 - T_i \frac{\partial u_i}{\partial x_i} ds \right), \tag{1.2.5}$$

where, Υ is an arbitrary contour around the tip of the crack. $T_i = \sigma_{ij} n_j$ is the traction vector, n is the unit vector normal to Υ; σ, ϵ, and u are the stress, strain, and displacement field, respectively. W is the strain energy density and defiened as

$$W = \int \sigma_{ij} d\varepsilon_{ij}. \tag{1.2.6}$$

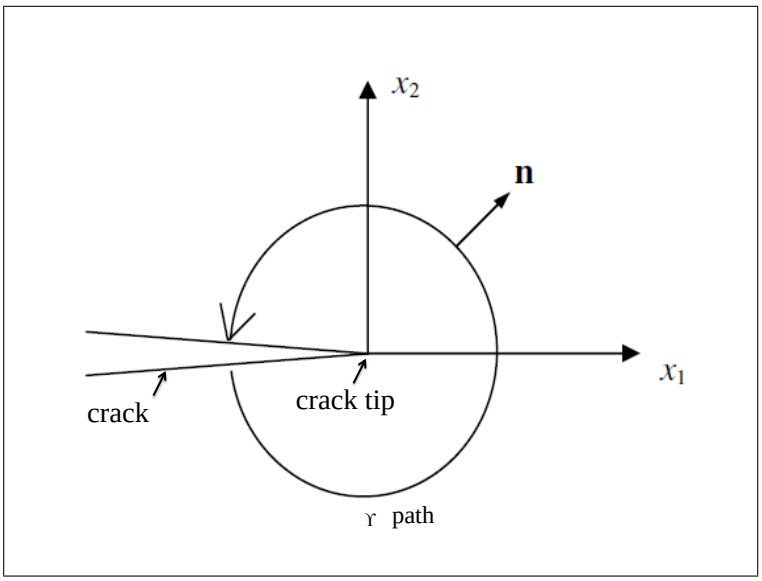

Figure 1.16: J-integral around a crack in two-dimensions

Fig. 1.16 shows J-integral contour around a crack tip for two-dimensional case.

1.2.4.4 Crack opening displacement (COD)

Crack opening displacement is the relative crack face opening between the two surfaces of the crack. Crack opening displacement can be used as a measure of the toughness of the materials under mode-I deformation.

1.2.4.5 Crack opening potential drop (COP)

Crack opening potential drop is the electric potential difference between the two surfaces of the crack. Same as COD, COP is used to measure the fracture and fatigue of materials.

1.2.5 Crack Arrest Model

For better understanding of material failure behavior in both macroscopic and microscopic sense, analysis at the crack tip is necessary. In case of ductile materials crack initiation, stable crack growth and the instability are the three main stages of fracture. While, nucleation, growth and coalescence of microcrack is involved in the case of brittle materials. During large deformation Irwin's approach of crack tip singularity is not useful as it is concerned with linear elastic fracture mechanics. To present the plastic deformation at the crack tip, Dugdale developed a macroscopic plasticity model for ductile materials in 1960.

1.2.5.1 Strip-yield model

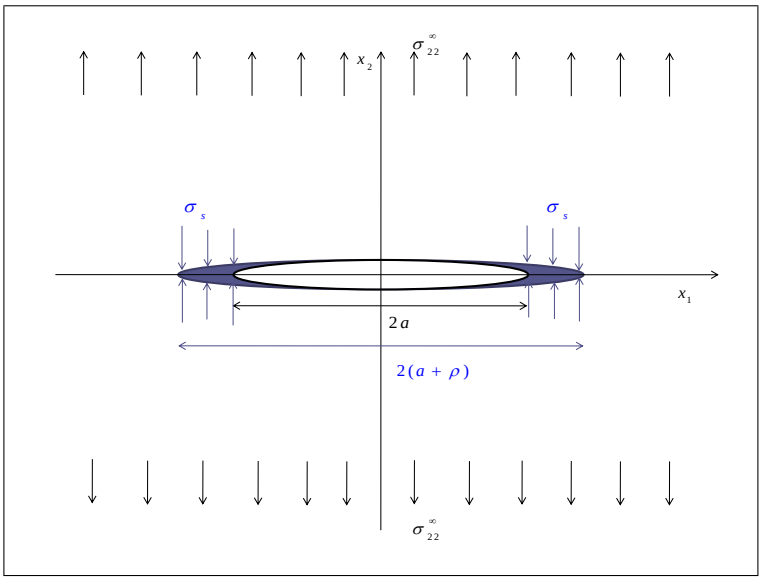

Figure 1.17: Dugdale crack arrest model for Mode-I

The strip-yield model is given by Dugdale [24] for mode-I fracture mechanics problem of an infinite plate containing straight cut with a far field uniform tensile stress. The rationale behind the Dugdale model is that the infinite stress of the purely elastic solution is physically unrealistic. The stresses should not become infinite, as observed empirically also. The only way to counter the stress generated at the crack tips by the remote stress at infinity is to generate opposing stresses with the same order of singularity and magnitude, thus arresting the collapse of structure instantaneously.

For the above problem shown in Fig. 1.17, the Westergaard function $Z(z)$ is obtained by superposition of Westergaard functions $Z_1(z)$ and $Z_2(z)$ as described below:

(i) For a crack of length $2(a+\rho)$ in an infinite plate subjected to a uniform stress σ_{22}^{∞} at infinite boundary, the Westergaard function $Z_1(z)$ is given (taken from Broek [15]) by

$$Z_1(z) = \frac{\sigma_{22}^{\infty} z}{\sqrt{z^2 - (a+\rho)^2}}. \tag{1.2.7}$$

(ii) For a crack of length $2(a+\rho)$ in an infinite plate subjected to a uniform stress σ_s at yield zone ρ, the Westergaard function $Z_2(z)$ is given by

$$Z_2(z) = \frac{2\sigma_s}{\pi}\left\{\frac{\sigma_{22}^{\infty} z}{\sqrt{z^2-(a+\rho)^2}}\cos^{-1}\left(\frac{a}{a+\rho}\right) - \cot^{-1}\left(\frac{a}{z}\sqrt{\frac{z^2-(a+\rho)^2}{(a+\rho)^2-a^2}}\right)\right\}. \tag{1.2.8}$$

The Westergaard function $Z(z)$ is the superimposition of $Z_1(z)$, $Z_2(z)$ and given by

$$Z(z) = Z_1(z) - Z_2(z). \tag{1.2.9}$$

On making zero the singular term, according to Dugdale's [24] hypothesis of stresses remain finite at every point of the body, involved in Westergaard function $Z(z)$, the length of plastic zone is obtained using

$$\frac{a+\rho}{a} = \sec\left(\frac{\pi\sigma_{22}^{\infty}}{2\sigma_s}\right). \tag{1.2.10}$$

1.2.5.2 Strip-saturation Model

Motivated by Dugdale's [24] model, Gao et al. [43] developed a strip-saturation model to understand the effect of electric saturation in piezoelectric ceramics as a class of mechanically brittle and electrically ductile solids. In this model the electrical saturation accounted, was based on a generalization of the Dugdale [24] approach. The concept of local and global energy release rates were defined and discussed. It was found that the local energy release rate gave predications in broad agreement with experimental observations.

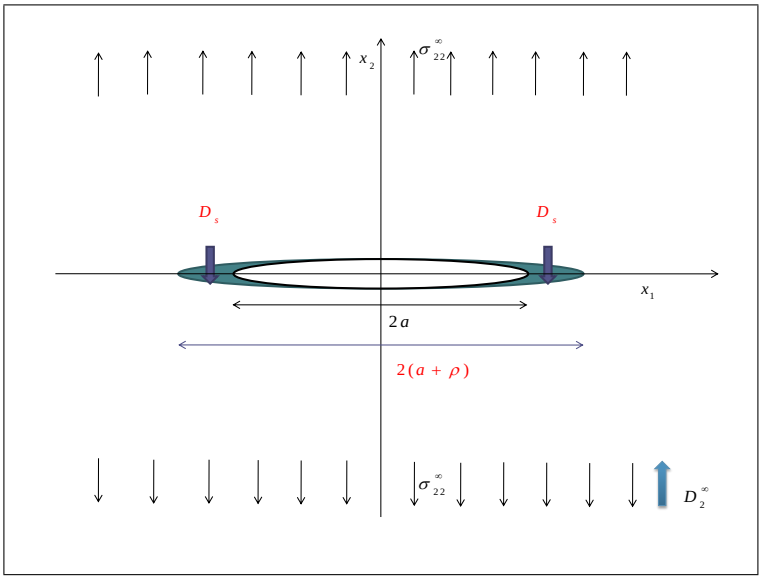

Figure 1.18: Strip-saturation model for Mode-I

For the above problem shown in Fig. 1.18, the desired complex potential function $\Omega_4(z)$ is given (taken from Wang [126]) by

$$\Omega_4(z) = -\frac{\Lambda_{42}}{\Lambda_{44}}\Omega_2(z) + \frac{D_2^{\infty}}{2\Lambda_{44}}\left\{\frac{z}{\sqrt{z^2-(a+\rho)^2}} - 1\right\} + \frac{D_s}{\pi\Lambda_{44}}\left\{\cot^{-1}\left(\frac{a}{z}\sqrt{\frac{z^2-(a+\rho)^2}{(a+\rho)^2-a^2}}\right) - \frac{z}{\sqrt{z^2-(a+\rho)^2}}\cos^{-1}\left(\frac{a}{a+\rho}\right)\right\} \tag{1.2.11}$$

where

$\Omega_2(z) = \frac{1}{2}\frac{\sigma_{22}^{\infty}\Lambda_{44} - D_2^{\infty}\Lambda_{24}}{\Lambda_{22}\Lambda_{44} - \Lambda_{24}\Lambda_{42}}\left\{\frac{z}{\sqrt{z^2-a^2}} - 1\right\}$, and Λ_{22}, Λ_{24}, Λ_{42}, Λ_{44} are the components of inverse of Irwin's matrix $\mathbf{H}^R$. The Irwin's matrix $\mathbf{H}^R$ depends only on the material properties and defined in Chapter 3.

And saturation zone length is determined from

$$\frac{a+\rho}{a} = \sec\left(\frac{\pi D_2^{\infty}}{2D_s}\right). \tag{1.2.12}$$

Chapter 2

Fundamentals of Piezoelectric Ceramics and an Overview of Development

Piezoelectricity stems from the Greek word "piezo" for pressure. It follows that a piezoelectric material develops a potential across its boundaries when subjected to a mechanical stress, and vice versa, when an electric field is applied to the material, a mechanical deformation ensues.

Piezoelectricity is a linear effect that is related to the microscopic structure of the solid. Some ceramic materials become electrically polarized when they are strained, this linear and reversible phenomenon is referred to as the direct piezoelectric effect and shown in Fig. 2.1. The direct piezoelectric effect is normally accompanied by the converse piezoelectric effect shown in Fig. 2.2 where a solid becomes strained when placed in an electric field. The microscopic origin of the piezoelectric effect is the displacement of ionic charges within a crystal structure. In the absence of external strain, the charge distribution within the crystal is symmetric and the net electric dipole moment is zero. However when an external stress is applied, the charges are displaced and the charge distribution is no longer symmetric. A net polarization develops and results in an internal electric field.

Piezoelectricity is a property possessed by a group of materials, discovered in 1880 by Pierre and Jacques Curie. In 1881, the term "piezoelectricity" was first suggested by W. Hankel, and the converse effect was deduced by Lipmann from thermodynamics principles.

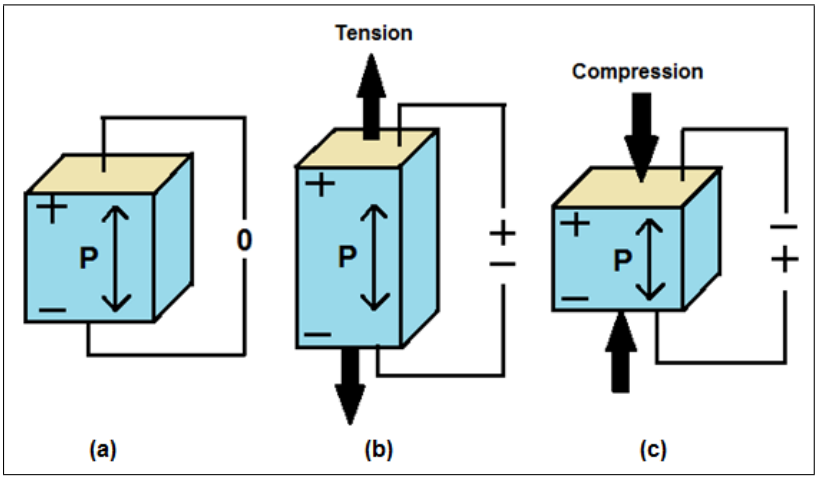

Figure 2.1: The direct piezoelectric effect

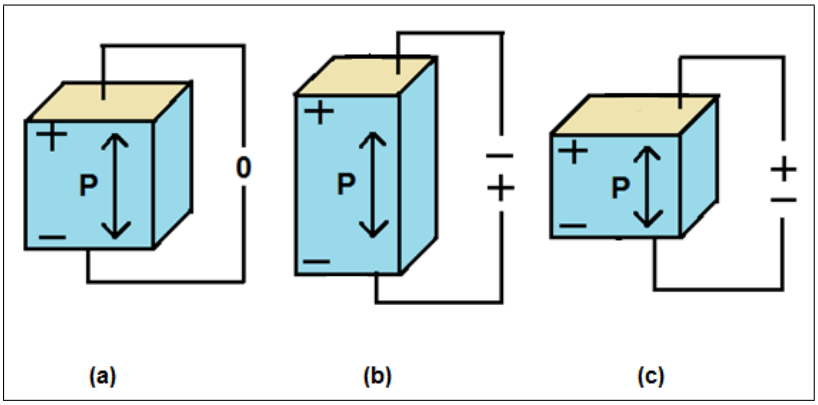

Figure 2.2: The reverse piezoelectric effect

2.1 Curie Temperature

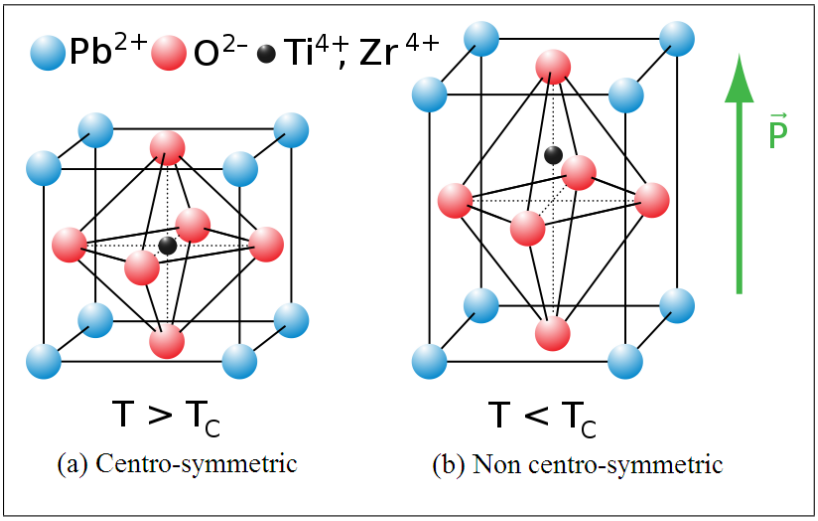

Figure 2.3: Tetragonal unit cell of PZT

The Curie temperature (T_c) in piezoelectric materials describes the temperature above which crystal structure changes from non-symmetrical (piezoelectric) to a symmetrical (non piezoelectric) form, expressed in degree Celsius. Hence, material loses its spontaneous polarization and piezoelectric characteristics.

Fig. 2.3 shows tetragonal unit cell of PZT above and below Curie temperature. Above the Curie temperature, the crystals are centrosymmetric but below this temperature the crystals are non-centrosymmetric.

2.2 Poling

Dipoles in the piezoelectric materials are permanently aligned with another for a useful macroscopic response through a process called poling. In poling process, material is heated above Curie temperature and inducing a DC voltage across the material. The direction of the field is the polarization direction, and dipoles shift into alignment with it. The material is then cooled below its Curie temperature while the poling field is maintained, with the result that alignment of the dipoles is permanently fixed. Material is now said to be poled.

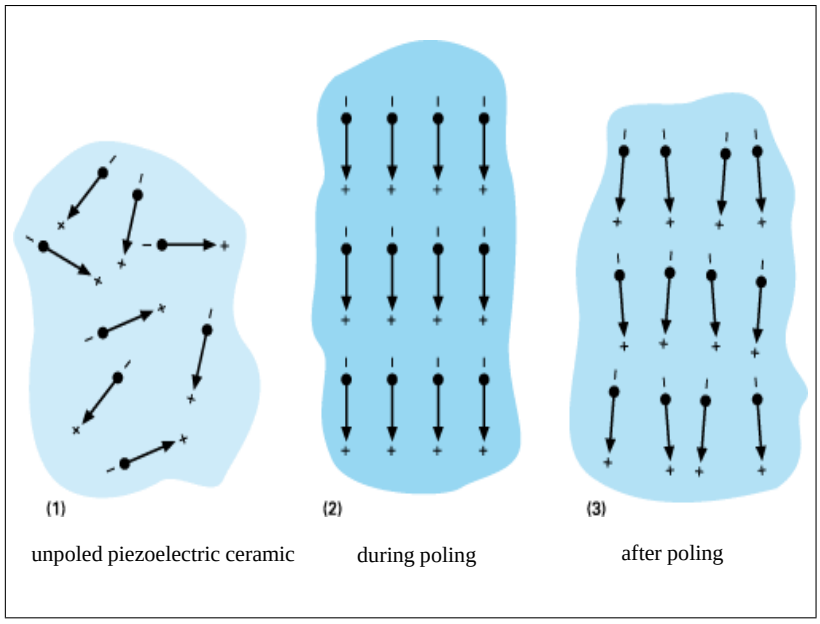

Figure 2.4: Polarizing a piezoelectric ceramic

When poled ceramic is maintained below Curie temperature and subjected to electric field than dipoles respond collectively to produce a macroscopic expansion

along the poling axis and contraction perpendicular to it. The development of poling process in which randomly oriented crystal axes are suitably aligned by the application of a strong electric field (smaller than one used in poling) at elevated temperature give rise to better and stable piezoceramics. Fig. 2.4 shows the direction of dipoles during polarizing process in piezoelectric ceramic.

For example, hard lead zirconium titanate (PZT) have Curie temperature above 300^0C and are not easily poled except at high temperatures. While soft PZT have Curie temperature below 200^0C and are readily poled or depoled at room temperature with strong electric fields.

2.3 Piezoelectric Constants

Piezoelectric ceramic being anisotropic, physical constants (elasticity, permittivity, etc.) relate to both the direction of the applied mechanical or electric loads and the direction perpendicular to the applied loads. Consequently, each constant generally has two subscripts that indicate the direction of the related quantities.

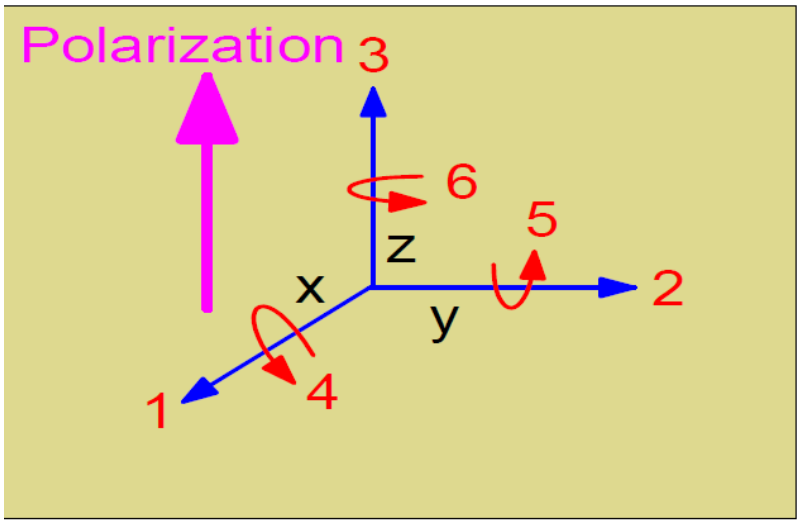

Figure 2.5: Directions of forces affecting a piezoelectric material

The direction of positive polarization is usually made to coincide with z-axis of a right handed rectangular system of x, y and z axes (Fig. 2.5). Direction x, y or z is represented by subscript 1, 2 or 3, respectively, and shear about one of these axes is represented by subscript 4, 5 or 6, respectively. The various constants may be written with subscript referring to these.

2.3.1 Dielectric constants

The permittivity or dielectric constants, κ_{ij} , for a piezoelectric ceramic material is the dielectric displacement per unit electric field. The first subscript indicate the direction of dielectric displacement; the second is the direction of electric field.

- κ_{11} permittivity for dielectric displacement and electric field in direction 1.
- κ_{33} permittivity for dielectric displacement and electric field in direction 3.
- κ_{13} permittivity for dielectric displacement in direction 1 and electric field in direction 3.

2.3.2 Piezoelectric voltage constant

The piezoelectric voltage constant, e_{ij}, is the electric field generated by a piezoelectric material per unit of mechanical stress applied to it. Alternatively, it is the mechanical strain experienced by the material per unit electric displacement applied to it. The first subscript refers to the direction of the electric field generated in the material or to the applied electric displacement, the second refers respectively to the direction of the applied stress or to the direction of the induced strain.

- e_{33} denotes induced electric field in direction 3 per unit stress applied in direction 3 or induced strain in direction 3 per unit electric displacement applied in direction 3.
- e_{31} denotes induced electric field in direction 3 per unit stress applied in direction 1 or induced strain in direction 1 per unit electric displacement applied in direction 3.
- e_{15} denotes induced electrical field in direction 1 per unit shear stress applied about direction 2 or induced shear strain about direction 2 per unit electric displacement applied in direction 1.

2.4 Fundamental Equations

The basic fundamental equations for piezoelectric ceramic are given below.

2.4.1 Constitutive equations

For transversely isotropic piezoelectric materials, constitutive equations are fully combined by electrical and mechanical material properties as

$$\sigma_{ij} = C_{ijks}\varepsilon_{ks} - e_{sij}E_s, \tag{2.4.1}$$

$$D_i = e_{iks}\varepsilon_{ks} + \kappa_{is}E_s. \tag{2.4.2}$$

Generally, two-index notations for elastic and piezoelectric constants are considered by replacing ij by p and ks by q i.e. $C_{ijks} = C_{pq}$ and $e_{iks} = e_{iq}$, where p, q assumes the values 1 to 6 according to following replacements $11 \to 1$, $22 \to 2$, $33 \to 3$, 23 or $32 \to 4$, 13 or $31 \to 5$, 12 or $21 \to 6$.

2.4.2 Gradient equations

(i) Strain-displacement relations are given as

$$\varepsilon_{ij} = \frac{1}{2}\left(u_{i,j} + u_{j,i}\right). \tag{2.4.3}$$

(ii) Relation between electric field and electric potential may be written as

$$E_i = -\phi_{,i}. \tag{2.4.4}$$

2.4.3 Equilibrium equations

(i) Stress equilibrium equations in absence of body force may be written as

$$\sigma_{ij,j} = 0. \tag{2.4.5}$$

(ii) Electric displacement equilibrium equation in absence of charge may be written as

$$D_{i,i} = 0. \tag{2.4.6}$$

The constitutive equations for a poled transversely isotropic piezoelectric ceramic with x_3 in the poling direction may be written as

$$\begin{pmatrix} \sigma_{xx} \\ \sigma_{yy} \\ \sigma_{zz} \\ \sigma_{yz} \\ \sigma_{xz} \\ \sigma_{xy} \end{pmatrix} = \begin{pmatrix} c_{11} & c_{12} & c_{13} & 0 & 0 & 0 \\ c_{12} & c_{11} & c_{13} & 0 & 0 & 0 \\ c_{13} & c_{13} & c_{33} & 0 & 0 & 0 \\ 0 & 0 & 0 & c_{44} & 0 & 0 \\ 0 & 0 & 0 & 0 & c_{44} & 0 \\ 0 & 0 & 0 & 0 & 0 & c_{66} \end{pmatrix} \begin{pmatrix} \varepsilon_{xx} \\ \varepsilon_{yy} \\ \varepsilon_{zz} \\ \varepsilon_{yz} \\ \varepsilon_{xz} \\ \varepsilon_{xy} \end{pmatrix} - \begin{pmatrix} 0 & 0 & e_{31} \\ 0 & 0 & e_{31} \\ 0 & 0 & e_{33} \\ 0 & e_{15} & 0 \\ e_{15} & 0 & 0 \\ 0 & 0 & 0 \end{pmatrix} \begin{pmatrix} E_x \\ E_y \\ E_z \end{pmatrix}, \tag{2.4.7}$$

$$\begin{pmatrix} D_x \\ D_y \\ D_z \end{pmatrix} = \begin{pmatrix} 0 & 0 & 0 & 0 & e_{15} & 0 \\ 0 & 0 & 0 & e_{15} & 0 & 0 \\ e_{31} & e_{31} & e_{33} & 0 & 0 & 0 \end{pmatrix} \begin{pmatrix} \varepsilon_{xx} \\ \varepsilon_{yy} \\ \varepsilon_{zz} \\ \varepsilon_{yz} \\ \varepsilon_{xz} \\ \varepsilon_{xy} \end{pmatrix} + \begin{pmatrix} \kappa_{11} & 0 & 0 \\ 0 & \kappa_{11} & 0 \\ 0 & 0 & \kappa_{33} \end{pmatrix} \begin{pmatrix} E_x \\ E_y \\ E_z \end{pmatrix}, \tag{2.4.8}$$

where $c_{66} = (c_{11} - c_{12})/2$.

2.5 Crack Face Boundary Conditions

The boundary conditions on crack face are categorized as impermeable, permeable and semi-permeable. These crack face boundary conditions may be represented mathematically as

(i) Impermeable boundary conditions

Impermeable crack-face boundary condition was proposed by Deeg [23] may be expressed as,

$$D_n(x, 0^+) = D_n(x, 0^-) = 0. \tag{2.5.1}$$

Here the superscripts + and − denote the value of function at the top and bottom crack faces.

(ii) Permeable boundary conditions

Permeable boundary condition was proposed by Parton [99] and mathematically

be written as,

$$\phi(x,0^+) = \phi(x,0^-),\ D_n(x,0^+) = D_n(x,0^-). \tag{2.5.2}$$

(iii) Semi-permeable boundary conditions

Semi-permeable boundary conditions proposed by Hao and Shen [50] for piezoelectric ceramics are more realistic boundary conditions and may be given as

$$D_n(x,0^+) = D_n(x,0^-),\ D_n(x,0^+)[u(x,0^+) - u(x,0^-)] = -\kappa_a[\phi(x,0^+) - \phi(x,0^-)]. \tag{2.5.3}$$

Semi-permeable boundary conditions can be reduced into impermeable when $\kappa_a = 0$, and to permeable when the jump in mechanical displacement vanishes. The pictorial representation of these boundary conditions is depicted in Fig. 2.6.

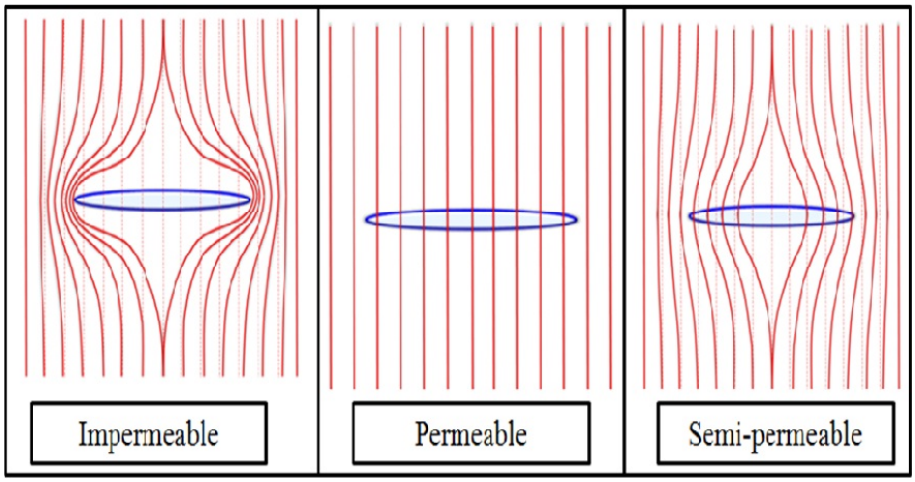

Figure 2.6: Different crack-face boundary conditions in piezoelectric ceramics

2.6 Material Constants for Piezoelectric Ceramics

Material constants for various piezoelectric ceramics considered for the analysis in the thesis is taken from Ou and Chen [92] and tabulated in Table 2.1.

Table 2.1: Material parameters of various piezoelectric ceramics

Material constants	PZT-5H	PZT-4	PZT-6B	PZT-7A	$BaTiO_3$
$c_{11}(10^{10}N/m^2)$	12.6	13.9	16.8	14.8	15
$c_{12}(10^{10}N/m^2)$	7.95	7.78	6.00	7.62	6.60
$c_{13}(10^{10}N/m^2)$	8.41	7.43	6.00	7.42	6.60
$c_{33}(10^{10}N/m^2)$	11.7	11.3	16.3	13.1	14.6
$c_{44}(10^{10}N/m^2)$	2.30	2.56	2.71	2.54	4.4
$e_{13}(C/m^2)$	-6.50	-6.98	-0.90	-2.10	-4.34
$e_{33}(C/m^2)$	23.3	13.8	7.10	9.50	17.5
$e_{15}(C/m^2)$	17.44	13.4	4.60	9.70	11.4
$\kappa_{11}[10^{-10}C/(V.m)]$	150.3	60.0	36.0	81.1	98.7
$\kappa_{33}[10^{-10}C/(V.m)]$	130	54.7	34.0	73.5	112

2.7 Fundamental Formulation and Solution Methodology

The methodology presented here is recapitulated from Zhang and Gao [138] for the self-sufficiency of the thesis.

For a two-dimensional problems all the field variables depend on x_1 and x_2. Therefore, we introduced the generalized displacement vector, $\mathbf{u}$, from Barnett and Lothe [2] as

$$\mathbf{u} = [u_1, u_2, u_3, \phi]^T = \mathbf{a} f(x_1 + p x_2), \tag{2.7.1}$$

where $f(x_1 + p x_2)$ is an analytic function, p is a complex number and $\mathbf{a}$ is a constant four element column vector. Equations (2.4.1 to 2.4.6) satisfy Equation (2.7.1) for an arbitrary function $f(x_1 + p x_2)$ if

$$[\mathbf{W} + p(\mathbf{R} + \mathbf{R}^T) + p^2 \mathbf{Q}]\mathbf{a} = 0, \tag{2.7.2}$$

which has non-trivial solution only if

$$|\mathbf{W} + p(\mathbf{R} + \mathbf{R}^T) + p^2 \mathbf{Q}| = 0. \tag{2.7.3}$$

The matrices $\mathbf{W}$, $\mathbf{R}$ and $\mathbf{Q}$ are given by

$$\mathbf{W} = \begin{bmatrix} c_{i1k1} & e_{11i} \\ e_{11i}^T & -\kappa_{11} \end{bmatrix},\ \mathbf{R} = \begin{bmatrix} c_{i1k2} & e_{21i} \\ e_{12i}^T & -\kappa_{12} \end{bmatrix},\ \mathbf{Q} = \begin{bmatrix} c_{i2k2} & e_{22i} \\ e_{22i}^T & -\kappa_{22} \end{bmatrix},\ i,k = 1,2,3. \tag{2.7.4}$$

Equation (2.7.3) has eight roots which are denoted by p_α and $\overline{p_\alpha}$ ($\alpha = 1,2,3,4$). The conditions of positive definiteness of the strain energy and electrical energy densities give that p_α is not real. To determine p_α the following standard eigen-equations are solved

$$\mathbf{N}\boldsymbol{\zeta} = p\boldsymbol{\zeta}, \tag{2.7.5}$$

where, $\mathbf{N} = \begin{pmatrix} \mathbf{N}_1 & \mathbf{N}_2 \\ \mathbf{N}_3 & \mathbf{N}_1^T \end{pmatrix}$, $\boldsymbol{\zeta} = \begin{pmatrix} \mathbf{a} \\ \mathbf{b} \end{pmatrix}$, $\mathbf{N}_1 = -\mathbf{Q}^{-1}\mathbf{R}^T$, $\mathbf{N}_2 = \mathbf{Q}^{-1} = \mathbf{N}_2^T$, $\mathbf{N}_3 = \mathbf{R}\mathbf{Q}^{-1}\mathbf{R}^T - \mathbf{W} = \mathbf{N}_3^T$.

According to Stroh formalism [117] the general solution of Equations (2.4.1 to 2.4.6) may be given as

$$\mathbf{u}_{,1} = \mathbf{A}\mathbf{F}(z) + \overline{\mathbf{A}}\overline{\mathbf{F}(z)}, \tag{2.7.6}$$

$$\boldsymbol{\Phi}_{,1} = \mathbf{B}\mathbf{F}(z) + \overline{\mathbf{B}}\overline{\mathbf{F}(z)}, \tag{2.7.7}$$

where, $\mathbf{A} = (\mathbf{a}_1, \mathbf{a}_2, \mathbf{a}_3, \mathbf{a}_4)$, $\mathbf{B} = (\mathbf{b}_1, \mathbf{b}_2, \mathbf{b}_3, \mathbf{b}_4)$, $\mathbf{F}(z) = \frac{d\mathbf{f}(z)}{dz}$, $z_\alpha = x_1 + p_\alpha x_2$, $\mathbf{f}(z_\alpha) = [f_1(z_1), f_2(z_2), f_3(z_3), f_4(z_4)]^T$.

The column vector of matrix $\mathbf{B} = (\mathbf{b}_1, \mathbf{b}_2, \mathbf{b}_3, \mathbf{b}_4)$ is related to the column vector of matrix $\mathbf{A} = (\mathbf{a}_1, \mathbf{a}_2, \mathbf{a}_3, \mathbf{a}_4)$ in the following form

$$\mathbf{b}_k = (\mathbf{R}^T + p_k\mathbf{Q})\mathbf{a}_k,\ k = 1,2,3,4.$$

and $\boldsymbol{\Phi}$ is the generalized stress function such that

$$\boldsymbol{\sigma}_2 = [\sigma_{2j}, D_2]^T = \boldsymbol{\Phi}_{,1},\ \boldsymbol{\sigma}_1 = [\sigma_{1j}, D_1]^T = -\boldsymbol{\Phi}_{,2}. \tag{2.7.8}$$

The problem is completely solved if we know the values of $\boldsymbol{\Phi}$ and $\mathbf{u}$. To find the values of $\boldsymbol{\Phi}$ and $\mathbf{u}$ a complex variable formulation for crack problems are recapitulated below.

2.7.1 Complex Representation of Stress

As is well-known the stress component, σ_{22}, may be expressed in terms of two complex potentials $\Psi(z)$ and $\chi(z)$ as

$$\sigma_{22} = \Psi(z) + \chi(\overline{z}) - (z - \overline{z})\overline{\Psi'(z)}, \tag{2.7.9}$$

where bar over the function represents their complex conjugate.

Crack problems discussed in the thesis are mathematically modeled and reduce to the Hilbert problems and methodology to solve these Hilbert problems is discussed in details below. Consequently the next sections are devoted to the concepts required for Hilbert problem.

2.7.2 Sectionally Holomorphic Function

Let S denote the plane cut along $L(= \bigcup_{i=1}^{n} L_i)$, where L_i are simple non-intersecting arcs in complex z-plane. The end points of L_i, if any, are denoted by a_i and $b_i (i = 1, 2....n)$, respectively.

The function $F(z)$ defined on S, except on L, is said to be sectionally holomorphic, if it satisfies the following conditions:

(i) The function $F(z)$ is holomorphic everywhere in S.

(ii) The function $F(z)$ is continuous from the left and from the right at all points on L, other than the end points a_k, b_k of $L_k (k = 1, 2...n)$.

(iii) Near the end points a_k and b_k,
$|F(z)| < \frac{A}{|z-d|^{\mu}}, \quad 0 \leq \mu < 1,$
where d is any one of the ends a_k, b_k and μ is a positive constant satisfying above stated conditions.

2.7.3 Hilbert Problem (Problem of Linear Relationship)

Statement: To find the sectionally holomorphic function $F(z)$, with line of discontinuity L, the boundary values of which from the left $F^+(t)$ and from the right $F^-(t)$ satisfy the condition

$$F^+(t) = G(t)F^-(t) + f(t), \text{ on } L, \tag{2.7.10}$$

except at the end points, $G(t)$ and $f(t)$ are the known functions on L and $G(t) \neq 0$, everywhere on L.

If $f(t) = 0$, everywhere on L the problem is called homogeneous Hilbert problem. From the point of view of this thesis the cases (I) $G(t) = 1$ and (II) $G(t) = -1$ are important and solutions for these cases are described below.

2.7.3.1 Case I: $G(t) = 1$

The Hilbert problem described above in this case may be stated as follows: find the sectionally holomorphic function $F(z)$, with line of discontinuity L, the boundary values of which from the left and from the right satisfy the condition

$$F^+(t) - F^-(t) = f(t), \text{ on } L, \tag{2.7.11}$$

except at the end points and $f(t)$ is the known function on L.

The solution of Equation (2.7.11) may be written using Cauchy's Integral formula and Liouville's theorem as

$$F(z) = \frac{1}{2\pi i} \int_L \frac{f(t)}{t - z} dt + C, \tag{2.7.12}$$

where C is an arbitrary constant.

If it is assumed that the sectionally holomorphic function $F(z)$, to be determined, may have pole of order not greater than m at infinity, then the solution of Equation (2.7.11) may be written as

$$F(z) = \frac{1}{2\pi i} \int_L \frac{f(t)}{t - z} dt + P_m(z), \tag{2.7.13}$$

where $P_m(z) = C_0 z^m + C_1 z^{m-1} + C_2 z^{m-2} + \text{.....} + C_m$, and $C_i (i = 0, 1, 2....m)$ are arbitrary constants to be determined by the boundary conditions of the problem under consideration.

According to Muskhelishvili [85] most general solution of Equation (2.7.11), when $F(z)$ is assumed to have poles of order not greater than $m_1, m_2.....m_n$ and m at the given points $z_1, z_2.....z_n$ and ∞ may be written as

$$F(z) = \frac{1}{2\pi i} \int_L \frac{f(t)}{t - z} dt + R(z), \tag{2.7.14}$$

where,

$$R(z) = \sum_{i=j}^{l} \left\{ \frac{D_{j1}}{(z-z_j)} + \frac{D_{j2}}{(z-z_j)^2} + ... + \frac{D_{jm_j}}{(z-z_j)^{m_j}} \right\} + P_m(z), \tag{2.7.15}$$

and $D_{ij}(i, j = 1, 2....n)$ are arbitrary constants.

2.7.3.2 Case II: $G(t) = -1$

The Hilbert problem in this case may be stated as follows: find the sectionally holomorphic function $F(z)$, with line of discontinuity L, the boundary values of which from the left and from the right satisfy the condition

$$F^+(t) + F^-(t) = f(t), \text{ on } L, \tag{2.7.16}$$

except at the end points and $f(t)$ is the known function on L.

To obtain the complete solution of the above problem, the general solution is found first for the homogeneous case when

$$F^+(t) + F^-(t) = 0, \text{ on } L, \tag{2.7.17}$$

The general solution of the Equation (2.7.17) may be written as

$$F(z) = X_0(z)P_n(z), \tag{2.7.18}$$

where $P_n(z) = C_0z^n + C_1z^{n-1} + C_2z^{n-2} + ... + C_n$ and $C_i(i = 0, 1, 2...n)$ are arbitrary constants to be determined by using the boundary conditions of the problem under consideration. And

$$X_0(z) = \prod_{j=1}^{n} (z-a_j)^{-1/2}(z-b_j)^{-1/2}. \tag{2.7.19}$$

We now find out the particular solution for

$$F^+(t) - gF^-(t) = f(t), \text{ on } L, \tag{2.7.20}$$

$$\text{where } g = \frac{X_0^+(t)}{X_0^-(t)}, \text{ on } L. \tag{2.7.21}$$

For present case $g = G(t) = -1$ and hence using the relation (2.7.21), $X_0^+(t) = -X_0^-(t)$, satisfied between the left hand and right hand values of $X_0(z)$ on L.

The Equation (2.7.20) may be re-written as

$$\frac{F^+(t)}{X_0^+(t)} - \frac{F^-(t)}{X_0^-(t)} = \frac{f(t)}{X_0^+(t)}, \text{ on } L. \tag{2.7.22}$$

The particular solution of which may be written as

$$F(z) = \frac{X_0(z)}{2\pi i} \int_L \frac{f(t)}{X_0^+(t)(t-z)} dt. \tag{2.7.23}$$

The general solution of Equation (2.7.16) may now be written combining solutions obtained in Equations (2.7.18 and 2.7.23) as

$$F(z) = \frac{X_0(z)}{2\pi i} \int_L \frac{f(t)}{X_0^+(t)(t-z)} dt + X_0(z)P_n(z). \tag{2.7.24}$$

Finally, most general solution for the case when $F(z)$ has poles of order not greater than $m_1, m_2.....m_n$ and m at the points $z_1, z_2.....z_n$ and ∞ may be written as

$$F(z) = \frac{X_0(z)}{2\pi i} \int_L \frac{f(t)}{X_0^+(t)(t-z)} dt + X_0(z)R(z), \tag{2.7.25}$$

where $R(z)$ is a rational function of the form

$$R(z) = \sum_{i=j}^{l} \left\{ \frac{D_{j1}}{(z-z_j)} + \frac{D_{j2}}{(z-z_j)^2} + ... + \frac{D_{jm_j}}{(z-z_j)^{m_j}} \right\} + P_n(z). \tag{2.7.26}$$

2.7.4 Problem for Plane cut along Straight Cracks

Consider a plate occupying the x_1ox_2 plane and cut along n-collinear straight cracks $L_i(i = 1, 2....n)$, with end points a_i, b_i, lying on ox_1-axis.

The rims of the cracks are subjected to uniform constant stress, σ_{22}, then Equation (2.7.9) yields, following Hilbert problems, under the assumption $\lim_{x_2 \to \infty} x_2\Psi'(t + ix_2) = 0$, where t being any point on $L_i(i = 1, 2....n)$

$$\Psi^+(t) + \chi^-(t) = \sigma_{22}^+; \qquad \Psi^-(t) + \chi^+(t) = \sigma_{22}^-. \tag{2.7.27}$$

The superscripts $+$ and $-$ denote the value of the function as it is approached from $x_2 > 0$ or $x_2 < 0$, respectively.

Adding and subtracting above two Hilbert problems, they may be re-written as

$$[\Psi(t) + \chi(t)]^+ + [\Psi(t) + \chi(t)]^- = \sigma_{22}, \tag{2.7.28}$$

$$[\Psi(t) - \chi(t)]^+ - [\Psi(t) - \chi(t)]^- = 0. \tag{2.7.29}$$

The solutions of Equations (2.7.28 and 2.7.29) may directly be written using Equations (2.7.12 and 2.7.24) as

$$\Psi(t) + \chi(t) = \frac{1}{2\pi i X(z)} \int_L \frac{X(t)\sigma_{22}}{t-z} dt + \frac{2P_n(z)}{X(z)}, \tag{2.7.30}$$

$$\Psi(t) - \chi(t) = -\overline{\Gamma}', \tag{2.7.31}$$

respectively, where

$$X(z) = \prod_{j=1}^{n} (z-a_j)^{1/2}(z-b_j)^{1/2}, \tag{2.7.32}$$

$$P_n(z) = C_0 z^n + C_1 z^{n-1} + C_2 z^{n-2} + ... + C_n, \tag{2.7.33}$$

$$\overline{\Gamma}' = -\frac{1}{2}(N_1 - N_2)e^{-2\beta i}, \tag{2.7.34}$$

and N_1, N_2 being the values of principal stresses prescribed at infinity, β is the angle between N_1 and ox_1-axis. The constant C_0 is determined using a boundary condition at infinity, and constants $C_i (i = 1, 2....n)$ are determined using the condition of single-valuedness of displacements on crack rims.

2.8 Overview of the Subject Development

By now composite piezoceramics have made an active research group because of their great utility in sensors/actuators/transducers. Many types of attire of these materials have drawn the attention of researchers depending upon their probable use. One such aspect is cracking of piezoceramics. Much work has been done on cracking of piezoceramics. The work on cracking of piezoelectric media was started back in 1980.

Parton [99] initiated the work on crack problems for piezoelectric materials by considering the problem of a finite conducting crack at the interface of a piezoelectric material and subjected to a far-field uniform tension.

Deeg [23] implemented the Green's function and dislocation method to study a more general defect mechanics of piezoelectric material. He considered impermeable crack face boundary conditions for this study.

Sosa and Pak [116] performed three dimensional analysis for a semi-infinite crack embedded in an unbounded transversely isotropic piezoelectric medium using eigenfunction expansion method.

Pak [94] studied a crack problem under out-of-plane deformation and in-plane electric loads. It was found that crack extension force is always negative in absence of mechanical load. It was also analyzed that for a given mechanical load, presence of electrical load could either promote or retard the crack growth, depending on magnitude and direction of electric load.

Pak [95] generalized the concept of linear elastic fracture mechanics and dislocation method to study the influence of the electric field on fracture behavior of piezoelectric materials. The study of crack tip singular stress field and the expressions for energy release rate were also presented.

Sosa [115] studied a center crack problem in an infinite two-dimensional piezoelectric medium using complex potential formulation. And derived the asymptotic expressions for the electromechanical fields in the vicinity of the crack.

Suo et al. [118] employed extended Stroh formalism to study the crack either in piezoelectric material, or at the interface between piezoelectric materials.

Tobin and Pak [120] performed the Vicker's indentation tests in poled piezoelectric material with a high electric field. It was found that its apparent fracture toughness may either decrease or increase, depending on the direction of applied electric field.

Hao and Shen [50] proposed a new electric boundary condition in which electric permeability of air in a crack gap was considered. It was found that electric permeability of air in a crack gap reduce the value of electric displacement intensity factor than impermeable crack. The effect of different crack face electric boundary conditions on the fracture mechanics of piezoelectric solids was studied by many researchers [25, 71, 127, 128] etc.

Park and Sun [98] used Stroh formalism to solve the problem of fracture for an infinite piezoelectric medium containing a center crack subjected to electromechanical loads. Closed form analytic expressions were derived for strain energy release rate, total energy release rate and mechanical energy release rate, and suitability of these fracture criterion were also discussed.

Liang and Hwu [76] solved the problem of holes, cracks and interface cracks in an infinite piezoelectric medium using the extended Stroh formalism. Special boundary

element method was used to solve the problem of finite piezoelectric plates containing holes and cracks.

Gao and Fan [40] analyzed the two-dimensional problem of an infinite piezoelectric material containing a center crack using Stroh formalism technique. It was found that the impermeable crack assumption is not valid in analyzing the fracture mechanics of piezoelectric materials.

Gao and Wang [36] gave a solution of the total energy release rate in piezoelectric media with a crack. The effect of electric field inside the crack on total energy release rate was computed. Finally, the total energy release rate was found by respective contribution of energy in the media and inside the crack.

McMeeking [82] summarized the fracture mechanics theory for brittle piezoelectric materials consistent with standard features of elasticity and dielectricity. The influence of electromechanical loads was considered in this approach and Griffith's style energy balance was used to establish the relevant energy release rates.

Shindo et al. [109] solved the plane strain electroelastic crack problem of an orthotropic piezoelectric ceramic strip. The central crack was situated symmetrically and oriented in a direction normal to the strip edges. Numerical values of intensity factors and energy release rate for some piezoelectric ceramics were obtained to display electroelastic interactions.

Kwon and Lee [65] employed Fourier transform and Fourier sine series to study the rectangular piezoelectric ceramic body containing a Griffith center crack under anti-plane shear loading. Numerical values of stress intensity factor and the energy release rate are obtained to show the influence of electric field.

Xu and Rajapakse [133] employed Lekhnitskii's complex potential and distributed dislocation method to study the plane problem of a brittle piezoelectric material with an arbitrary oriented branch crack. It was found that the branch length, branch angle, crack orientation and the type of loading affect asymptotic electroelastic fields at a branch tip.

Sih and Zuo [111] explored a multiscale nature of cracking in ferroelectric ceramics vis-a-vis the crack growth enhancement and retardation behavior when the direction of applied electric field was reversed with reference to that of poling by

application of energy density criterion.

Gao and Wang [38] employed Stroh's formalism to solve the problem of a permeable interface crack between two dissimilar piezoelectric media. The fundamental solutions for the Green's function and the field intensity factors were also presented.

Xu and Rajapakse [134] also investigated the influence of electric boundary conditions and crack orientation on fracture mechanics parameters by solving an elliptical crack problem in a piezoelectric plane using the approach of Lekhnitskii's complex potential function.

Wang and Mai [121] studied a cracked piezoelectric strip under combined mechanical and electrical loads using Fourier integral transform technique. The three benchmark problems namely an edge-cracked, double edge-cracked and a center-cracked strip were considered and numerical solution under both permeable and impermeable crack face electric boundary conditions were obtained.

Beom and Atluri [5] investigated the effect of electric fields on fracture behavior of ferroelectric ceramics subjected to combined electric and mechanical loading considering a semi-infinite crack lying perpendicular to the poling direction in a ferroelectric ceramic. Relations between the crack tip stress intensity factor and the applied intensity factors of stress and electric displacement were obtained.

Beom et al. [6] studied the problem of subinterface crack lying parallel to an interface between two dissimilar piezoelectric solids. Relations between the intensity factors for subinterface crack and interface crack were obtained for conducting and insulating crack.

Li and Tang [72] studied the problem of anti-plane permeable crack situated in the interface between two bonded dissimilar piezoelectric layers subjected to longitudinal shear stress and electric loading. The field intensity factors and energy release rate were obtained in terms of auxiliary function.

Li [68] proposed a mode III permeable crack model to analyse the crack growth in a piezoelectric ceramic. Both local and global energy release rates were derived based on permeable crack solution. It was found that global energy release rate derived for permeable crack was in broad agreement with some known experimental observations [98]. Thus it might be considered as a fracture criterion for piezoelectric

materials in general.

Huang and Kuang [53] presented a mixed boundary value problem for a $2D$ crack, in the sense that the crack face was partially conducting and partially impermeable. They found that the electric field and electric displacement were singular not only at the crack tips but also at the junctures between the conducting part and impermeable parts.

Zhang and Gao [138] presented theoretical and experimental analyses of the failure and fracture behaviors of piezoelectric materials. A charge-free zone model for conducting cracks in the depoled lead zirconate titanate was considered to understand the failure behavior under electrical and/or mechanical loads.

Gao et al. [39] examined the energy release rate and the J-integral of an electrically insulated crack in an infinite piezoelectric medium under remotely uniform combined electro-mechanical loads. It was found that the energy release rate is the sum of the J-integral around the crack tip and the average driving force produced by the electric field on the entire crack surface.

Chen et al. [17] solved the physical problem of semi-infinite crack interacting with a line dislocation under the loading of a line force and a line charge in $2D$ infinite anisotropic piezoelectric medium. It was found that the image force always attracted the dislocation to the crack tip in the case of a conventional crack, while it always repelled the dislocation for the anti-crack case.

Jelitto et al. [59] presented an experimental method to measure all the components of the total energy release rate in a piezoelectric material under conditions of control crack growth in a four-point-bending device. They concluded that total energy release rate, almost vanish and could not be taken as a valid fracture criterion.

Gao et al. [35] used Stroh formalism to study the interaction of an electric dipole with an interface crack between two dissimilar piezoelectric materials. Three crack models, the electrically impermeable, permeable and conducting cracks were studied. Numerical calculations were performed to investigate the effect of the dipole's rotation on energy release rate at the crack tip. It was found that the energy release rate for all the three crack models reach their maximum values when

the direction of dipole was perpendicular to the crack surface.

Huang and Wang [52] investigated the dynamic behavior of a piezoelectric layer bonded to an elastic medium containing multiple interfacial cracks subjected to steady state mechanical loads. The effect of the geometry of the cracks, the material constants and the loading frequency of the incident Love wave upon the dynamic SIF is examined and discussed.

Chen and Ou [18] investigated the problem of a center crack in an infinite piezoelectric material to evaluate electric potential drop across the crack. It was found that, under moderate mechanical loadings the crack opened less, the electric potential drop was very high under highly applied electric field, which might lead to electric discharge.

Li and Chen [67] studied the semi-permeable interface crack problem between dissimilar piezoelectric materials for accounting the permittivity of the medium inside the crack gap. The model showed more physically reasonable features than either the impermeable interface crack model or the permeable interface crack model.

Mukherjee and Das [84] analyzed the interaction of three interfacial Griffith cracks between bonded dissimilar orthotropic half-planes. Also, Das et al. [21, 22] determined the stress intensity factor around a moving interfacial Griffith crack between an elastic orthotropic half-plane and a dissimilar orthotropic layer.

Sills et al. [112] examined a conservative M-integral for calculating intensity factors of impermeable cracks in piezoelectric materials. The accuracy of this integral was examined for various loading situations in which the crack may be parallel, perpendicular or at some angle to the poling direction.

Rao and Kuna [102–104] used the interaction integrals for computation of the stress and electric displacement intensity factors for cracks in functionally graded piezoelectric/piezoelectromagnetic materials.

Motola et al. [83] presented fracture test on four-point bend specimens for poled and unpoled PZT-5H ceramic. The crack faces were parallel to the poling direction. Fracture tests on four-point bend PIC-151 specimens with the crack faces perpendicular to the poling directions were also analyzed. Excellent agreement was found between the fracture curve and the experimental results of the specimens with the

crack faces perpendicular to the poling direction.

Beom et al. [7] presented electrical fracture tests to study the influence of the directions of poling and electrical loading for a piezoelectric ceramic with a conductive crack under purely electrical loading. It was observed that positive electric field could decrease the breakdown resistance of piezoelectric materials, whereas a negative electric field could increase the breakdown resistance of piezoelectric materials. Also the poling direction could effect the breakdown resistance of piezoelectric materials.

Kuna [63] gave a detailed survey of different techniques to solve piezoelectric fracture mechanics problems and present status of the work done in piezoelectric materials. Cracks under static, cyclic and dynamic loading by electrical and mechanical fields were taken into account.

Fan and Zhao [27] studied the influence of an arbitrary poling direction and electric boundary conditions on fracture behavior for a finite crack in two-dimensional infinite piezoelectric medium.

Guo et al. [49] solved the problem of a semi-infinite crack in a piezoelectric strip under the anti-plane shear stress and the in-plane electric field via complex function method and the conformal mapping technique. The analytic closed form expressions were derived for the field intensity factors and mechanical strain energy release rate. Numerical case study was also given to show the influence of the loaded crack length, height of the strip and prescribed mechanical/electrical loads on mechanical strain energy release rate.

Li et al. [74] solved the problem of center mode-I crack in a piezoelectric strip based on real fundamental solution. Mixed boundary value conditions of the crack were transformed into Cauchy singular integral equations, which were then solved numerically to get the fracture parameters including the energy release rate and intensity factors.

Due to the tendency of developing multiple cracks in piezoelectric ceramics, the interaction among these cracks played an important role in the fracture behavior of these type of materials.

Gao and Wang [41] employed the Stroh formalism to solve the generalized $2D$

problem in piezoelectric media with N-collinear cracks subjected to uniform loads at infinity. It was found that the stress intensity factor remained the same as that of an isotropic material when uniform loads were applied. While the intensity factor of electric displacement depended on both the material properties and mechanical loads, but not on the applied electric loads. Also, it was shown that the electric field inside any crack was not equal to zero.

Gao and Wang [37] studied the generalized $2D$ problem of collinear interfacial permeable cracks, between two dissimilar piezoelectric media subjected to piecewise uniform loads at infinity, by means of the Stroh formalism. Explicit, closed from expressions were derived for the electric field inside cracks, complex potentials in piezoelectric media and field intensity factors near the crack tips.

Zhou et al. [141] investigated the problem of two collinear impermeable anti-plane shear cracks in a piezoelectric layer bonded to two half spaces, using the Fourier transform and Schmidt method. It was noted that stress intensity factor depended on the geometry of the interacting cracks as well as piezoelectric constants of the material.

Li [70] analyzed the anti-plane problem of two collinear cracks of equal length and normal to the strip boundaries in an infinitely long piezoelectric strip of finite width, using the Fourier series method. Closed form analytic expressions were derived for the electro-elastic field.

Gao and Balke [33] investigated the anti-plane problem of N arc-shaped interfacial permeable cracks between a circular piezoelectric inhomogeneity and an infinite piezoelectric matrix, by means of the complex variable method. Explicit expressions were presented for the electric field on the crack faces, complex potentials in media and the intensity factors near the crack-tips.

Zhong and Li [140] used the Fourier transform technique to investigate the problem of two collinear permeable anti-plane cracks lying at the mid-plane of a piezoelectric strip. Numerical case study was presented for PZT-5H piezoelectric ceramic, and the results revealed that the effect of electric field on crack growth in piezoelectric materials strongly depended on applied elastic displacement.

Zhou and Wu [143] employed the Schmidt method to solve the problem of two

parallel cracks or four parallel cracks in the piezoelectric materials for the permeable crack face electric boundary conditions. The effects of the distance between two parallel cracks as well as two collinear cracks on the stress and electric intensity factors were analyzed.

Xiao et al. [131] studied the interaction between a screw dislocation and collinear rigid lines along the interface of two dissimilar piezoelectric media using complex variable and perturbation techniques under remote anti-plane mechanical and in-plane electrical loads. The rigid lines were either conducting or dielectric. The influence of the angular position of the dislocation, material properties and electromechanical coupling factor on the force was studied.

Liang [75] applied the non-local theory and Fourier integral transform to obtain the solution of two collinear cracks in a piezoelectric plane subjected to uniform tension load. Numerical case study were presented to show the effects of interaction of two cracks, the material constants and the lattice parameters on the stress field and the electric displacement field near the crack tips.

Li and Lee [73] presented the problem of two unequal collinear cracks in a piezoelectric plane under mode-I electromechanical loads via a new approach. Parametric studies were conducted to reveal the effects of crack space, crack length, electric loading and remanent electric displacement on energy release rate. It was found that negative electric displacement loading could decrease both the total energy release rate (TERR) and the mechanical strain energy release rate (MSERR). Positive electric displacement loading could enhance MSERR, but it could reduce TERR.

Lu et al. [81] solved the fracture problem of two semi-infinite collinear impermeable cracks in a piezoelectric strip under the anti-plane shear stress and in-plane electrical loads, by means of complex function method and conformal technique. Analytical expressions of the field intensity factors and the mechanical strain energy release rate were derived. Numerical case study were presented to show the influence of loaded crack length, the width of the strip, the distance between the two crack tips, and the prescribed electro-mechanical loads on the mechanical strain energy release rate.

Feng et al. [31] investigated the problem of multiple cracks on the interface between a piezoelectric layer and an orthotropic substrate. The method of dislocation simulation and singular integral equation were used to solve the crack problem. The theoretical derivation was verified by the classical result for a special case.

Analysis based on a linear piezoelectric model predicts that an electric field does not produce any stress intensity factor and positive driving force for a crack. However, experimental observations [94, 98, 125] suggested that crack growth could be enhanced or retarded by prescribed electric field. In order to explain experimental observations, a simplified model of perfect electrical displacement saturation had been used to cracks for piezoelectric materials.

Gao et al. [43] proposed a strip saturation model for a finite crack in an infinite poled piezoelectric plate. In this model the electrical saturation accounted was based on a generalization of the Dugdale [24] approach. The concept of local and global energy release rates were defined and discussed. It was found that the local energy release rate gave predications in broad agreement with experimental observations. Further, it was observed that the local energy release rate is independent of strength and size of the electrical yielding.

Gao and Barnett [42] provided the proof of an interesting result coming out of the simplified analysis in the paper of Gao et al. [43] that the local energy release rate was independent of strength and size of the electrical yielding. Further, the significance of local energy release rate based on linear piezoelectric crack analysis proved that it could be used as a fracture criterion.

Ru [106] proposed a strip saturation model for a finite crack in a piezoelectric medium of limited electrical polarization and evaluated stress intensity factor induced by electric field. The effect of saturation condition on crack tip field and the stress intensity factor was examined.

Ru and Mao [107] proposed a strip saturation model for a conducting cracks in a poled ferroelectric of limited electric polarization. The complete solution was obtained for conducting cracks perpendicular or parallel to the poling axis. It was found that only electric-field applied parallel to the poling axis did not induce any stress intensity factor.

Wang [126] presented a fully anisotropic analysis of a strip electric saturation model proposed by Gao et al. [43] for piezoelectric materials. And derived the relationship between the size of the strip saturation zone ahead of a crack tip and the electric displacement. It was revealed that the critical fracture stresses (for a crack perpendicular to the poling axis) linearly decreased/increased with the increase/decrease of the positive and negative applied electric field, respectively. Moreover, the failure stress was not affected by the parallel applied electric field for a crack parallel to the poling axis.

Li [69] re-examined the strip saturation model for piezoelectric crack in a permeable environment to analyse the fracture toughness of a piezoelectric ceramic. And found that the global energy release depended on several different parameters, namely, saturation, charge distribution, and permeability.

Kwon [64] used strip saturation model to analyze the electrical nonlinear behavior of an anti-plane shear crack in a functionally graded piezoelectric strip. The mixed boundary value problem was solved and near tip field solutions were obtained by using the integral transform techniques.

Jeong et al. [61] analyzed a crack problem in a ferroelectric ceramic with perfect saturation under electric loading. The electric displacement saturation zone ahead of the crack tip was assumed to be elliptical. The stress intensity factor was numerically obtained as a function of electric saturation zone parameter and the ratio of the coercive electric field to the yield electric field.

Govorukha et al. [47] examined a plane strain problem for an interface crack along the fixed edges of a semi-infinite piezoelectric strip under concentrated electromechanical loads. The model of an interface crack with an artificial contact zone near its tips was considered. Fourier integral transform technique was employed to solve the physical problem. Influence of the permeability of the crack on electrical and mechanical fields near the crack tip was discussed.

Wang and Zhang [123, 124] proposed an electric field saturation concept to predict the fracture behavior of piezoelectric materials containing impermeable cracks. Closed form expressions were derived for stress intensity factor and energy release rate. It was found that crack propagation could either be enhanced or be retarded

depending on the direction of the electric field.

Zhang and Gao [138] proposed a strip dielectric breakdown model to estimate the effect of electrical non-linearity on the piezoelectric fracture of electrically insulated cracks, by the use of Stroh formalism.

Further, Zhang [137] presented a strip dielectric breakdown (DB) model for a finite impermeable crack in a piezoelectric material. Total energy release rate and local energy release rate were calculated. It was found that under the small yielding conditions, local energy release rate could be used as a fracture criterion as it gives a linear relationship between the applied stress intensity factor and the applied electric intensity factor.

Zhang et al. [139] presented the DB model for a finite impermeable crack in a piezoelectric medium based on the general linear constitutive equations. The obtained results were compared with the PS model proposed by Wang [126]. It was found that the PS model gives higher value of the local energy release rate than that derived from the DB model.

Gao et al. [34] used the strip dielectric breakdown (DB) model proposed by Zhang and Gao [138] to study the generalized problem of a conductive crack and an electrode in an infinite piezoelectric medium. The energy release rate and stress intensity factors were derived based on Stroh formalism.

Beom et al. [8] analyzed a crack with an electric displacement saturation zone in an electrostrictive material under purely electric loading. Complex function theory was used to obtain the closed from expressions of electric and elastic fields for the crack with strip saturation zone. It was found that K_I - dominant region was very small as compared to the strip saturation zone.

Bhargava and Setia [13, 14] proposed a strip saturation model for a semi-infinite piezoelectric strip of finite width weakened by a crack parallel to edges of the strip. The piezoelectric strip edges were prescribed out-of-plane shear stress and in-plane electric displacement. Consequently, the rims of the crack yield electrically forming saturation zones ahead each tip of the crack. To arrest the crack from further opening the rims of the saturation zones were subjected to normal cohesive saturation limit electric displacement. The expressions for different intensity factors and energy

release rate were derived and the case study showed that proposed model is capable to arrest strip-saturation zone.

Fan and Zhao [26] studied the difference between the polarization saturation (PS) model and dielectric breakdown (DB) model in piezoelectric ceramics via dislocation theory. Closed form analytical expressions were derived for the saturation zone, extended displacement discontinuity, extended intensity factors and local J-integrals based on these two models. Numerical case study demonstrated that the DB model gives almost the same results as the PS model for fracture load.

Fan et al. [28] presented the nonlinear hybrid extended displacement discontinuity-fundamental solution method (NLHEDD-FSM) for numerical analysis of both the PS and DB models for $2D$ finite piezoelectric media under impermeable and semi-permeable electric boundary conditions. Numerical case study was presented for the electric yielding zone and local J-integral. It was found that the DB model gives the same results as the PS model for a crack in an infinite or a finite medium.

Zhang and Gao [136] studied the $2D$ problem for a conductive crack in an infinite electrostrictive material based on the strip dielectric breakdown (DB) model via complex variable method. Explicit solutions were obtained for electric and electroelastic fields. Finally, all the solutions were extended to the case of a soft electrode in an infinite electrostrictive material. It was found that for a conducting crack, prescribed electric field parallel to the crack retards its growth before DB, but it might enhance its growth once DB takes place ahead of the conductive crack.

Linder and Miehe [77] investigated the effect of electric displacement saturation on problems related to the hysteretic behavior of ferroelectric ceramics and the initiation and propagation of cracks in piezoelectric ceramics.

Fan et al. [29] analyzed a polarization saturation model for a non-linear semi-permeable crack in a piezoelectric plane. Closed form expressions were derived for various fracture parameters. Numerical case study showed that the effect of different boundary conditions on the electric yielding zone and the stress intensity factor is significant and should not be ignored. Also, the influence of the saturated electric displacement on the stress intensity factor was demonstrated.

In electromechanical devices, piezoelectric materials with identical physical properties could be connected by means of a very thin ductile interlayer. Cracks occured either in this layer or at one of the interfaces between this interlayer and one of the substrates. Taking into account that the interlayer was usually much softer and had a smaller yield stress than the adjacent materials, considerable zones of mechanical and electrical nonlinearity could appear in this interlayer at the crack continuations.

Shen et al. [108] analyzed a strip-electric-saturation and mechanical yielding model for a interfacial crack between ferroelectric-plastic bimaterials. They assumed that the electric polarization reaches a saturation limit and shear stress reaches a yield stress along a line segment in front of the crack. The energy release rate and crack opening displacement were also obtained, which indicates the possibility of fracture criterion based on crack opening displacement.

Narita and Shindo [90] proposed a yield strip model for a finite crack in a narrow transversely isotropic piezoelectric ceramic body under tensile loading by the use of integral transform technique. The crack was situated in the mid-plane and was parallel to the edges of the body.

Bhargava and Saxena [11] proposed a strip-electro-elastic yielding model for a poled piezoelectric plate weakened by a finite crack under mode-I deformation using complex variable technique. Two cases were investigated: when crack lie perpendicular to the poling axis and when crack lie parallel to the poling axis. Further, they [12] proposed a strip-electro-elastic yielding model for a poled piezoelectric plate weakened by a finite crack under mode III deformation employing Fourier integral transform technique. Two cases were investigated when (i) the saturation zone was bigger than the developed yield zone, and (ii) saturation zone was smaller than the developed yield zone. Closed form analytical expressions were derived for developed zones, crack opening displacement, crack opening potential drop and energy release rate.

Bhargava and Kumar [10] studied the arrest of opening of a finite crack for a transversely isotropic piezoelectric ceramic under mode III deformation by the use of Fourier integral transform technique. The developed yield zone rims were subjected to quadratically varying yield point cohesive anti-plane shear stress to arrest the

crack from further opening. Closed form analytical expressions were derived for the length of slide zone, crack opening displacement and crack growth rate.

Loboda et al. [78] proposed a strip-electro-elastic yielding model for a crack in a thin ductile layer between two piezoelectric materials which were under remote electromechanical loadings. Problem was solved by complex variable technique. The closed form analytical expressions were derived for zones length, crack opening and electric potential jumps. Further, Lapusta and Loboda [66] analyzed the same physical problem for a limited permeable crack in a thin ductile layer between two piezoelectric materials.

Loboda et al. [80] proposed a strip-electro-elastic yielding model for a semi-permeable crack in two identical semi-infinite piezoelectric spaces adhered by means of a thin isotropic interlayer. They assumed that two distinct zones of different lengths- a zone of mechanical yielding and a zone of electrical saturation developed by the application of prescribed combined electromechanical loads. Closed form analytical expressions were derived for crack opening displacement, crack opening potential drop and energy release rate.

Xue et al. [135] proposed a electro-elastic yielding model for a crack in piezoelectric materials. Closed form expressions were obtained for mechanical crack opening displacement (MCOD) and electrical crack tip opening displacement (ECOD). Numerical case study showed that the MCOD was in agreement with experiments, while ECOD was contradictory to the experiments in piezoelectric ceramics.

Cui et al. [20] proposed a strip saturation model for periodic collinear cracks in an infinite piezoelectric body. Analytical closed form expressions were derived for the stress intensity factors and the saturation strip size. The effect of periodicity on the stress intensity factors and the size of saturation strip of cracks was studied.

2.9 Objective of the Present Work

The problems investigated in the present thesis explore the possibilities of crack arrest under various conditions for a poled transversely isotropic piezoelectric plate. The plate is weakened by two equal collinear hairline straight cracks. The cracks rims open on account of combined in-plane mechanical stress and electric displacement

applied at infinite boundary of the plate. Consequently, a yield zone/saturation zone or both protrudes ahead each tip of the cracks. The thesis includes the following eight chapters.

Chapter 1 is introductory in nature. The smart materials, their categories, utility and applications are discussed at length. Basics of crack and fracture are also introduced.

Chapter 2, gives introduction to piezoelectric materials, their fundamental formalism. The Stroh formalism and complex variable methodology are also discussed for piezoelectric materials. Current status of the field, objective of work done and layout of the thesis is also presented in this chapter.

Chapter 3 provides analytical solution for two equal collinear cuts in an infinite piezoelectric plate with semi-permeable crack face electric boundary conditions prevailing on crack faces. The numerical study is also presented for PZT-4, PZT-5H, PZT-7A and $BaTiO_3$ poled ceramic plates to show the effect of prescribed mechanical stress and electric displacement on various fracture parameters. Also, intensity and energy analysis for PZT-4 ceramic are specially studied under three different conditions: (i) the electrically impermeable crack, (ii) the crack gap is filled with air or vacuum, and (iii) the electrically permeable crack. Detailed comparisons are performed among the three cases.

In **Chapter 4**, strip-saturation model is proposed for an infinite piezoelectric plate weakened by two equal collinear cracks. The saturation zones developed are arrested by distributing over them the cohesive saturation limit electric displacement. A qualitative analysis is carried out to find the behavior of load required to close the saturation zones.

In **Chapter 5**, the problem of two equal collinear hairline straight cracks weakening a plate is discussed. In-plane mechanical stress and electric displacement applied at infinity causes coalesces of each saturation zone developed at the interior tips of two cracks. The other rims of two saturation zones, each developed at the remaining tip of the two cracks, and the coalesced saturation zone are subjected to saturation limit electric displacement D_s to arrest crack opening.

In **Chapter 6**, strip-electro-mechanical yield model is proposed for an infinite

piezoelectric plate weakened by two equal collinear cracks. Developed mechanical and electric strip zones are arrested by prescribing over their rims uniform, normal, cohesive yield point stress and saturation limit electric displacement. Three different situations are investigated when developed electrical saturation zone is bigger/smaller or equal to the developed mechanical yield zone.

In **Chapter 7**, strip-electro-mechanical yield model is proposed for an infinite piezoelectric plate weakened by two equal collinear cracks with semi-permeable crack face electric boundary conditions prevailing on crack faces. Developed mechanical and electric strip zones are arrested by prescribing over their rims uniform, normal, cohesive yield point stress and saturation limit electric displacement. Three different situations are investigated when developed electrical saturation zone is bigger/smaller or equal to the developed mechanical yield zone. It is observed that COD is maximum for case when developed zones are equal and little less for the case when saturation zone is smaller and least for the case when saturation zone is biggest.

In **Chapter 8**, the effect of change in poling direction on a strip-electro-mechanical yield model is proposed for an infinite piezoelectric plate weakened by two equal collinear cracks with semi-permeable crack face electric boundary conditions prevailing on crack faces. The study shows that poling direction perpendicular to crack length opens the crack maximum. And when poling direction axis moved towards the length of the crack, the crack opening is reduced. Consequently the poling direction may also assist in crack arrest.

Chapter 3

A Study on Semi-permeable Cracks in a Piezoelectric Plate

In the theoretical study of cracked piezoelectric bodies, the issue of assigning consistent electric boundary conditions on the crack faces is of central importance, as pointed out by many researchers. Because cracks are usually filled with some media (air, water etc.), the properties of this media should not be ignored. Three different boundary conditions on crack faces are commonly accepted in literature; the permeable crack model proposed by Parton [99], the impermeable model assumed by Deeg [23], and the semi-permeable (limited-permeable) model, proposed by Hao and Shen [50]. The permeable and impermeable crack models are the limiting cases of a semi-permeable crack model full of a dielectric with a finite dielectric permittivity. Numerous literatures are available on permeable and impermeable crack models, see e.g. Sosa [114], Fang et al. [30], Qi et al. [101], Beom and Atluri [4], Zhou et al. [142], Beom et al. [3], Chue and Weng [19], Chen et al. [16] and Jelitto et al. [60] etc. While less work is available on semi-permeable crack face conditions, which accounts for the dielectric permittivity of the crack medium. Dunn [25], McMeeking [82], Xu and Rajpakse [134], Wang and Mai [122] and Wippler et al. [130] applied these boundary conditions to solve the crack problems.

Mostly, reported semi-permeable crack problems have been investigated for single crack case only. Therefore, in this chapter, we considered the two equal collinear crack in an infinite piezoelectric plate with semi-permeable crack face electric boundary conditions prevailing on crack faces. The plate being subjected to combined

This chapter is published in ZAMM-Journal of Applied Mathematics and Mechanics (Wiley publication), DOI: 10.1002/zamm.201300109

in-plane mechanical stress and electric displacement. Problem is formulated using Stroh formalism and solved using complex variable technique. Closed form analytical expressions are derived for crack opening displacement (COD), crack opening potential drop (COP), field intensity factors (IFs), mechanical energy release rates (MERR) and total energy release rates (TERR). Theoretical derivations are validated by exact solutions existing in literature. Some interesting conclusions are observed.

The numerical study is also presented for PZT-4, PZT-5H, PZT-7A and $BaTiO_3$ poled ceramic plates to show the effect of prescribed mechanical stress and electric displacement on IFs, MERR and TERR. Also, intensity and energy analysis for PZT-4 ceramic are specially studied under three different conditions: (i) the electrically impermeable crack, (ii) the crack gap is filled with air, and (iii) the electrically permeable crack. Detailed comparisons are performed among the three cases. Moreover, the effect of inter-crack distance on IFs, MERR and TERR is presented graphically and discussed.

3.1 Statement of the Problem

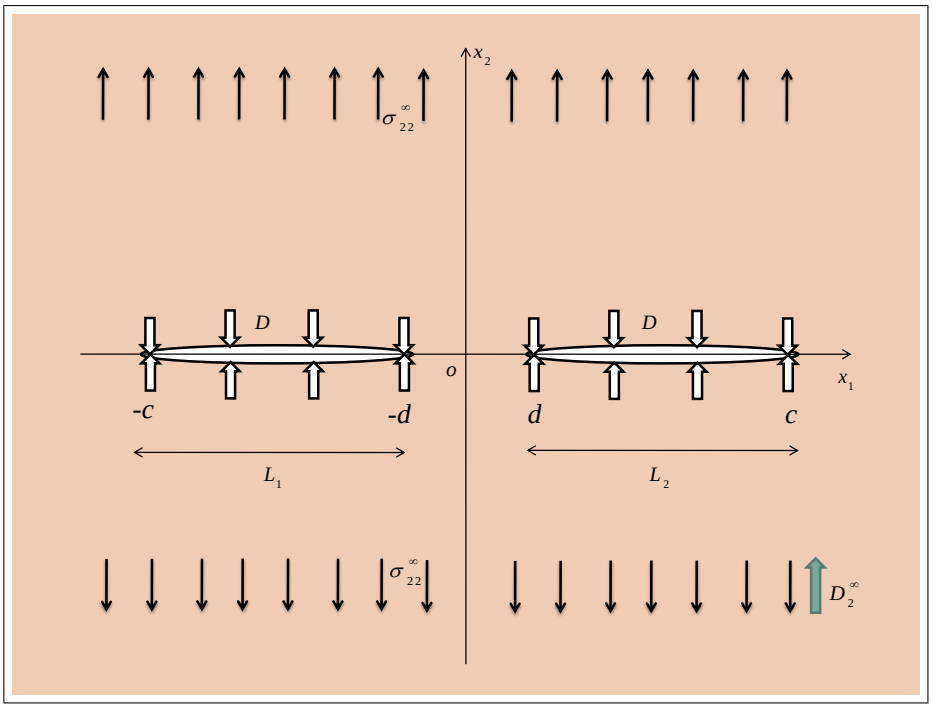

Figure 3.1: Schematic representation of the problem

An infinite transversely isotropic piezoelectric plate occupies the x_1ox_2 plane and is poled along ox_2 direction. The plate is cut along two equal collinear straight cracks L_1 and L_2 which occupy, respective, intervals $[-c,-d]$ and $[d,c]$ on ox_1-axis. The crack surfaces are assumed to be mechanically traction free and dielectric medium inside the cracks gap is finite. The plate being subjected to combined in-plane mechanical stress σ_{22}^{∞} and electric displacement load D_2^{∞}. The schematic representation of the problem is given in Fig. 3.1.

3.2 Mathematical Model of the Problem

Mathematically the boundary conditions, prescribed in section 3.1, may be translated as

(i) $\sigma_{22}^{+} = \sigma_{22}^{-} = 0, \quad D_2 = D,$ on $L = \bigcup_{i=1}^{2} L_i,$

(ii) $\sigma_{22} = \sigma_{22}^{\infty}, \quad D_2 = D_2^{\infty},$ for $|x_2| \to \infty,$

(iii) $u_2^{+} = u_2^{-},\ \sigma_{22}^{+} = \sigma_{22}^{-},\ D_2^{+} = D_2^{-},\ \phi^{+} = \phi^{-},$ for $|x_1| > c,$

(iv) $\mathbf{\Phi}_{,1}^{+} = \mathbf{\Phi}_{,1}^{-} = -\mathbf{V},\ \mathbf{V} = [0, \sigma_{22}^{\infty}, 0, D_2^{\infty}]^T,$ for $d < |x_1| < c,$

where D is the electric flux through the crack regions $(-c,-d)$ and (d,c) which can be determined using Equation (2.5.3).

A mathematical model is obtained with the help of above mentioned boundary conditions as follows:

The continuity of $\mathbf{\Phi}_{,1}$ (defined by Equation (2.7.7)) on x_1-axis yields

$$[\mathbf{BF}(x_1) - \overline{\mathbf{BF}}(x_1)]^{+} - [\mathbf{BF}(x_1) - \overline{\mathbf{BF}}(x_1)]^{-} = 0. \tag{3.2.1}$$

The solution of which may directly be written using Equation (2.7.31) as

$$\mathbf{BF}(z) = \overline{\mathbf{BF}}(z) = \mathbf{h}(z) \qquad \text{(say)} \tag{3.2.2}$$

Using principal of superposition, boundary condition (i) and (iv) together with Equations (3.2.2 and 2.7.7) leads to following vector Hilbert problem

$$\mathbf{h}^{+}(x_1) + \mathbf{h}^{-}(x_1) = \mathbf{V}^0 - \mathbf{V},\ \mathbf{V}^0 = [0,0,0,D]^T,\ d < |x_1| < c. \tag{3.2.3}$$

Introducing a complex function vector $\mathbf{\Omega}(z) = [\Omega_1(z), \Omega_2(z), \Omega_3(z), \Omega_4(z)]^T$ as

$$\mathbf{\Omega}(z) = \mathbf{H}^R \mathbf{B} \mathbf{F}(z), \tag{3.2.4}$$

which using Equation (3.2.2) gives the relation

$$\mathbf{h}(z) = \mathbf{\Lambda}\mathbf{\Omega}(z), \tag{3.2.5}$$

where $\mathbf{\Lambda} = [\mathbf{H}^R]^{-1}$, $\mathbf{H}^R = 2Re\mathbf{Y}$, $\mathbf{Y} = i\mathbf{A}\mathbf{B}^{-1}$.
Consequently Equation's (3.2.3) second and fourth components give scalar Hilbert problem in potentials $\Omega_2(z)$ and $\Omega_4(z)$ as

$$\Lambda_{22}[\Omega_2^+(x_1) + \Omega_2^-(x_1)] + \Lambda_{24}[\Omega_4^+(x_1) + \Omega_4^-(x_1)] = -\sigma_{22}^{\infty},\ d < |x_1| < c, \tag{3.2.6}$$

$$\Lambda_{42}[\Omega_2^+(x_1) + \Omega_2^-(x_1)] + \Lambda_{44}[\Omega_4^+(x_1) + \Omega_4^-(x_1)] = D - D_2^{\infty},\ d < |x_1| < c. \tag{3.2.7}$$

3.3 Solution of the Problem

Eliminating $\Omega_4^+(x_1) + \Omega_4^-(x_1)$ from Equations (3.2.6 and 3.2.7), one obtains

$$\Omega_2^+(x_1) + \Omega_2^-(x_1) = -\frac{\Lambda_{44}\sigma_{22}^{\infty} + (D - D_2^{\infty})\Lambda_{24}}{\Lambda_{22}\Lambda_{44} - \Lambda_{24}\Lambda_{42}}, \qquad d < |x_1| < c. \tag{3.3.1}$$

The general solution of Equation (3.3.1) using Equation (2.7.30) is written as

$$\Omega_2(z) = \frac{P_1(z)}{2X_1(z)} - \frac{1}{2}\frac{\Lambda_{44}\sigma_{22}^{\infty} + (D - D_2^{\infty})\Lambda_{24}}{\Lambda_{22}\Lambda_{44} - \Lambda_{24}\Lambda_{42}}, \tag{3.3.2}$$

where $X_1(z) = \sqrt{(z^2 - d^2)(z^2 - c^2)}$ and $P_1(z) = C_0 z^2 + C_1 z + C_2$.

Constant

$$C_0 = \frac{\Lambda_{44}\sigma_{22}^{\infty} + (D - D_2^{\infty})\Lambda_{24}}{\Lambda_{22}\Lambda_{44} - \Lambda_{24}\Lambda_{42}}$$

is determined using condition $\lim_{z\to\infty} \Omega_2(z) = 0$.
The condition of single-valuedness around the cracks i.e.,

$$\int_{L_i} [\Omega_2^+(x_1) - \Omega_2^-(x_1)]dx_1 = \int_{L_i} \frac{P_1(x_1)}{X_1(x_1)}dx_1 = 0, \qquad i = 1, 2, \tag{3.3.3}$$

gives $C_1 = 0$ and $C_2 = -C_0 c^2 E(k)/F(k)$, where $F(k)$ and $E(k)$ are the complete elliptic integrals of first and second kind, respectively.

Thus the desired stress function $\Omega_2(z)$ may be written as

$$\Omega_2(z) = \frac{1}{2}\frac{\Lambda_{44}\sigma_{22}^{\infty} + (D - D_2^{\infty})\Lambda_{24}}{\Lambda_{22}\Lambda_{44} - \Lambda_{24}\Lambda_{42}} \left\{ \frac{z^2 - c^2\lambda^2}{X_1(z)} - 1 \right\}, \tag{3.3.4}$$

where $k^2 = 1 - (d/c)^2$, $\lambda^2 = E(k)/F(k)$.

Analogously $\Omega_4(z)$ is determined by solving Equation (3.2.7), the solution may be written as

$$\Omega_4(z) = -\frac{1}{2}\frac{\Lambda_{42}\sigma_{22}^{\infty} + (D - D_2^{\infty})\Lambda_{22}}{\Lambda_{22}\Lambda_{44} - \Lambda_{24}\Lambda_{42}} \left\{ \frac{z^2 - c^2\lambda^2}{X_1(z)} - 1 \right\}. \tag{3.3.5}$$

3.4 Applications

In this section the expressions for crack opening displacement, crack opening potential drop, intensity factors, mechanical and total energy release rates are derived. We introduced the jump displacement vector $\Delta\mathbf{u}_{,1}$, using Equations (2.7.6 and 3.2.4) as

$$i\Delta\mathbf{u}_{,1} = i[u_{1,1}^{+} - u_{1,1}^{-}, u_{2,1}^{+} - u_{2,1}^{-}, u_{3,1}^{+} - u_{1,1}^{-}, \phi^{+} - \phi^{-}]^T = \mathbf{H}^R[\mathbf{B}\mathbf{F}^{+}(x_1) - \mathbf{B}\mathbf{F}^{-}(x_1)], \tag{3.4.1}$$

where the symbol Δ indicates the difference between the values on the upper and lower crack surfaces.

3.4.1 Crack opening displacement (COD)

The relative crack face opening displacement, $\Delta u_2(x_1)$ is obtained using second component from Equation (3.4.1) and substituting the value of $\Omega_2(x_1)$ from Equation (3.3.4) and integrating, we obtain

$$\Delta u_2(x_1) = -c\frac{\Lambda_{44}\sigma_{22}^{\infty} + (D - D_2^{\infty})\Lambda_{24}}{\Lambda_{22}\Lambda_{44} - \Lambda_{24}\Lambda_{42}} \left\{ \lambda^2 F(\psi, k) - E(\psi, k) \right\}, \tag{3.4.2}$$

where $\psi = sin^{-1}\sqrt{\frac{c^2 - x_1^2}{c^2 - d^2}}$.

3.4.2 Crack opening potential drop (COP)

Comparing the fourth component from Equation (3.4.1) and using the value of $\Omega_4(x_1)$ from Equation (3.3.5) and integrating, one obtains COP drop, $\Delta\phi(x_1)$, between the two faces of the crack

$$\Delta\phi(x_1) = -c\frac{\Lambda_{42}\sigma_{22}^{\infty} + (D - D_2^{\infty})\Lambda_{22}}{\Lambda_{22}\Lambda_{44} - \Lambda_{24}\Lambda_{42}} \left\{ \lambda^2 F(\psi, k) - E(\psi, k) \right\}. \tag{3.4.3}$$

The value of electric flux D is obtained by substituting the required values from Equations (3.4.2 and 3.4.3) into Equation (2.5.3) simplifying and solving the quadratic equation

$$\eta_1 D^2 + \eta_2 D + \eta_3 = 0, \tag{3.4.4}$$

where $\eta_1 = \Lambda_{24}, \quad \eta_2 = \Lambda_{44}\sigma_{22}^{\infty} - D_2^{\infty}\Lambda_{24} - \kappa_a\Lambda_{22}, \quad \eta_3 = -\kappa_a(\Lambda_{42}\sigma_{22}^{\infty} - D_2^{\infty}\Lambda_{22})$.
The value of D is chosen for which $\Delta u_2(x_1)$ is positive.

3.4.3 Stress intensity factor (SIF)

Stress intensity factor, K_I, at the tips $x_1 = d$ and $x_1 = c$ are defined as

$$K_I(d) = \lim_{x_1 \to d^-} \sqrt{2\pi(d - x_1)}\sigma_{22}(x_1), \tag{3.4.5}$$

$$K_I(c) = \lim_{x_1 \to c^+} \sqrt{2\pi(x_1 - c)}\sigma_{22}(x_1). \tag{3.4.6}$$

Substituting $\sigma_{22}(x_1)$ obtained from Equations (2.7.7, 3.2.5 and 3.3.4) into above equations and simplifying, one obtains

$$K_I(d) = -\left[\sigma_{22}^{\infty} + (D - D_2^{\infty})\frac{\Lambda_{24}}{\Lambda_{44}}\right]\sqrt{\frac{\pi}{d(c^2 - d^2)}}(d^2 - c^2\lambda^2), \tag{3.4.7}$$

$$K_I(c) = \left[\sigma_{22}^{\infty} + (D - D_2^{\infty})\frac{\Lambda_{24}}{\Lambda_{44}}\right]\sqrt{\frac{\pi}{c(c^2 - d^2)}}(c^2 - c^2\lambda^2). \tag{3.4.8}$$

3.4.4 Electric displacement intensity factor (EDIF)

The electric displacement intensity factor, K_{IV}, at the tips $x_1 = d$ and $x_1 = c$ are defined as

$$K_{IV}(d) = \lim_{x_1 \to d^-} \sqrt{2\pi(d - x_1)}D_2(x_1), \tag{3.4.9}$$

$$K_{IV}(c) = \lim_{x_1 \to c^+} \sqrt{2\pi(x_1 - c)}D_2(x_1). \tag{3.4.10}$$

And substituting $D_2(x_1)$ obtained from Equations (2.7.7, 3.2.5 and 3.3.5) into above Equations (3.4.9 and 3.4.10) and simplifying, one obtains

$$K_{IV}(d) = \left[(D - D_2^{\infty}) + \sigma_{22}^{\infty}\frac{\Lambda_{42}}{\Lambda_{22}}\right]\sqrt{\frac{\pi}{d(c^2 - d^2)}}(d^2 - c^2\lambda^2), \tag{3.4.11}$$

$$K_{IV}(c) = -\left[(D - D_2^{\infty}) + \sigma_{22}^{\infty}\frac{\Lambda_{42}}{\Lambda_{22}}\right]\sqrt{\frac{\pi}{c(c^2 - d^2)}}(c^2 - c^2\lambda^2). \tag{3.4.12}$$

3.4.5 Energy release rate (ERR)

Mechanical energy release rate (MERR), G_M, and total energy release rate (TERR), G_T, at the inner and outer crack tips $x_1 = d$ and $x_1 = c$ are calculated using formulae

$$G_M = \frac{1}{2}\sum_{i=1}^{3}\sum_{k=1}^{4} H_{ik}^R K_i K_k, \tag{3.4.13}$$

$$G_T = \frac{1}{2}\mathbf{K}\mathbf{H}^R\mathbf{K}^T,\ \mathbf{K} = (K_{II}, K_I, K_{III}, K_{IV}). \tag{3.4.14}$$

Since for fracture opening mode-I, $K_{II} = 0$ and $K_{III} = 0$, therefor we obtain

$$G_M = \frac{1}{2}(H_{22}^R K_I^2 + H_{24}^R K_I K_{IV}), \tag{3.4.15}$$

$$G_T = \frac{1}{2}(H_{22}^R K_I^2 + 2H_{24}^R K_I K_{IV} + H_{44}^R K_{IV}^2), \tag{3.4.16}$$

taken from Jelitto et al. [60].

3.5 Validation

The case of a single semi-permeable straight crack occupying the interval $[-c, c]$ on ox_1-axis is obtained directly making $d \to 0$. The Equations (3.3.4, 3.3.5, 3.4.2, 3.4.3, 3.4.8 and 3.4.12) reduce to

$$\Omega_2(z) = \frac{1}{2}\frac{\Lambda_{44}\sigma_{22}^{\infty} + (D - D_2^{\infty})\Lambda_{24}}{\Lambda_{22}\Lambda_{44} - \Lambda_{24}\Lambda_{42}}\left\{\frac{z}{\sqrt{z^2 - c^2}} - 1\right\}, \tag{3.5.1}$$

$$\Omega_4(z) = -\frac{1}{2}\frac{\Lambda_{42}\sigma_{22}^{\infty} + (D - D_2^{\infty})\Lambda_{22}}{\Lambda_{22}\Lambda_{44} - \Lambda_{24}\Lambda_{42}}\left\{\frac{z}{\sqrt{z^2 - c^2}} - 1\right\}, \tag{3.5.2}$$

$$\Delta u_2(x_1) = -c\frac{\Lambda_{44}\sigma_{22}^{\infty} + (D - D_2^{\infty})\Lambda_{24}}{\Lambda_{22}\Lambda_{44} - \Lambda_{24}\Lambda_{42}}\sqrt{x_1^2 - c^2}, \tag{3.5.3}$$

$$\Delta\phi(x_1) = -c\frac{\Lambda_{42}\sigma_{22}^{\infty} + (D - D_2^{\infty})\Lambda_{22}}{\Lambda_{22}\Lambda_{44} - \Lambda_{24}\Lambda_{42}}\sqrt{x_1^2 - c^2}, \tag{3.5.4}$$

$$K_I(c) = \left[\sigma_{22}^{\infty} + (D - D_2^{\infty})\frac{\Lambda_{24}}{\Lambda_{44}}\right]\sqrt{\pi c}, \tag{3.5.5}$$

$$K_{IV}(c) = -\left[(D - D_2^{\infty}) + \sigma_{22}^{\infty}\frac{\Lambda_{42}}{\Lambda_{22}}\right]\sqrt{\pi c}, \tag{3.5.6}$$

which validates with results of Ou and Chen [93].

3.6 Case Study

An illustrative example is presented for PZT-4 piezoelectric ceramic plate weakened by two equal collinear semi-permeable cracks. The material constants are given in

Table 2.1.

We assume that cracks are electrically semi-permeable with permeability $\kappa_a = \kappa_r\kappa_o$ ($\kappa_o = 8.85 \times 10^{-12} C/Vm$). The value of $\kappa_a = 10^{-10}\kappa_o$ corresponds to an electrically impermeable crack, $\kappa_a = \kappa_o$ to the air and $\kappa_a = 4000\kappa_o$ can be considered as corresponding to an electrically permeable crack. And the length of equal collinear cracks, prescribed mechanical load and electric displacement is $10mm$ each, $\sigma_{22}^{\infty} = 1MPa$ and $D_2^{\infty} = 0.001C/m^2$, respectively, till specified otherwise.

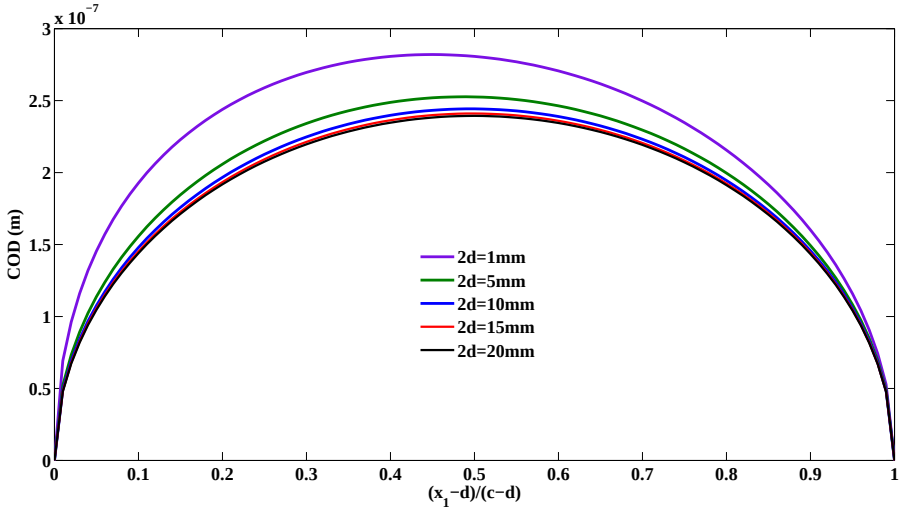

Figure 3.2: COD profile over the crack surface for different inter-crack distance

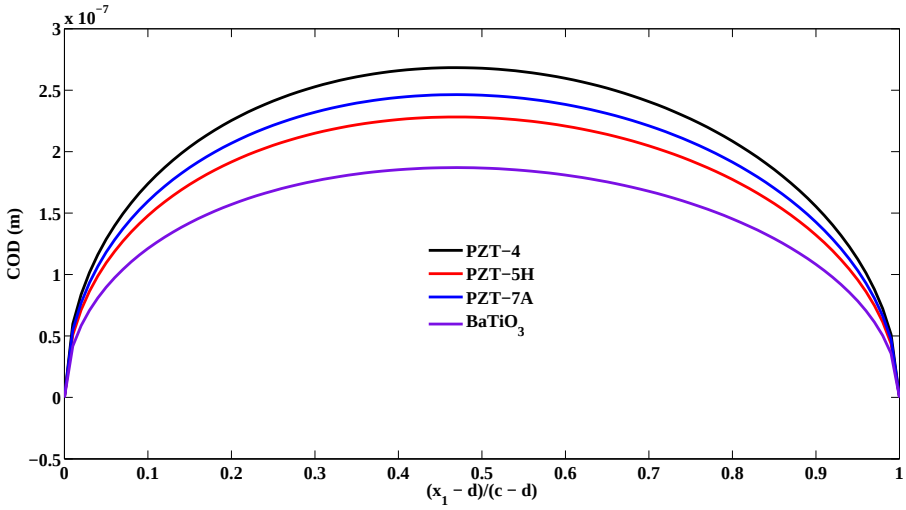

Figure 3.3: COD profile over the crack surface for different piezoelectric materials

The COD profile over the crack rims for a fixed crack length as the distance between two cracks is increased can be noted from Fig. 3.2. It is observed that if distance

between two cracks is much more than the crack length then crack opens symmetrically. While if the cracks are brought close to each other then the crack opening shifts more towards the interior crack tip side and the symmetry of crack opening is disturbed. Also, the dependency of COD over the material constants is shown in Fig. 3.3. It is observed that COD is maximum for PZT-4 while lowest for $BaTiO_3$ ceramic. This study assists for making a choice of correct ceramic depending on the specific task.

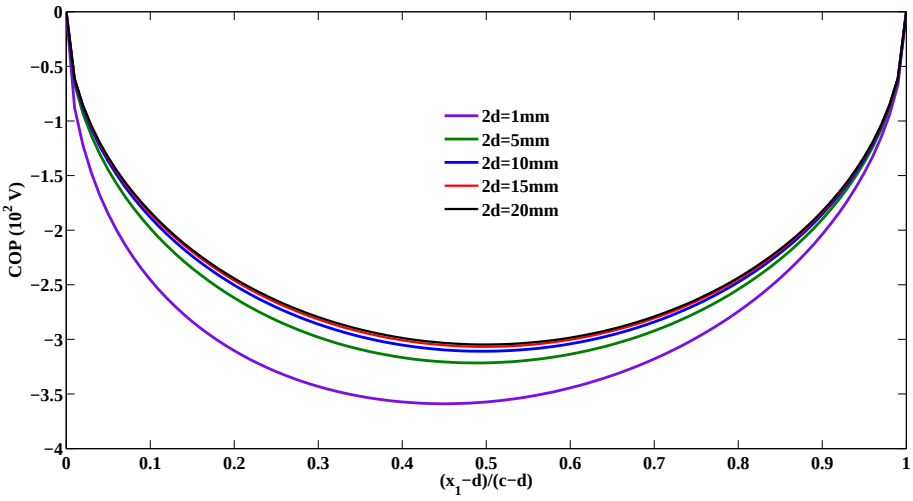

Figure 3.4: COP drop over the crack surface for different inter-crack distance

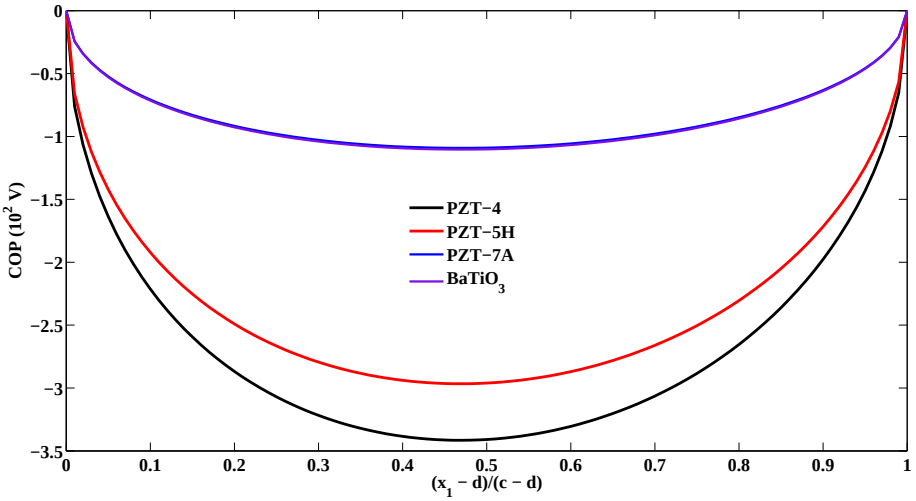

Figure 3.5: COP drop over the crack surface for different piezoelectric materials

Fig. 3.4 depicts the variation of COP over crack rims for different inter-crack distance. It is to be noted that COP remains negative although the behavior is opposite

to that of COD. COP is maximum for $2d = 1mm$ and tilted towards inner tip of the crack. And as the inter-crack distance is increased the COP becomes more symmetric about the mid point of the crack. Moreover, the effect of material constants over the COP is shown in Fig. 3.5. It shows the same variation as like that of COD, COP drop is maximum for PZT-4 ceramic and minimum for PZT-7A ceramic. This assists the designer/metallurgist to correctly select piezoelectric ceramic for specific job.

3.6.1 Effect of inter-crack distance

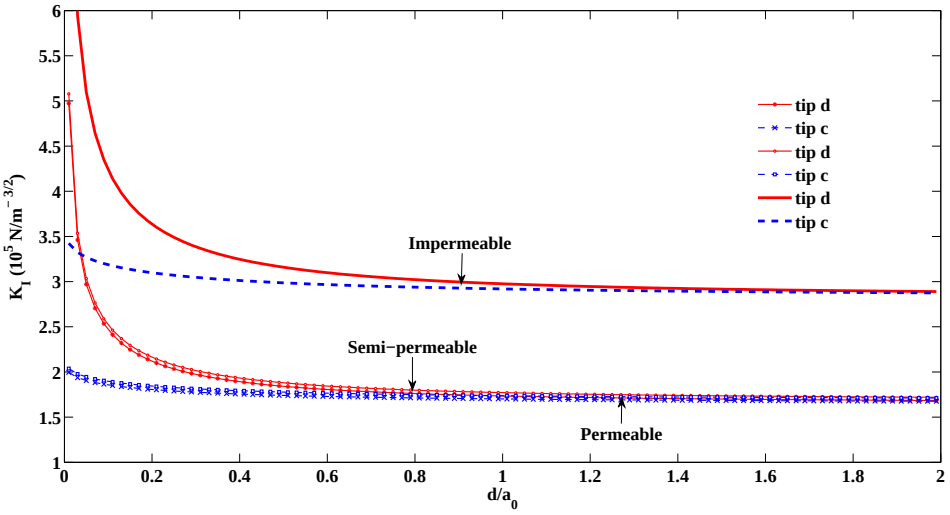

Figure 3.6: K_I versus inter-crack distance for different electric boundary conditions

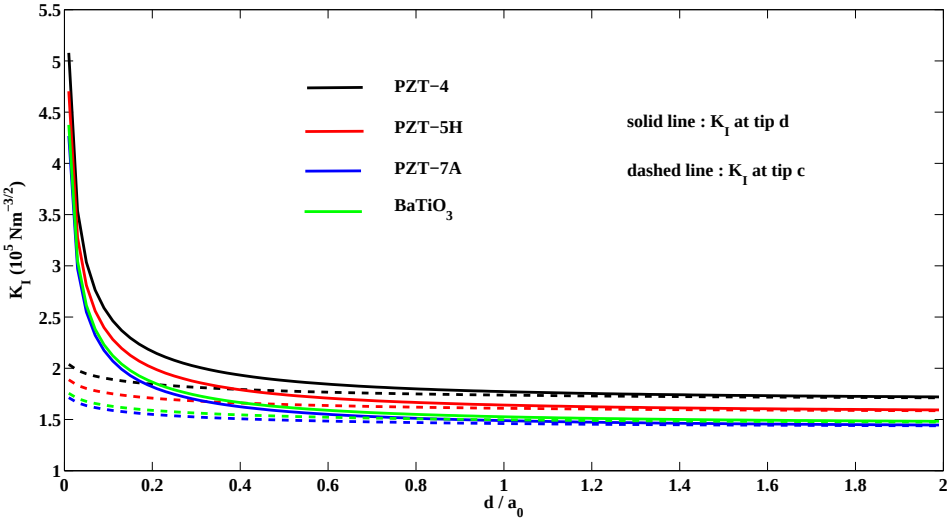

Figure 3.7: K_I versus inter-crack distance for different piezoelectric ceramics

Fig. 3.6 depicts the variation of open mode stress intensity factor, K_I, (at inner and outer tips of the crack) with respect to inter-crack distance to crack length ratio, $d/a_0, (a_0 = \frac{c-d}{2})$. It may be noted that stress intensity factor is much higher at inner tip of the crack as compared to that at outer tip, as expected. However, for this case when inter-crack distance is bigger than the crack length, the K_I at inner and outer tips of the cracks coincides. It may also be noted from Fig. 3.6 that for impermeable crack boundary conditions the SIF, K_I, is higher at both exterior and interior crack tips vis-a-vis permeable/semi-permeable crack case conditions. While for the semi-permeable and permeable boundary conditions, K_I, is almost equal and variation is similar at both the tips of the crack.

Fig. 3.7 shows the variation of K_I versus normalized inter-crack distance for different piezoelectric ceramics, PZT-4, PZT-5H, PZT-7A and $BaTiO_3$. It is observed that K_I is maximum for PZT-4 piezoelectric ceramic at both the crack tips and minimum for PZT-7A piezoelectric ceramic.

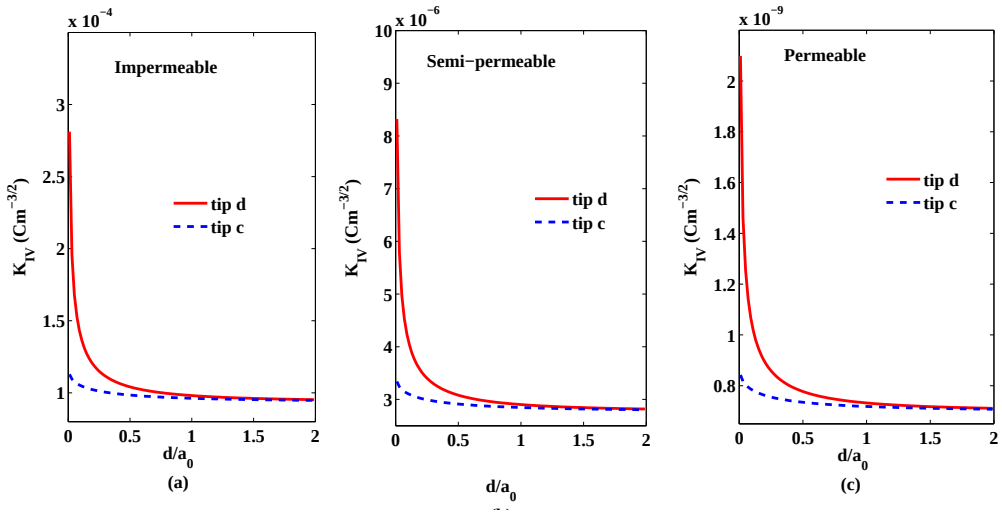

Figure 3.8: K_{IV} versus inter-crack distance for different electric boundary conditions

Figs. 3.8(a, b, c) show the variation of electric displacement intensity factor, K_{IV} versus d/a_0, at inner and outer tips of the cracks for impermeable, semi-permeable and permeable electric boundary conditions. It may be noted from Figs. 3.8(a, b, c) that K_{IV} is maximum for impermeable case and also there is a marked difference in value of K_{IV} at inner and outer tips of the crack. The behavior of reduction for

K_{IV} for semi-permeable case Fig. 3.8(b) remains the same as in case of Fig. 3.8(a) i.e., impermeable case. For permeable boundary condition, K_{IV}, further reduces as compared to semi-permeable/impermeable case.

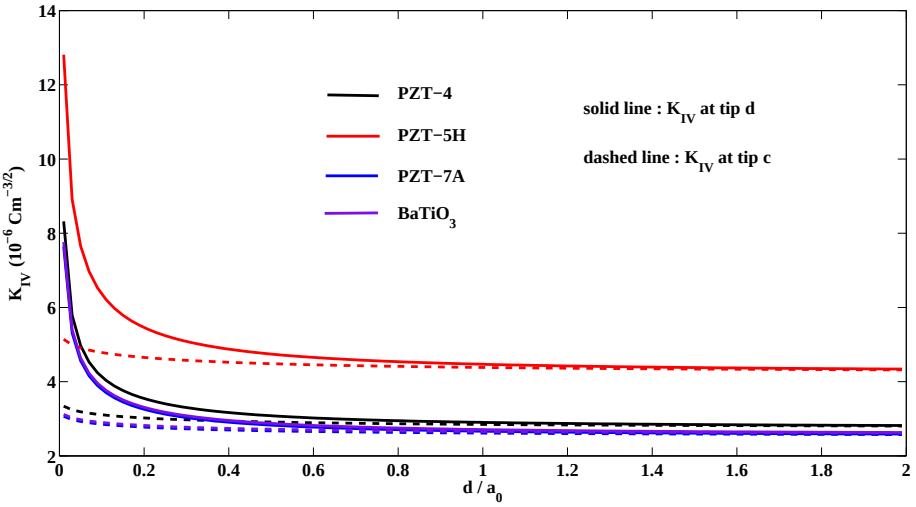

Figure 3.9: K_{IV} versus inter-crack distance for different piezoelectric ceramics

Variation of K_{IV} versus inter-crack distance for different piezoelectric ceramics is plotted in Fig. 3.9. It shows that K_{IV} is maximum for PZT-5H piezoelectric ceramic at both the crack tips and minimum for PZT-7A piezoelectric ceramic.

Next, we analyze the influence of three well defined crack-face electric boundary conditions as well as different piezoelectric materials variation on MERR and TERR with respect to normalized inter-crack distance at both inner and outer crack tips.

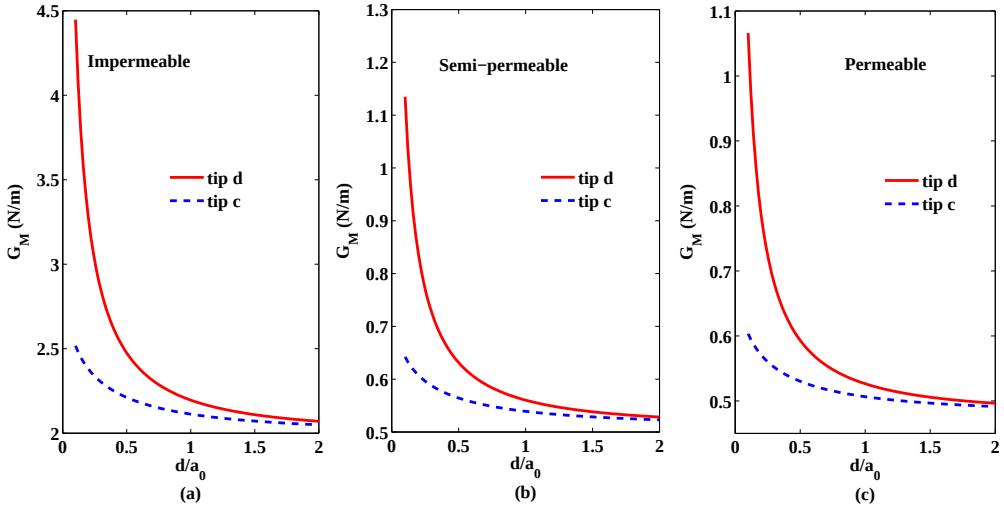

Figure 3.10: G_M versus inter-crack distance for different electric boundary conditions

Variation of MERR vis-a-vis d/a_0 for impermeable, semi-permeable and permeable cases are plotted in Figs. 3.10(a, b, c). As expected the MERR is maximum for impermeable case. While MERR is almost equal for semi-permeable and permeable cases. The difference in MERR for the three electric boundary conditions, ascertains that the crack gap medium could not be ignored.

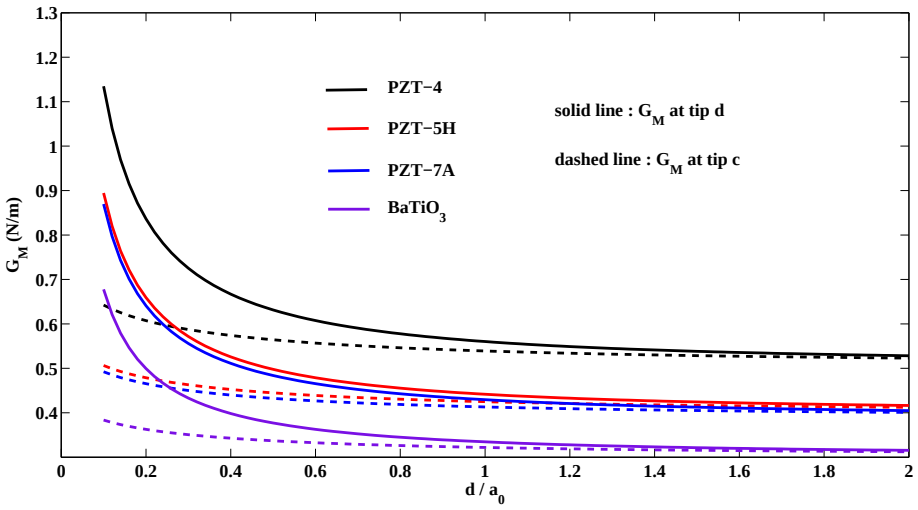

Figure 3.11: G_M versus inter-crack distance for different piezoelectric ceramics

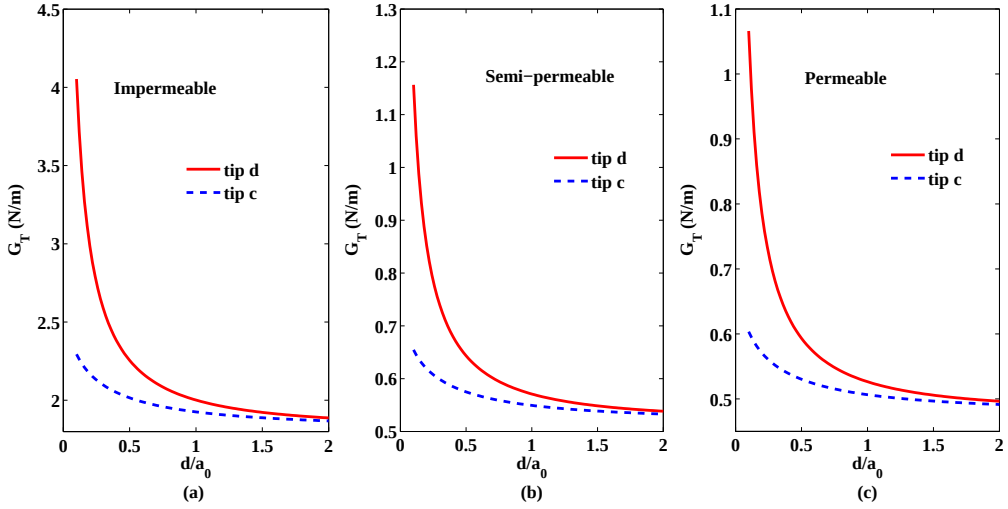

Figure 3.12: G_T versus inter-crack distance for different electric boundary conditions

Fig. 3.11 shows the variation of MERR for different piezoceramics, PZT-4, PZT-5H, PZT-7A and $BaTiO_3$ at inner and outer tips of cracks with respect to inter-crack distance. It shows that $BaTiO_3$ has a lower MERR vis-a-vis PZT-4.

Figs. 3.12(a, b, c) depict the variation of TERR versus d/a_0 for different crack-face electric boundary conditions. Same behavior is observed for TERR versus d/a_0 as in MERR versus d/a_0 case. Also it may be pointed that for impermeable crack condition the TERR at both interior and exterior tips of the crack diminishes as compared to that for MERR. While for permeable and semi-permeable crack face conditions it remains the same as in case of MERR.

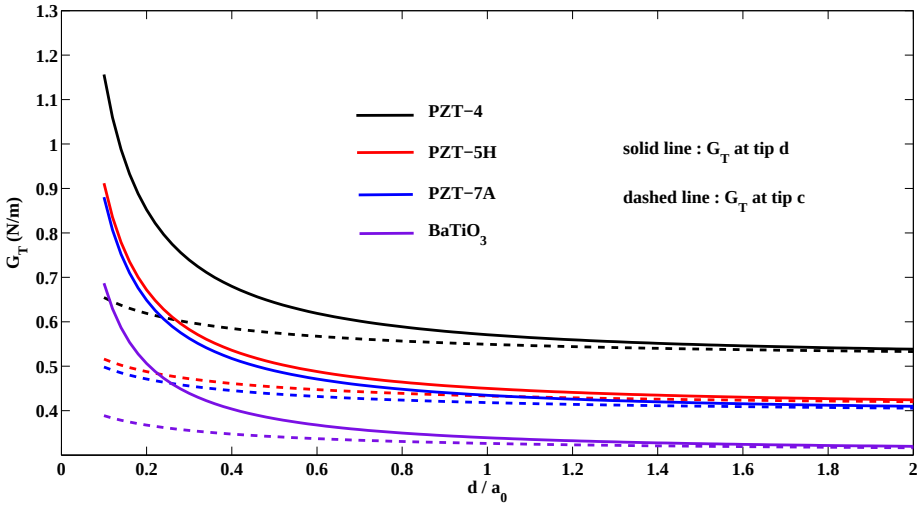

Figure 3.13: G_T versus inter-crack distance for different piezoelectric ceramics

In Fig. 3.13 variation of TERR for different piezoceramics, PZT-4, PZT-5H and PZT-7A is plotted at inner and outer tips of cracks with respect to inter-crack distance. It shows that PZT-5H and PZT-7A show a lower TERR vis-a-vis PZT-4. This may assist the designer to select the proper ceramic for the specific utility.

3.6.2 Effect of prescribed electric displacement load

In Fig. 3.14 the variation of K_I is plotted versus prescribed electric displacement, D_2^{∞}, for different prescribed mechanical load σ_{22}^{∞}. It is observed as the D_2^{∞} is increased the K_I increases linearly although the increase is not much and K_I remains more at inner tip as compared to that at outer tip. It is also to be noted that an increase in the prescribed mechanical load, steps up the K_I, as uniformly as one increases the mechanical load.

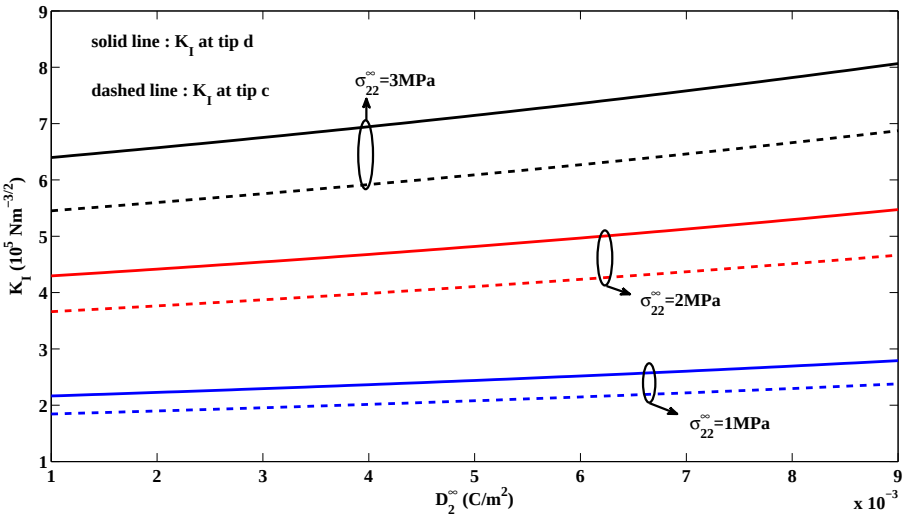

Figure 3.14: K_I versus prescribed electric displacement load for different mechanical load

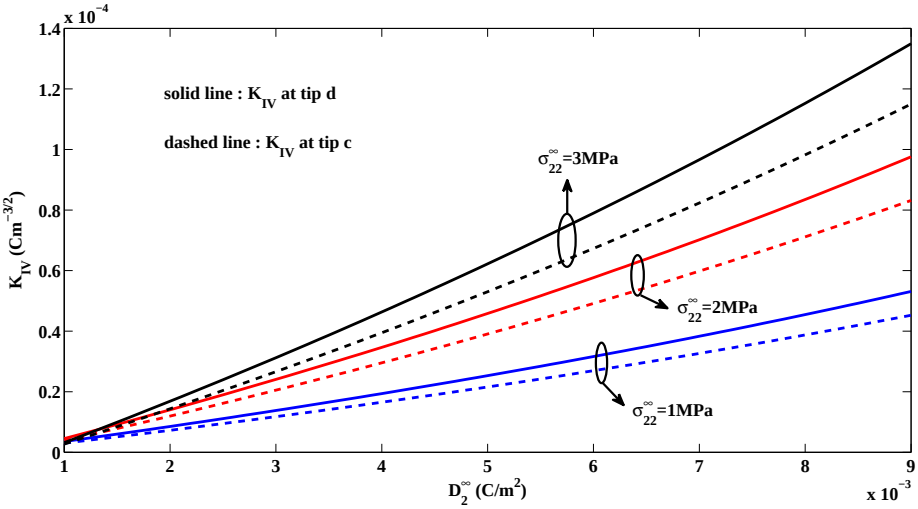

Figure 3.15: K_{IV} versus prescribed electric displacement load for different mechanical load

In Fig. 3.15 the variation of K_{IV}, electric displacement intensity factor, is presented with increasing prescribed D_2^∞. It is observed that as the D_2^∞ is increased K_{IV} also increases but it is more steep and shows a more fan like increase starting from almost zero value. Further when prescribed mechanical load is increased then K_{IV}, increases but behavior remains the same.

Fig. 3.16 depicts the variation of G_M versus dimensionless electric displacement loading factor $\lambda_d\{= (c_{33}/e_{33})(\sigma_{22}^\infty/D_2^\infty)\}$, for different prescribed mechanical load

σ_{22}^{∞}. It shows the same variation as shown in Fig. 3.14.

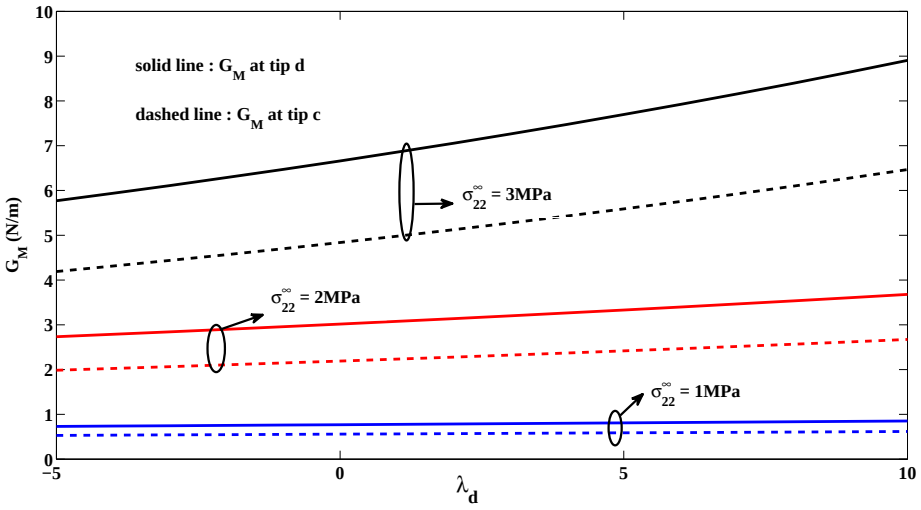

Figure 3.16: G_M versus prescribed electric displacement load for different mechanical load

3.6.3 Effect of prescribed loadings

Three cases of prescribed loadings are considered in this section when

(i) $\sigma_{22}^{\infty} = 0MPa, \quad D_2^{\infty} = 0.001C/m^2,$

(ii) $\sigma_{22}^{\infty} = 1MPa, \quad D_2^{\infty} = 0C/m^2,$

(iii) $\sigma_{22}^{\infty} = 1MPa, \quad D_2^{\infty} = 0.001C/m^2,$

and their effect on COD, COP, K_I, K_{IV}, G_M and G_T are studied. It is noted for $\sigma_{22}^{\infty} = 0MPa$ all above parameters remain zero and for non-zero prescribed mechanical loading the variations are observed.

Fig. 3.17 shows the variation of COD on crack face. It may be noted from curved graph drawn that for prescribed zero and non-zero electric displacement load there is not much difference.

COP gets most affected and it drops further when non-zero electric loading is prescribed as compared to the case when electric displacement loading is zero as shown in Fig. 3.18.

There is not much effect seen on K_I behaviors for zero and non-zero value of electrical loading as may be noted in Fig. 3.19.

A similar behavior is seen for K_{IV}, from Fig. 3.20 K_{IV} versus inter-crack distance is plotted. It is seen that for non-zero prescribed electrical loading the electric displacement intensity factor increases but the behavior remains the same as that in case of zero electrical loading.

Figs. 3.21 and 3.22 show the variation of G_M and G_T versus normalized inter-crack distance, respectively. There is almost negligible difference in the variation for zero and non-zero prescribed electrical displacement.

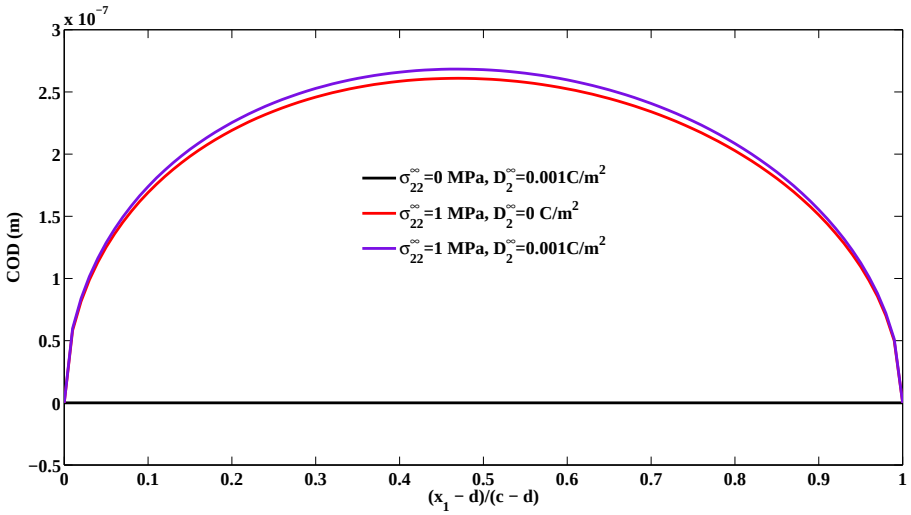

Figure 3.17: COD profile over the crack surface for different electro-mechanical loads

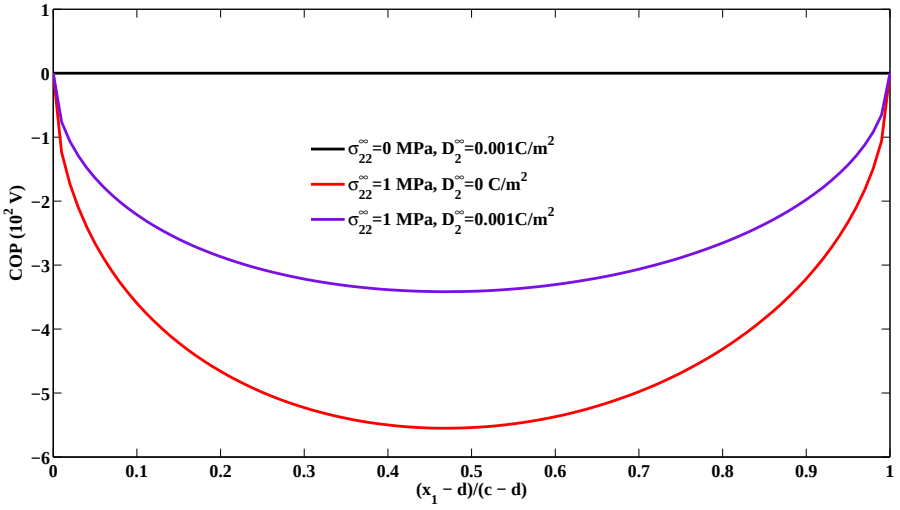

Figure 3.18: COP drop over the crack surface for different electro-mechanical loads

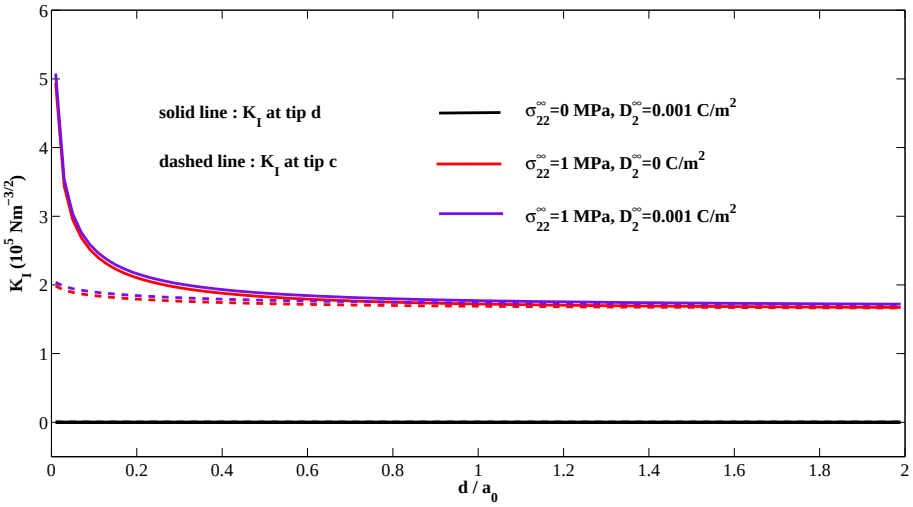

Figure 3.19: K_I versus inter-crack distance for different electro-mechanical loads

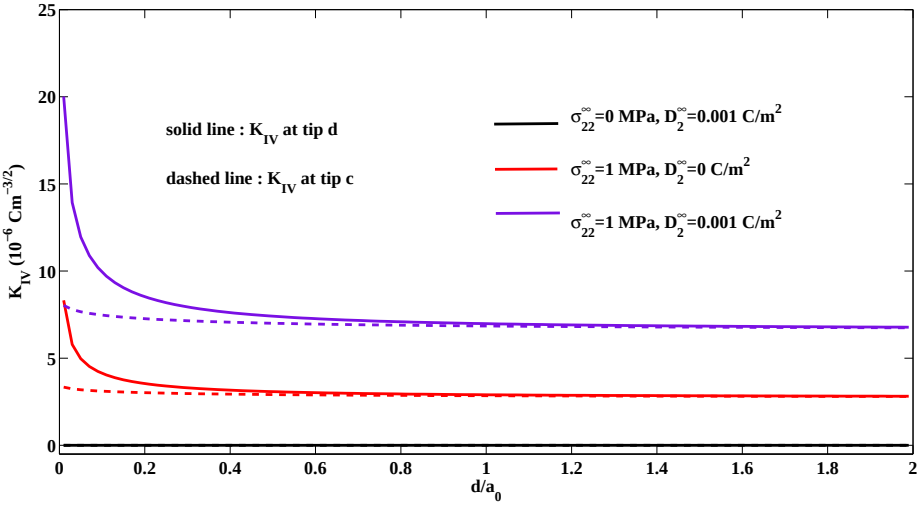

Figure 3.20: K_{IV} versus inter-crack distance for different electro-mechanical loads

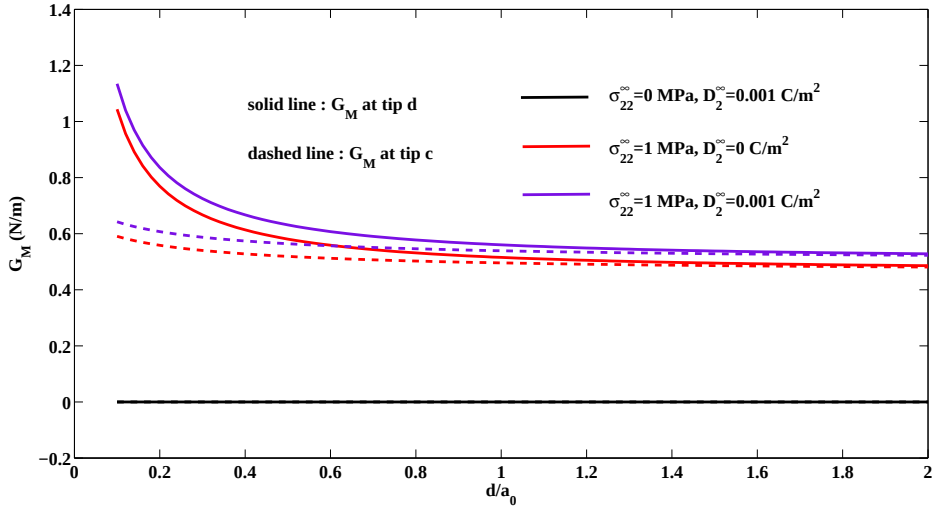

Figure 3.21: G_M versus inter-crack distance for different electro-mechanical loads

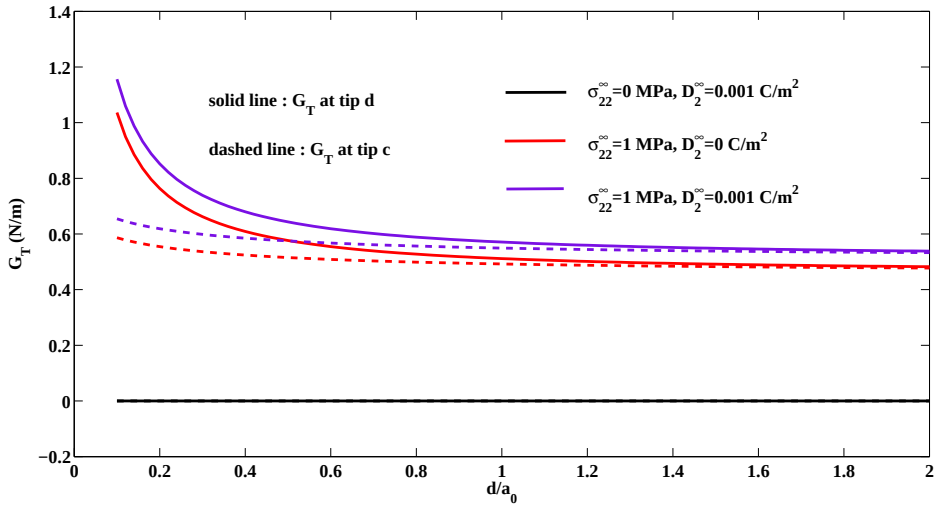

Figure 3.22: G_T versus inter-crack distance for different electro-mechanical loads

3.7 Conclusions

- The problem of two equal collinear semi-permeable cracks embedded in a piezoelectric plate is proposed. Closed form expressions are derived for COD, COP, SIF, EDIF, MERR and TERR using Stroh formalism and complex variable techniques.

- The effect of cracks on K_I, K_{IV}, G_M and G_T strongly depends on the distance between the cracks. The effect of cracks on each other weakens when the distance between the cracks is greater than or equal to the length of the crack.

- Opening of relative crack faces also strongly depends on the dielectric permittivity of crack gap media i.e., crack-face electric boundary conditions. As the permeability of the medium increases the opening of relative crack faces decreases, that is the permittivity in the crack gap media can not be ignored.

- The dependence of K_I, K_{IV}, G_M and G_T on material constants is shown graphically. It assist the designer/metallurgist to correctly select piezoelectric ceramic for specific job.

Chapter 4

Strip-saturation Model for a Piezoelectric Plate

Piezoelectric ceramic being sensitive to both mechanical and electrical loading conditions has found utility in a wide variety of mechanical and electronic equipments. For these materials, there were unexplained discrepancies between theory and experiments.

In order to explain experimental observations, Gao et al. [43] proposed a strip saturation model for a finite crack in an infinite poled piezoelectric plate. In this model the electrical saturation accounted was based on a generalization of the Dugdale [24] approach. Wang [126] presented a fully anisotropic analysis of a strip-saturation model proposed by Gao et al. [43] for piezoelectric materials. A relationship between the size of the saturation zone ahead of a crack tip and the electric displacement was derived. Bhargava and Setia [13, 14] proposed a strip-saturation model for a semi-infinite piezoelectric strip of finite height weakened by a crack parallel to the strip edges.

Most of the reported strip-saturation models that have been proposed are for single crack only. Therefore, a strip-saturation model is proposed in this chapter for a poled transversely isotropic piezoelectric plate cut along two equal collinear straight cracks. The Stroh formalism and complex variable technique are adopted to obtain the analytical solution of the problem. Closed-form expressions are derived for the developed saturation zone length, crack opening displacement (COD), crack opening potential drop (COP), stress intensity factors (SIFs) and the energy release

This chapter is published in Mathematics and Mechanics of Solids (SAGE publication), Vol. 19 (2014), pp. 714-725.

rate (ERR). Theoretical derivations are validated by exact solutions existing in literature.

A qualitative numerical case study is presented for ceramics PZT-4, PZT-5H, PZT-7A and $BaTiO_3$ to study the effects of various parameters as follows: developed saturation zone length and prescribed load, stress intensity factor, energy release rate and crack opening displacement on crack growth resistance. The energy release rate and the stress intensity factor variations are investigated with respect to the inter-crack distance. The results obtained are presented graphically and discussed.

4.1 Statement of the Problem

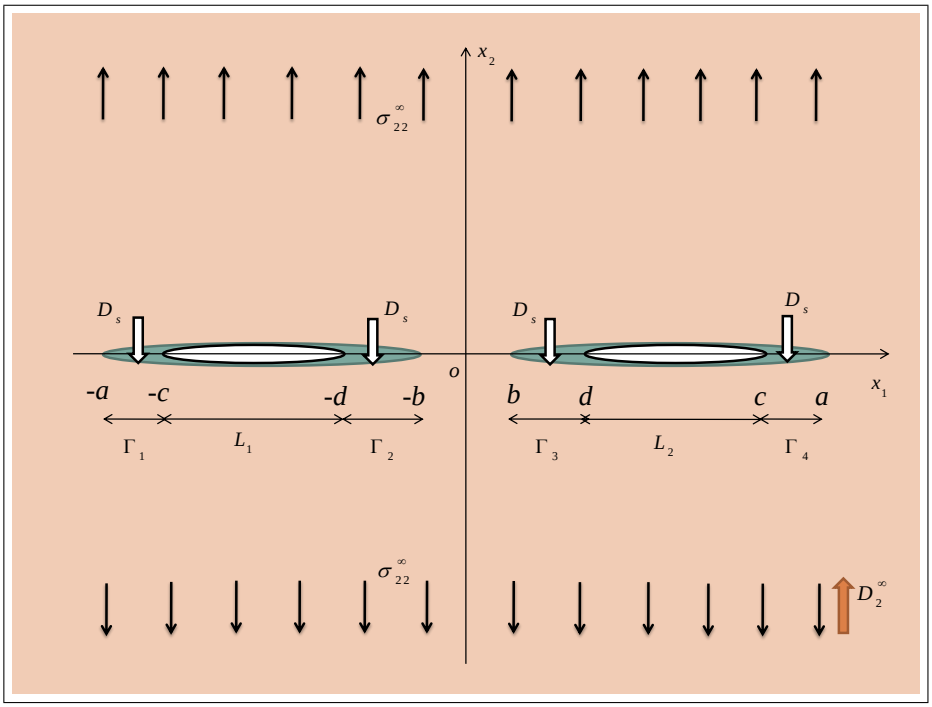

Figure 4.1: Schematic representation of the problem

A transversely isotropic piezoelectric plate occupying entire x_1ox_2 plane, poled along ox_2-direction is considered. The plate is cut along two equal collinear hairline straight cracks, L_1 and L_2. The cracks L_1 and L_2 occupy, the respective, intervals $[-c, -d]$ and $[d, c]$ on x_1-axis. The cracks faces are mechanically traction free and electrically impermeable. Uniform constant normal stress $\sigma_{22} = \sigma_{22}^{\infty}$ and electrical displacement $D_2 = D_2^{\infty}$ are prescribed at remote boundary of the plate, consequently cracks open in self-similar fashion forming a strip-saturation zone ahead each tip of

the cracks. The respective saturation zones Γ_1, Γ_2, Γ_3 and Γ_4 developed at each tip $-c$, $-d$, d and c occupies the respective intervals $[-a,-c]$, $[-d,-b]$, $[b,d]$ and $[c,a]$ on x_1-axis. The developed saturation zones are arrested by a normal cohesive saturation limit electric displacement $D_2 = D_s$. The schematic configuration of the problem is depicted in Fig. 4.1.

4.2 Mathematical Model of the Problem

The boundary conditions of the problem may mathematically be written as

(i) $\sigma_{22}^{+} = \sigma_{22}^{-} = 0, \quad D_2 = 0,$ on $L = \bigcup_{i=1}^{2} L_i,$

(ii) $\sigma_{22} = \sigma_{22}^{\infty}, \quad D_2 = D_2^{\infty},$ for $|x_2| \to \infty,$

(iii) $u_2^{+} = u_2^{-}, \quad \sigma_{22}^{+} = \sigma_{22}^{-}, \quad D_2 = D_s,$ on $\Gamma = \bigcup_{i=1}^{4} \Gamma_i,$

(iv) $\mathbf{\Phi}_{,1}^{+} = \mathbf{\Phi}_{,1}^{-} = -\mathbf{V}, \quad \mathbf{V} = [0, \sigma_{22}^{\infty}, 0, D_2^{\infty}]^T$ for $d < |x_1| < c,$

(v) $\mathbf{\Phi}_{,1}^{+} = \mathbf{\Phi}_{,1}^{-}, \quad u_2^{+} = u_2^{-}, \quad D_2^{+} = D_2^{-} = D_s - D_2^{\infty},$ on $\Gamma = \bigcup_{i=1}^{4} \Gamma_i.$

A mathematical model is obtained with the help of above mentioned boundary conditions as follows:

The continuity of $\mathbf{\Phi}_{,1}$ (defined by Equation (2.7.7)) on x_1-axis yields

$$[\mathbf{BF}(x_1) - \overline{\mathbf{BF}}(x_1)]^{+} - [\mathbf{BF}(x_1) - \overline{\mathbf{BF}}(x_1)]^{-} = 0. \tag{4.2.1}$$

The solution of which may directly be written using Equation (2.7.31) as

$$\mathbf{BF}(z) = \overline{\mathbf{BF}}(z) = \mathbf{h}(z) \qquad \text{(say)} \tag{4.2.2}$$

Boundary condition (iv) together with Equations (4.2.2 and 2.7.7) leads to following vector Hilbert problem

$$\mathbf{h}^{+}(x_1) + \mathbf{h}^{-}(x_1) = -\mathbf{V},\ d < |x_1| < c. \tag{4.2.3}$$

Introducing a complex function vector $\mathbf{\Omega}(z) = [\Omega_1(z), \Omega_2(z), \Omega_3(z), \Omega_4(z)]^T$ as

$$\mathbf{\Omega}(z) = \mathbf{H}^{R}\mathbf{BF}(z), \tag{4.2.4}$$

which on using Equation (4.2.2) gives the relation

$$\mathbf{h}(z) = \mathbf{\Lambda\Omega}(z), \tag{4.2.5}$$

where $\mathbf{\Lambda} = [\mathbf{H}^R]^{-1},\ \mathbf{H}^R = 2Re\mathbf{Y},\ \mathbf{Y} = i\mathbf{A}\mathbf{B}^{-1}$.

Consequently Equation's (4.2.3) may be written in component form for $\Omega_2(z)$ and $\Omega_4(z)$, yield following scalar Hilbert problem

$$\Lambda_{22}[\Omega_2^+(x_1) + \Omega_2^-(x_1)] + \Lambda_{24}[\Omega_4^+(x_1) + \Omega_4^-(x_1)] = -\sigma_{22}^\infty,\ d < |x_1| < c, \tag{4.2.6}$$

$$\Lambda_{42}[\Omega_2^+(x_1) + \Omega_2^-(x_1)] + \Lambda_{44}[\Omega_4^+(x_1) + \Omega_4^-(x_1)] = -D_2^\infty,\ d < |x_1| < c. \tag{4.2.7}$$

4.3 Solution of the Problem

Eliminating $\Omega_4^+(x_1) + \Omega_4^-(x_1)$ from Equations (4.2.6 and 4.2.7), one obtains

$$\Omega_2^+(x_1) + \Omega_2^-(x_1) = -\frac{\sigma_{22}^\infty\Lambda_{44} - D_2^\infty\Lambda_{24}}{\Lambda_{22}\Lambda_{44} - \Lambda_{24}\Lambda_{42}}, \qquad d < |x_1| < c. \tag{4.3.1}$$

The general solution of Equation (4.3.1) using Equation (2.7.30) may be written as

$$\Omega_2(z) = \frac{P_1(z)}{2X_1(z)} - \frac{1}{2}\frac{\Lambda_{44}\sigma_{22}^\infty - D_2^\infty\Lambda_{24}}{\Lambda_{22}\Lambda_{44} - \Lambda_{24}\Lambda_{42}}, \tag{4.3.2}$$

where $X_1(z) = \sqrt{(z^2 - d^2)(z^2 - c^2)}$ and $P_1(z) = C_0z^2 + C_1z + C_2$.

Constant

$$C_0 = \frac{\Lambda_{44}\sigma_{22}^\infty - D_2^\infty\Lambda_{24}}{\Lambda_{22}\Lambda_{44} - \Lambda_{24}\Lambda_{42}}$$

is determined using condition $\lim_{z\to\infty}\Omega_2(z) = 0$.

The condition of single-valuedness around the cracks i.e.,

$$\int_{L_i}[\Omega_2^+(x_1) - \Omega_2^-(x_1)]dx_1 = \int_{L_i}\frac{P_1(x_1)}{X_1(x_1)}dx_1 = 0, \qquad i = 1, 2, \tag{4.3.3}$$

gives $C_1 = 0$ and $C_2 = -C_0c^2E(k)/F(k)$, where $F(k)$ and $E(k)$ are the complete elliptic integrals of first and second kind, respectively.

Thus the desired stress function $\Omega_2(z)$ may be written as

$$\Omega_2(z) = \frac{1}{2}\frac{\Lambda_{44}\sigma_{22}^\infty - D_2^\infty\Lambda_{24}}{\Lambda_{22}\Lambda_{44} - \Lambda_{24}\Lambda_{42}}\left\{\frac{z^2 - c^2\lambda^2}{X_1(z)} - 1\right\}, \tag{4.3.4}$$

where $k^2 = 1 - (d/c)^2,\quad \lambda^2 = E(k)/F(k)$.

Analogously to determine $\Omega_4(z)$, Equation (4.2.7) is solved using the boundary condition (iii) and Equation (2.7.30), the solution may be written as

$$\Omega_4(z) = \frac{1}{2\pi i \Lambda_{44} X_2(z)} \int_\Gamma \frac{D_s X_2(t)}{t-z} dt + \frac{P_2(z)}{2\Lambda_{44} X_2(z)} - \frac{D_2^\infty}{2\Lambda_{44}} - \frac{\Lambda_{42}}{\Lambda_{44}} \Omega_2(z), \qquad (4.3.5)$$

where $X_2(z) = \sqrt{(z^2-a^2)(z^2-b^2)}$ and $P_2(z) = A_0 z^2 + A_1 z + A_2$.
Again constant $A_0 = D_2^\infty$ is determined using condition $\lim_{z\to\infty} \Omega_4(z) = 0$. Also A_1 and A_2 are determined from the condition of single-valuedness of displacement around cracks i.e.,

$$\int_{C'} [\Omega_4^+(x_1) - \Omega_4^-(x_1)] dx_1 = 0, \qquad C' = [-a,-b] \cup [b,a]. \qquad (4.3.6)$$

Finally, evaluating the integral in Equation (4.3.5) and substituting the values of constants A_0, A_1 and A_2, the required potential $\Omega_4(z)$, may be written as

$$\begin{aligned}\Omega_4(z) = &-\frac{D_s}{\pi\Lambda_{44}} \left\{ (z^2 - a^2\lambda_1^2) \left(\frac{\pi}{2} - \psi_d + \psi_c \right) - \frac{\pi D_2^\infty}{2D_s} (z^2 - a^2\lambda_1^2) \right\} \frac{1}{X_2(z)} \\ &+ \frac{D_s}{\pi\Lambda_{44}} \left(\frac{\pi}{2} - \theta_d + \theta_c \right) - \frac{D_s}{\pi\Lambda_{44} X_2(z)} a^2 R_1 - \frac{D_2^\infty}{2\Lambda_{44}} - \frac{\Lambda_{42}}{\Lambda_{44}} \Omega_2(z), \qquad (4.3.7)\end{aligned}$$

where,

$$\begin{aligned} k_1^2 &= \frac{a^2-b^2}{a^2},\ \lambda_1^2 = E(k_1)/F(k_1),\ \sin^2\psi_d = \frac{a^2-d^2}{a^2-b^2},\ \sin^2\psi_c = \frac{a^2-c^2}{a^2-b^2}, \\ \theta_d &= \tan^{-1}\sqrt{\frac{(a^2-z^2)(d^2-b^2)}{(b^2-z^2)(a^2-d^2)}},\ \theta_c = \tan^{-1}\sqrt{\frac{(a^2-z^2)(c^2-b^2)}{(b^2-z^2)(a^2-c^2)}}, \\ R_1 &= \frac{d}{a}\left\{E(\psi_d,k_1) - \lambda_1^2 F(\psi_d,k_1)\right\} - \frac{c}{a}\left\{E(\psi_c,k_1) - \lambda_1^2 F(\psi_c,k_1)\right\} \\ &\quad - k_1^2 \left(\sin\psi_d \cos\psi_d - \sin\psi_c \cos\psi_c\right). \end{aligned}$$

4.4 Applications

In this section closed form analytic expressions are derived for developed saturation zones size, crack opening displacement, crack opening potential drop, stress intensity factor and energy release rate.

4.4.1 Saturation zone size

The electric displacement ahead of crack tip is determined using

$$D_2(x_1) = \Lambda_{42}[\Omega_2^+(x_1) + \Omega_2^-(x_1)] + \Lambda_{44}[\Omega_4^+(x_1) + \Omega_4^-(x_1)]. \qquad (4.4.1)$$

Substituting the values of $\Omega_2(x_1)$ and $\Omega_4(x_1)$ from Equations (4.3.4 and 4.3.7) and simplifying one obtains

$$D_2(x_1) = -\frac{2D_s}{\pi}\left\{(x_1^2 - a^2\lambda_1^2)\left(\frac{\pi}{2} - \psi_d + \psi_c\right) + a^2 R_1\right\}\frac{1}{X_2(x_1)} + \frac{2D_s}{\pi}\left(\frac{\pi}{2} - \theta_d + \theta_c\right) + D_2^{\infty}\left\{\frac{x_1^2 - a^2\lambda_1^2}{X_2(x_1)} - 1\right\}. \tag{4.4.2}$$

Extending Dugdale's hypothesis [43] for electric displacement to remain finite at every point of a piezoelectric ceramic under linear piezoelectricity theory assumption, one obtains two non-linear equations

at the tip $x_1 = b$

$$\left(\frac{b^2}{a^2} - \lambda_1^2\right)\left(\frac{\pi D_2^{\infty}}{2D_s} - \frac{\pi}{2} + \psi_d - \psi_c\right) - R_1 = 0, \tag{4.4.3}$$

and at the tip $x_1 = a$

$$\left(1 - \lambda_1^2\right)\left(\frac{\pi D_2^{\infty}}{2D_s} - \frac{\pi}{2} + \psi_d - \psi_c\right) - R_1 = 0. \tag{4.4.4}$$

These results enable one to determine a and b, and the saturation zone is than determined by $(a - c)$ and $(d - b)$, respectively.

4.4.2 Crack opening displacement (COD)

We introduced the jump displacement vector $\Delta\mathbf{u}_{,1}$, with the aid of Equations (2.7.6 and 4.2.4) as

$$i\Delta\mathbf{u}_{,1} = \mathbf{H}^R[\mathbf{B}\mathbf{F}^+(x_1) - \mathbf{B}\mathbf{F}^-(x_1)] = i[u_{1,1}^+ - u_{1,1}^-, u_{2,1}^+ - u_{2,1}^-, u_{3,1}^+ - u_{1,1}^-, \phi^+ - \phi^-]^T. \tag{4.4.5}$$

The relative crack face opening displacement, $\Delta u_2(x_1)$ is obtained using second component from Equation (4.4.5) and substituting the value of $\Omega_2(x_1)$ from Equation (4.3.4) and integrating we obtain

$$\Delta u_2(x_1) = \frac{2c(\sigma_{22}^{\infty}\Lambda_{44} - D_2^{\infty}\Lambda_{24})}{\Lambda_{22}\Lambda_{44} - \Lambda_{24}\Lambda_{42}}\left\{E(\varphi, k) - \lambda^2 F(\varphi, k)\right\},\ d < |x_1| < c \tag{4.4.6}$$

where, $\sin^2\varphi = (c^2 - x_1^2)/(c^2 - d^2)$.

4.4.3 Crack opening potential drop (COP)

The COP at the crack tips d and c, are obtained using fourth component of Equation (4.4.5) and required value from Equation (4.3.7) as

at the tip $x_1 = d$

$$\Delta u_4(d) = -\frac{D_s}{\pi\Lambda_{44}}\left\{R_3 - \frac{\pi a D_2^{\infty}}{D_s}R_4\right\}, \tag{4.4.7}$$

and at the tip $x_1 = c$

$$\Delta u_4(c) = \frac{D_s}{\pi\Lambda_{44}}R_5 - \frac{aD_2^{\infty}}{\Lambda_{44}}\left\{E(\psi_c,k_1) - \lambda_1^2 F(\psi_c,k_1)\right\}, \tag{4.4.8}$$

where,

$$R_2 = a\lambda_1^2\left(\frac{\pi}{2} - \psi_d + \psi_c\right) - aR_1,\ \sin^2\vartheta_d = \frac{a^2(d^2-b^2)}{d^2(a^2-b^2)},$$

$$G(d,c) = -d\ln\left(\frac{\sqrt{(d^2-b^2)(a^2-c^2)} + \sqrt{(a^2-d^2)(c^2-b^2)}}{\sqrt{(d^2-b^2)(a^2-c^2)} - \sqrt{(a^2-d^2)(c^2-b^2)}}\right) + \frac{2b^2}{a}\sqrt{\frac{a^2-c^2}{c^2-b^2}}II(\vartheta_d, \frac{c^2k_1^2}{c^2-b^2}, k_1),$$

$$H(c,d) = c\ln\left(\frac{\sqrt{(c^2-b^2)(a^2-d^2)} + \sqrt{(a^2-c^2)(d^2-b^2)}}{\sqrt{(c^2-b^2)(a^2-d^2)} - \sqrt{(a^2-c^2)(d^2-b^2)}}\right) - \frac{2}{a}\sqrt{(d^2-b^2)(a^2-d^2)}\left\{F(\psi_c,k_1) + \frac{d^2}{a^2-d^2}II(\psi_c, \frac{a^2-b^2}{a^2-d^2}, k_1)\right\},$$

$$R_3 = \frac{2b^2}{a}\sqrt{\frac{a^2-d^2}{d^2-b^2}}\left\{F(\vartheta_d,k_1) - II(\vartheta_d, \frac{d^2-b^2}{d^2}, k_1)\right\} - d\ln\left(\frac{a^2-d^2}{a^2-b^2} + \frac{a^2(d^2-b^2)}{d^2(a^2-b^2)}\right) + 2a\left(\frac{\pi}{2} - \psi_d + \psi_c\right)\left\{E(\vartheta_d,k_1) - \frac{k_1^2\sin\vartheta_d\cos\vartheta_d}{\sqrt{1-k_1^2\sin^2\vartheta_d}}\right\} - 2R_2F(\vartheta_d,k_1) - G(d,c),$$

$$R_4 = E(\vartheta_d,k_1) - \lambda_1^2F(\vartheta_d,k_1) - \frac{k_1^2\sin\vartheta_d\cos\vartheta_d}{\sqrt{1-k_1^2\sin^2\vartheta_d}},$$

$$R_5 = -c\ln\left(\frac{(a^2-c^2)(c^2-b^2)}{c^2(a^2-b^2)} + 1\right) + \frac{2}{a}\sqrt{\frac{c^2-b^2}{a^2-c^2}}\left\{a^2F(\psi_c,k_1) - c^2II(\psi_c, \frac{a^2-c^2}{a^2}, k_1)\right\} + 2a\left(\frac{\pi}{2} - \psi_d + \psi_c\right)E(\psi_c,k_1) - 2R_2F(\psi_c,k_1) + H(c,d).$$

4.4.4 Stress intensity factor (SIF)

The stress intensity factor K_I, at the crack tips $x_1 = d$ and $x_1 = c$, is determined using the definition

$$K_I(d) = \lim_{x_1 \to d^-} \sqrt{2\pi(d - x_1)}\sigma_{22}(x_1), \tag{4.4.9}$$

$$K_I(c) = \lim_{x_1 \to c^+} \sqrt{2\pi(x_1 - c)}\sigma_{22}(x_1). \tag{4.4.10}$$

Evaluating $\sigma_{22}(x_1)$ using Equations (2.7.7, 4.2.5 and 4.3.4) substituting in Equations (4.4.9 and 4.4.10) and simplifying one obtains

$$K_I(d) = -\sqrt{\frac{\pi}{d(c^2 - d^2)}}\left(\sigma_{22}^{\infty} - D_2^{\infty}\frac{\Lambda_{24}}{\Lambda_{44}}\right)(d^2 - c^2\lambda^2), \tag{4.4.11}$$

$$K_I(c) = \sqrt{\frac{\pi}{c(c^2 - d^2)}}\left(\sigma_{22}^{\infty} - D_2^{\infty}\frac{\Lambda_{24}}{\Lambda_{44}}\right)(c^2 - c^2\lambda^2). \tag{4.4.12}$$

4.4.5 Energy release rate (ERR)

The local energy release rate (LERR) at the actual crack tips $x_1 = d$ and $x_1 = c$ is calculated using definition of Gao et al. [34]

at the tip $x_1 = d$

$$\begin{aligned} J(d) &= \frac{\pi(d^2 - c^2\lambda^2)^2}{2d(c^2 - d^2)}[\mathbf{V}^T\mathbf{H}^R\mathbf{V} - \frac{1}{\Lambda_{44}}(D_2^{\infty})^2] \\ &= \frac{\pi(d^2 - c^2\lambda^2)^2}{2d(c^2 - d^2)}\left\{H^R(2,2)(\sigma_{22}^{\infty})^2 + 2H^R(2,4)\sigma_{22}^{\infty}D_2^{\infty} + \frac{(H^R(2,4))^2}{H^R(2,2)}(D_2^{\infty})^2\right\}, \end{aligned} \tag{4.4.13}$$

and at the tip $x_1 = c$

$$\begin{aligned} J(c) &= \frac{\pi(c^2 - c^2\lambda^2)^2}{2c(c^2 - d^2)}[\mathbf{V}^T\mathbf{H}^R\mathbf{V} - \frac{1}{\Lambda_{44}}(D_2^{\infty})^2] \\ &= \frac{\pi(c^2 - c^2\lambda^2)^2}{2c(c^2 - d^2)}\left\{H^R(2,2)(\sigma_{22}^{\infty})^2 + 2H^R(2,4)\sigma_{22}^{\infty}D_2^{\infty} + \frac{(H^R(2,4))^2}{H^R(2,2)}(D_2^{\infty})^2\right\}. \end{aligned} \tag{4.4.14}$$

The global energy release rate (GERR), J_a, at the inner and outer crack tips is calculated using

$$J_a(d) = J(d) + D_s\Delta u_4(d), \tag{4.4.15}$$

$$J_a(c) = J(c) + D_s\Delta u_4(c). \tag{4.4.16}$$

4.5 Validation

The case of a strip-saturation model for a single crack occupying the interval $[-c, c]$ on ox_1-axis is obtained directly making $b = d \to 0$. The Equations (4.3.4, 4.3.7, 4.4.2, 4.4.4 and 4.4.12) reduce to

$$\Omega_2(z) = \frac{1}{2}\frac{\Lambda_{44}\sigma_{22}^{\infty} - D_2^{\infty}\Lambda_{24}}{\Lambda_{22}\Lambda_{44} - \Lambda_{24}\Lambda_{42}}\left\{\frac{z}{\sqrt{z^2-c^2}} - 1\right\}, \tag{4.5.1}$$

$$\begin{aligned}\Omega_4(z) = &-\frac{\Lambda_{42}}{\Lambda_{44}}\Omega_2(z) + \frac{D_2^{\infty}}{2\Lambda_{44}}\left(\frac{z}{\sqrt{z^2-a^2}} - 1\right)\\ &+ \frac{D_s}{\pi\Lambda_{44}}\left\{\frac{\pi}{2} - \frac{1}{2i}\ln\frac{\frac{z}{c}\frac{\sqrt{a^2-c^2}}{\sqrt{z^2-a^2}} + i}{\frac{z}{c}\frac{\sqrt{a^2-c^2}}{\sqrt{z^2-a^2}} - i} - \frac{z}{\sqrt{z^2-a^2}}\cos^{-1}(\frac{c}{a})\right\},\end{aligned} \tag{4.5.2}$$

$$D_2(x_1) = \left(D_2^{\infty} - \frac{2}{\pi}D_s\cos^{-1}(\frac{c}{a})\right)\frac{x_1}{\sqrt{x_1^2-a^2}} - D_2^{\infty} + \frac{2D_s}{\pi}\left\{\frac{\pi}{2} - \frac{1}{2i}\ln\frac{\frac{z}{c}\frac{\sqrt{a^2-c^2}}{\sqrt{z^2-a^2}} + i}{\frac{z}{c}\frac{\sqrt{a^2-c^2}}{\sqrt{z^2-a^2}} - i}\right\}, \tag{4.5.3}$$

$$\frac{c}{a} = \cos\left(\frac{\pi}{2}\frac{D_2^{\infty}}{D_s}\right), \tag{4.5.4}$$

$$K_I(c) = \sqrt{\pi c}\left(\sigma_{22}^{\infty} - \frac{\Lambda_{24}}{\Lambda_{44}}D_2^{\infty}\right). \tag{4.5.5}$$

which validates with results of Wang [126].

4.6 Case Study

A case study is presented to investigate the behavior of parameters affecting viz. saturation zone size, stress intensity factor, crack opening displacement, energy release rate, as the applied load is increased resisting the crack opening. The material constants are given in Table 2.1.

We assume the lengths of the cracks are $10mm$ each and saturation limit electric displacement, $D_s = 0.03C/m^2$.

Fig. 4.2, depicts the saturation zone sizes for PZT-4 ceramic at the interior and exterior tips of the crack when electric load ratio D_2^{∞}/D_s, is increased. It is observed that the zone developed at the interior tip is bigger than that at exterior tip for the same applied load D_2^{∞}/D_s. Further the prescribed load is increased then developed zone sizes also increases at both interior and exterior tips, as expected. Also the zone size is more when the two cracks are situated close to each other.

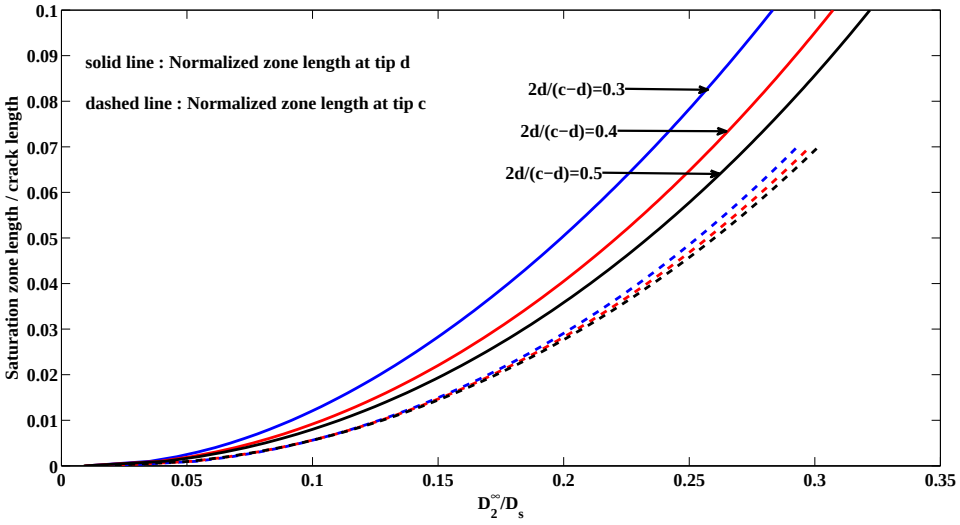

Figure 4.2: Normalized saturation zone length versus electric displacement load ratio for PZT-4 ceramic

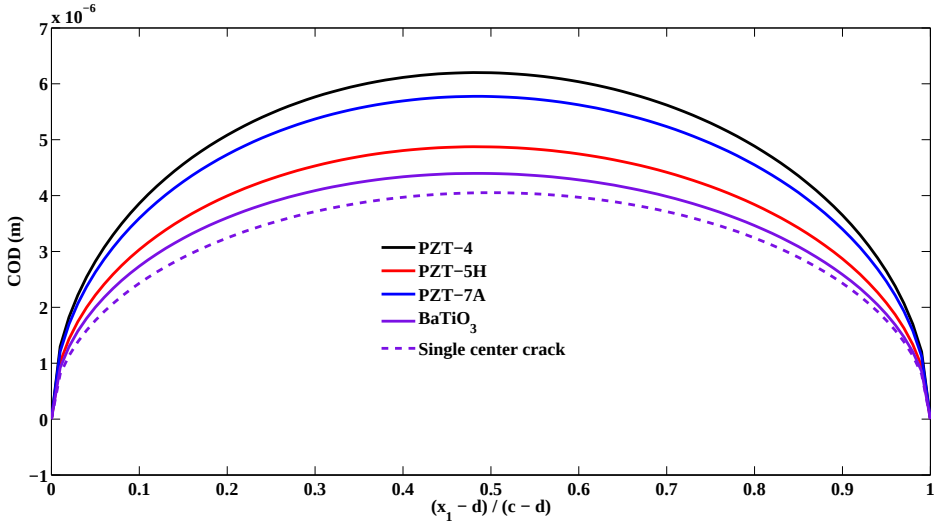

Figure 4.3: COD profile over the crack surface for different piezoelectric ceramics

COD over the rims of the cracks is plotted in Fig. 4.3. The dotted line shows the COD for a single center crack problem for $BaTiO_3$ ceramic. It may be noted that the crack rims open symmetrically with respect to middle point of the crack. The COD for two symmetrically situated cracks shows a shift in COD toward the internal crack tip. Also the COD is more in this case as compared to single center crack, as expected. It may also be noted from the Fig. 4.3 that PZT-4 ceramic shows maximum opening and for $BaTiO_3$ ceramic the crack opens less.

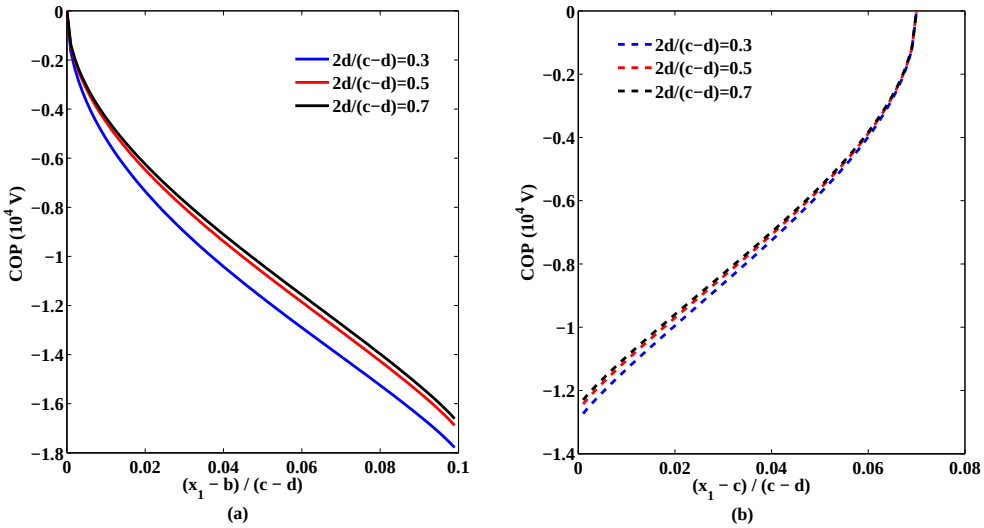

Figure 4.4: COP at (a) inner and (b) outer saturation zones for PZT-4 ceramic

Variation of COP drop versus normalized inner and outer saturation zones is drawn in Figs. 4.4(a) and 4.4(b) for PZT-4 ceramic, respectively. It is observed that potential drop is more at inner zone than that at outer zone, as expected. As the inter crack distance $2d/(c-d)$, is increased than the COP decreases at both the crack tips, but drop in COP is higher at inner tip as compared to that at outer tip.

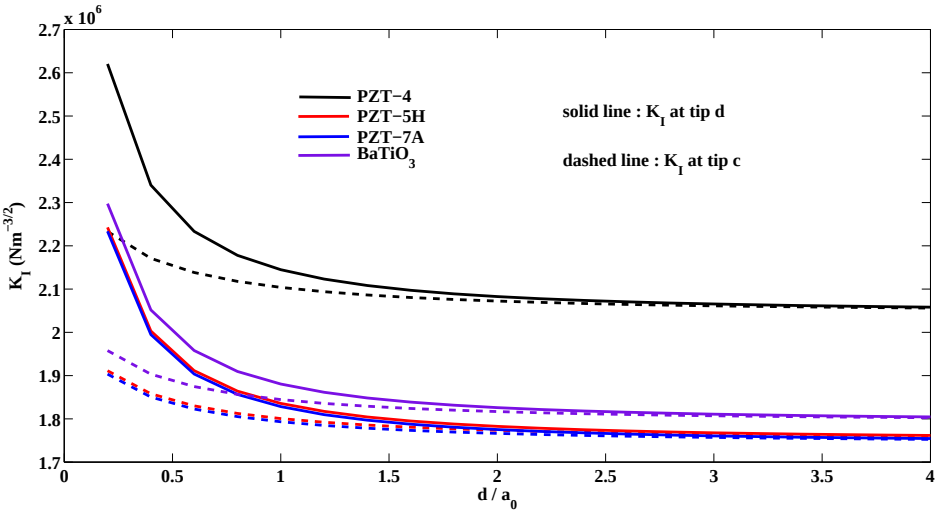

Figure 4.5: K_I versus inter-crack distance for different piezoelectric ceramics

Variation of SIF, K_I, versus normalized inter-crack distance is plotted in Fig. 4.5 for different piezoelectric ceramics and prescribed $D_2^{\infty} = 0.005 C/m^2$, $\sigma_{22}^{\infty} = 10 MPa$. It is observed that K_I at interior crack tip is higher than that at exterior tip. It is

to be noted that when the two cracks are nearer to each other there is higher stress singularity at the interior tips, this is because of the mutual interactions of the two cracks on each other and as the inter-crack distance increases the stress singularity decreases, stabilizes and coincides with the results of single center crack problem. It is also observed that K_I is maximum for the ceramic PZT-4 as compared to the other ceramics PZT-5H, PZT-7A and $BaTiO_3$, this is because of the dependence of K_I on the components of Irwin's material constant matrix $\mathbf{H}^R$ and the ratio $\frac{\Lambda_{24}}{\Lambda_{44}}$. It is maximum for PZT-4 and minimum for PZT-7A. The numerical values of components of Irwin's matrix $\mathbf{H}^R$ are given in Table 4.1 for all the four ceramics.

Table 4.1: Components of Irwin's matrix $\mathbf{H}^R$ and inverse matrix $\mathbf{\Lambda} = [\mathbf{H}^R]^{-1}$ for different piezoelectric ceramics

Material	H^R_{22}	H^R_{24}	H^R_{44}	Λ_{24}	Λ_{44}
PZT-4	3.4989×10^{-11}	0.0443	-1.7486×10^{8}	5.4817	-4.3303×10^{-9}
PZT-5H	3.2131×10^{-11}	0.0256	-0.9156×10^{8}	7.1078	-8.9384×10^{-9}
PZT-7A	3.8232×10^{-11}	0.0300	-2.0031×10^{8}	3.5024	-4.4682×10^{-9}
$BaTiO_3$	3.8303×10^{-11}	0.0244	-1.4642×10^{8}	5.1534	-5.9695×10^{-9}

Units: H^R_{22}, $N^{-1}m^2$; H^R_{24}, $C^{-1}m^2$; H^R_{44}, $C^{-1}(V.m)$; Λ_{24}, $N(V.m)^{-1}$; Λ_{44}, $C(V.m)^{-1}$.

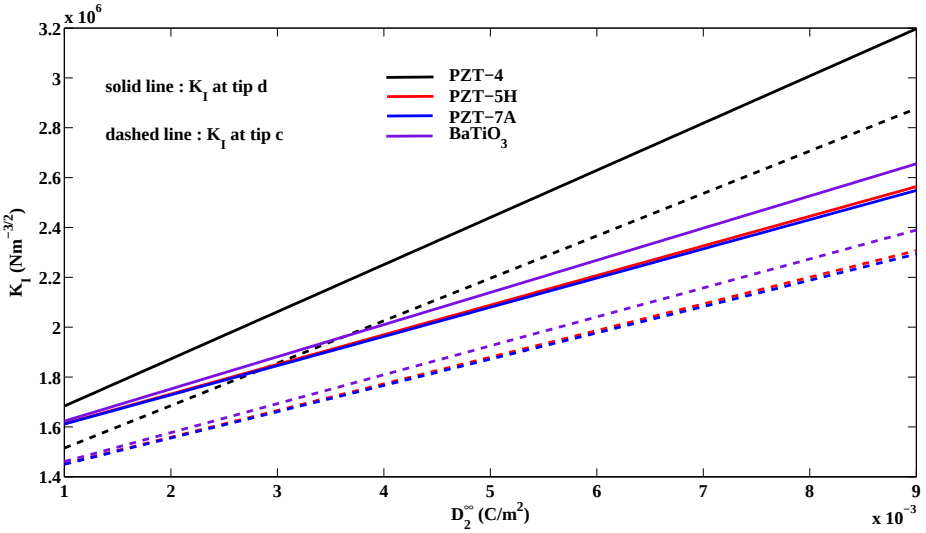

Figure 4.6: K_I versus electric displacement for different piezoelectric ceramics

SIF, K_I, is plotted against increasing value of prescribed electric displacement in Fig. 4.6 for different piezoelectric ceramics. It is observed that as the load is increased

the K_I also increases at both inner and outer tips of the crack. It is to be noted that K_I is considerably higher at the inner tip vis-a-vis that at exterior tip of the crack for all the ceramics considered. PZT-4 ceramic shows a higher stress concentration and PZT-7A ceramic shows the least concentration.

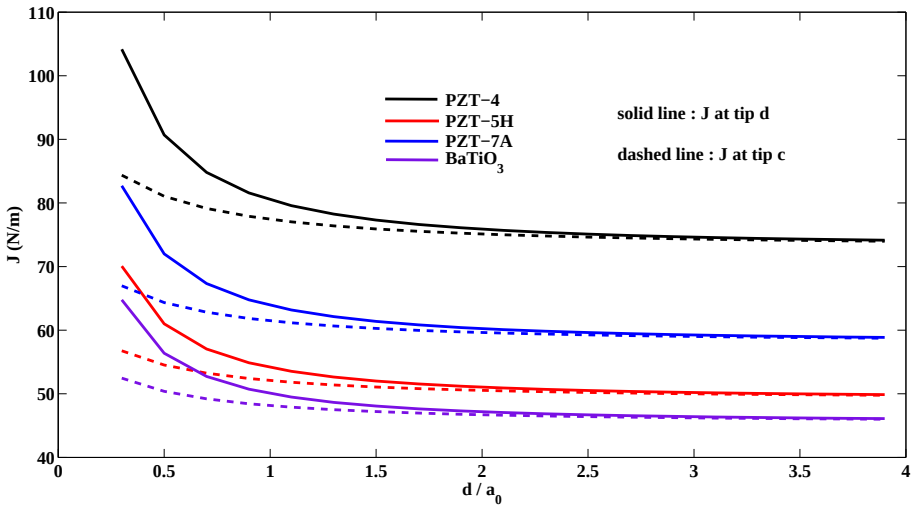

Figure 4.7: LERR (J) versus inter-crack distance for different piezoelectric ceramics

Fig. 4.7 depicts the variation of the LERR at the inner and outer crack tips versus normalized inter-crack distance for different piezoelectric ceramics. It can be seen from the Fig. 4.7 that the LERR is more at the inner crack tip compared to that at outer crack tip. It is also observed that with increase in inter-crack distance; the local energy release rate at the inner and the outer tips becomes equal. This is because the mutual influence of cracks on each other decreases as the distance between them is increased. Also as the LERR depends on factor $\mathbf{V}^T\mathbf{H}^R\mathbf{V}$. It is maximum for ceramic PZT-4 and minimum for $BaTiO_3$ ceramic, therefore LERR is maximum for PZT-4 and minimum for $BaTiO_3$.

Fig. 4.8 shows the variation of open mode stress intensity factor versus inter-crack distance at both inner and outer tips of the crack for following mechanical and electrical loading conditions

case (i) $\sigma_{22}^{\infty} = 0MPa, \quad D_2^{\infty} = 0.005C/m^2,$

case (ii) $\sigma_{22}^{\infty} = 10MPa, \quad D_2^{\infty} = 0C/m^2,$

case (iii) $\sigma_{22}^{\infty} = 10MPa, \quad D_2^{\infty} = 0.005C/m^2.$

It is noted that for case (i) (i.e., mechanical loading is zero) the open mode stress intensity factor, K_I, is minimum at both the crack tips. It stabilizes for $\frac{d}{a_0} \geq 1.5$. It increases but shows the same behavior when electrical loading is zero and mechanical loading is non-zero i.e. case (ii). It further increases almost 2.6 times of that in case (i) with same behavior for case (iii) loading.

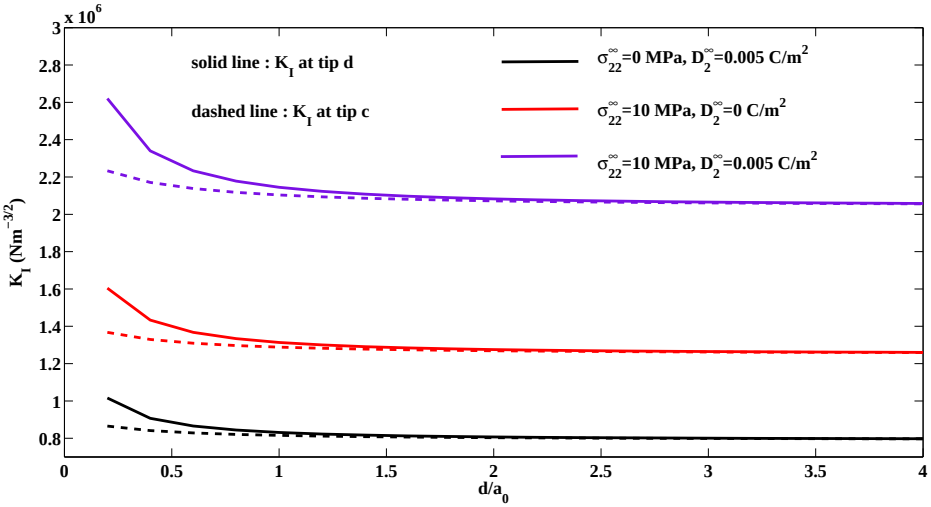

Figure 4.8: K_I versus inter-crack distance for different electro-mechanical loads

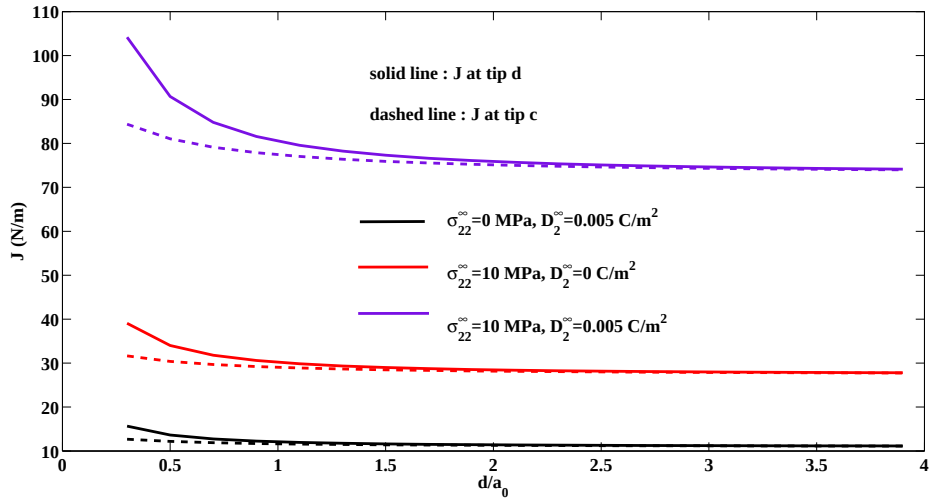

Figure 4.9: LERR (J) versus inter-crack distance for different electro-mechanical loads

Fig. 4.9 depicts the LERR variation with respect to inter-crack distance for above stated three cases. LERR is minimum for case (i) implying the crack arrest is more effective in this case. The LERR stabilizes for $\frac{d}{a_0} \geq 2$. For case (ii) when electrical

loading is zero the energy release rate increases by four times but with the same behavior as in case (i) at both the tips of the crack. For case (iii) the LERR further increases and stabilizes for $\frac{d}{a_0} \geq 2$.

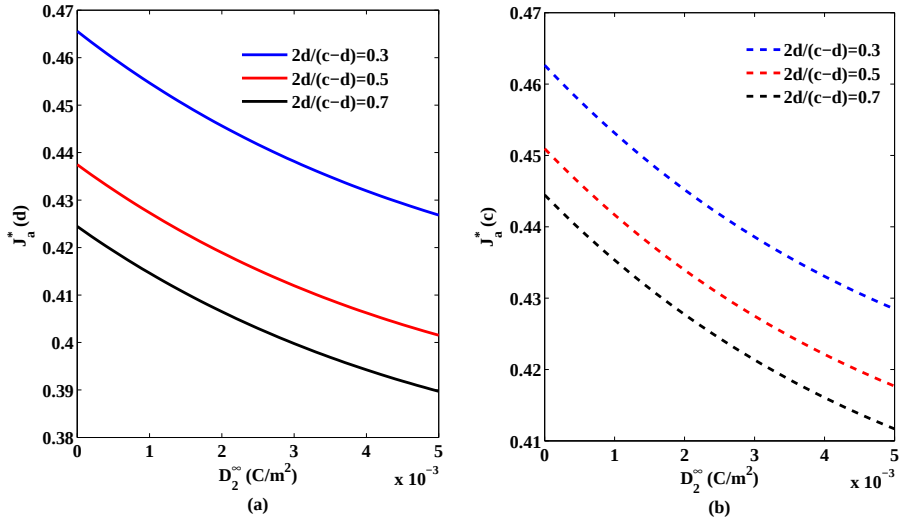

Figure 4.10: Normalized GERR versus applied electric displacement load for different inter-crack distance and PZT-4 ceramic

Fig. 4.10 shows the variation of normalized GERR versus applied electric loading D_2^{∞} for PZT-4 ceramic and different inter-crack distance. It shows that normalized GERR decreases as the applied electric displacement loading increases.

4.7 Conclusions

- A strip-saturation model is proposed for a poled piezoelectric plate cut along two equal collinear hairline straight cracks under in-plane mechanical and electric loads.

- Closed-form expressions are derived for the SIF, ERR, COD and COP drop. Two non-linear simultaneous equations are obtained to determine the saturation zone length.

- The crack effect on the SIF and ERR's depends on the distance between them. The effect of cracks on each other weakens when the distance between the cracks increases.

Chapter 5

Strip-saturation Model with Coalesced Interior Zones

It is observed that if the piezoelectric plate is weakened by two or more cracks and the plate is subjected to electro-mechanical loading which causes opening of the faces of the cracks then a saturation zone developed ahead each of the tip of the cracks. If the load applied is increased, size of developed saturation zones becomes bigger and the saturation zone developed at the two adjacent tips of the two cracks get coalesced. This type of effect for ordinary elastic materials was first studied by Theocaris [119] for an infinite plate weakened by two collinear straight cracks with unified interior plastic zone. The model was modified by Bhargava and Agrawal [9] for the case when developed plastic zone were closed by variable loads, for the case of two equal straight cracks with coalesced plastic zone weakening a plate. Also, Xu et al. [132] studied the problem of two equal length collinear cracks in an infinite sheet using weight function method. While this type of effect is not studied for piezoelectric materials. Therefore to address this paucity a strip-saturation model for a transversely isotropic piezoelectric plate weakened by two equal collinear cracks with coalesced interior saturation zones is proposed.

5.1 Statement of the Problem

Let a poled transversely isotropic piezoelectric plate occupy the x_1ox_2 plane and the polling direction for it is parallel to x_2-axis. It is cut along two equal collinear

This chapter is published in Applied Mathematical Modelling (Elsevier publication), Vol. 37 (2013), pp. 4093-4102.

hairline straight cracks, L_1 and L_2. The cracks L_1 and L_2 occupy, the respective, intervals $[-c,-d]$ and $[d,c]$ on x_1-axis. The cracks surfaces are traction free and electrically impermeable. Unidirectional, normal, uniform constant stress σ_{22}^{∞} and electric displacement D_2^{∞} prescribed at remote boundary open the cracks in self-similar fashion forming a strip- saturation zone ahead of each tip of the two cracks. The loads are increased to the limit that the saturation zones developed at the interior tip of the two cracks get coalesced. The developed three saturation zones are denoted by Γ_1, Γ_2 and Γ_3. These occupy, respective, intervals $[-a,-c]$, $[-d,d]$ and $[c,a]$ on x_1-axis. To stop the crack from further opening the developed saturation zones are subjected to normal, cohesive saturation-limit electric displacement $D_2 = D_s$. Schematically the configuration of the problem is depicted in Fig. 5.1.

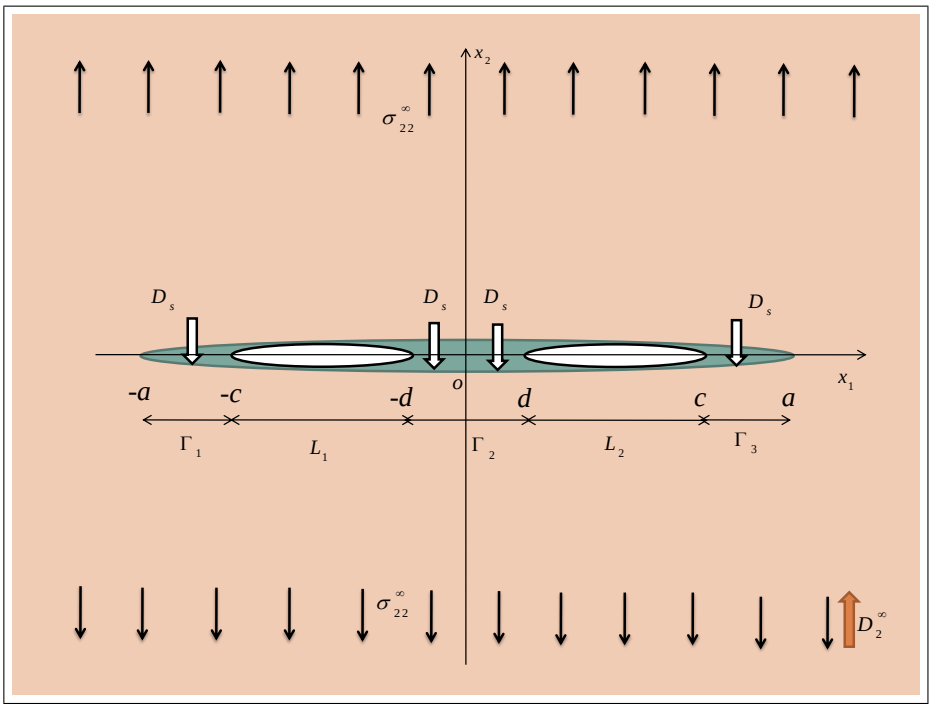

Figure 5.1: Schematic representation of the problem

5.2 Mathematical Model of the Problem

The boundary conditions of the problem may mathematically be expressed as

(i) $\sigma_{22}^{+} = \sigma_{22}^{-} = 0, \;\; D_2 = 0,$ on $L = \bigcup_{i=1}^{2} L_i,$

(ii) $\sigma_{22} = \sigma_{22}^{\infty}, \quad D_2 = D_2^{\infty},$ for $|x_2| \to \infty,$

(iii) $u_2^+ = u_2^-,\ \sigma_{22}^+ = \sigma_{22}^-,\ D_2 = D_s,$ on $\Gamma = \bigcup_{i=1}^{3} \Gamma_i,$

(iv) $\mathbf{\Phi}_{,1}^+ = \mathbf{\Phi}_{,1}^- = -\mathbf{V},\ \mathbf{V} = [0, \sigma_{22}^\infty, 0, D_2^\infty]^T,$ for $d < |x_1| < c,$

(v) $\mathbf{\Phi}_{,1}^+ = \mathbf{\Phi}_{,1}^-,\ \ u_2^+ = u_2^-,\ \ D_2^+ = D_2^- = D_s - D_2^\infty,$ on $\Gamma = \bigcup_{i=1}^{3} \Gamma_i.$

A mathematical model is obtained with the help of above mentioned boundary conditions as follows:

The continuity of $\mathbf{\Phi}_{,1}$ (defined by Equation (2.7.7)) on x_1-axis yields

$$[\mathbf{BF}(x_1) - \overline{\mathbf{BF}}(x_1)]^+ - [\mathbf{BF}(x_1) - \overline{\mathbf{BF}}(x_1)]^- = 0. \tag{5.2.1}$$

The solution of which may directly be written using Equation (2.7.31) as

$$\mathbf{BF}(z) = \overline{\mathbf{BF}}(z) = \mathbf{h}(z) \qquad \text{(say)} \tag{5.2.2}$$

Boundary condition (iv) together with Equations (5.2.2 and 2.7.7) leads to following vector Hilbert problem

$$\mathbf{h}^+(x_1) + \mathbf{h}^-(x_1) = -\mathbf{V},\ d < |x_1| < c. \tag{5.2.3}$$

Introducing a complex function vector $\mathbf{\Omega}(z) = [\Omega_1(z), \Omega_2(z), \Omega_3(z), \Omega_4(z)]^T$ as

$$\mathbf{\Omega}(z) = \mathbf{H}^R \mathbf{BF}(z), \tag{5.2.4}$$

which on using Equation (5.2.2) gives the relation

$$\mathbf{h}(z) = \mathbf{\Lambda\Omega}(z), \tag{5.2.5}$$

where $\mathbf{\Lambda} = [\mathbf{H}^R]^{-1},\ \mathbf{H}^R = 2Re\mathbf{Y},\ \mathbf{Y} = i\mathbf{AB}^{-1}.$

Consequently Equation's (5.2.3) may be written in component form for $\Omega_2(z)$ and $\Omega_4(z)$, yield following scalar Hilbert problem

$$\Lambda_{22}[\Omega_2^+(x_1) + \Omega_2^-(x_1)] + \Lambda_{24}[\Omega_4^+(x_1) + \Omega_4^-(x_1)] = -\sigma_{22}^\infty,\ d < |x_1| < c, \tag{5.2.6}$$

$$\Lambda_{42}[\Omega_2^+(x_1) + \Omega_2^-(x_1)] + \Lambda_{44}[\Omega_4^+(x_1) + \Omega_4^-(x_1)] = -D_2^\infty,\ d < |x_1| < c. \tag{5.2.7}$$

5.3 Solution of the Problem

Eliminating $\Omega_4^+(x_1) + \Omega_4^-(x_1)$ from Equations (5.2.6 and 5.2.7), one obtains

$$\Omega_2^+(x_1) + \Omega_2^-(x_1) = -\frac{\sigma_{22}^\infty \Lambda_{44} - D_2^\infty \Lambda_{24}}{\Lambda_{22}\Lambda_{44} - \Lambda_{24}\Lambda_{42}}, \qquad d < |x_1| < c. \tag{5.3.1}$$

The general solution of Equation (5.3.1) using Equation (2.7.30) may be written as

$$\Omega_2(z) = \frac{P_1(z)}{2X_1(z)} - \frac{1}{2}\frac{\Lambda_{44}\sigma_{22}^\infty - D_2^\infty \Lambda_{24}}{\Lambda_{22}\Lambda_{44} - \Lambda_{24}\Lambda_{42}}, \tag{5.3.2}$$

where $X_1(z) = \sqrt{(z^2 - d^2)(z^2 - c^2)}$ and $P_1(z) = C_0 z^2 + C_1 z + C_2$.

Constant

$$C_0 = \frac{\Lambda_{44}\sigma_{22}^\infty - D_2^\infty \Lambda_{24}}{\Lambda_{22}\Lambda_{44} - \Lambda_{24}\Lambda_{42}}$$

is determined using condition $\lim_{z\to\infty} \Omega_2(z) = 0$.

The condition of single-valuedness around the cracks i.e.,

$$\int_{L_i} [\Omega_2^+(x_1) - \Omega_2^-(x_1)]dx_1 = \int_{L_i} \frac{P_1(x_1)}{X_1(x_1)}dx_1 = 0, \qquad i = 1, 2, \tag{5.3.3}$$

gives $C_1 = 0$ and $C_2 = -C_0 c^2 E(k)/F(k)$, where $F(k)$ and $E(k)$ are the complete elliptic integrals of first and second kind, respectively.

Thus the desired stress function $\Omega_2(z)$ may be written as

$$\Omega_2(z) = \frac{1}{2}\frac{\Lambda_{44}\sigma_{22}^\infty - D_2^\infty \Lambda_{24}}{\Lambda_{22}\Lambda_{44} - \Lambda_{24}\Lambda_{42}} \left\{ \frac{z^2 - c^2\lambda^2}{X_1(z)} - 1 \right\}, \tag{5.3.4}$$

where $k^2 = 1 - (d/c)^2$, $\lambda^2 = E(k)/F(k)$.

Analogously to determine $\Omega_4(z)$, Equation (5.2.7) is solved using the boundary condition (iii) and Equation (2.7.30), the solution may be written as

$$\Omega_4(z) = \frac{1}{2\pi i \Lambda_{44} X_2(z)} \int_\Gamma \frac{D_s X_2(t)}{t - z}dt + \frac{P_2(z)}{2\Lambda_{44}X_2(z)} - \frac{D_2^\infty}{2\Lambda_{44}} - \frac{\Lambda_{42}}{\Lambda_{44}}\Omega_2(z), \tag{5.3.5}$$

where $X_2(z) = \sqrt{z^2 - a^2}$ and $P_2(z) = A_0 z + A_1$.

Again constant $A_0 = D_2^\infty$ is determined using condition $\lim_{z\to\infty} \Omega_4(z) = 0$. Also $A_1 = 0$ is determined from the condition of single-valuedness of displacement around cracks i.e.,

$$\int_{-a}^{a} [\Omega_4^+(x_1) - \Omega_4^-(x_1)]dx_1 = 0. \tag{5.3.6}$$

Finally, evaluating the integral in Equation (5.3.5) and substituting the values of constants A_0 and A_1, the required potential $\Omega_4(z)$, may be written as

$$\Omega_4(z) = \frac{D_s}{\pi\Lambda_{44}}\left\{\frac{\pi}{2} - \tan^{-1}\left(\frac{c}{z}\sqrt{\frac{z^2-a^2}{a^2-c^2}}\right) + \tan^{-1}\left(\frac{d}{z}\sqrt{\frac{z^2-a^2}{a^2-d^2}}\right)\right\} - \frac{\Lambda_{42}}{\Lambda_{44}}\Omega_2(z) - \frac{D_s}{\pi\Lambda_{44}}\left(\frac{\pi}{2} - \sin^{-1}\frac{c}{a} + \sin^{-1}\frac{d}{a}\right)\frac{z}{\sqrt{z^2-a^2}} + \frac{D_2^\infty}{2\Lambda_{44}}\left(\frac{z}{\sqrt{z^2-a^2}} - 1\right). \tag{5.3.7}$$

5.4 Applications

In this section the closed form analytical expressions are derived for developed saturation zone length at the exterior crack tips, crack opening displacement, crack opening potential drop, stress intensity factor and energy release rate.

5.4.1 Saturation zone size

The electric displacement ahead of crack tip is determined using

$$D_2(x_1) = \Lambda_{42}[\Omega_2^+(x_1) + \Omega_2^-(x_1)] + \Lambda_{44}[\Omega_4^+(x_1) + \Omega_4^-(x_1)]. \tag{5.4.1}$$

Substituting the values of $\Omega_2(x_1)$ and $\Omega_4(x_1)$ from Equations (5.3.4 and 5.3.7) and simplifying we obtain

$$D_2(x_1) = D_s\left\{1 - \frac{2}{\pi}\left(\tan^{-1}\frac{c}{x_1}\sqrt{\frac{x_1^2-a^2}{a^2-c^2}} - \tan^{-1}\frac{d}{x_1}\sqrt{\frac{x_1^2-a^2}{a^2-d^2}}\right)\right\} - D_2^\infty + \left\{D_2^\infty - D_s + \frac{2D_s}{\pi}\left(\sin^{-1}\frac{c}{a} - \sin^{-1}\frac{d}{a}\right)\right\}\frac{x_1}{\sqrt{x_1^2-a^2}},\ |x_1| > a. \tag{5.4.2}$$

Extending Dugdale's hypothesis [43] for electric displacement to remain finite at every point of a piezoelectric ceramic under linear piezoelectricity theory assumption, one obtains non-linear equation

$$\frac{a}{d} = \left[1 + \left\{\frac{c}{d}\sec\left(\frac{\pi D_2^\infty}{2D_s}\right) - \tan\left(\frac{\pi D_2^\infty}{2D_s}\right)\right\}^2\right]^{1/2}. \tag{5.4.3}$$

Determining a from Equation (5.4.3), the saturation zone is determined using $|c-a|$.

5.4.2 Crack opening displacement (COD)

We introduced the jump displacement vector $\Delta\mathbf{u}_{,1}$, with the aid of Equations (2.7.6 and 5.2.4) as

$$i\Delta\mathbf{u}_{,1} = i[u^+_{1,1} - u^-_{1,1}, u^+_{2,1} - u^-_{2,1}, u^+_{3,1} - u^-_{1,1}, \phi^+ - \phi^-]^T = \mathbf{H}^R[\mathbf{BF}^+(x_1) - \mathbf{BF}^-(x_1)]. \tag{5.4.4}$$

The relative crack face opening displacement, $\Delta u_2(x_1)$ is obtained using second component from Equation (5.4.4) and substituting the value of $\Omega_2(x_1)$ from Equation (5.3.4) and integrating we obtain

$$\Delta u_2(x_1) = \frac{2c(\sigma^\infty_{22}\Lambda_{44} - D^\infty_2\Lambda_{24})}{\Lambda_{22}\Lambda_{44} - \Lambda_{24}\Lambda_{42}} \left\{E(\varphi, k) - \lambda^2 F(\varphi, k)\right\},\ d < |x_1| < c \tag{5.4.5}$$

where, $\sin^2\varphi = (c^2 - x_1^2)/(c^2 - d^2)$.

5.4.3 Crack opening potential drop (COP)

The COP, $\Delta u_4(x_1)$ is obtained using fourth component of Equation (5.4.4) substituting required value from Equation (5.3.7) and noting that $\Delta u_4 = 0$ at $x_1 = \pm a$ one obtains,

$$\begin{aligned}\Delta u_4(x_1) = -\frac{2D_s}{\pi\Lambda_{44}}[&(c - x_1)\omega(x_1, a, c) + (c + x_1)\omega(-x_1, a, c) - (d - x_1)\omega(x_1, a, d) \\ &-(d + x_1)\omega(-x_1, a, d)] - \frac{\Lambda_{42}}{\Lambda_{44}}\Delta u_2(x_1),\ |x_1| < a\end{aligned} \tag{5.4.6}$$

where, $\omega(x_1, c, a) = \cosh^{-1}|\frac{a^2-c^2}{a(c-x_1)} + \frac{c}{a}|$, $\omega(x_1, d, a) = \cosh^{-1}|\frac{a^2-d^2}{a(d-x_1)} + \frac{d}{a}|$.

5.4.4 Stress intensity factor (SIF)

The stress intensity factor K_I, at the crack tips $x_1 = d$ and $x_1 = c$, is determined using the definition

$$K_I(d) = \lim_{x_1 \to d^-} \sqrt{2\pi(d - x_1)}\sigma_{22}(x_1), \tag{5.4.7}$$

$$K_I(c) = \lim_{x_1 \to c^+} \sqrt{2\pi(x_1 - c)}\sigma_{22}(x_1). \tag{5.4.8}$$

Evaluating $\sigma_{22}(x_1)$ using Equations (2.7.7, 5.2.5 and 5.3.4) and substituting in Equations (5.4.7 and 5.4.8) and simplifying one obtains

$$K_I(d) = -\sqrt{\frac{\pi}{d(c^2-d^2)}}\left(\sigma_{22}^{\infty} - D_2^{\infty}\frac{\Lambda_{24}}{\Lambda_{44}}\right)(d^2 - c^2\lambda^2), \tag{5.4.9}$$

$$K_I(c) = \sqrt{\frac{\pi}{c(c^2-d^2)}}\left(\sigma_{22}^{\infty} - D_2^{\infty}\frac{\Lambda_{24}}{\Lambda_{44}}\right)(c^2 - c^2\lambda^2). \tag{5.4.10}$$

5.4.5 Energy release rate (ERR)

The local energy release rate (LERR) at the actual crack tips $x_1 = d$ and $x_1 = c$ is calculated using definition given by Gao et al. [34]

at the tip $x_1 = d$

$$\begin{aligned} J(d) &= \frac{\pi(d^2 - c^2\lambda^2)^2}{2d(c^2-d^2)}[\mathbf{V}^T\mathbf{H}^R\mathbf{V} - \frac{1}{\Lambda_{44}}(D_2^{\infty})^2] \\ &= \frac{\pi(d^2 - c^2\lambda^2)^2}{2d(c^2-d^2)}\left\{H^R(2,2)(\sigma_{22}^{\infty})^2 + 2H^R(2,4)\sigma_{22}^{\infty}D_2^{\infty} + \frac{(H^R(2,4))^2}{H^R(2,2)}(D_2^{\infty})^2\right\}, \end{aligned} \tag{5.4.11}$$

and at the tip $x_1 = c$

$$\begin{aligned} J(c) &= \frac{\pi(c^2 - c^2\lambda^2)^2}{2c(c^2-d^2)}[\mathbf{V}^T\mathbf{H}^R\mathbf{V} - \frac{1}{\Lambda_{44}}(D_2^{\infty})^2] \\ &= \frac{\pi(c^2 - c^2\lambda^2)^2}{2c(c^2-d^2)}\left\{H^R(2,2)(\sigma_{22}^{\infty})^2 + 2H^R(2,4)\sigma_{22}^{\infty}D_2^{\infty} + \frac{(H^R(2,4))^2}{H^R(2,2)}(D_2^{\infty})^2\right\}. \end{aligned} \tag{5.4.12}$$

The global energy release rate (GERR), J_a, at the inner and outer crack tips is calculated using

$$J_a(d) = J(d) + D_s\Delta u_4(d), \tag{5.4.13}$$

$$J_a(c) = J(c) + D_s\Delta u_4(c). \tag{5.4.14}$$

5.5 Case Study

An illustrative example for PZT-4, PZT-5H, PZT-7A and $BaTiO_3$ cracked unbounded piezoceramic plates is presented to study the capability of crack arrest of the model proposed.

The crack length, prescribed mechanical stress and electric displacement are respectively, taken as $10mm$, $100MPa$ and $0.003C/m^2$.

Fig. 5.2 depicts the behavior of normalized outer saturation zone length to electric displacement load ratio. It is observed when more load is prescribed then a bigger saturation zone develops, as expected.

Variation of normalized SIF, $K_I^*(= K_I/\sqrt{\pi a_0}\sigma_{22}^{\infty})$ versus a_0/c_0, $(a_0 = (c - d)/2, c_0 = (c + d)/2)$ is plotted in Fig. 5.3. It may be noted as a_0/c_0 ratio is increased the SIF also increases. The normalized SIF at the inner crack tip of the crack is always higher than that at outer crack tip i.e., the inner tip of the crack is more stressed, as could also be inferred from Fig. 5.3.

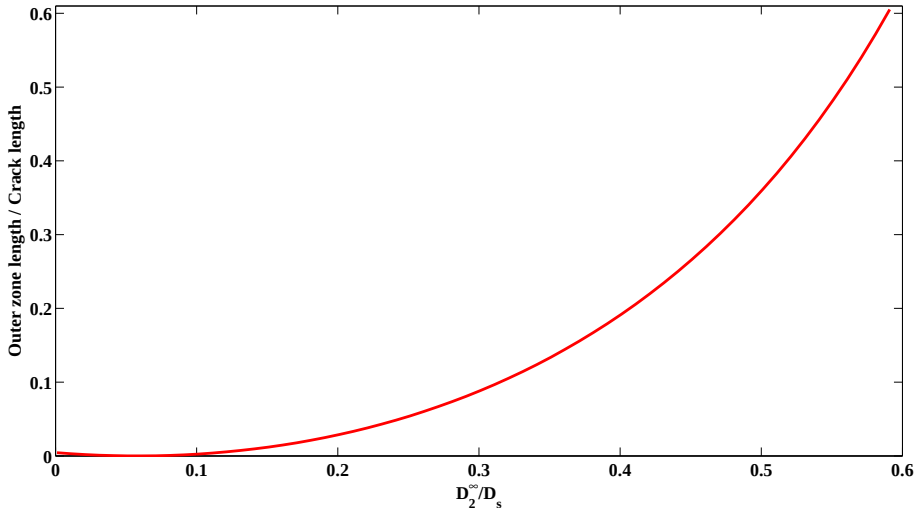

Figure 5.2: Variations of normalized outer zone length versus D_2^{∞}/D_s for PZT-4 ceramic

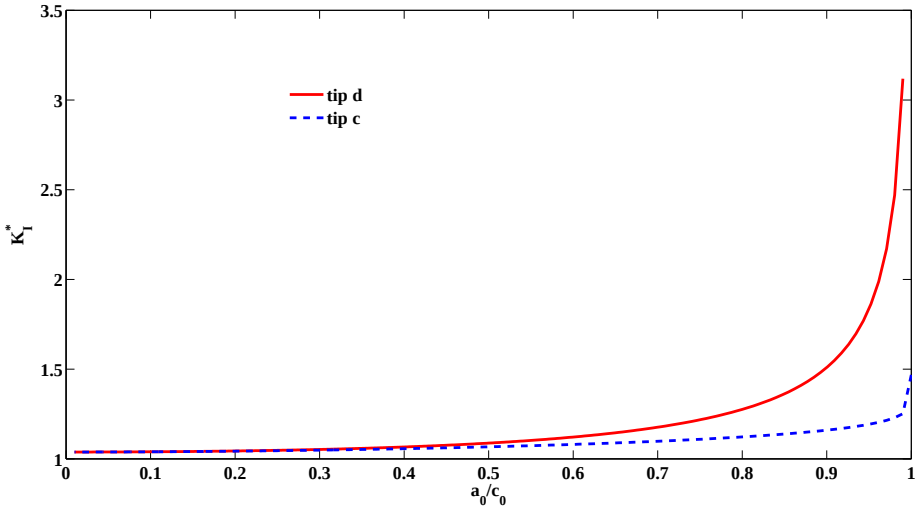

Figure 5.3: Variations of normalized SIF versus a_0/c_0 for PZT-4 ceramic

Normalized SIF, $K_I^*(= K_I/\sqrt{\pi a_0}\sigma_{22}^{\infty})$ study versus prescribed electric displacement load D_2^{∞} is plotted in Fig. 5.4 for PZT-4, PZT-5H, PZT-7A and $BaTiO_3$ ceramics. For all the ceramics as D_2^{∞} is increased the SIF increase linearly, as expected. Also it may be noted that the SIF at inner tip is higher as compared to that at outer tips of the cracks. It is also observed that SIF is the least for PZT-7A ceramic while highest for the case of PZT-4 ceramic.

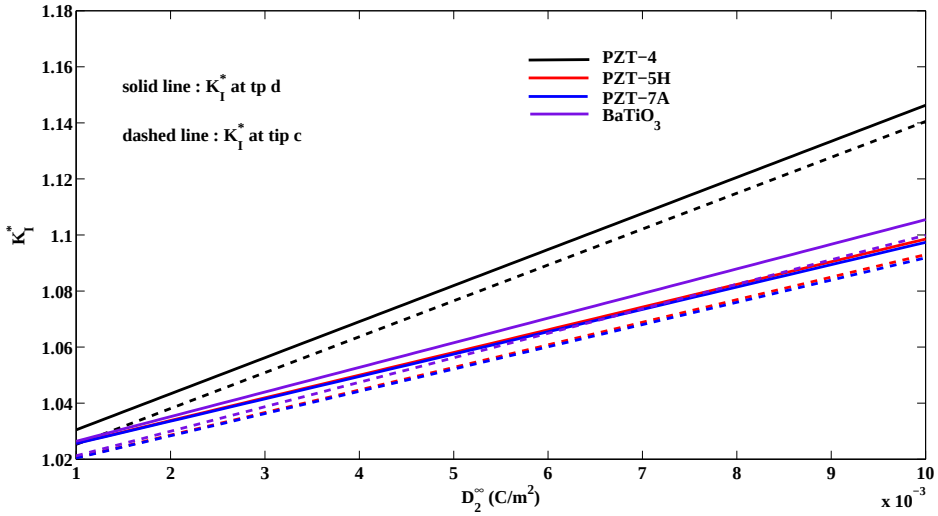

Figure 5.4: Variations of normalized SIF versus D_2^{∞}

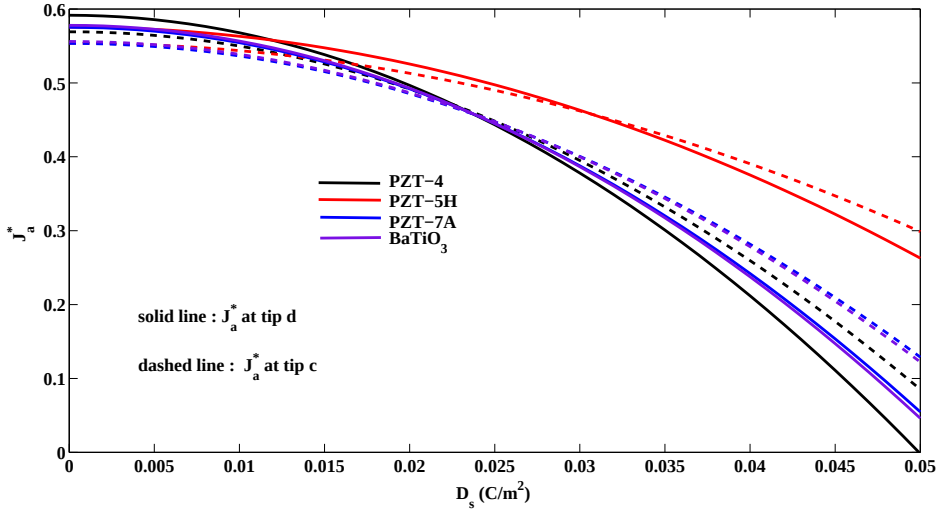

Figure 5.5: Variations of normalized GERR versus D_s

The crack arrest study vis-a-vis distributed saturation-limit electric displacement load D_s, on the developed saturation zones is presented in Fig. 5.5 for $D_2^{\infty} = 0.003C/m^2$ and $\sigma_{22}^{\infty} = 100MPa$. It is observed that normalized GERR, $J_a^*(=$

$J_a/\pi a_0 H^R(2,2)(\sigma_{22}^{\infty})^2)$ for all ceramics reduce (amounting to the arrest of crack opening) as D_s value increased.

5.6 Conclusions

- A strip-saturation model for a transversely isotropic piezoelectric plate weakened with coalesced interior saturation zones is proposed.
- Analytic closed form expressions are obtained to determine the saturation zone length, open mode stress intensity factor, crack opening displacement and energy release rate.
- The results for saturation zone length, stress intensity factor, and energy release rate with respect to prescribed load ratio, inter crack distance show that if the cracks are brought close to each other then the interior tips of the cracks are more stressed as compared to exterior tips. If the cracks are moved far apart the effect on each other reduces.
- The energy release rate reduction concludes that model proposed is capable of crack arrest under small-scale electric saturation.

Chapter 6

Strip-electro-mechanical Yielding Model for a Piezoelectric Plate

Very few papers which consider both mechanical and electrical yielding of piezoelectric plate are available in literature. Shen et al. [108] was first to address the problem of mechanical and electrical yielding for a cracked piezoelectric plate under anti-plane shear mechanical loading and in-plane electrical loading. Bhargava and Saxena [12] further investigated the problem under different loading conditions and different mechanical and electrical yielding. Also Loboda et al. [78] investigated a crack problem in a thin ductile layer between two piezoelectric material under remote in-plane electric and mechanical loading. They too considered both electric and mechanical yielding.

Most of the reported strip-electro-mechanical yield models that have been proposed are for single crack case only. We propose a strip-electro-mechanical yielding model for a piezoelectric plate weakened by two equal collinear cracks with electrical polarization reaching a saturation limit and normal stress reaching a yield stress along a line segment in front of the cracks. Three different situations are investigated when developed electrical saturation zones are bigger/smaller or equal to the developed mechanical yield zones.

This chapter is published in Applied Mathematical Modelling (Elsevier publication) Vol. 37 (2013), pp. 9101-9116.

6.1 Statement of the Problem

An unbounded transversely isotropic piezoelectric plate occupies the plane x_1ox_2 and poled along ox_2-direction is weakened by two equal collinear cracks L_1 and L_2, which occupy respective, intervals $[-c,-d]$ and $[d,c]$ on x_1-axis. In-plane unidirectional, normal, uniform constant tension $\sigma_{22}=\sigma_{22}^{\infty}$ and electric displacement $D_2=D_2^{\infty}$ are prescribed at remote boundary of the plate. Consequently the cracks yield open in self-similar fashion forming an electric saturation and a mechanical yield zone ahead of each tip of the cracks. These developed strip saturation $\Gamma_i(i=1,2,3,4)$ and mechanical yield zones $\Gamma_i'(i=1,2,3,4)$ occupy respective, intervals $[-a,-c]$, $[-d,-b]$, $[b,d]$, $[c,a]$, and $[-c_1,-c]$, $[-d,-d_1]$, $[d_1,d]$ and $[c,c_1]$ on x_1-axis. The crack opening is stopped by distributing on the saturation zone rims a saturation-limit electric displacement $D_2=D_s$ and a yield point stress $\sigma_{22}=\sigma_s$, on the yield zone rims, respectively. Three cases are considered

Case I: when saturation zones are bigger than developed yield zones,

Case II: when saturation zones are smaller than developed yield zones,

Case III: when saturation and yield zones are equal.

6.2 Mathematical Model and Solution of the Problem

6.2.1 Case I: When saturation zones are bigger than developed yield zones ($|b|<|d_1|$ and $|a|>|c_1|$)

Schematically the configuration of the problem is depicted in Fig. 6.1.

Mathematically the boundary conditions of the problem may be written as

(i) $\sigma_{22}^{+}=\sigma_{22}^{-}=0, \quad D_2=0, \qquad$ on $L=\bigcup_{i=1}^{2}L_i,$

(ii) $\sigma_{22}=\sigma_{22}^{\infty}, \quad D_2=D_2^{\infty}, \qquad$ for $|x_2|\to\infty,$

(iii) $\sigma_{22}^{+}=\sigma_{22}^{-}=\sigma_s, \qquad$ for $\Gamma'=\bigcup_{i=1}^{4}\Gamma_i',$

(iv) $D_2^+ = D_2^- = D_s,$ for $\Gamma = \bigcup_{i=1}^{4} \Gamma_i,$

(v) $\mathbf{\Phi}_{,1}^{I+} = \mathbf{\Phi}_{,1}^{I-} = -\mathbf{V}^I,$ for $d < |x_1| < c,$

where $\mathbf{V}^I = [0, \sigma_{22}^{\infty}, 0, D_2^{\infty}]^T$, and superscript I denotes that quantity refers to the Case I.

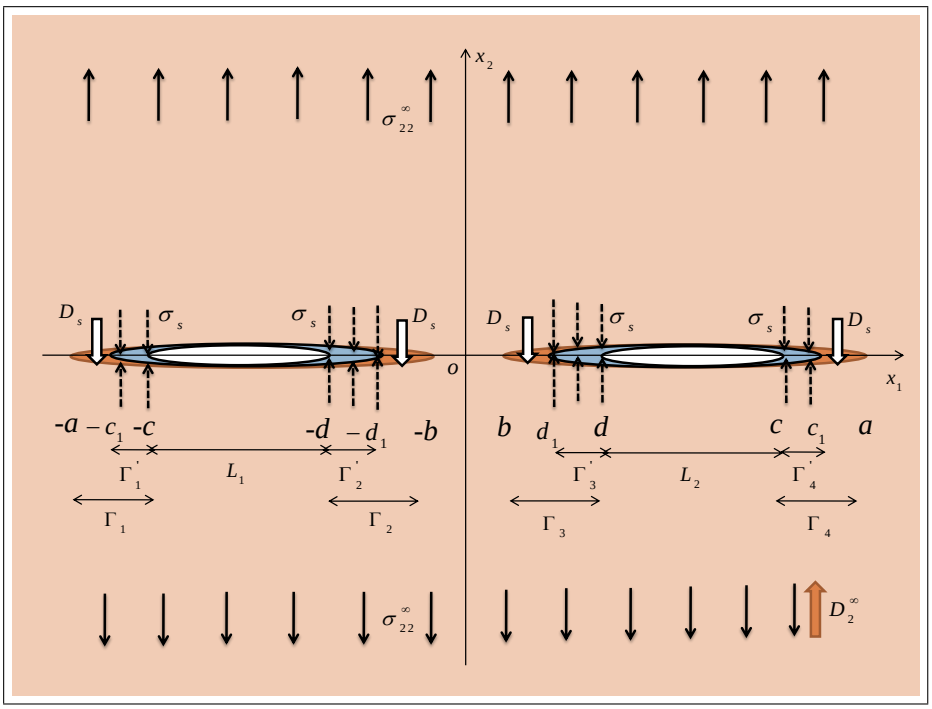

Figure 6.1: Schematic representation of the configuration of problem for Case I, when saturation zones are bigger than developed yield zones

A mathematical model obtained with the help of above mentioned boundary conditions is solved as follows:

The continuity of $\mathbf{\Phi}_{,1}$ (defined by Equation (2.7.7)) on x_1-axis yields

$$[\mathbf{BF}^I(x_1) - \overline{\mathbf{B}}\overline{\mathbf{F}^I}(x_1)]^+ - [\mathbf{BF}^I(x_1) - \overline{\mathbf{B}}\overline{\mathbf{F}^I}(x_1)]^- = 0. \tag{6.2.1}$$

The solution of which may directly be written using Equation (2.7.31) as

$$\mathbf{BF}^I(z) = \overline{\mathbf{B}}\overline{\mathbf{F}^I}(z) = \mathbf{h}^I(z) \qquad \text{(say)} \tag{6.2.2}$$

Boundary condition (v) together with Equations (6.2.2 and 2.7.7) leads to following vector Hilbert problem

$$\mathbf{h}^{I+}(x_1) + \mathbf{h}^{I-}(x_1) = -\mathbf{V}^I,\ d < |x_1| < c. \tag{6.2.3}$$

Introducing a complex function vector $\mathbf{\Omega}^I(z) = [\Omega_1^I(z), \Omega_2^I(z), \Omega_3^I(z), \Omega_4^I(z)]^T$ as

$$\mathbf{\Omega}^I(z) = \mathbf{H}^R\mathbf{B}\mathbf{F}^I(z), \tag{6.2.4}$$

which on using Equation (6.2.2) gives the relation

$$\mathbf{h}^I(z) = \mathbf{\Lambda}\mathbf{\Omega}^I(z), \tag{6.2.5}$$

where $\mathbf{\Lambda} = [\mathbf{H}^R]^{-1},\ \mathbf{H}^R = 2Re\mathbf{Y},\ \mathbf{Y} = i\mathbf{A}\mathbf{B}^{-1}$.

Consequently Equation's (6.2.3) may be written in component form for $\Omega_2^I(z)$ and $\Omega_4^I(z)$, yield following scalar Hilbert problem

$$\Lambda_{22}[\Omega_2^{I+}(x_1) + \Omega_2^{I-}(x_1)] + \Lambda_{24}[\Omega_4^{I+}(x_1) + \Omega_4^{I-}(x_1)] = -\sigma_{22}^{\infty},\ d < |x_1| < c, \tag{6.2.6}$$

$$\Lambda_{42}[\Omega_2^{I+}(x_1) + \Omega_2^{I-}(x_1)] + \Lambda_{44}[\Omega_4^{I+}(x_1) + \Omega_4^{I-}(x_1)] = -D_2^{\infty},\ d < |x_1| < c. \tag{6.2.7}$$

6.2.1.1 Solution of the Problem

Eliminating $\Omega_4^{I+}(x_1) + \Omega_4^{I-}(x_1)$ from Equations (6.2.6 and 6.2.7) and then solving using Equation (2.7.30) together with boundary condition (iii) one obtains

$$\Omega_2^I(z) = \frac{\Lambda_{44}\sigma_s - D_s\Lambda_{24}}{2\pi i X_1(z)\Sigma}\int_{\Gamma'}\frac{X_1(t)}{t-z}dt + \frac{P_1(z)}{2X_1(z)} - \frac{1}{2}\frac{\Lambda_{44}\sigma_{22}^{\infty} - D_2^{\infty}\Lambda_{24}}{\Lambda_{22}\Lambda_{44} - \Lambda_{24}\Lambda_{42}} \tag{6.2.8}$$

where

$$P_1(z) = C_0z^2 + C_1z + C_2,\ X_1(z) = \sqrt{(z^2 - d_1^2)(z^2 - c_1^2)} \text{ and } \Sigma = \Lambda_{22}\Lambda_{44} - \Lambda_{24}\Lambda_{42}.$$

Constant

$$C_0 = \frac{\Lambda_{44}\sigma_{22}^{\infty} - D_2^{\infty}\Lambda_{24}}{\Lambda_{22}\Lambda_{44} - \Lambda_{24}\Lambda_{42}}$$

is determined using condition $\lim_{z\to\infty}\Omega_2^I(z) = 0$. Also C_1 and C_2 are determined from the condition of single-valuedness of displacement around cracks i.e.,

$$\int_{C_i'}[\Omega_2^{I+}(x_1) - \Omega_2^{I-}(x_1)]dx_1 = 0,\ i = 1, 2, \tag{6.2.9}$$

C_1' and C_2' denote the respective intervals $[-c_1, -d_1]$ and $[d_1, c_1]$ on x_1-axis.

Finally, evaluating the integral in Equation (6.2.8) and substituting the values of constants C_0, C_1 and C_2, the required potential $\Omega_2^I(z)$, may be written as

$$\begin{aligned}\Omega_2^I(z) = \frac{1}{2}\frac{\Lambda_{44}\sigma_{22}^{\infty} - D_2^{\infty}\Lambda_{24}}{\Lambda_{22}\Lambda_{44} - \Lambda_{24}\Lambda_{42}}\left\{\frac{z^2 - c_1^2\lambda_1^2}{X_1(z)} - 1\right\} + \frac{\Lambda_{44}\sigma_s - \Lambda_{24}D_s}{\pi\Sigma}\left(\frac{\pi}{2} - \varphi_d + \varphi_c\right)\\ -\frac{\Lambda_{44}\sigma_s - \Lambda_{24}D_s}{\pi\Sigma X_1(z)}\left\{(z^2 - c_1^2\lambda_1^2)\left(\frac{\pi}{2} - \psi_d + \psi_c\right) + R_1\right\},\end{aligned} \tag{6.2.10}$$

where,

$$k_1^2 = \frac{c_1^2 - d_1^2}{c_1^2},\ \lambda_1^2 = E(k_1)/F(k_1),\ \sin^2\psi_d = \frac{c_1^2 - d^2}{c_1^2 - d_1^2},\ \sin^2\psi_c = \frac{c_1^2 - c^2}{c_1^2 - d_1^2},$$
$$\varphi_d = \tan^{-1}\sqrt{\frac{(d_1^2 - z^2)(d^2 - c_1^2)}{(c_1^2 - z^2)(d_1^2 - d^2)}},\ \varphi_c = \tan^{-1}\sqrt{\frac{(d_1^2 - z^2)(c^2 - c_1^2)}{(c_1^2 - z^2)(d_1^2 - c^2)}},$$
$$R_1 = dc_1\left\{E(\psi_d, k_1) - \lambda_1^2 F(\psi_d, k_1)\right\} - cc_1\left\{E(\psi_c, k_1) - \lambda_1^2 F(\psi_c, k_1)\right\}$$
$$- k_1^2 c_1^2\left(\sin\psi_d\cos\psi_d - \sin\psi_c\cos\psi_c\right).$$

Analogously to determine $\Omega_4^I(z)$, Equation (6.2.7) is solved using the boundary condition (iv) and Equation (2.7.30), the solution may be written as

$$\Omega_4^I(z) = \frac{1}{2\pi i\Lambda_{44}X_2(z)}\int_\Gamma \frac{D_s X_2(t)}{t - z}dt + \frac{P_2(z)}{2\Lambda_{44}X_2(z)} - \frac{D_2^\infty}{2\Lambda_{44}} - \frac{\Lambda_{42}}{\Lambda_{44}}\Omega_2^I(z), \quad (6.2.11)$$

where $P_2(z) = A_0z^2 + A_1z + A_2$ and $X_2(z) = \sqrt{(z^2 - a^2)(z^2 - b^2)}$.
Again constant $A_0 = D_2^\infty$ is determined using condition $\lim_{z\to\infty}\Omega_4^I(z) = 0$. Also A_1 and A_2 are determined from the condition of single-valuedness of displacement around cracks i.e.,

$$\int_{C_i''}[\Omega_4^{I+}(x_1) - \Omega_4^{I-}(x_1)]dx_1 = 0,\ i = 1, 2,\ C_1'' = [-a, -b],\ C_2'' = [b, a] \text{ on } x_1 - \text{axis}. \quad (6.2.12)$$

Finally, evaluating the integral in Equation (6.2.11) and substituting the values of constants A_0, A_1 and A_2, the required potential $\Omega_4^I(z)$, may be written as

$$\Omega_4^I(z) = -\frac{\Lambda_{42}}{\Lambda_{44}}\Omega_2^I(z) + \frac{D_2^\infty}{2\Lambda_{44}}\left\{\frac{z^2 - a^2\lambda_2^2}{X_2(z)} - 1\right\} + \frac{D_s}{\pi\Lambda_{44}}\left(\frac{\pi}{2} - \upsilon_d + \upsilon_c\right)$$
$$- \frac{D_s}{\pi\Lambda_{44}X_2(z)}\left\{(z^2 - a^2\lambda_2^2)\left(\frac{\pi}{2} - \vartheta_d + \vartheta_c\right) + R_2\right\}, \quad (6.2.13)$$

where,

$$k_2^2 = 1 - (b/a)^2,\ \lambda_2^2 = E(k_2)/F(k_2),\ \sin^2\vartheta_d = \frac{a^2 - d^2}{a^2 - b^2},\ \sin^2\vartheta_c = \frac{a^2 - c^2}{a^2 - b^2},$$
$$\upsilon_d = \tan^{-1}\sqrt{\frac{(b^2 - z^2)}{(a^2 - z^2)}\frac{(a^2 - d^2)}{(d^2 - b^2)}},\ \upsilon_c = \tan^{-1}\sqrt{\frac{(b^2 - z^2)}{(a^2 - z^2)}\frac{(a^2 - c^2)}{(c^2 - b^2)}},$$
$$R_2 = da\left\{E(\vartheta_d, k_2) - \lambda_2^2 F(\vartheta_d, k_2)\right\} - ca\left\{E(\vartheta_c, k_2) - \lambda_2^2 F(\vartheta_c, k_2)\right\}$$
$$- a^2k_2^2\left(\sin\vartheta_d\cos\vartheta_d - \sin\vartheta_c\cos\vartheta_c\right).$$

6.2.1.2 Applications

In this section the expressions are derived for length of saturation zone, yield zone, crack opening displacement, crack opening potential drop and energy release rate.

Saturation zone

The electric displacement is determined using Equations (2.7.7 and 6.2.5) as

$$\mathbf{\Phi}^{I}_{,1}(x_1) = \mathbf{B}\mathbf{F}^{I+}(x_1) + \mathbf{B}\mathbf{F}^{I-}(x_1) = \mathbf{\Lambda}\mathbf{\Omega}^{I+}(x_1) + \mathbf{\Lambda}\mathbf{\Omega}^{I-}(x_1),\ |x_1| > a. \tag{6.2.14}$$

Taking the fourth component of above Equation (6.2.14), we get

$$D^{I}_{2}(x_1) = \Lambda_{42}\left[\Omega^{I+}_{2}(x_1) + \Omega^{I-}_{2}(x_1)\right] + \Lambda_{44}\left[\Omega^{I+}_{4}(x_1) + \Omega^{I-}_{4}(x_1)\right]. \tag{6.2.15}$$

Substituting values of $\Omega^{I}_{2}(x_1)$ and $\Omega^{I}_{4}(x_1)$ from Equations (6.2.10 and 6.2.13) and simplifying one finally arrives at

$$\begin{aligned} D^{I}_{2}(x_1) = {} & \frac{2D_s}{\pi}\left(\frac{\pi}{2} - \upsilon_d + \upsilon_c\right) + D^{\infty}_{2}\left\{\frac{x_1^2 - a^2\lambda_2^2}{X_2(x_1)} - 1\right\} \\ & - \frac{2D_s}{\pi X_2(x_1)}\left\{(x_1^2 - a^2\lambda_2^2)\left(\frac{\pi}{2} - \vartheta_d + \vartheta_c\right) + R_2\right\}. \end{aligned} \tag{6.2.16}$$

The saturation zones lengths are now obtained by extending Dugdale [43] hypothesis to the electric displacement to remain finite at every point of the plate. This leads to the determination of two non-linear equations

$$\left(\frac{b^2}{a^2} - \lambda_2^2\right)\left(\frac{\pi D^{\infty}_{2}}{2D_s} - \frac{\pi}{2} + \vartheta_d - \vartheta_c\right) - \frac{R_2}{a^2} = 0, \tag{6.2.17}$$

$$\left(1 - \lambda_2^2\right)\left(\frac{\pi D^{\infty}_{2}}{2D_s} - \frac{\pi}{2} + \vartheta_d - \vartheta_c\right) - \frac{R_2}{a^2} = 0, \tag{6.2.18}$$

to determine a and b. Hence saturation zone length at the tips c and d are calculated from $(a - c)$ and $(d - b)$, respectively.

Yield zone

To calculate yield zones lengths the required stress component is obtained by writing second component of Equation (6.2.14),

$$\sigma^{I}_{22}(x_1) = \Lambda_{22}\left[\Omega^{I+}_{2}(x_1) + \Omega^{I-}_{2}(x_1)\right] + \Lambda_{24}\left[\Omega^{I+}_{4}(x_1) + \Omega^{I-}_{4}(x_1)\right]. \tag{6.2.19}$$

Substituting values from Equations (6.2.10 and 6.2.13) and simplifying, we get

$$\sigma_{22}^{I}(x_1) = \frac{2}{\pi}\left(\sigma_s - \frac{\Lambda_{24}}{\Lambda_{44}}D_s\right)\left(\frac{\pi}{2} - \varphi_d + \varphi_c\right) + \left(\sigma_{22}^{\infty} - \frac{\Lambda_{24}}{\Lambda_{44}}D_2^{\infty}\right)\left\{\frac{x_1^2 - c_1^2\lambda_1^2}{X_1(x_1)} - 1\right\}$$
$$-\frac{2}{\pi X_1(x_1)}\left(\sigma_s - \frac{\Lambda_{24}}{\Lambda_{44}}D_s\right)\left\{(x_1^2 - c_1^2\lambda_1^2)\left(\frac{\pi}{2} - \psi_d + \psi_c\right) + R_1\right\}. \tag{6.2.20}$$

Using Dugdale's [24] hypothesis that the stress remain finite at every point of the plate consequently at the points $x_1 = d_1$ and $x_1 = c_1$ also we get the following transcendental equations, respectively

$$\left(\frac{d_1^2}{c_1^2} - \lambda_1^2\right)\left(\frac{\pi}{2}\frac{\Lambda_{44}\sigma_{22}^{\infty} - \Lambda_{24}D_2^{\infty}}{\Lambda_{44}\sigma_s - \Lambda_{24}D_s} - \frac{\pi}{2} + \psi_d - \psi_c\right) - \frac{R_1}{c_1^2} = 0, \tag{6.2.21}$$

$$\left(1 - \lambda_1^2\right)\left(\frac{\pi}{2}\frac{\Lambda_{44}\sigma_{22}^{\infty} - \Lambda_{24}D_2^{\infty}}{\Lambda_{44}\sigma_s - \Lambda_{24}D_s} - \frac{\pi}{2} + \psi_d - \psi_c\right) - \frac{R_1}{c_1^2} = 0. \tag{6.2.22}$$

These enable us to determine c_1 and d_1 for prescribed loads. The yield zone lengths are than calculated from $(c_1 - c)$ and $(d - d_1)$.

Crack opening displacement (COD)

The jump displacement vector $\Delta\mathbf{u}_{,1}^{I}$ is determined as

$$i\Delta\mathbf{u}_{,1}^{I}(x_1) = i[u_{1,1}^{+} - u_{1,1}^{-}, u_{2,1}^{+} - u_{2,1}^{-}, u_{3,1}^{+} - u_{3,1}^{-}, E_1^{-} - E_1^{+}]^T = \mathbf{H}^R[\mathbf{BF}^{I+}(x_1) - \mathbf{BF}^{I-}(x_1)]. \tag{6.2.23}$$

The jump displacement component Δu_2^I at the crack tips d and c are obtained by remembering that $\Delta u_2^I = 0$ at the tips $x_1 = \pm d_1, \pm c_1$

at the inner crack tip $x_1 = d$

$$\Delta u_2^I(d) = -\frac{(\Lambda_{44}\sigma_s - \Lambda_{24}D_s)}{\pi\Sigma}\left\{\frac{2d_1^2}{c_1}\sqrt{\frac{c_1^2 - d^2}{d^2 - d_1^2}}R_3 - d\ln(A) + 2F(\tau_d, k_1)\frac{R_1}{c_1}\right\}$$
$$-\frac{(\Lambda_{44}\sigma_s - \Lambda_{24}D_s)}{\pi\Sigma}\left\{G(d,c) + 2c_1\left(\frac{\pi}{2} - \psi_d + \psi_c\right)R_4\right\}$$
$$+\frac{c_1}{\Sigma}(\Lambda_{44}\sigma_{22}^{\infty} - \Lambda_{24}D_2^{\infty})R_4, \tag{6.2.24}$$

at the outer crack tip $x_1 = c$

$$\Delta u_2^I(c) = \frac{(\Lambda_{44}\sigma_s - \Lambda_{24}D_s)}{\pi\Sigma}\left\{2c_1\left(\frac{\pi}{2} - \psi_d + \psi_c\right)R_5 + H(c,d) - c\ln(B)\right\}$$
$$+\frac{(\Lambda_{44}\sigma_s - \Lambda_{24}D_s)}{\pi\Sigma}\left\{2F(\psi_c, k_1)\frac{R_1}{c_1} + \frac{2}{c_1}\sqrt{\frac{c^2 - d_1^2}{c_1^2 - c^2}}R_6\right\}$$
$$-\frac{c_1}{\Sigma}(\Lambda_{44}\sigma_{22}^{\infty} - \Lambda_{24}D_2^{\infty})R_5, \tag{6.2.25}$$

where,

$$\ln(A) = \ln\left(\frac{c_1^2 - d^2}{c_1^2 - d_1^2} + \frac{c_1^2(d_1^2 - d^2)}{d^2(c_1^2 - d_1^2)}\right),\ \ln(B) = \ln\left(\frac{(c_1^2 - c^2)(c^2 - d_1^2)}{c^2(c_1^2 - d_1^2)} + 1\right),$$

$$\sin^2\tau_d = c_1^2(d^2 - d_1^2)/\left(d^2(c_1^2 - d_1^2)\right),\ R_3 = \left(F(\tau_d, k_1) - II(\tau_d, \frac{d^2 - d_1^2}{d^2}, k_1)\right),$$

$$R_4 = \left(E(\tau_d, k_1) - \frac{k_1^2 \sin\tau_d \cos\tau_d}{\sqrt{1 - k_1^2\sin^2\tau_d}} - \lambda_1^2 F(\tau_d, k_1)\right),$$

$$R_5 = \left(E(\psi_c, k_1) - \lambda_1^2 F(\psi_c, k_1)\right),\ R_6 = \left(c_1^2 F(\psi_c, k_1) - c^2 II(\psi_c, \frac{c_1^2 - c^2}{c_1^2}, k_1)\right),$$

$$G(d,c) = d\ln\left(\frac{\sqrt{(d^2 - d_1^2)(c_1^2 - c^2)} + \sqrt{(c_1^2 - d^2)(c^2 - d_1^2)}}{\sqrt{(d^2 - d_1^2)(c_1^2 - c^2)} - \sqrt{(c_1^2 - d^2)(c^2 - d_1^2)}}\right)$$
$$- \frac{2d_1^2}{c_1}\sqrt{\frac{c_1^2 - c^2}{c^2 - d_1^2}}\, II(\tau_d, \frac{c^2 k_1^2}{c^2 - d_1^2}, k_1),$$

$$H(c,d) = c\ln\left(\frac{\sqrt{(c^2 - d_1^2)(c_1^2 - d^2)} + \sqrt{(c_1^2 - c^2)(d^2 - d_1^2)}}{\sqrt{(c^2 - d_1^2)(c_1^2 - d^2)} - \sqrt{(c_1^2 - c^2)(d^2 - d_1^2)}}\right)$$
$$- \frac{2}{c_1}\sqrt{(d^2 - d_1^2)(c_1^2 - d^2)}\left(F(\psi_c, k_1) + \frac{d^2}{c_1^2 - d^2} II(\psi_c, \frac{c_1^2 - d_1^2}{c_1^2 - d^2}, k_1)\right).$$

Crack opening potential drop (COP)

COP is calculated by taking fourth component from Equation (6.2.23) and substituting from Equation (6.2.13) and integrating, one gets

at the inner crack tip $x_1 = d$

$$\Delta u_4^I(d) = -\frac{D_s}{\pi\Lambda_{44}}\left\{-d\ln(C) + 2F(\xi_d, k_2)\frac{R_2}{a} + G_1(d,c) + \frac{2b^2}{a}\sqrt{\frac{a^2 - d^2}{d^2 - b^2}}R_7\right\}$$
$$- \frac{2aD_s}{\pi\Lambda_{44}}\left(\frac{\pi}{2} - \vartheta_d + \vartheta_c\right)R_8 + \frac{aD_2^\infty}{\Lambda_{44}}R_8 - \frac{\Lambda_{42}}{\Lambda_{44}}\Delta u_2^I(d), \qquad (6.2.26)$$

and at the outer crack tip $x_1 = c$

$$\Delta u_4^I(c) = \frac{D_s}{\pi\Lambda_{44}}\left\{-c\ln(D) + H_1(c,d) + 2F(\vartheta_c, k_2)\frac{R_2}{a} + \frac{2}{a}\sqrt{\frac{c^2 - b^2}{a^2 - c^2}}R_9\right\}$$
$$+ \frac{2aD_s}{\pi\Lambda_{44}}\left(\frac{\pi}{2} - \vartheta_d + \vartheta_c\right)R_{10} - \frac{aD_2{}^\infty}{\Lambda_{44}}R_{10} - \frac{\Lambda_{42}}{\Lambda_{44}}\Delta u_2^I(c), \qquad (6.2.27)$$

where,

$$\ln(C) = \ln\left(\frac{a^2 - d^2}{a^2 - b^2} + \frac{a^2(b^2 - d^2)}{d^2(a^2 - b^2)}\right),\ \ln(D) = \ln\left(\frac{(a^2 - c^2)(c^2 - b^2)}{c^2(a^2 - b^2)} + 1\right),$$

$$\sin^2\xi_d = a^2(d^2 - b^2)/\left(d^2(a^2 - b^2)\right),\ R_7 = \left(F(\xi_d, k_2) - II(\xi_d, \frac{d^2 - b^2}{d^2}, k_2)\right),$$

$$R_8 = \left(E(\xi_d, k_2) - \frac{k_2^2 \sin\xi_d \cos\xi_d}{\sqrt{1-k_2^2\sin^2\xi_d}} - \lambda_2^2 F(\xi_d, k_2) \right),$$

$$R_9 = \left(a^2 F(\vartheta_c, k_2) - c^2 II(\vartheta_c, \frac{a^2-c^2}{a^2}, k_2) \right),\ R_{10} = \left(E(\vartheta_c, k_2) - \lambda_2^2 F(\vartheta_c, k_2) \right),$$

$$G_1(d,c) = d \ln \left(\frac{\sqrt{(d^2-b^2)(a^2-c^2)} + \sqrt{(a^2-d^2)(c^2-b^2)}}{\sqrt{(d^2-b^2)(a^2-c^2)} - \sqrt{(a^2-d^2)(c^2-b^2)}} \right)$$
$$- \frac{2b^2}{a}\sqrt{\frac{a^2-c^2}{c^2-b^2}}\, II(\xi_d, \frac{c^2k_2^2}{c^2-b^2}, k_2),$$

$$H_1(c,d) = c \ln \left(\frac{\sqrt{(c^2-b^2)(a^2-d^2)} + \sqrt{(a^2-c^2)(d^2-b^2)}}{\sqrt{(c^2-b^2)(a^2-d^2)} - \sqrt{(a^2-c^2)(d^2-b^2)}} \right)$$
$$- \frac{2}{a}\sqrt{(d^2-b^2)(a^2-d^2)} \left(F(\vartheta_c, k_2) + \frac{d^2}{a^2-d^2} II(\vartheta_c, \frac{a^2-b^2}{a^2-d^2}, k_2) \right).$$

Energy release rate (ERR)

Energy release rate is calculated at the interior tip $x_1 = d$ and $x_1 = c$ exterior tip using the formulae

$$J_a^I(d) = \sigma_s \Delta u_2^I(d) + D_s \Delta u_4^I(d), \tag{6.2.28}$$

$$J_a^I(c) = \sigma_s \Delta u_2^I(c) + D_s \Delta u_4^I(c). \tag{6.2.29}$$

6.2.1.3 Case I: Results and Discussions

A qualitative study is presented for a PZT-4 ceramic plate. The material constants used for different ceramics are listed in Table 2.1.

The crack length, prescribed mechanical stress and electric displacement are respectively, taken as $10mm$, $10MPa$ and $0.01C/m^2$.

Fig. 6.2 depicts the variation of saturation zone to crack length ratio vis-a-vis electric load ratio D_2^∞/D_s. It is observed that as prescribed electric load is increased a bigger saturation zone develops, as expected. It may be noted that for the same load saturation zone at the inner tip is bigger than that at the outer tip. Also when two cracks are nearer the difference in crack zone length of the saturation zone at interior and exterior tip is remarkable but as the distance between two cracks is increased the variation in size of saturation zone at interior and exterior tips decreases. This is because the effect of one crack on other reduces.

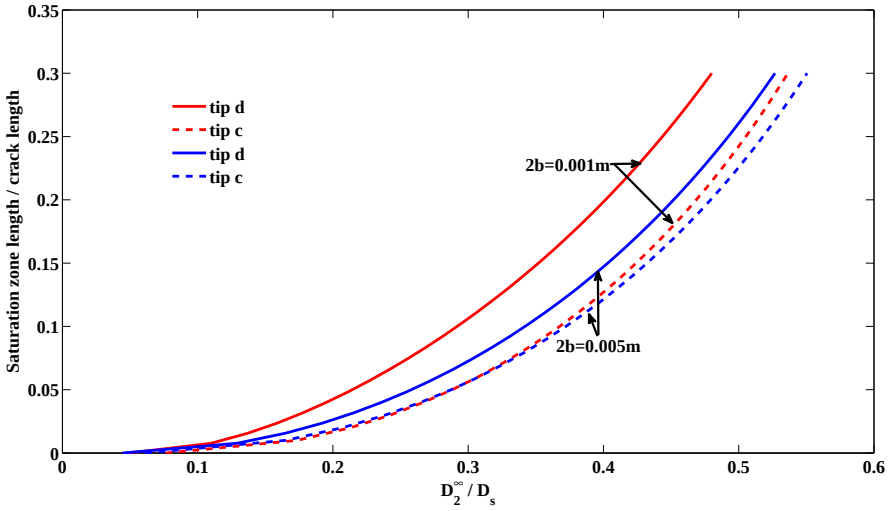

Figure 6.2: Normalized saturation zone length versus D_2^∞/D_s

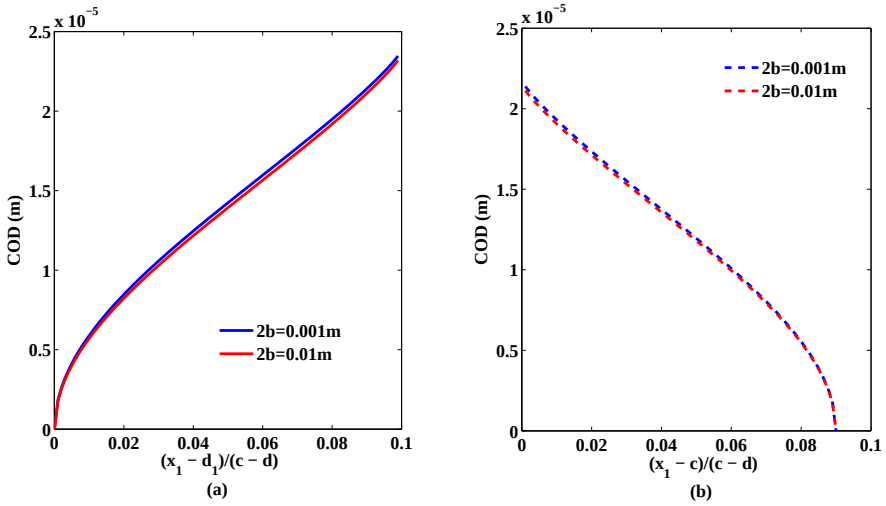

Figure 6.3: COD profile at (a) interior and (b) exterior yield zones

The profile of COD over the yield zone length at interior and exterior tips is plotted in Figs. 6.3(a and b), respectively. The yield zone opens more at the interior tip while less COD is shown at the outer yield zone, as expected.

Variation of COD, Δu_2^I with respect to prescribed electric load at the inner and outer tips $x_1 = d$ and $x_1 = c$ are respectively plotted in Figs. 6.4(a and b). It is noted that COD at each of the tips increases linearly. And it is more at inner tip than that at outer tip. It is also noted that as mechanical loading is increased the cracks open more, as expected.

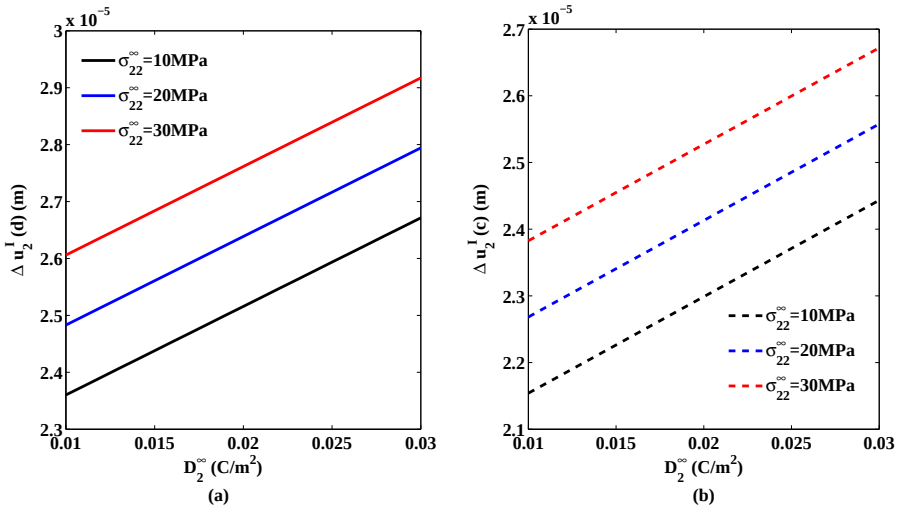

Figure 6.4: COD versus D_2^{∞} for different mechanical loads

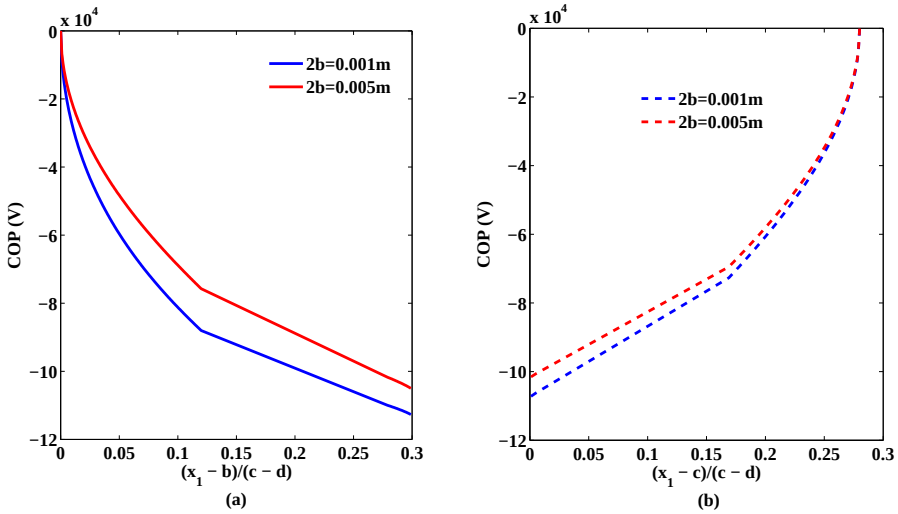

Figure 6.5: COP drop at (a) interior and (b) exterior saturation zones

Variation of COP, Δu_4^I versus normalized inner and outer saturation zones is drawn in Figs. 6.5(a and b), respectively. It is observed that potential drop is more at the inner zone than that at outer zone, as expected. Also as the distance $2b$ is increased than the difference of COP at inner tip is more as compared to that at outer tip.

Figs. 6.6(a and b) show that COP decreases with increase in mechanical loading although COP increases with increase in electric loading. Potential drop is higher at the interior tip, as expected.

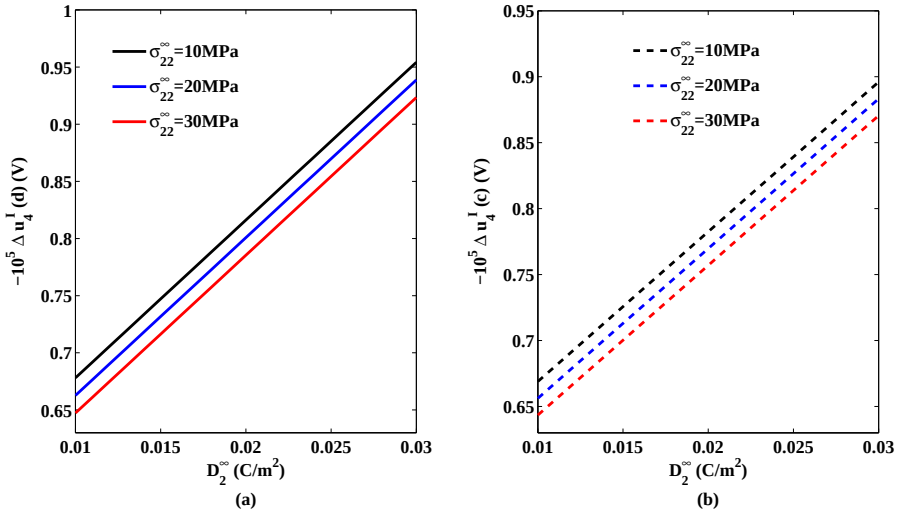

Figure 6.6: COP versus D_2^{∞} for different mechanical loads

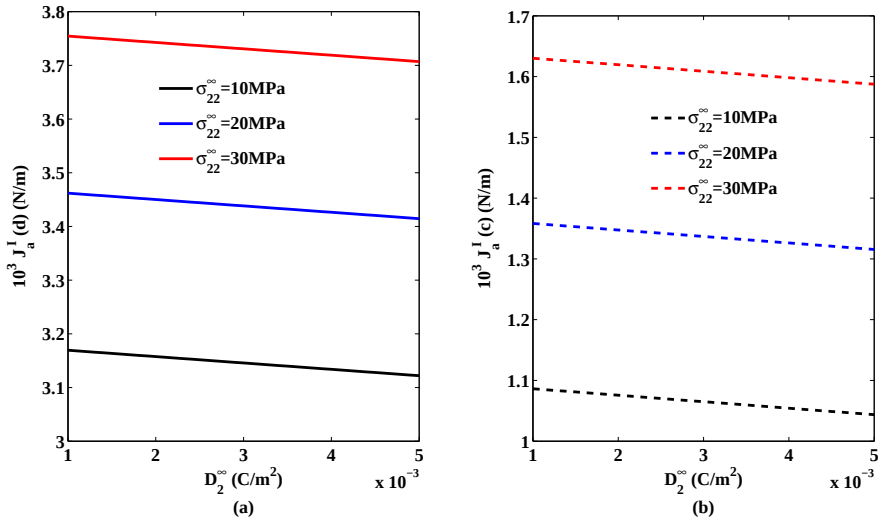

Figure 6.7: ERR versus D_2^{∞} for different mechanical loads

Energy release rate at inner and outer tips versus prescribed electric load for various values of prescribed mechanical load $\sigma_{22}^{\infty} = 10MPa, 20MPa, 30MPa$ are plotted in Figs. 6.7(a and b), respectively. The results show that the energy release rate decreases as the electric load is increased, which assures the crack arrest. It is also observed as the prescribed mechanical load is increased the value of energy release rate increases.

Figs. 6.8(a, b) depict the energy release rate variation vis-a-vis prescribed electric load for PZT-4, PZT-5H, PZT-7A and $BaTiO_3$ ceramics. It is observed that $BaTiO_3$ ceramic has minimum energy release rate and it is maximum for PZT-4 ceramic.

This may help designers to select the appropriate ceramic as desired.

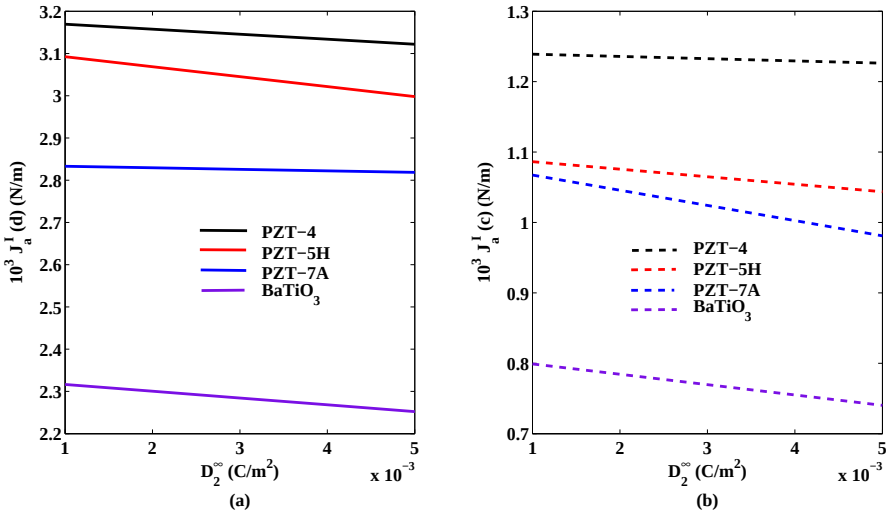

Figure 6.8: ERR versus D_2^{∞} for different piezoceramics

6.2.2 Case II: When saturation zones are smaller than developed yield zones ($|c_1| > |a|$ and $|b| > |d_1|$)

Schematically the configuration of the problem is depicted in Fig. 6.9.

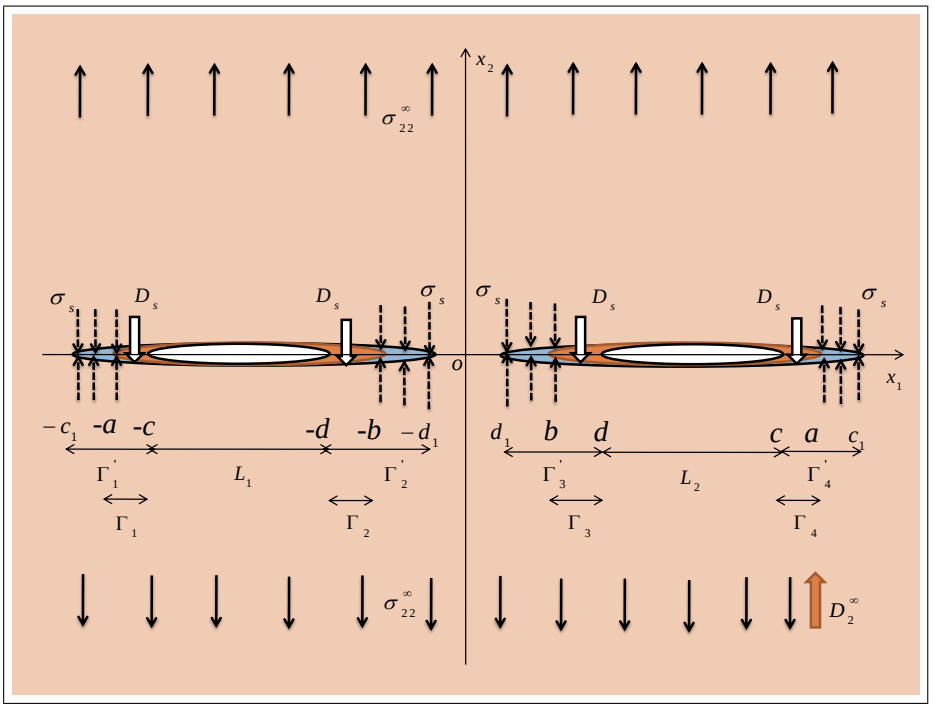

Figure 6.9: Schematic representation of the configuration of problem for Case II, when saturation zones are smaller than developed yield zones

The boundary conditions from (i) to (iv) remain the same as in Case I. And the

boundary condition (v) is replaced by condition (vi) as

(vi) $\mathbf{\Phi}_{,1}^{II+} = \mathbf{\Phi}_{,1}^{II-} = -\mathbf{V}^{II},$ for $d < |x_1| < c$

where, $\mathbf{V}^{II} = [0, \sigma_{22}^{\infty}, 0, D_2^{\infty}]^T$, and superscript II represents that the quantity refers to Case II.

6.2.2.1 Solution of the Problem

Carrying out calculations analogous to Case I with the boundary condition (vi) for this case yield the following two dual Hilbert problems for potentials $\Omega_2^{II}(z)$ and $\Omega_4^{II}(z)$ as

$$\Lambda_{22}[\Omega_2^{II+}(x_1) + \Omega_2^{II-}(x_1)] + \Lambda_{24}[\Omega_4^{II+}(x_1) + \Omega_4^{II-}(x_1)] = -\sigma_{22}^{\infty},\ d < |x_1| < c, \tag{6.2.30}$$

$$\Lambda_{42}[\Omega_2^{II+}(x_1) + \Omega_2^{II-}(x_1)] + \Lambda_{44}[\Omega_4^{II+}(x_1) + \Omega_4^{II-}(x_1)] = -D_2^{\infty},\ d < |x_1| < c. \tag{6.2.31}$$

The solution of which may be written, carrying the similar calculation as in Case I, as

$$\begin{aligned}\Omega_4^{II}(z) =& \frac{\Lambda_{22}D_2^{\infty} - \Lambda_{42}\sigma_{22}^{\infty}}{2\Sigma}\left\{\frac{z^2 - a^2\lambda_2^2}{X_2(z)} - 1\right\} + \frac{\Lambda_{22}D_s - \Lambda_{42}\sigma_s}{\pi\Sigma}\left(\frac{\pi}{2} - \upsilon_d + \upsilon_c\right) \\ &- \frac{\Lambda_{22}D_s - \Lambda_{42}\sigma_s}{\pi\Sigma X_2(z)}\left\{(z^2 - a^2\lambda_2^2)\left(\frac{\pi}{2} - \vartheta_d + \vartheta_c\right) + R_2\right\}, \qquad (6.2.32)\\ \Omega_2^{II}(z) =& -\frac{\Lambda_{42}}{\Lambda_{22}}\Omega_4^{II}(z) + \frac{\sigma_{22}^{\infty}}{2\Lambda_{22}}\left\{\frac{z^2 - c_1^2\lambda_1^2}{X_1(z)} - 1\right\} + \frac{\sigma_s}{\pi\Lambda_{22}}\left(\frac{\pi}{2} - \varphi_d + \varphi_c\right) \\ &- \frac{\sigma_s}{\pi\Lambda_{22}X_1(z)}\left\{(z^2 - c_1^2\lambda_1^2)\left(\frac{\pi}{2} - \psi_d + \psi_c\right) + R_1\right\}. \qquad (6.2.33)\end{aligned}$$

6.2.2.2 Applications

As in Case I here we obtain the expression for calculations of yield zone, saturation zone length, crack opening displacement, crack opening potential drop and energy release rate.

The stress and electric displacement for this case are obtained using

$$\mathbf{\Phi}_{,1}^{II}(x_1) = \mathbf{B}\mathbf{F}^{II+}(x_1) + \mathbf{B}\mathbf{F}^{II-}(x_1) = \mathbf{\Lambda}\mathbf{\Omega}^{II+}(x_1) + \mathbf{\Lambda}\mathbf{\Omega}^{II-}(x_1),\ |x_1| > c_1. \tag{6.2.34}$$

Comparing second and fourth components from above equation, we get

$$\sigma_{22}^{II}(x_1) = \Lambda_{22}[\Omega_2^{II+}(x_1) + \Omega_2^{II-}(x_1)] + \Lambda_{24}[\Omega_4^{II+}(x_1) + \Omega_4^{II-}(x_1)], \tag{6.2.35}$$

$$D_2^{II}(x_1) = \Lambda_{42}[\Omega_2^{II+}(x_1) + \Omega_2^{II-}(x_1)] + \Lambda_{44}[\Omega_4^{II+}(x_1) + \Omega_4^{II-}(x_1)]. \tag{6.2.36}$$

Substituting the values of $\Omega_2^{II}(x_1)$ and $\Omega_4^{II}(x_1)$ from Equations (6.2.32 and 6.2.33) and simplifying one obtains

$$\begin{aligned}\sigma_{22}^{II}(x_1) =& \frac{2\sigma_s}{\pi}\left(\frac{\pi}{2} - \varphi_d + \varphi_c\right) + \sigma_{22}^{\infty}\left\{\frac{x_1^2 - c_1^2\lambda_1^2}{X_1(x_1)} - 1\right\} \\ &- \frac{2\sigma_s}{\pi X_1(x_1)}\left\{(x_1^2 - c_1^2\lambda_1^2)\left(\frac{\pi}{2} - \psi_d + \psi_c\right) + R_1\right\}, \end{aligned} \tag{6.2.37}$$

$$\begin{aligned}D_2^{II}(x_1) =& \frac{2(\Lambda_{22}D_s - \Lambda_{42}\sigma_s)}{\pi\Lambda_{22}}\left(\frac{\pi}{2} - \upsilon_d + \upsilon_c\right) + \frac{(\Lambda_{22}D_2^{\infty} - \Lambda_{42}\sigma_{22}^{\infty})}{\Lambda_{22}}\left\{\frac{x_1^2 - a^2\lambda_2^2}{X_2(x_1)} - 1\right\} \\ &- \frac{2(\Lambda_{22}D_s - \Lambda_{42}\sigma_s)}{\pi\Lambda_{22}X_2(x_1)}\left\{(x_1^2 - a^2\lambda_2^2)\left(\frac{\pi}{2} - \vartheta_d + \vartheta_c\right) + R_2\right\}. \end{aligned} \tag{6.2.38}$$

Yield zone

Using Dugdale's [24] hypothesis that the stress remains finite at every point of the body, consequently at the tips $x_1 = d_1$ and $x_1 = c_1$ of the yield zones, one obtains non-linear equations to determine d_1 and c_1 from

$$\left(\frac{d_1^2}{c_1^2} - \lambda_1^2\right)\left(\frac{\pi\sigma_{22}^{\infty}}{2\sigma_s} - \frac{\pi}{2} + \psi_d - \psi_c\right) - \frac{R_1}{c_1^2} = 0, \tag{6.2.39}$$

$$\left(1 - \lambda_1^2\right)\left(\frac{\pi\sigma_{22}^{\infty}}{2\sigma_s} - \frac{\pi}{2} + \psi_d - \psi_c\right) - \frac{R_1}{c_1^2} = 0. \tag{6.2.40}$$

Saturation zone

Assuming Dugdale's hypothesis to be true for electric displacement as well hence the condition of finiteness of electrical displacements at every point of the plate yields the following two equations

$$\left(\frac{b^2}{a^2} - \lambda_2^2\right)\left(\frac{\pi}{2}\frac{\Lambda_{22}D_2^{\infty} - \Lambda_{42}\sigma_{22}^{\infty}}{\Lambda_{22}D_s - \Lambda_{42}\sigma_s} - \frac{\pi}{2} + \vartheta_d - \vartheta_c\right) - \frac{R_2}{a^2} = 0, \tag{6.2.41}$$

$$\left(1 - \lambda_2^2\right)\left(\frac{\pi}{2}\frac{\Lambda_{22}D_2^{\infty} - \Lambda_{42}\sigma_{22}^{\infty}}{\Lambda_{22}D_s - \Lambda_{42}\sigma_s} - \frac{\pi}{2} + \vartheta_d - \vartheta_c\right) - \frac{R_2}{a^2} = 0. \tag{6.2.42}$$

Crack opening potential drop (COP)

The crack opening potential drop for this case is determined analogous to Equation (6.2.23) as

$$i\Delta\mathbf{u}_{,1}^{II}(x_1) = \mathbf{\Lambda}[\mathbf{\Omega}^{II+}(x_1) - \mathbf{\Omega}^{II-}(x_1)]. \tag{6.2.43}$$

Comparing the fourth component of the above equation and substituting value of $\Omega_4^{II}(x_1)$ from Equation (6.2.32) one obtains potential drop at the crack tips $x_1 = d$ and $x_1 = c$ as

$$\begin{aligned}\Delta u_4^{II}(d) =& -\frac{(\Lambda_{22}D_s - \Lambda_{42}\sigma_s)}{\pi\Sigma}\left\{-d\ln(C) + 2F(\xi_d, k_2)\frac{R_2}{a} + G_1(d,c)\right\} \\ & -\frac{(\Lambda_{22}D_s - \Lambda_{42}\sigma_s)}{\pi\Sigma}\left\{2a\left(\frac{\pi}{2} - \vartheta_d + \vartheta_c\right)R_8 + \frac{2b^2}{a}\sqrt{\frac{a^2-d^2}{d^2-b^2}}R_7\right\} \\ & + \frac{a(\Lambda_{22}D_2^{\infty} - \Lambda_{42}\sigma_{22}^{\infty})}{\Sigma}R_8, \end{aligned} \tag{6.2.44}$$

$$\begin{aligned}\Delta u_4^{II}(c) =& \frac{(\Lambda_{22}D_s - \Lambda_{42}\sigma_s)}{\pi\Sigma}\left\{-c\ln(D) + H_1(c,d) + 2F(\vartheta_c, k_2)\frac{R_2}{a}\right\} \\ & + \frac{(\Lambda_{22}D_s - \Lambda_{42}\sigma_s)}{\pi\Sigma}\left\{2a\left(\frac{\pi}{2} - \vartheta_d + \vartheta_c\right)R_{10} + \frac{2}{a}\sqrt{\frac{c^2-b^2}{a^2-c^2}}R_9\right\} \\ & - \frac{a(\Lambda_{22}D_2^{\infty} - \Lambda_{42}\sigma_{22}^{\infty})}{\Sigma}R_{10}. \end{aligned} \tag{6.2.45}$$

Crack opening displacement (COD)

The COD at the crack tips $x_1 = d$ and $x_1 = c$ are obtained comparing second component of Equation (6.2.43) and substituting value of $\Omega_2^{II}(x_1)$ from Equation (6.2.33) and simplifying, one obtains

$$\begin{aligned}\Delta u_2^{II}(d) =& -\frac{\sigma_s}{\pi\Lambda_{22}}\left\{-d\ln(A) + \frac{2d_1^2}{c_1}\sqrt{\frac{c_1^2-d^2}{d^2-d_1^2}}R_3 + 2F(\tau_d, k_1)\frac{R_1}{c_1} + G(d,c)\right\} \\ & -\frac{2c_1\sigma_s}{\pi\Lambda_{22}}\left(\frac{\pi}{2} - \psi_d + \psi_c\right)R_4 + \frac{c_1\sigma_{22}^{\infty}}{\Lambda_{22}}R_4 - \frac{\Lambda_{24}}{\Lambda_{22}}\Delta u_4^{II}(d), \end{aligned} \tag{6.2.46}$$

$$\begin{aligned}\Delta u_2^{II}(c) =& \frac{\sigma_s}{\pi\Lambda_{22}}\left\{-c\ln(B) + H(c,d) + 2F(\psi_c, k_1)\frac{R_1}{c_1} + \frac{2}{c_1}\sqrt{\frac{c^2-d_1^2}{c_1^2-c^2}}R_6\right\} \\ & + \frac{2c_1\sigma_s}{\pi\Lambda_{22}}\left(\frac{\pi}{2} - \psi_d + \psi_c\right)R_5 - \frac{c_1\sigma_{22}^{\infty}}{\Lambda_{22}}R_5 - \frac{\Lambda_{24}}{\Lambda_{22}}\Delta u_4^{II}(c). \end{aligned} \tag{6.2.47}$$

Energy release rate (ERR)

Energy release rate at the interior and exterior tips of the crack is calculated using formulae

$$J_a^{II}(d) = \sigma_s\Delta u_2^{II}(d) + D_s\Delta u_4^{II}(d), \tag{6.2.48}$$

$$J_a^{II}(c) = \sigma_s\Delta u_2^{II}(c) + D_s\Delta u_4^{II}(c). \tag{6.2.49}$$

6.2.2.3 Case II: Results and Discussions

A similar study as in Case I is carried for Case II as well.

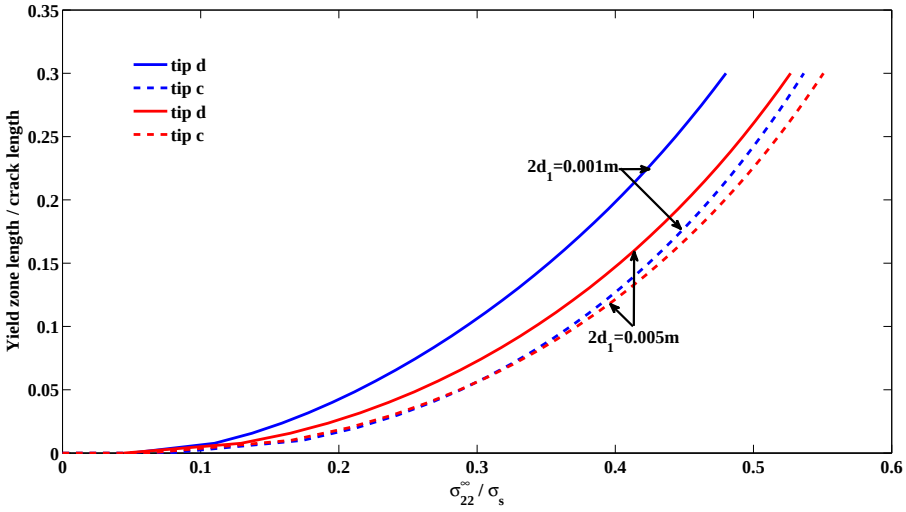

Figure 6.10: Normalized mechanical zone length versus load ratio $\sigma_{22}^{\infty}/\sigma_s$

Fig. 6.10 shows the variation of developed yield zone versus the applied load ratio $\sigma_{22}^{\infty}/\sigma_s$. As expected, as the prescribed load is increased the yield zone increases in size. It may be noted that for the same load, a bigger yield zone develops at the inner tip than that at the outer tip. Also when two cracks are nearer the difference of the yield zone at interior and exterior tip is remarkable but as the distance between two cracks is increased the variation in size of yield zones at interior and exterior tips decreases. This is because the effect of one crack on other reduces.

Variation of COP at the interior and exterior saturation zones is plotted in Figs. 6.11(a and b). Comparing the Figs. 6.5 and 6.11 the difference between two cases may easily be noted. Also it is to be pointed out that COP is much smaller in this Case as compared to the Case I.

Figs. 6.12(a and b) show that COP decreases with increase in mechanical loading although COP increases with increase in electric loading. Potential drop is higher at the interior tips, as expected.

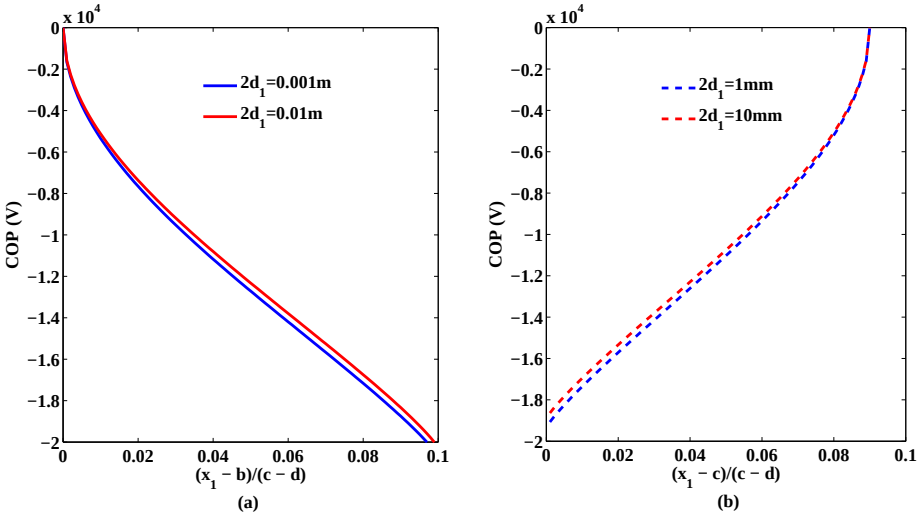

Figure 6.11: COP drop over the saturation zones

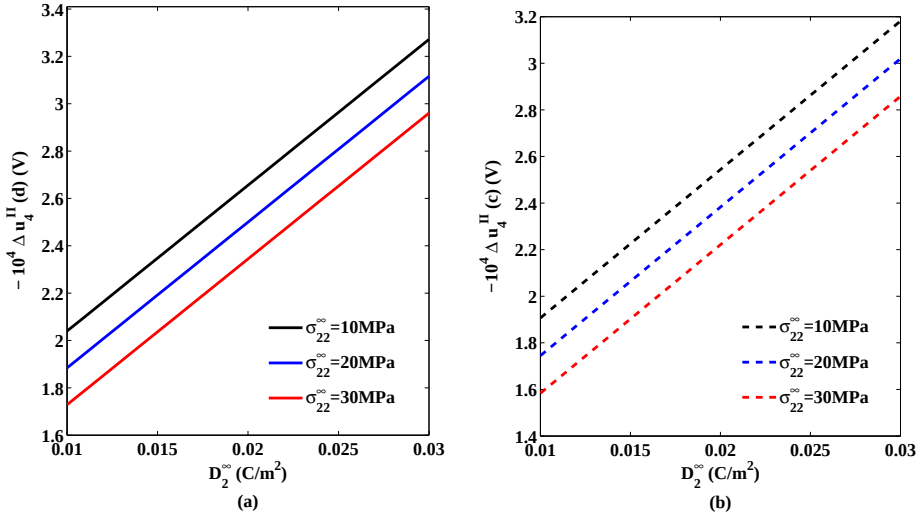

Figure 6.12: COP versus D_2^{∞} for different σ_{22}^{∞}

Figs. 6.13(a and b) depict the opening of interior and exterior yield zones. It may be observed from Fig. 6.13(a) that the inner yield zone opens more and as the distance $2d_1$, between two interior yield zone is increased the crack opening reduces. Also when the variation is compared with that in Fig. 6.3(a) one can note that the inner distance $2d_1$, has more effect in Case II.

Figs. 6.14(a, b) depict the variation of COD at the inner and outer crack tips for different prescribed mechanical loads. It is noted that COD at each of the tips increases linearly. It is more at inner tip than that at outer tip.

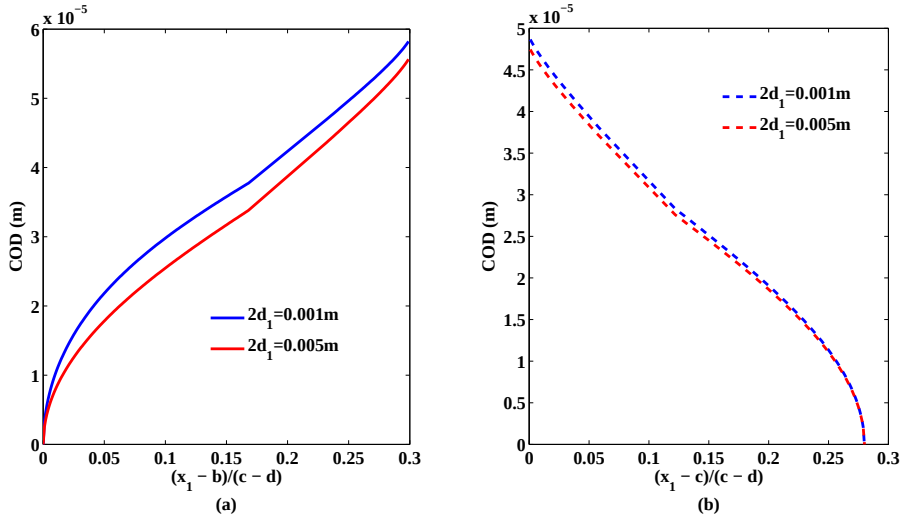

Figure 6.13: Behavior of COD over yield zones

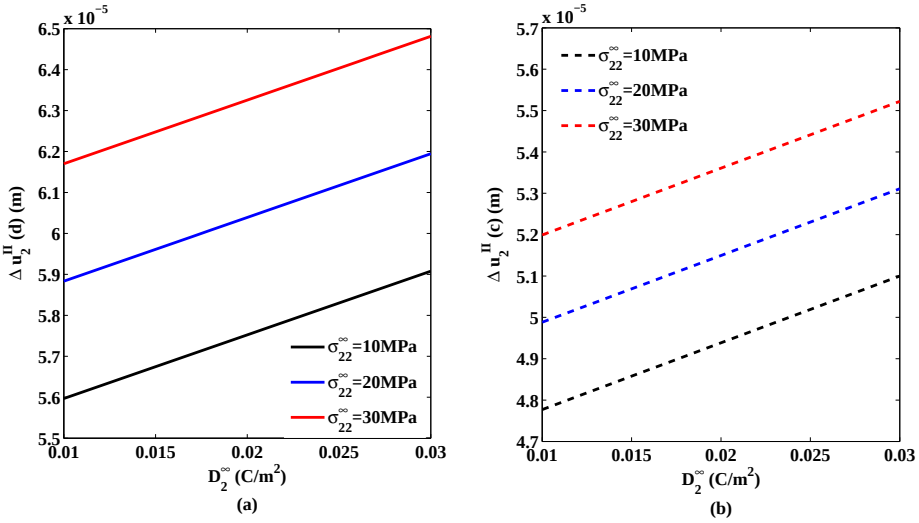

Figure 6.14: COD versus D_2^∞ for different σ_{22}^∞

Variation of ERR at the inner and outer crack tips versus D_2^∞ for different values of prescribed mechanical stress σ_{22}^∞ is shown in Figs. 6.15(a, b). The results show that the energy release rate decreases as the electric load is increased, which assures the crack arrest. It is also observed that as the prescribed mechanical load is increased the value of energy release rate increases.

Figs. 6.16(a, b) depict the ERR for various ceramics as the prescribed electric load D_2^∞ is increased. It is observed that $BaTiO_3$ ceramic has minimum energy release rate and it is maximum for PZT-4 ceramic.

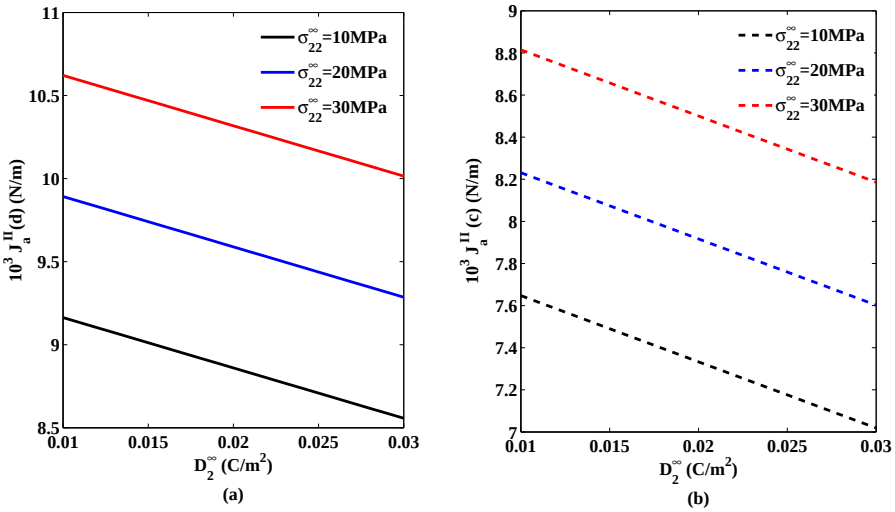

Figure 6.15: ERR versus D_2^∞ for different σ_{22}^∞

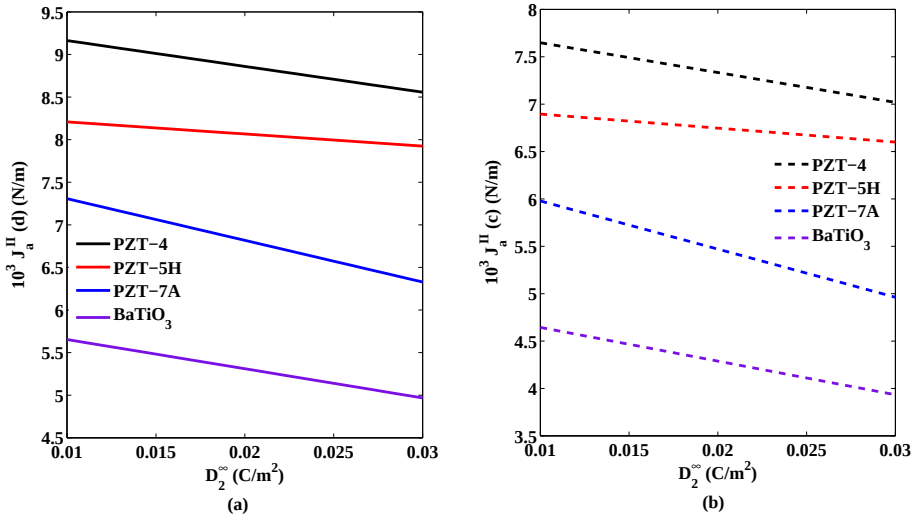

Figure 6.16: ERR versus D_2^∞ for different piezoceramics

6.2.3 Case III: When saturation and yield zones are equal ($|c_1| = |a|$ and $|b| = |d_1|$)

Schematically the configuration of the problem is depicted in Fig. 6.17.

The boundary conditions form (i) to (iv) remain the same as in Case I. And the boundary condition (v) is replaced by condition (vii) as

(vii) $\mathbf{\Phi}_{,1}^{III+} = \mathbf{\Phi}_{,1}^{III-} = -\mathbf{V}^{III}, \quad \text{for } d < |x_1| < c$

where, $\mathbf{V}^{III} = [0, \sigma_{22}^\infty, 0, D_2^\infty]^T$ and superscript III represents that the quantity refers to Case III.

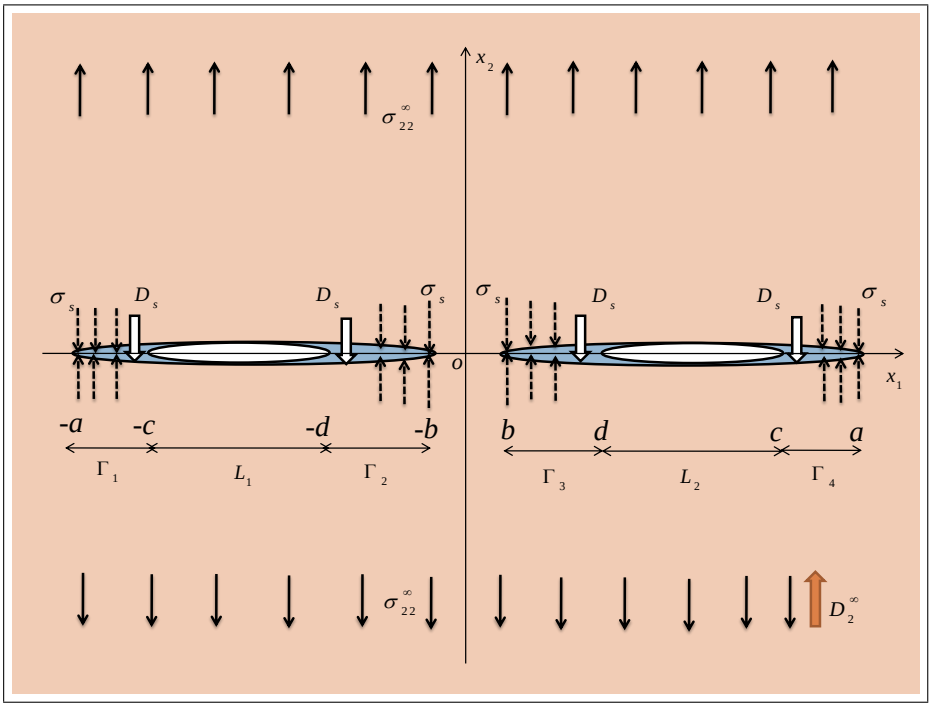

Figure 6.17: Schematic representation of the configuration of problem for Case III, when saturation and yield zones are equal

6.2.3.1 Solution of the Problem

Carrying out calculations analogous to Case I with the boundary condition (vii) for this case yield the following two dual Hilbert problems for potentials $\Omega_2^{III}(z)$ and $\Omega_4^{III}(z)$ as

$$\Lambda_{22}[\Omega_2^{III+}(x_1) + \Omega_2^{III-}(x_1)] + \Lambda_{24}[\Omega_4^{III+}(x_1) + \Omega_4^{III-}(x_1)] = -\sigma_{22}^{\infty},\ d < |x_1| < c, \tag{6.2.50}$$

$$\Lambda_{42}[\Omega_2^{III+}(x_1) + \Omega_2^{III-}(x_1)] + \Lambda_{44}[\Omega_4^{III+}(x_1) + \Omega_4^{III-}(x_1)] = -D_2^{\infty},\ d < |x_1| < c. \tag{6.2.51}$$

The solution of which, carrying the similar calculation as in Case I, may be written as

$$\begin{aligned}\Omega_2^{III}(z) = &-\frac{\Lambda_{44}\sigma_s - \Lambda_{24}D_s}{\pi\Sigma X_2(z)}\left\{(z^2 - a^2\lambda_2^2)\left(\frac{\pi}{2} - \vartheta_d + \vartheta_c\right) + R_2\right\} \\ &+ \frac{\Lambda_{44}\sigma_{22}^{\infty} - \Lambda_{24}D_2^{\infty}}{2\Sigma}\left\{\frac{z^2 - a^2\lambda_2^2}{X_2(z)} - 1\right\} \\ &+ \frac{\Lambda_{44}\sigma_s - \Lambda_{24}D_s}{\pi\Sigma}\left(\frac{\pi}{2} - \upsilon_d + \upsilon_c\right),\end{aligned} \tag{6.2.52}$$

$$\Omega_4^{III}(z) = \frac{\Lambda_{42}\sigma_s - \Lambda_{22}D_s}{\pi\Sigma X_2(z)}\left\{(z^2 - a^2\lambda_2^2)\left(\frac{\pi}{2} - \vartheta_d + \vartheta_c\right) + R_2\right\} - \frac{\Lambda_{42}\sigma_{22}^{\infty} - \Lambda_{22}D_2^{\infty}}{2\Sigma}\left\{\frac{z^2 - a^2\lambda_2^2}{X_2(z)} - 1\right\} - \frac{\Lambda_{42}\sigma_s - \Lambda_{22}D_s}{\pi\Sigma}\left(\frac{\pi}{2} - \upsilon_d + \upsilon_c\right), \tag{6.2.53}$$

6.2.3.2 Applications

Expressions for crack opening displacement, crack opening potential drop, energy release rate and developed zones are derived in this section.

Zone size

As in Case II, the stress and electric displacement for this case are obtained using

$$\mathbf{\Phi}_{,1}^{III}(x_1) = \mathbf{B}\mathbf{F}^{III+}(x_1) + \mathbf{B}\mathbf{F}^{III-}(x_1) = \mathbf{\Lambda}[\mathbf{\Omega}^{III+}(x_1) + \mathbf{\Omega}^{III-}(x_1)],\ |x_1| > a. \tag{6.2.54}$$

Comparing second and fourth components and substituting $\Omega_2^{III}(z)$ and $\Omega_4^{III}(z)$ from Equations (6.2.52 and 6.2.53) and simplifying one obtains

$$\sigma_{22}^{III}(x_1) = \frac{2\sigma_s}{\pi}\left(\frac{\pi}{2} - \upsilon_d + \upsilon_c\right) + \sigma_{22}^{\infty}\left\{\frac{x_1^2 - a^2\lambda_2^2}{X_2(x_1)} - 1\right\} - \frac{2\sigma_s}{\pi X_2(x_1)}\left\{(x_1^2 - a^2\lambda_2^2)\left(\frac{\pi}{2} - \vartheta_d + \vartheta_c\right) + R_2\right\}, \tag{6.2.55}$$

$$D_2^{III}(x_1) = \frac{2D_s}{\pi}\left(\frac{\pi}{2} - \upsilon_d + \upsilon_c\right) + D_2^{\infty}\left\{\frac{x_1^2 - a^2\lambda_2^2}{X_2(x_1)} - 1\right\} - \frac{2D_s}{\pi X_2(x_1)}\left\{(x_1^2 - a^2\lambda_2^2)\left(\frac{\pi}{2} - \vartheta_d + \vartheta_c\right) + R_2\right\}. \tag{6.2.56}$$

Applying Dugdale's hypothesis of stresses and electric displacement remain finite at the tips $x_1 = b$ and $x_1 = a$ of the zones, one obtains non-linear equations to determine b and a from

$$\left(\frac{b^2}{a^2} - \lambda_2^2\right)\left(\frac{\pi}{2}R - \frac{\pi}{2} + \vartheta_d - \vartheta_c\right) - \frac{R_2}{a^2} = 0, \tag{6.2.57}$$

$$\left(1 - \lambda_2^2\right)\left(\frac{\pi}{2}R - \frac{\pi}{2} + \vartheta_d - \vartheta_c\right) - \frac{R_2}{a^2} = 0. \tag{6.2.58}$$

where, $R = \sigma_{22}^{\infty}/\sigma_s$ or D_2^{∞}/D_s.

Crack opening displacement (COD)

The crack opening displacement for this case is determined using

$$i\Delta\mathbf{u}_{,1}^{III}(x_1) = \mathbf{\Lambda}[\mathbf{\Omega}^{III+}(x_1) - \mathbf{\Omega}^{III-}(x_1)]. \tag{6.2.59}$$

Comparing the second component of the above equation and substituting value of $\Omega_2^{III}(z)$ from Equation (6.2.52) one obtains COD at tips $x_1 = d$ and $x_1 = c$, as

$$\begin{aligned}\Delta u_2^{III}(d) =& -\frac{(\Lambda_{44}\sigma_s - \Lambda_{24}D_s)}{\pi\Sigma}\left\{-d\ln(C) + 2F(\xi_d, k_2)\frac{R_2}{a} + G_1(d,c)\right\}\\ &-\frac{(\Lambda_{44}\sigma_s - \Lambda_{24}D_s)}{\pi\Sigma}\left\{2a\left(\frac{\pi}{2} - \vartheta_d + \vartheta_c\right)R_8 + \frac{2b^2}{a}\sqrt{\frac{a^2-d^2}{d^2-b^2}}R_7\right\}\\ &+\frac{a(\Lambda_{44}\sigma_{22}^{\infty} - \Lambda_{24}D_2^{\infty})}{\Sigma}R_8,\end{aligned} \tag{6.2.60}$$

$$\begin{aligned}\Delta u_2^{III}(c) =& \frac{(\Lambda_{44}\sigma_s - \Lambda_{24}D_s)}{\pi\Sigma}\left\{-c\ln(D) + H_1(c,d) + 2F(\vartheta_c, k_2)\frac{R_2}{a}\right\}\\ &+\frac{(\Lambda_{44}\sigma_s - \Lambda_{24}D_s)}{\pi\Sigma}\left\{2a\left(\frac{\pi}{2} - \vartheta_d + \vartheta_c\right)R_{10} + \frac{2}{a}\sqrt{\frac{c^2-b^2}{a^2-c^2}}R_9\right\}\\ &-\frac{a(\Lambda_{44}\sigma_{22}^{\infty} - \Lambda_{24}D_2^{\infty})}{\Sigma}R_{10}.\end{aligned} \tag{6.2.61}$$

Crack opening potential drop (COP)

COP at the tips $x_1 = d$ and $x_1 = c$ are obtained, comparing fourth component of Equation (6.2.59) and substituting value of $\Omega_4^{III}(x_1)$ from Equation (6.2.53) and simplifying, as

$$\begin{aligned}\Delta u_4^{III}(d) =& \frac{(\Lambda_{42}\sigma_s - \Lambda_{22}D_s)}{\pi\Sigma}\left\{-d\ln(C) + 2F(\xi_d, k_2)\frac{R_2}{a} + G_1(d,c)\right\}\\ &+\frac{(\Lambda_{42}\sigma_s - \Lambda_{22}D_s)}{\pi\Sigma}\left\{2a\left(\frac{\pi}{2} - \vartheta_d + \vartheta_c\right)R_8 + \frac{2b^2}{a}\sqrt{\frac{a^2-d^2}{d^2-b^2}}R_7\right\}\\ &-\frac{a(\Lambda_{42}\sigma_{22}^{\infty} - \Lambda_{22}D_2^{\infty})}{\Sigma}R_8,\end{aligned} \tag{6.2.62}$$

$$\begin{aligned}\Delta u_4^{III}(c) =& -\frac{(\Lambda_{42}\sigma_s - \Lambda_{22}D_s)}{\pi\Sigma}\left\{-c\ln(D) + H_1(c,d) + 2F(\vartheta_c, k_2)\frac{R_2}{a}\right\}\\ &-\frac{(\Lambda_{42}\sigma_s - \Lambda_{22}D_s)}{\pi\Sigma}\left\{2a\left(\frac{\pi}{2} - \vartheta_d + \vartheta_c\right)R_{10} + \frac{2}{a}\sqrt{\frac{c^2-b^2}{a^2-c^2}}R_9\right\}\\ &+\frac{a(\Lambda_{42}\sigma_{22}^{\infty} - \Lambda_{22}D_2^{\infty})}{\Sigma}R_{10}.\end{aligned} \tag{6.2.63}$$

Energy release rate (ERR)

Energy release rate at the interior and exterior tips of the crack is calculated using

$$J_a^{III}(d) = \sigma_s \Delta u_2^{III}(d) + D_s \Delta u_4^{III}(d), \tag{6.2.64}$$

$$J_a^{III}(c) = \sigma_s \Delta u_2^{III}(c) + D_s \Delta u_4^{III}(c). \tag{6.2.65}$$

6.2.3.3 Case III: Results and Discussion

A study similar to that in the Case I and Case II is carried for this case too.

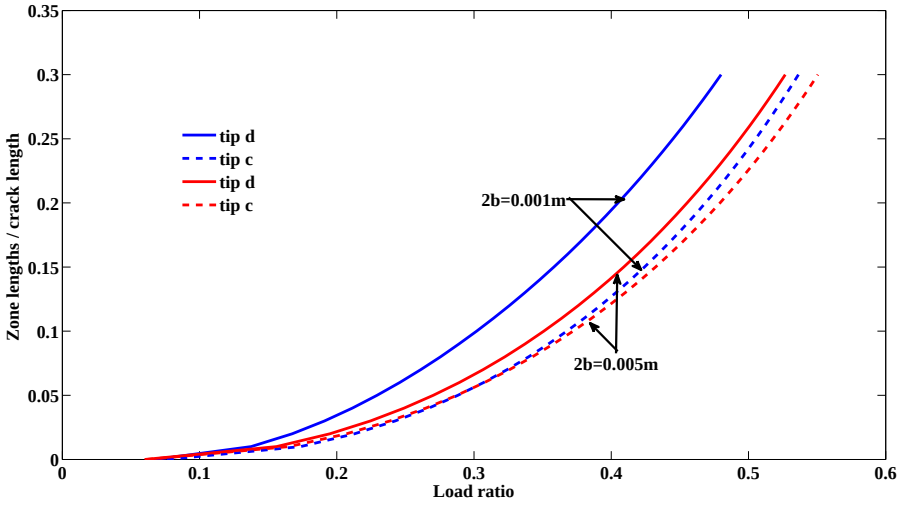

Figure 6.18: Yield-saturation zone length versus load ratio

Fig. 6.18 depicts the variation of yield-saturation zone length versus electric/mechanical load ratio for a fixed crack length. It is observed from the Fig. 6.18 that as the load ratio is increased the size of the yield-saturation zone also increases. A bigger zone develops at the interior tips of the two cracks as compared to that at exterior tips. It is due to the fact that when two cracks are close to each other their presence affects the stress concentration. It is to be further noted that if the interior distance between the two cracks is increased the developed zone size decreases at the interior and exterior tips, as expected.

Crack opening displacement profile at the interior and exterior yield-saturation zones is depicted in Figs. 6.19(a, b). It may be noticed from Fig. 6.19(a) that COD has maximum value at the interior crack tip and becomes zero at the tip of yield-saturation zone. When the two cracks are close to each other the crack opens more and as the distance between the cracks is increased, COD is less at developed

interior zone, as expected. Fig. 6.19(b) depicts variation of COD profile at the exterior yield-saturation zone. Here too it is observed that COD is more when two cracks are close but in this case when distance between the cracks is increased COD reduces but this reduction is smaller as compared to that at the interior zone.

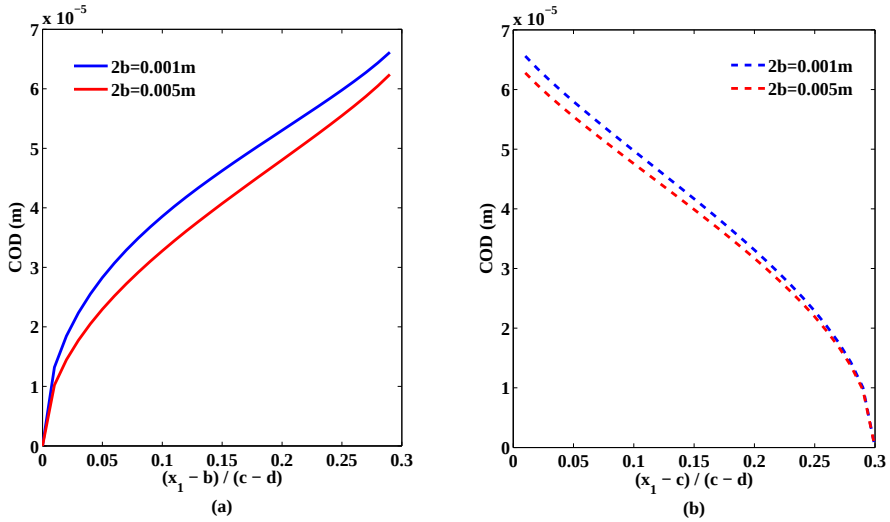

Figure 6.19: Variation of COD over the inner and outer yield-saturation zone

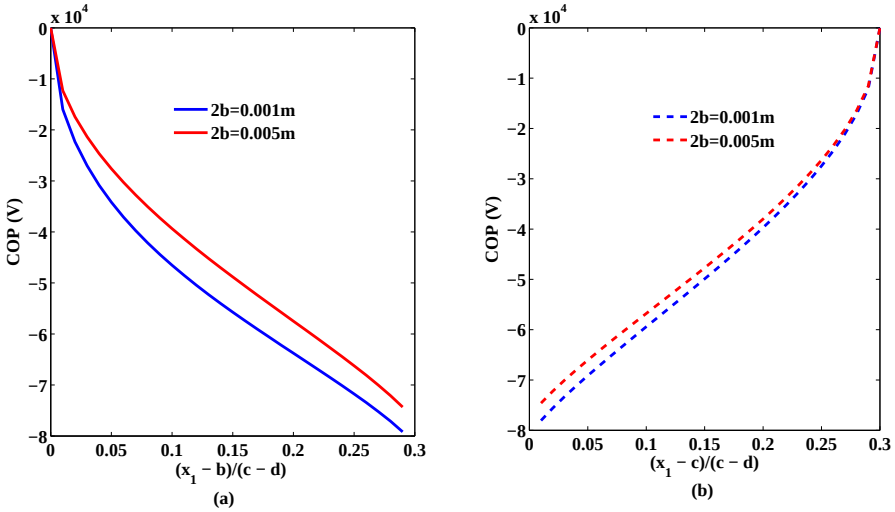

Figure 6.20: Variation of COP drop over the inner and outer yield-saturation zone

Electric potential drop at the interior and exterior yield-saturation zone is plotted in Figs. 6.20(a, b). It is observed that COP is more when distance between the two cracks is decreased at both interior and exterior yield-saturation zone. This effect is more at interior zone as compared to that at exterior zone.

Figs. 6.21(a, b) depict energy release rate at the interior and exterior crack tips. Graphs are drawn between the prescribed electric displacement variations for different values of prescribed stress. It may be noted that energy release rate is slightly lower at exterior tip than that at interior tips.

Figs. 6.22(a, b) depict the energy release rate variation vis-a-vis prescribed electric load for PZT-4, PZT-5H, PZT-7A and $BaTiO_3$ ceramics. It is observed that $BaTiO_3$ ceramic has minimum energy release rate and it is maximum for PZT-4 ceramic.

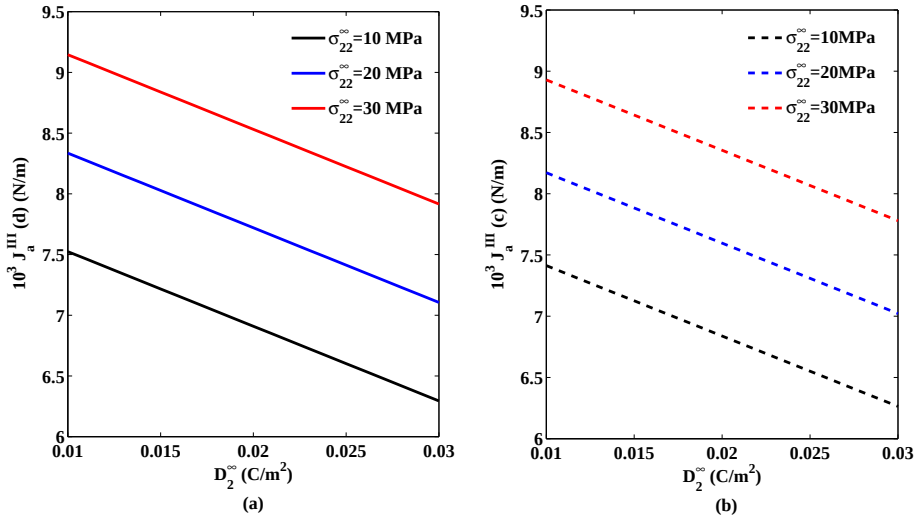

Figure 6.21: ERR versus D_2^∞ for different σ_{22}^∞

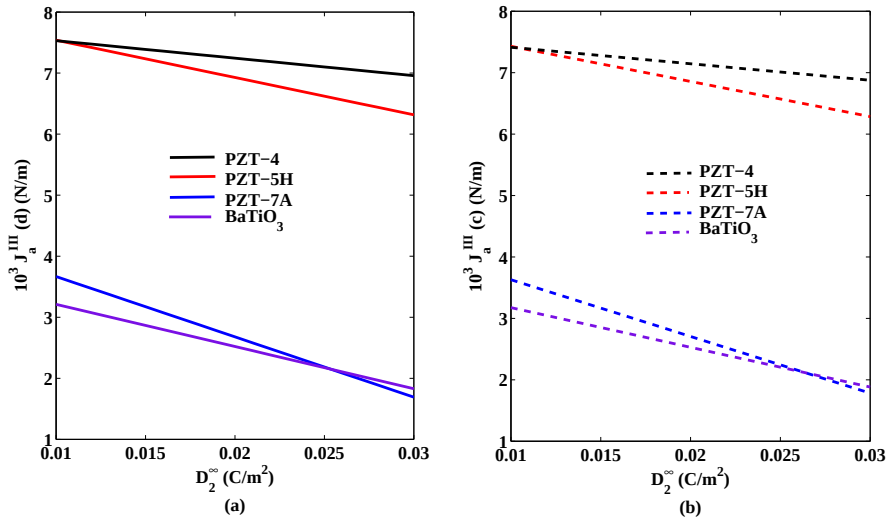

Figure 6.22: ERR versus D_2^∞ for different piezoceramics

6.3 Conclusions

- Strip-electro-mechanical yield model is proposed and solved analytically using Stroh formalism and complex variable technique. Three cases are considered when saturation zones are bigger/smaller or equal to the developed yield zones.
- Analytical expressions are obtained for saturation and yield zones, crack opening displacement, crack opening potential drop and energy release rate.
- It has been found that for all the three cases the energy release rate is higher at the inner tip as compared to that at outer tip. This is because the mutual influences of two cracks when they are closely located.
- The reduction of energy release rate for increased prescribed load ensures the arrest of crack opening.

Chapter 7

Strip-electro-mechanical Yielding Model for Semi-permeable Cracks

Crack arrest problems in piezoelectric media have attracted a lot of attention and have been investigated by many researchers. A lot of crack arrest problems [32, 43, 45, 46, 51, 61, 79, 89, 90] have been investigated for single crack in piezoelectric media. But there is no study available for crack arrest problems in piezoelectric media weakened by two or more cracks. Therefore to address this paucity a strip-electro-elastic model is proposed for piezoelectric media weakened by two collinear impermeable cracks in Chapters 4, 5 and 6 under different conditions. Also as we have studied the effect of different crack face electric boundary conditions on various fracture parameters in Chapter 3. It is found that the dielectric permittivity of the crack gap media could not be ignored.

In this chapter, a strip-electric-saturation and mechanical yielding model solution is proposed for a piezoelectric plate cut along two equal collinear semi-permeable mode-I cracks with electrical polarization reaching a saturation-limit electric, displacement and normal stress reaching a yield stress along a line segment in front of the cracks. Three different situations are investigated when developed electrical saturation zones are bigger/smaller or equal to the developed mechanical yield zones.

Numerical results show that the effect of different electric boundary conditions on the crack opening displacement and crack opening potential drop is significant. The influence of electric displacement load on the energy release rate is also investigated

This chapter is published in Archive of Applied Mechanics (Springer publication) Vol. 83 (2013), pp. 1469-1491.

for PZT-4, PZT-5H and $BaTiO_3$ ceramics, it may assist for the correct choosing of ceramic for specific job.

7.1 Statement of the Problem

A transversely isotropic piezoelectric plate occupies entire x_1ox_2 plane. The plate is poled along ox_2-direction. The plate is cut along two horizontal collinear semi-permeable cracks L_1 and L_2, these occupy the respective, intervals $[-c,-d]$ and $[d,c]$ on x_1-axis. The crack rims are free of any mechanical load and electrically semi-permeable. The in-plane unidirectional, normal, uniform constant tension $\sigma_{22}=\sigma_{22}^{\infty}$ and electric displacement $D_2=D_2^{\infty}$ are prescribed at remote boundary of the plate. Consequently the cracks open in self-similar fashion forming an electric saturation and a mechanical yield zone ahead of each tip of the cracks. The developed strip saturation $\Gamma_i(i=1,2,3,4)$ and mechanical yield zones $\Gamma_i'(i=1,2,3,4)$ occupy respective, intervals $[-a,-c]$, $[-d,-b]$, $[b,d]$, $[c,a]$, and $[-c_1,-c]$, $[-d,-d_1]$, $[d_1,d]$ and $[c,c_1]$ on x_1-axis. The crack opening is arrested by distributing on the saturation zone rims a saturation-limit electric displacement $D_2=D_s$ and a yield point stress $\sigma_{22}=\sigma_s$, on the developed yield zone rims, respectively. Following three cases are considered

Case I: when saturation zones are bigger than developed yield zones,

Case II: when saturation zones are smaller than developed yield zones,

Case III: when saturation and yield zones are equal.

7.2 Mathematical Model and Solution of the Problem

7.2.1 Case I: When saturation zones are bigger than developed yield zones ($|b|<|d_1|$ and $|a|>|c_1|$)

Schematically the configuration of the problem is depicted in Fig. 7.1.

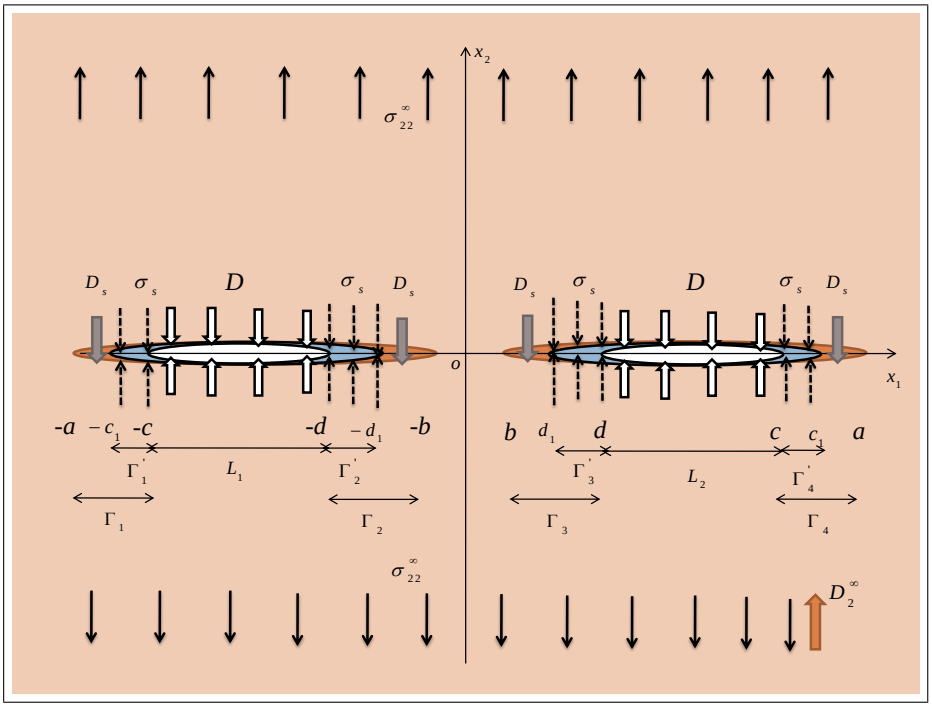

Figure 7.1: Schematic representation of the configuration of problem for Case I, when saturation zones are bigger than developed yield zones

Mathematically the boundary conditions of the problem may be written as

(i) $\sigma_{22}^{+} = \sigma_{22}^{-} = 0, \quad D_2 = D,$ on $L = \bigcup_{i=1}^{2} L_i,$

(ii) $\sigma_{22} = \sigma_{22}^{\infty}, \quad D_2 = D_2^{\infty},$ for $|x_2| \to \infty,$

(iii) $\sigma_{22}^{+} = \sigma_{22}^{-} = \sigma_s - \sigma_{22}^{\infty},$ for $\Gamma' = \bigcup_{i=1}^{4} \Gamma_i',$

(iv) $D_2^{+} = D_2^{-} = D_s - D_2^{\infty},$ for $\Gamma = \bigcup_{i=1}^{4} \Gamma_i,$

(v) $\mathbf{\Phi}_{,1}^{I+} = \mathbf{\Phi}_{,1}^{I-} = -\mathbf{V}^{I},$ for $d < |x_1| < c,$

where, D is the electric flux through the crack regions $(-c, -d)$ and (d, c) determined from the Equation (2.5.3) and $\mathbf{V}^{I} = [0, \sigma_{22}^{\infty}, 0, D_2^{\infty}]^{T}$, where superscript I denotes that quantity refers to the Case I.

A mathematical model is obtained with the help of above mentioned boundary conditions as follows:

The continuity of $\mathbf{\Phi}_{,1}$ (defined by Equation (2.7.7)) on x_1-axis yields

$$[\mathbf{BF}^{I}(x_1) - \overline{\mathbf{BF}^{I}}(x_1)]^{+} - [\mathbf{BF}^{I}(x_1) - \overline{\mathbf{BF}^{I}}(x_1)]^{-} = 0. \tag{7.2.1}$$

The solution of which may directly be written using Equation (2.7.31) as

$$\mathbf{BF}^I(z) = \overline{\mathbf{B}}\overline{\mathbf{F}^I}(z) = \mathbf{h}^I(z) \qquad \text{(say)} \tag{7.2.2}$$

Using principal of superposition, boundary conditions (i) and (v) together with Equations (7.2.2 and 2.7.7) leads to following vector Hilbert problem

$$\mathbf{h}^{I+}(x_1) + \mathbf{h}^{I-}(x_1) = \mathbf{V}^0 - \mathbf{V}^I,\ \mathbf{V}^0 = [0,0,0,D]^T,\ d < |x_1| < c. \tag{7.2.3}$$

Introducing a complex function vector $\mathbf{\Omega}^I(z) = [\Omega_1^I(z), \Omega_2^I(z), \Omega_3^I(z), \Omega_4^I(z)]^T$ as

$$\mathbf{\Omega}^I(z) = \mathbf{H}^R\mathbf{BF}^I(z), \tag{7.2.4}$$

and using Equation (7.2.2) gives the relation

$$\mathbf{h}^I(z) = \mathbf{\Lambda\Omega}^I(z), \tag{7.2.5}$$

where $\mathbf{\Lambda} = [\mathbf{H}^R]^{-1},\ \mathbf{H}^R = 2Re\mathbf{Y},\ \mathbf{Y} = i\mathbf{AB}^{-1}$.
Consequently Equation's (7.2.3) may be written in component form for $\Omega_2^I(z)$ and $\Omega_4^I(z)$, yield following scalar Hilbert problem

$$\Lambda_{22}[\Omega_2^{I+}(x_1) + \Omega_2^{I-}(x_1)] + \Lambda_{24}[\Omega_4^{I+}(x_1) + \Omega_4^{I-}(x_1)] = -\sigma_{22}^{\infty},\ d < |x_1| < c, \tag{7.2.6}$$

$$\Lambda_{42}[\Omega_2^{I+}(x_1) + \Omega_2^{I-}(x_1)] + \Lambda_{44}[\Omega_4^{I+}(x_1) + \Omega_4^{I-}(x_1)] = D - D_2^{\infty},\ d < |x_1| < c. \tag{7.2.7}$$

7.2.1.1 Solution of the Problem

Eliminating $\Omega_4^{I+}(x_1) + \Omega_4^{I-}(x_1)$ from Equations (7.2.6 and 7.2.7) and solving with the help of Equation (2.7.30) together with boundary condition (iii) one obtains

$$\Omega_2^I(z) = \frac{\Lambda_{44}\sigma_s + (D - D_s)\Lambda_{24}}{2\pi i X_1(z)\Sigma}\int_{\Gamma'}\frac{X_1(t)}{t-z}dt + \frac{P_1(z)}{2X_1(z)} - \frac{1}{2}\frac{\Lambda_{44}\sigma_{22}^{\infty} + (D - D_2^{\infty})\Lambda_{24}}{\Lambda_{22}\Lambda_{44} - \Lambda_{24}\Lambda_{42}}, \tag{7.2.8}$$

where

$$P_1(z) = C_0z^2 + C_1z + C_2,\ X_1(z) = \sqrt{(z^2 - d_1^2)(z^2 - c_1^2)} \text{ and } \Sigma = \Lambda_{22}\Lambda_{44} - \Lambda_{24}\Lambda_{42}.$$

Constant

$$C_0 = \frac{\Lambda_{44}\sigma_{22}^{\infty} + (D - D_2^{\infty})\Lambda_{24}}{\Lambda_{22}\Lambda_{44} - \Lambda_{24}\Lambda_{42}}$$

is determined using condition $\lim_{z\to\infty}\Omega_2^I(z)=0$. Also C_1 and C_2 are determined from the condition of single-valuedness of displacement around cracks i.e.,

$$\int_{C_i'}[\Omega_2^{I+}(x_1)-\Omega_2^{I-}(x_1)]dx_1=0,\ i=1,2,\ C_1'=[-c_1,-d_1],\ C_2'=[d_1,c_1]. \quad (7.2.9)$$

Finally, evaluating the integral in Equation (7.2.8) and substituting the values of constants C_0, C_1 and C_2, the required potential $\Omega_2^I(z)$, may be written as

$$\begin{aligned}\Omega_2^I(z)=&-\frac{\Lambda_{44}\sigma_s+\Lambda_{24}(D-D_s)}{\pi\Sigma X_1(z)}\left\{(z^2-c_1^2\lambda_1^2)\left(\frac{\pi}{2}-\psi_d+\psi_c\right)+R_1\right\}\\&+\frac{1}{2}\frac{\Lambda_{44}\sigma_{22}^{\infty}+(D-D_2^{\infty})\Lambda_{24}}{\Lambda_{22}\Lambda_{44}-\Lambda_{24}\Lambda_{42}}\left\{\frac{z^2-c_1^2\lambda_1^2}{X_1(z)}-1\right\}\\&+\frac{\Lambda_{44}\sigma_s+\Lambda_{24}(D-D_s)}{\pi\Sigma}\left(\frac{\pi}{2}-\varphi_d+\varphi_c\right), \quad (7.2.10)\end{aligned}$$

where,

$$\begin{aligned}&k_1^2=\frac{c_1^2-d_1^2}{c_1^2},\ \lambda_1^2=E(k_1)/F(k_1),\ \sin^2\psi_d=\frac{c_1^2-d^2}{c_1^2-d_1^2},\ \sin^2\psi_c=\frac{c_1^2-c^2}{c_1^2-d_1^2},\\&\varphi_d=\tan^{-1}\sqrt{\frac{(d_1^2-z^2)(d^2-c_1^2)}{(c_1^2-z^2)(d_1^2-d^2)}},\ \varphi_c=\tan^{-1}\sqrt{\frac{(d_1^2-z^2)(c^2-c_1^2)}{(c_1^2-z^2)(d_1^2-c^2)}},\\&R_1=dc_1\left\{E(\psi_d,k_1)-\lambda_1^2F(\psi_d,k_1)\right\}-cc_1\left\{E(\psi_c,k_1)-\lambda_1^2F(\psi_c,k_1)\right\}\\&\quad-k_1^2c_1^2\left(\sin\psi_d\cos\psi_d-\sin\psi_c\cos\psi_c\right).\end{aligned}$$

Analogously to determine $\Omega_4^I(z)$, Equation (7.2.7) is solved using the boundary condition (iv) and Equation (2.7.30), the solution may finally be written as

$$\Omega_4^I(z)=-\frac{D-D_s}{2\pi i\Lambda_{44}X_2(z)}\int_{\Gamma}\frac{X_2(t)}{t-z}dt+\frac{P_2(z)}{2\Lambda_{44}X_2(z)}+\frac{D-D_2^{\infty}}{2\Lambda_{44}}-\frac{\Lambda_{42}}{\Lambda_{44}}\Omega_2^I(z), \quad (7.2.11)$$

where $P_2(z)=A_0z^2+A_1z+A_2$ and $X_2(z)=\sqrt{(z^2-a^2)(z^2-b^2)}$.

Again constant $A_0=-D+D_2^{\infty}$ is determined using condition $\lim_{z\to\infty}\Omega_4^I(z)=0$. Also A_1 and A_2 are determined from the condition of single-valuedness of displacement around cracks as before i.e.,

$$\int_{C_i''}[\Omega_4^{I+}(x_1)-\Omega_4^{I-}(x_1)]dx_1=0,\ i=1,2,\ C_1''=[-a,-b],\ C_2''=[b,a]. \quad (7.2.12)$$

Finally, evaluating the integral in Equation (7.2.11) and substituting the values of

constants A_0, A_1 and A_2, the required potential $\Omega_4^I(z)$, may be written as

$$\Omega_4^I(z) = -\frac{\Lambda_{42}}{\Lambda_{44}}\Omega_2^I(z) - \frac{(D-D_2^\infty)}{2\Lambda_{44}}\left\{\frac{z^2-a^2\lambda_2^2}{X_2(z)} - 1\right\} - \frac{(D-D_s)}{\pi\Lambda_{44}}\left(\frac{\pi}{2} - \upsilon_d + \upsilon_c\right) + \frac{(D-D_s)}{\pi\Lambda_{44}X_2(z)}\left\{(z^2-a^2\lambda_2^2)\left(\frac{\pi}{2} - \vartheta_d + \vartheta_c\right) + R_2\right\}, \tag{7.2.13}$$

where,

$$k_2^2 = 1-(b/a)^2,\ \lambda_2^2 = E(k_2)/F(k_2),\ \sin^2\vartheta_d = \frac{a^2-d^2}{a^2-b^2},\ \sin^2\vartheta_c = \frac{a^2-c^2}{a^2-b^2},$$

$$\upsilon_d = \tan^{-1}\sqrt{\frac{(b^2-z^2)}{(a^2-z^2)}\frac{(a^2-d^2)}{(d^2-b^2)}},\ \upsilon_c = \tan^{-1}\sqrt{\frac{(b^2-z^2)}{(a^2-z^2)}\frac{(a^2-c^2)}{(c^2-b^2)}},$$

$$R_2 = da\left\{E(\vartheta_d,k_2) - \lambda_2^2F(\vartheta_d,k_2)\right\} - ca\left\{E(\vartheta_c,k_2) - \lambda_2^2F(\vartheta_c,k_2)\right\} - a^2k_2^2\left(\sin\vartheta_d\cos\vartheta_d - \sin\vartheta_c\cos\vartheta_c\right).$$

7.2.1.2 Applications

The important parameters affecting the crack arrest are obtained in this section.

Saturation zone

The electric displacement is determined using Equations (2.7.7 and 7.2.5) as

$$\mathbf{\Phi}_{,1}^I(x_1) = \mathbf{B}\mathbf{F}^{I+}(x_1) + \mathbf{B}\mathbf{F}^{I-}(x_1) = \mathbf{\Lambda}\mathbf{\Omega}^{I+}(x_1) + \mathbf{\Lambda}\mathbf{\Omega}^{I-}(x_1),\ |x_1| > a. \tag{7.2.14}$$

Taking the fourth component of above equation, we get

$$D_2^I(x_1) = \Lambda_{42}\left[\Omega_2^{I+}(x_1) + \Omega_2^{I-}(x_1)\right] + \Lambda_{44}\left[\Omega_4^{I+}(x_1) + \Omega_4^{I-}(x_1)\right]. \tag{7.2.15}$$

Substituting values of $\Omega_2^I(x_1)$ and $\Omega_4^I(x_1)$ from Equations (7.2.10 and 7.2.13) and simplifying one finally arrives at

$$D_2^I(x_1) = -\frac{2(D-D_s)}{\pi}\left(\frac{\pi}{2} - \upsilon_d + \upsilon_c\right) - (D-D_2^\infty)\left\{\frac{x_1^2-a^2\lambda_2^2}{X_2(x_1)} - 1\right\} + \frac{2(D-D_s)}{\pi X_2(x_1)}\left\{(x_1^2-a^2\lambda_2^2)\left(\frac{\pi}{2} - \vartheta_d + \vartheta_c\right) + R_2\right\}. \tag{7.2.16}$$

The saturation zones lengths are now obtained by extending Dugdale's [43] hypothesis to the electric displacement to remain finite at every point of the plate. This leads to the determination of two non-linear equations

$$\left(\frac{b^2}{a^2} - \lambda_2^2\right)\left(\frac{\pi}{2}\frac{D-D_2^\infty}{D-D_s} - \frac{\pi}{2} + \vartheta_d - \vartheta_c\right) - \frac{R_2}{a^2} = 0, \tag{7.2.17}$$

$$\left(1-\lambda_2^2\right)\left(\frac{\pi}{2}\frac{D-D_2^{\infty}}{D-D_s}-\frac{\pi}{2}+\vartheta_d-\vartheta_c\right)-\frac{R_2}{a^2}=0, \tag{7.2.18}$$

to determine a and b. Hence saturation zone length at the tip c and d are calculated from $(a-c)$ and $(d-b)$, respectively.

Yield zone

To calculate yield zones lengths the required stress component is obtained by writing second component of Equation (7.2.14),

$$\sigma_{22}^I(x_1)=\Lambda_{22}\left[\Omega_2^{I+}(x_1)+\Omega_2^{I-}(x_1)\right]+\Lambda_{24}\left[\Omega_4^{I+}(x_1)+\Omega_4^{I-}(x_1)\right]. \tag{7.2.19}$$

Substituting values from Equations (7.2.10 and 7.2.13) and simplifying, we get

$$\begin{aligned}\sigma_{22}^I(x_1)=&-\frac{2}{\pi X_1(x_1)}\left(\sigma_s+\frac{\Lambda_{24}}{\Lambda_{44}}(D-D_s)\right)\left\{(x_1^2-c_1^2\lambda_1^2)\left(\frac{\pi}{2}-\psi_d+\psi_c\right)+R_1\right\}\\&+\left(\sigma_{22}^{\infty}+\frac{\Lambda_{24}}{\Lambda_{44}}(D-D_2^{\infty})\right)\left\{\frac{x_1^2-c_1^2\lambda_1^2}{X_1(x_1)}-1\right\}\\&+\frac{2}{\pi}\left(\sigma_s+\frac{\Lambda_{24}}{\Lambda_{44}}(D-D_s)\right)\left(\frac{\pi}{2}-\varphi_d+\varphi_c\right).\end{aligned} \tag{7.2.20}$$

Using Dugdale's [24] hypothesis that the stress remain finite at every point of the plate consequently at the points $x_1=d_1$ and $x_1=c_1$ also, we get the following transcendental equations

$$\left(\frac{d_1^2}{c_1^2}-\lambda_1^2\right)\left(\frac{\pi}{2}\frac{\Lambda_{44}\sigma_{22}^{\infty}+\Lambda_{24}(D-D_2^{\infty})}{\Lambda_{44}\sigma_s+\Lambda_{24}(D-D_s)}-\frac{\pi}{2}+\psi_d-\psi_c\right)-\frac{R_1}{c_1^2}=0, \tag{7.2.21}$$

$$\left(1-\lambda_1^2\right)\left(\frac{\pi}{2}\frac{\Lambda_{44}\sigma_{22}^{\infty}+\Lambda_{24}(D-D_2^{\infty})}{\Lambda_{44}\sigma_s+\Lambda_{24}(D-D_s)}-\frac{\pi}{2}+\psi_d-\psi_c\right)-\frac{R_1}{c_1^2}=0. \tag{7.2.22}$$

These enable us to determine c_1 and d_1 for prescribed loads. The yield zone lengths are than calculated from (c_1-c) and $(d-d_1)$.

Crack opening displacement (COD)

The jump displacement vector $\Delta\mathbf{u}_{,1}^I$ is determined as

$$i\Delta\mathbf{u}_{,1}^I(x_1)=i[u_{1,1}^+-u_{1,1}^-,u_{2,1}^+-u_{2,1}^-,u_{3,1}^+-u_{3,1}^-,E_1^--E_1^+]^T=\mathbf{H}^R[\mathbf{BF}^{I+}(x_1)-\mathbf{BF}^{I-}(x_1)]. \tag{7.2.23}$$

The jump displacement component Δu_2^I at the crack tips d and c are obtained by remembering that $\Delta u_2^I=0$ at the tips $x_1=\pm d_1,\pm c_1$,

at the inner crack tip $x_1 = d$

$$\begin{aligned}\Delta u_2^I(d) = &- \frac{\Lambda_{44}\sigma_s + \Lambda_{24}(D - D_s)}{\pi\Sigma}\left\{\frac{2d_1^2}{c_1}\sqrt{\frac{c_1^2 - d^2}{d^2 - d_1^2}}R_3 - d\ln(A) + 2F(\tau_d, k_1)\frac{R_1}{c_1}\right\} \\ &- \frac{\Lambda_{44}\sigma_s + \Lambda_{24}(D - D_s)}{\pi\Sigma}\left\{G(d,c) + 2c_1\left(\frac{\pi}{2} - \psi_d + \psi_c\right)R_4\right\} \\ &+ \frac{c_1}{\Sigma}(\Lambda_{44}\sigma_{22}^{\infty} + \Lambda_{24}(D - D_2^{\infty}))R_4, \end{aligned} \tag{7.2.24}$$

and at the outer crack tip $x_1 = c$

$$\begin{aligned}\Delta u_2^I(c) = &\frac{\Lambda_{44}\sigma_s + \Lambda_{24}(D - D_s)}{\pi\Sigma}\left\{2c_1\left(\frac{\pi}{2} - \psi_d + \psi_c\right)R_5 + H(c,d) - c\ln(B)\right\} \\ &+ \frac{\Lambda_{44}\sigma_s + \Lambda_{24}(D - D_s)}{\pi\Sigma}\left\{2F(\psi_c, k_1)\frac{R_1}{c_1} + \frac{2}{c_1}\sqrt{\frac{c^2 - d_1^2}{c_1^2 - c^2}}R_6\right\} \\ &- \frac{c_1}{\Sigma}(\Lambda_{44}\sigma_{22}^{\infty} + \Lambda_{24}(D - D_2^{\infty}))R_5, \end{aligned} \tag{7.2.25}$$

where,

$$\ln(A) = \ln\left(\frac{c_1^2 - d^2}{c_1^2 - d_1^2} + \frac{c_1^2(d_1^2 - d^2)}{d^2(c_1^2 - d_1^2)}\right),\ \ln(B) = \ln\left(\frac{(c_1^2 - c^2)(c^2 - d_1^2)}{c^2(c_1^2 - d_1^2)} + 1\right),$$

$$\sin^2\tau_d = c_1^2(d^2 - d_1^2)/\left(d^2(c_1^2 - d_1^2)\right),\ R_3 = \left(F(\tau_d, k_1) - II(\tau_d, \frac{d^2 - d_1^2}{d^2}, k_1)\right),$$

$$R_4 = \left(E(\tau_d, k_1) - \frac{k_1^2\sin\tau_d\cos\tau_d}{\sqrt{1 - k_1^2\sin^2\tau_d}} - \lambda_1^2 F(\tau_d, k_1)\right),$$

$$R_5 = \left(E(\psi_c, k_1) - \lambda_1^2 F(\psi_c, k_1)\right),\ R_6 = \left(c_1^2 F(\psi_c, k_1) - c^2 II(\psi_c, \frac{c_1^2 - c^2}{c_1^2}, k_1)\right),$$

$$\begin{aligned}G(d,c) = &\, d\ln\left(\frac{\sqrt{(d^2 - d_1^2)(c_1^2 - c^2)} + \sqrt{(c_1^2 - d^2)(c^2 - d_1^2)}}{\sqrt{(d^2 - d_1^2)(c_1^2 - c^2)} - \sqrt{(c_1^2 - d^2)(c^2 - d_1^2)}}\right) \\ &- \frac{2d_1^2}{c_1}\sqrt{\frac{c_1^2 - c^2}{c^2 - d_1^2}}II(\tau_d, \frac{c^2k_1^2}{c^2 - d_1^2}, k_1), \end{aligned}$$

$$\begin{aligned}H(c,d) = &\, c\ln\left(\frac{\sqrt{(c^2 - d_1^2)(c_1^2 - d^2)} + \sqrt{(c_1^2 - c^2)(d^2 - d_1^2)}}{\sqrt{(c^2 - d_1^2)(c_1^2 - d^2)} - \sqrt{(c_1^2 - c^2)(d^2 - d_1^2)}}\right) \\ &- \frac{2}{c_1}\sqrt{(d^2 - d_1^2)(c_1^2 - d^2)}\left(F(\psi_c, k_1) + \frac{d^2}{c_1^2 - d^2}II(\psi_c, \frac{c_1^2 - d_1^2}{c_1^2 - d^2}, k_1)\right). \end{aligned}$$

Crack opening potential drop (COP)

COP is calculated by taking fourth component from Equation (7.2.23) and substituting value from Equation (7.2.13) and integrating, one arrives

at the inner crack tip $x_1 = d$

$$\begin{aligned}\Delta u_4^I(d) =& \frac{(D-D_s)}{\pi\Lambda_{44}}\left\{-d\ln(C) + 2F(\xi_d,k_2)\frac{R_2}{a} + G_1(d,c) + \frac{2b^2}{a}\sqrt{\frac{a^2-d^2}{d^2-b^2}}R_7\right\} \\ &+ \frac{2a(D-D_s)}{\pi\Lambda_{44}}\left(\frac{\pi}{2} - \vartheta_d + \vartheta_c\right)R_8 - \frac{a(D-D_2^\infty)}{\Lambda_{44}}R_8 - \frac{\Lambda_{42}}{\Lambda_{44}}\Delta u_2^I(d),\end{aligned} \tag{7.2.26}$$

and at the outer crack tip $x_1 = c$

$$\begin{aligned}\Delta u_4^I(c) =& -\frac{(D-D_s)}{\pi\Lambda_{44}}\left\{-c\ln(D) + H_1(c,d) + 2F(\vartheta_c,k_2)\frac{R_2}{a} + \frac{2}{a}\sqrt{\frac{c^2-b^2}{a^2-c^2}}R_9\right\} \\ &- \frac{2a(D-D_s)}{\pi\Lambda_{44}}\left(\frac{\pi}{2} - \vartheta_d + \vartheta_c\right)R_{10} + \frac{a(D-D_2{}^\infty)}{\Lambda_{44}}R_{10} - \frac{\Lambda_{42}}{\Lambda_{44}}\Delta u_2^I(c),\end{aligned} \tag{7.2.27}$$

where,

$$\ln(C) = \ln\left(\frac{a^2-d^2}{a^2-b^2} + \frac{a^2(b^2-d^2)}{d^2(a^2-b^2)}\right),\ \ln(D) = \ln\left(\frac{(a^2-c^2)(c^2-b^2)}{c^2(a^2-b^2)} + 1\right),$$

$$\sin^2\xi_d = a^2(d^2-b^2)/\left(d^2(a^2-b^2)\right),\ R_7 = \left(F(\xi_d,k_2) - II(\xi_d,\frac{d^2-b^2}{d^2},k_2)\right),$$

$$R_8 = \left(E(\xi_d,k_2) - \frac{k_2^2\sin\xi_d\cos\xi_d}{\sqrt{1-k_2^2\sin^2\xi_d}} - \lambda_2^2 F(\xi_d,k_2)\right),$$

$$R_9 = \left(a^2F(\vartheta_c,k_2) - c^2II(\vartheta_c,\frac{a^2-c^2}{a^2},k_2)\right),\ R_{10} = \left(E(\vartheta_c,k_2) - \lambda_2^2F(\vartheta_c,k_2)\right),$$

$$\begin{aligned}G_1(d,c) =& \, d\ln\left(\frac{\sqrt{(d^2-b^2)(a^2-c^2)} + \sqrt{(a^2-d^2)(c^2-b^2)}}{\sqrt{(d^2-b^2)(a^2-c^2)} - \sqrt{(a^2-d^2)(c^2-b^2)}}\right) \\ &- \frac{2b^2}{a}\sqrt{\frac{a^2-c^2}{c^2-b^2}}II(\xi_d,\frac{c^2k_2^2}{c^2-b^2},k_2),\end{aligned}$$

$$\begin{aligned}H_1(c,d) =& \, c\ln\left(\frac{\sqrt{(c^2-b^2)(a^2-d^2)} + \sqrt{(a^2-c^2)(d^2-b^2)}}{\sqrt{(c^2-b^2)(a^2-d^2)} - \sqrt{(a^2-c^2)(d^2-b^2)}}\right) \\ &- \frac{2}{a}\sqrt{(d^2-b^2)(a^2-d^2)}\left(F(\vartheta_c,k_2) + \frac{d^2}{a^2-d^2}II(\vartheta_c,\frac{a^2-b^2}{a^2-d^2},k_2)\right).\end{aligned}$$

As for semi-permeable crack model, the electric displacement, D (defined by Equation (2.5.3)) inside the crack gap media is related to the crack opening displacement and the potential drop. Thus the value of electric flux D, is obtained from the quadratic Equation (3.4.4) for two-collinear cracks problem.

Energy release rate (ERR)

Energy release rate is calculated at the interior tip $x_1 = d$ and exterior tip $x_1 = c$

using the formulae

$$J_a^I(d) = \sigma_s \Delta u_2^I(d) + D_s \Delta u_4^I(d), \tag{7.2.28}$$

$$J_a^I(c) = \sigma_s \Delta u_2^I(c) + D_s \Delta u_4^I(c). \tag{7.2.29}$$

7.2.1.3 Case I: Results and Discussions

The variation of crack opening displacement, crack opening potential drop, energy release rate with respect to crack closure affecting parameters are presented in this section for PZT-4, PZT-5H and $BaTiO_3$ ceramics. The material constants are given in Table 2.1.

We assumed that the lengths of the collinear cracks, saturation limit electric displacement and yield stress are $10mm$, $D_s = 0.1C/m^2$ and $\sigma_s = 200MPa$, respectively.

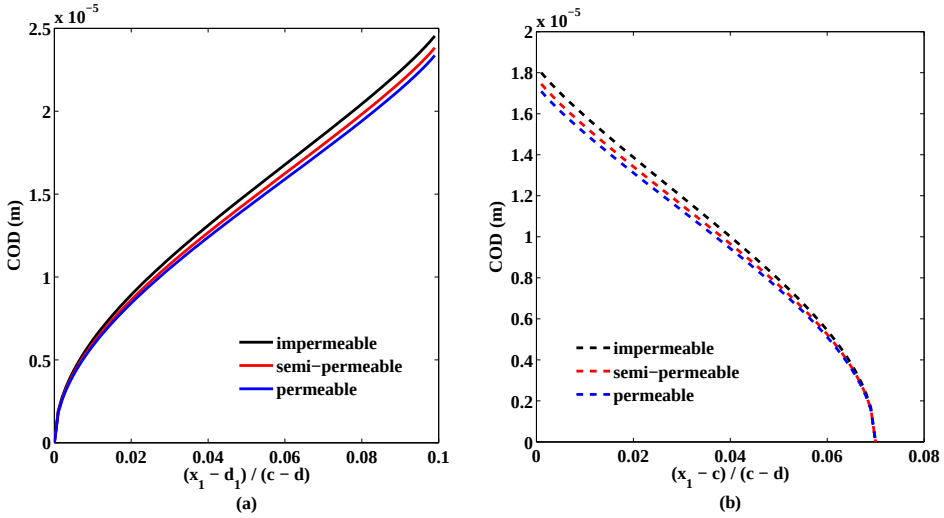

Figure 7.2: COD profile over the interior and exterior yield zones for different electric boundary conditions

Figs. 7.2(a, b) present COD variation over the interior and exterior yield zones for the cases of impermeable, semi-permeable and permeable cracks. It may be noted from the Fig. 7.2(a) that COD is zero at the tips of the yield zone and increases non-linearly as the ratio $(x_1 - d_1)/(c - d)$ is increased. It is also observed that the COD is higher for impermeable crack than those for the permeable ones. At the considered loading levels the semi-permeable results are closer to the permeable ones. A similar variation is observed for COD at exterior yield zone.

Variation of COD, Δu_2^I with respect to prescribed electric displacement load at the inner and outer tips $x_1 = d$ and $x_1 = c$ is plotted in Figs. 7.3(a and b), respectively. It is noted that COD at each of the tips increases almost linearly. It is more at inner tip than that at outer tip. It is also noted that as mechanical loading is increased the cracks open more.

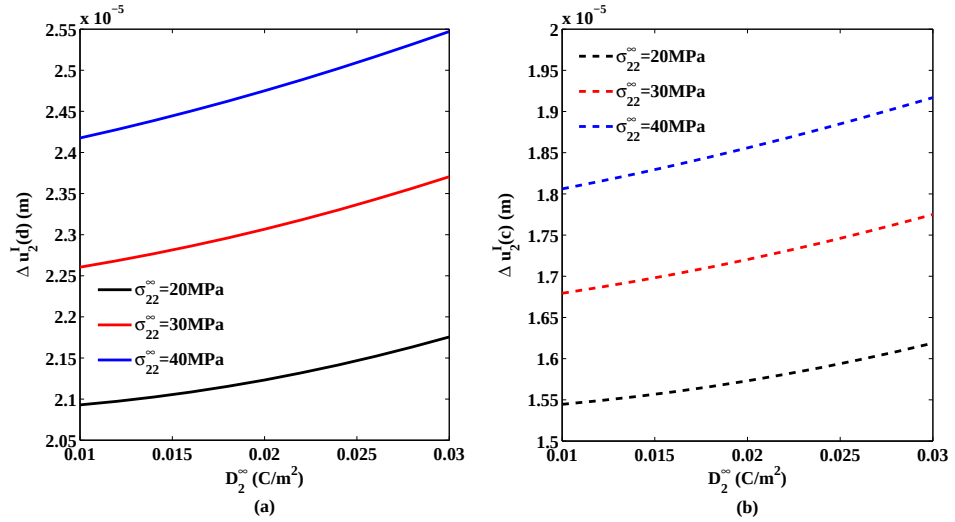

Figure 7.3: COD versus D_2^∞ for different mechanical loads

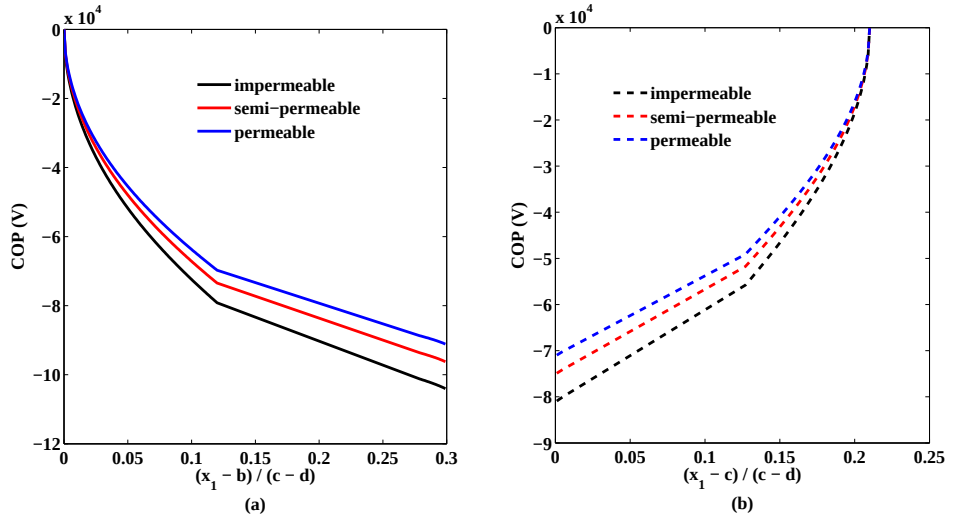

Figure 7.4: COP drop over the interior and exterior saturation zones for different electric boundary conditions

Variation of COP over the interior and exterior saturation zones is depicted in Figs. 7.4(a, b). It may be pointed out that COP drop is maximum at the interior saturation zone as compared to that at exterior saturation zone, this is because of

the mutual interactions of the collinear cracks. The kink in both the Figs. 7.4(a, b) is the tip of yield zone.

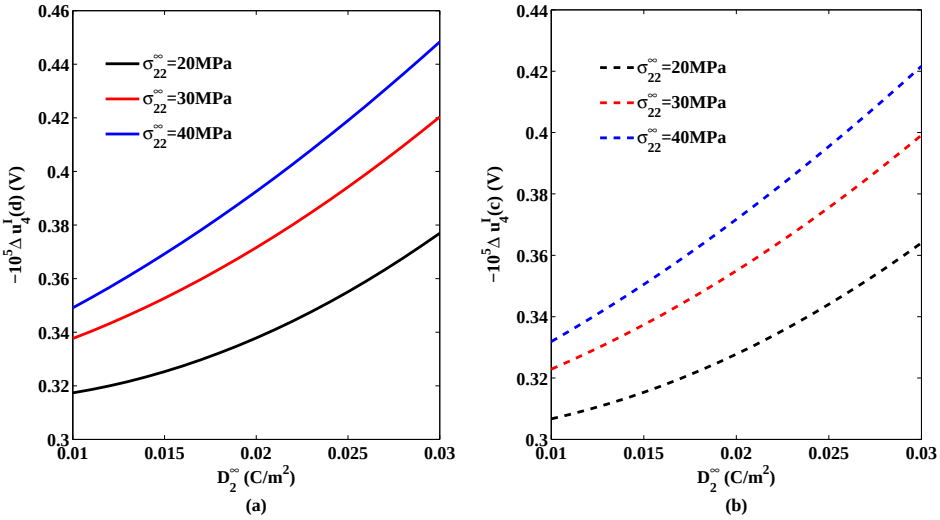

Figure 7.5: COP versus D_2^{∞} for different mechanical loads

Figs. 7.5(a and b) show that COP decreases with increase in mechanical loading although COP increases with increase in electric loading. Potential drop is higher at the interior tip, as expected.

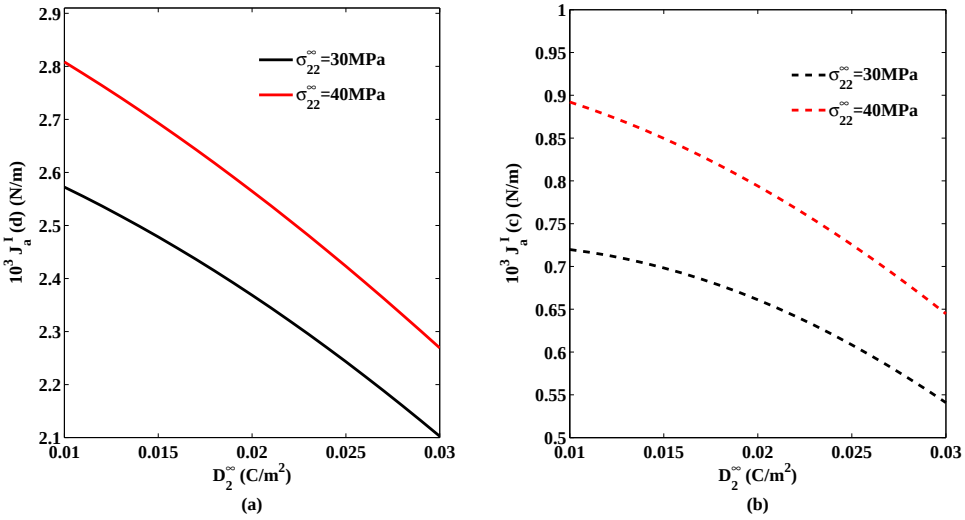

Figure 7.6: ERR versus D_2^{∞} for different mechanical loads

Figs. 7.6(a, b) depict the variation of ERR at the interior and exterior tips of the crack for increasing value of prescribed electric displacement load, for different prescribed mechanical load. It may be seen that ERR at the interior tip of the crack drops continuously as D_2^{∞} is increased. As the prescribed mechanical load is

increased a higher ERR is observed but it decreases with increasing D_2^{∞}. It is also seen that ERR is much less at exterior tip as compared to that at interior tip, this is because of the mutual interactions of two closely located cracks.

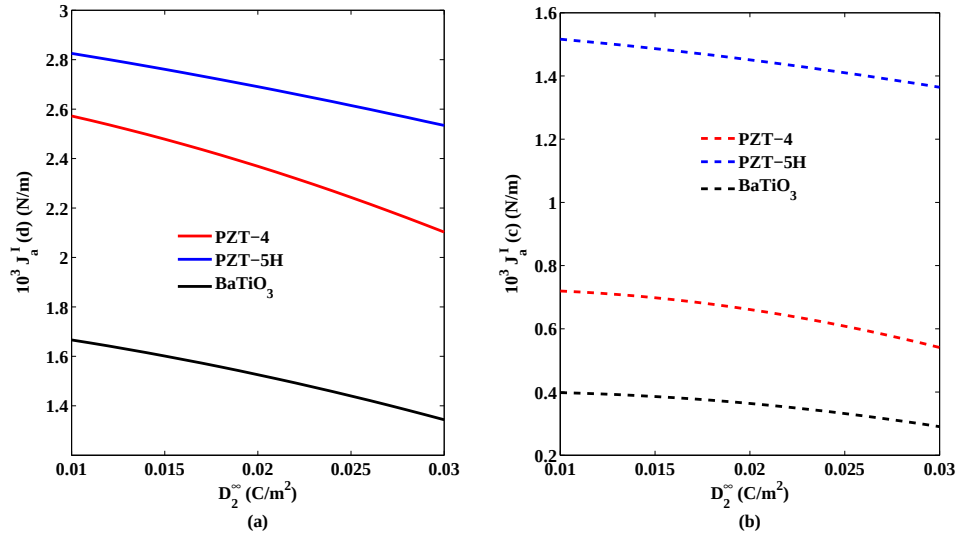

Figure 7.7: ERR versus D_2^{∞} for PZT-4, PZT-5H and $BaTiO_3$

Figs. 7.7(a, b) show the ERR for PZT-4, PZT-5H and $BaTiO_3$ ceramics versus D_2^{∞}, all the ceramics show ERR drop at the interior and exterior tips of the cracks. These results may assist the designer to select the appropriate ceramic.

7.2.2 Case II: When saturation zones are smaller than developed yield zones ($|c_1| > |a|$ and $|b| > |d_1|$)

The boundary conditions from (i) to (iv) in subsection (7.2.1), remain the same as in Case I and the boundary condition (v) is replaced by (vi) as

$$\text{(vi)}\quad \mathbf{\Phi}_{,1}^{II+}(x_1) = \mathbf{\Phi}_{,1}^{II-}(x_1) = -\mathbf{V}^{II}, \quad \text{for } d < |x_1| < c$$

where, $\mathbf{V}^{II} = [0, \sigma_{22}^{\infty}, 0, D_2^{\infty}]^T$, and superscript II represents that the quantity refers to Case II.

Schematically the configuration of the problem is depicted in Fig. 7.8.

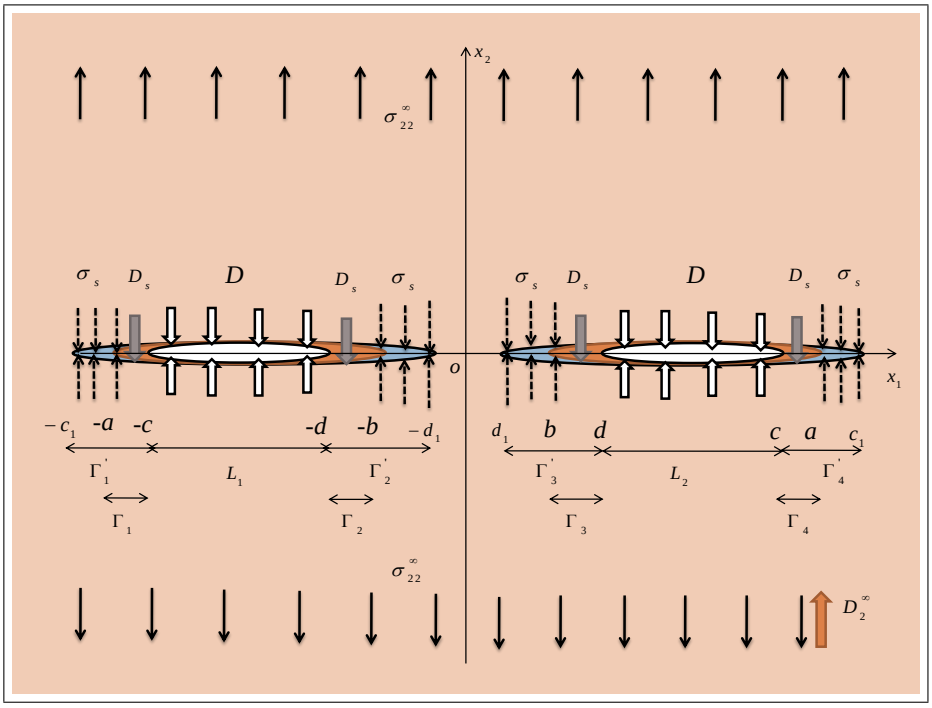

Figure 7.8: Schematic representation of configuration of the problem for Case II, when saturation zones are smaller than developed yield zones

7.2.2.1 Solution of the Problem

Carrying out calculations analogous to Case I the boundary condition (vi) for this case yields the following two dual Hilbert problems for potentials $\Omega_2^{II}(z)$ and $\Omega_4^{II}(z)$ as

$$\Lambda_{22}[\Omega_2^{II+}(x_1) + \Omega_2^{II-}(x_1)] + \Lambda_{24}[\Omega_4^{II+}(x_1) + \Omega_4^{II-}(x_1)] = -\sigma_{22}^{\infty},\ d < |x_1| < c, \tag{7.2.30}$$

$$\Lambda_{42}[\Omega_2^{II+}(x_1) + \Omega_2^{II-}(x_1)] + \Lambda_{44}[\Omega_4^{II+}(x_1) + \Omega_4^{II-}(x_1)] = D - D_2^{\infty},\ d < |x_1| < c. \tag{7.2.31}$$

The solution of which may be written, carrying the similar calculation as in Case I, as

$$\begin{aligned}\Omega_4^{II}(z) =& \frac{\Lambda_{42}\sigma_s + \Lambda_{22}(D - D_s)}{\pi\Sigma X_2(z)}\left\{(z^2 - a^2\lambda_2^2)\left(\frac{\pi}{2} - \vartheta_d + \vartheta_c\right) + R_2\right\} \\ &- \frac{\Lambda_{42}\sigma_{22}^{\infty} + \Lambda_{22}(D - D_2^{\infty})}{2\Sigma}\left\{\frac{z^2 - a^2\lambda_2^2}{X_2(z)} - 1\right\} \\ &- \frac{\Lambda_{42}\sigma_s + \Lambda_{22}(D - D_s)}{\pi\Sigma}\left(\frac{\pi}{2} - \upsilon_d + \upsilon_c\right),\end{aligned} \tag{7.2.32}$$

$$\Omega_2^{II}(z) = -\frac{\Lambda_{42}}{\Lambda_{22}}\Omega_4^{II}(z) + \frac{\sigma_{22}^{\infty}}{2\Lambda_{22}}\left\{\frac{z^2 - c_1^2\lambda_1^2}{X_1(z)} - 1\right\} + \frac{\sigma_s}{\pi\Lambda_{22}}\left(\frac{\pi}{2} - \varphi_d + \varphi_c\right) - \frac{\sigma_s}{\pi\Lambda_{22}X_1(z)}\left\{(z^2 - c_1^2\lambda_1^2)\left(\frac{\pi}{2} - \psi_d + \psi_c\right) + R_1\right\}. \quad (7.2.33)$$

7.2.2.2 Applications

In this section closed form expressions are derived for developed zones lengths, crack opening displacement, crack opening potential drop and energy release rate.
The stress and electric displacement for this case are obtained using

$$\mathbf{\Phi}_{,1}^{II}(x_1) = \mathbf{B}\mathbf{F}^{II+}(x_1) + \mathbf{B}\mathbf{F}^{II-}(x_1) = \mathbf{\Lambda}\mathbf{\Omega}^{II+}(x_1) + \mathbf{\Lambda}\mathbf{\Omega}^{II-}(x_1),\ |x_1| > c_1. \quad (7.2.34)$$

Comparing second and fourth components of the above vector equation, we get

$$\sigma_{22}^{II}(x_1) = \Lambda_{22}[\Omega_2^{II+}(x_1) + \Omega_2^{II-}(x_1)] + \Lambda_{24}[\Omega_4^{II+}(x_1) + \Omega_4^{II-}(x_1)], \quad (7.2.35)$$

$$D_2^{II}(x_1) = \Lambda_{42}[\Omega_2^{II+}(x_1) + \Omega_2^{II-}(x_1)] + \Lambda_{44}[\Omega_4^{II+}(x_1) + \Omega_4^{II-}(x_1)]. \quad (7.2.36)$$

Substituting the values of $\Omega_2^{II}(x_1)$ and $\Omega_4^{II}(x_1)$ from Equations (7.2.33 and 7.2.32) and simplifying one obtains

$$\sigma_{22}^{II}(x_1) = \frac{2\sigma_s}{\pi}\left(\frac{\pi}{2} - \varphi_d + \varphi_c\right) + \sigma_{22}^{\infty}\left\{\frac{x_1^2 - c_1^2\lambda_1^2}{X_1(x_1)} - 1\right\} - \frac{2\sigma_s}{\pi X_1(x_1)}\left\{(x_1^2 - c_1^2\lambda_1^2)\left(\frac{\pi}{2} - \psi_d + \psi_c\right) + R_1\right\}, \quad (7.2.37)$$

$$D_2^{II}(x_1) = \frac{2(\Lambda_{42}\sigma_s + \Lambda_{22}(D - D_s))}{\pi\Lambda_{22}X_2(x_1)}\left\{(x_1^2 - a^2\lambda_2^2)\left(\frac{\pi}{2} - \vartheta_d + \vartheta_c\right) + R_2\right\} - \frac{\Lambda_{42}\sigma_{22}^{\infty} + \Lambda_{22}(D - D_2^{\infty})}{\Lambda_{22}}\left\{\frac{x_1^2 - a^2\lambda_2^2}{X_2(x_1)} - 1\right\} - \frac{2(\Lambda_{42}\sigma_s + \Lambda_{22}(D - D_s))}{\pi\Lambda_{22}}\left(\frac{\pi}{2} - \upsilon_d + \upsilon_c\right). \quad (7.2.38)$$

Yield zone

Using Dugdale's assumption that the stress remains finite at every point of the body, consequently at the tips $x_1 = d_1$ and $x_1 = c_1$ of the yield zones, one obtains non-linear equations to determine d_1 and c_1 from

$$\left(\frac{d_1^2}{c_1^2} - \lambda_1^2\right)\left(\frac{\pi\sigma_{22}^{\infty}}{2\sigma_s} - \frac{\pi}{2} + \psi_d - \psi_c\right) - \frac{R_1}{c_1^2} = 0, \quad (7.2.39)$$

$$\left(1-\lambda_1^2\right)\left(\frac{\pi\sigma_{22}^{\infty}}{2\sigma_s}-\frac{\pi}{2}+\psi_d-\psi_c\right)-\frac{R_1}{c_1^2}=0. \tag{7.2.40}$$

Saturation zone

Assuming Dugdale's hypothesis to be true for electric displacement as well hence the condition of finiteness of electrical displacements at every point of the plate yields the following two equations

$$\left(\frac{b^2}{a^2}-\lambda_2^2\right)\left(\frac{\pi}{2}\frac{\Lambda_{42}\sigma_{22}^{\infty}+\Lambda_{22}(D-D_2^{\infty})}{\Lambda_{42}\sigma_s+\Lambda_{22}(D-D_s)}-\frac{\pi}{2}+\vartheta_d-\vartheta_c\right)-\frac{R_2}{a^2}=0, \tag{7.2.41}$$

$$\left(1-\lambda_2^2\right)\left(\frac{\pi}{2}\frac{\Lambda_{42}\sigma_{22}^{\infty}+\Lambda_{22}(D-D_2^{\infty})}{\Lambda_{42}\sigma_s+\Lambda_{22}(D-D_s)}-\frac{\pi}{2}+\vartheta_d-\vartheta_c\right)-\frac{R_2}{a^2}=0. \tag{7.2.42}$$

Crack opening potential drop (COP)

The crack opening potential drop for this case is determined using analogous equation to Equation (6.2.23) as

$$i\Delta\mathbf{u}_{,1}^{II}(x_1)=\mathbf{\Lambda}[\mathbf{\Omega}^{II+}(x_1)-\mathbf{\Omega}^{II-}(x_1)]. \tag{7.2.43}$$

Comparing the fourth component of the above equation and substituting value of $\Omega_4^{II}(x_1)$ from Equation (7.2.32) one obtains potential drop at the crack tips $x_1=d$ and $x_1=c$ as

$$\begin{aligned}\Delta u_4^{II}(d)=&\frac{\Lambda_{42}\sigma_s+\Lambda_{22}(D-D_s)}{\pi\Sigma}\left\{-d\ln(C)+2F(\xi_d,k_2)\frac{R_2}{a}+G_1(d,c)\right\}\\&+\frac{\Lambda_{42}\sigma_s+\Lambda_{22}(D-D_s)}{\pi\Sigma}\left\{2a\left(\frac{\pi}{2}-\vartheta_d+\vartheta_c\right)R_8+\frac{2b^2}{a}\sqrt{\frac{a^2-d^2}{d^2-b^2}}R_7\right\}\\&-\frac{a(\Lambda_{42}\sigma_{22}^{\infty}+\Lambda_{22}(D-D_2^{\infty}))}{\Sigma}R_8,\end{aligned} \tag{7.2.44}$$

$$\begin{aligned}\Delta u_4^{II}(c)=&-\frac{\Lambda_{42}\sigma_s+\Lambda_{22}(D-D_s)}{\pi\Sigma}\left\{-c\ln(D)+H_1(c,d)+2F(\vartheta_c,k_2)\frac{R_2}{a}\right\}\\&-\frac{\Lambda_{42}\sigma_s+\Lambda_{22}(D-D_s)}{\pi\Sigma}\left\{2a\left(\frac{\pi}{2}-\vartheta_d+\vartheta_c\right)R_{10}+\frac{2}{a}\sqrt{\frac{c^2-b^2}{a^2-c^2}}R_9\right\}\\&+\frac{a(\Lambda_{42}\sigma_{22}^{\infty}+\Lambda_{22}(D-D_2^{\infty}))}{\Sigma}R_{10}.\end{aligned} \tag{7.2.45}$$

Crack opening displacement (COD)

The COD at the crack tips $x_1=d$ and $x_1=c$ are obtained comparing second

component of Equation (7.2.43) and substituting value of $\Omega_2^{II}(x_1)$ from Equation (7.2.33) and simplifying, one obtains

$$\Delta u_2^{II}(d) = -\frac{\sigma_s}{\pi\Lambda_{22}}\left\{-d\ln(A) + \frac{2d_1^2}{c_1}\sqrt{\frac{c_1^2-d^2}{d^2-d_1^2}}R_3 + 2F(\tau_d,k_1)\frac{R_1}{c_1} + G(d,c)\right\} - \frac{2c_1\sigma_s}{\pi\Lambda_{22}}\left(\frac{\pi}{2}-\psi_d+\psi_c\right)R_4 + \frac{c_1\sigma_{22}^{\infty}}{\Lambda_{22}}R_4 - \frac{\Lambda_{24}}{\Lambda_{22}}\Delta u_4^{II}(d), \tag{7.2.46}$$

$$\Delta u_2^{II}(c) = \frac{\sigma_s}{\pi\Lambda_{22}}\left\{-c\ln(B) + H(c,d) + 2F(\psi_c,k_1)\frac{R_1}{c_1} + \frac{2}{c_1}\sqrt{\frac{c^2-d_1^2}{c_1^2-c^2}}R_6\right\} + \frac{2c_1\sigma_s}{\pi\Lambda_{22}}\left(\frac{\pi}{2}-\psi_d+\psi_c\right)R_5 - \frac{c_1\sigma_{22}^{\infty}}{\Lambda_{22}}R_5 - \frac{\Lambda_{24}}{\Lambda_{22}}\Delta u_4^{II}(c). \tag{7.2.47}$$

Energy release rate (ERR)

Energy release rate at the interior and exterior tips of the crack is calculated using formulae

$$J_a^{II}(d) = \sigma_s\Delta u_2^{II}(d) + D_s\Delta u_4^{II}(d), \tag{7.2.48}$$

$$J_a^{II}(c) = \sigma_s\Delta u_2^{II}(c) + D_s\Delta u_4^{II}(c). \tag{7.2.49}$$

7.2.2.3 Case II: Results and Discussions

Variations of COP, COD and ERR vis-a-vis parameters affecting the crack closure namely saturation zone length, yield zone, prescribed mechanical and electrical loads are presented in this section for PZT-4, PZT-5H and $BaTiO_3$ ceramics.

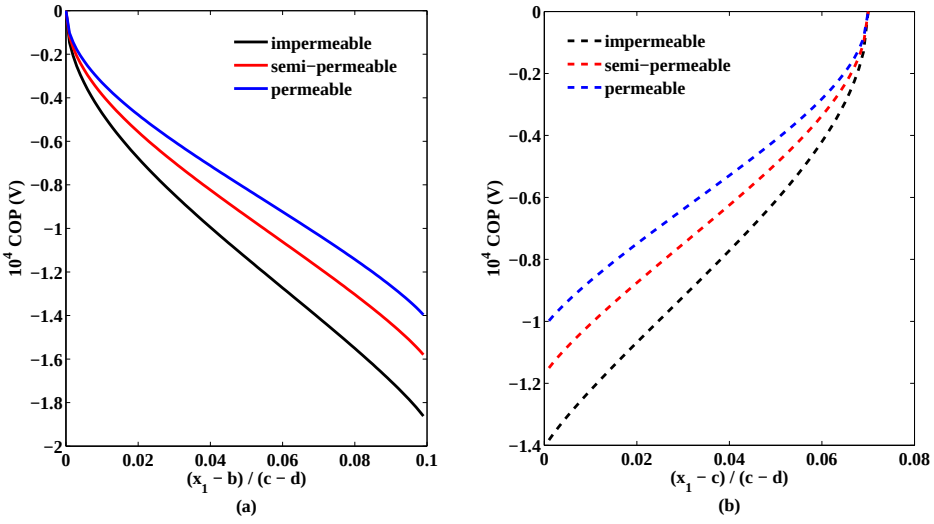

Figure 7.9: COP drop over the interior and exterior saturation zones for different electric boundary conditions

Figs. 7.9(a, b) show the variation of COP drop with respect to zone length to crack length ratio. It may be noted from Figs. 7.9(a, b), that the COP drops more at the interior zone as compared to that at exterior zone. Also the COP drop decreases when we move from impermeable crack to permeable crack face boundary conditions.

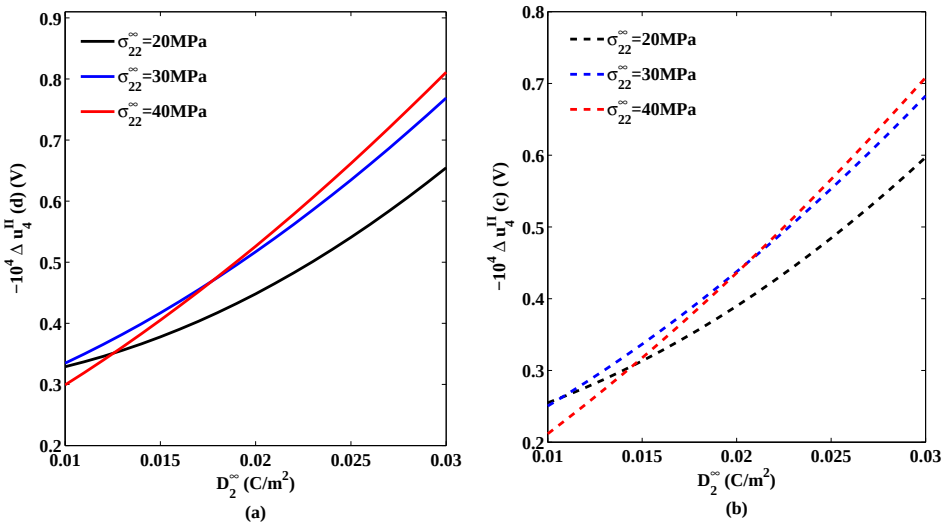

Figure 7.10: COP versus D_2^{∞} for different mechanical loads

Figs. 7.10(a and b) show that COP decreases with increase in mechanical loading although COP increases with increase in electric loading. Potential drop is higher at the interior tip, as expected. It may also be noted that there is a steep decrease in COP at both the crack tips when mechanical loading is $40MPa$.

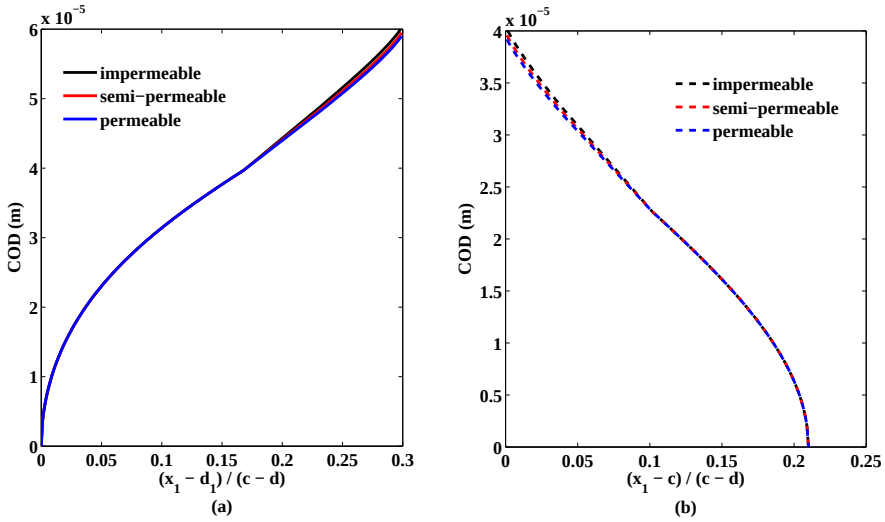

Figure 7.11: COD profile over the interior and exterior yield zones for different electric boundary conditions

Crack opening displacement over the developed interior and exterior yield zones are plotted in Figs. 7.11(a, b). The COD is more at interior zone as compared to that at exterior zone. The permeability/impermeability does not have much significant effect on COD in this case.

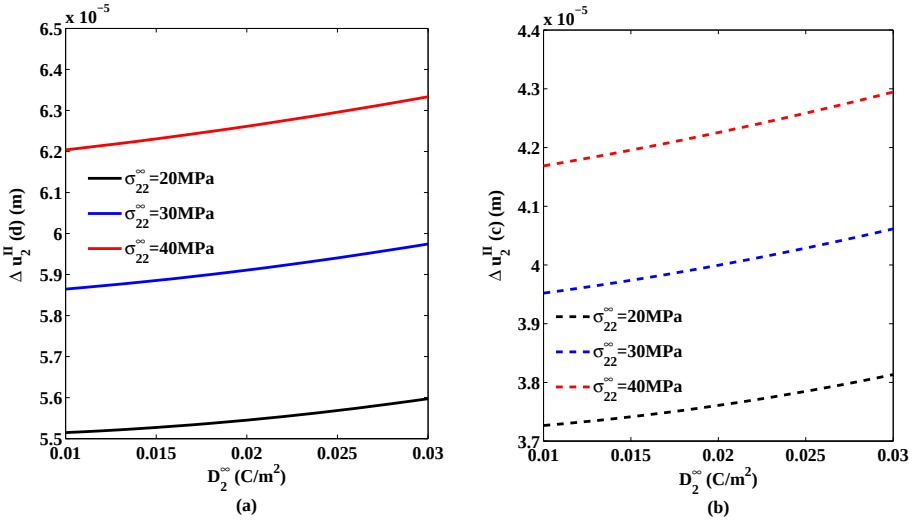

Figure 7.12: COD versus D_2^{∞} for different mechanical loads

Variation of COD, Δu_2^{II} with respect to prescribed electric displacement at the inner and outer tips $x_1 = d$ and $x_1 = c$ is respectively, plotted in Figs. 7.12(a and b). It is noted that COD at each of the tips increases almost linearly. It is more at inner tip than that at outer tip. It is also noted as mechanical loading is increased the cracks open more.

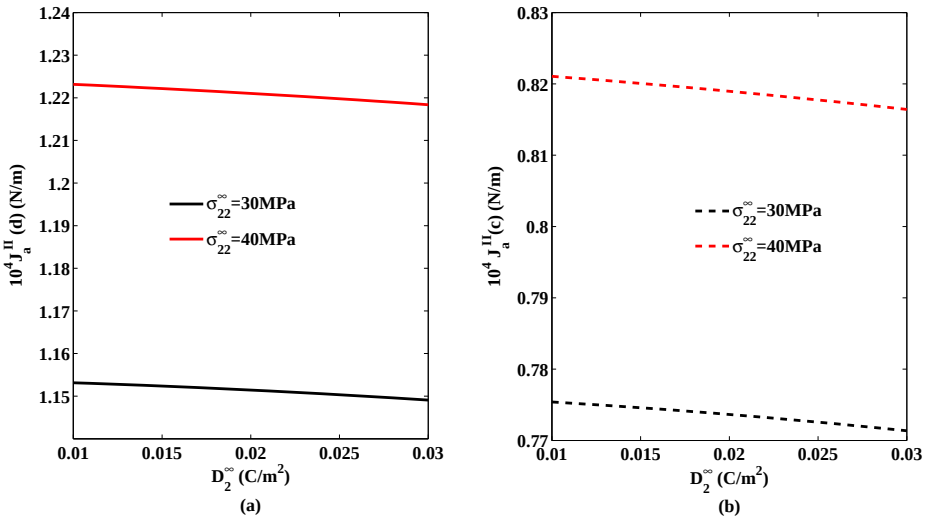

Figure 7.13: ERR versus D_2^{∞} for different mechanical loads

Energy release rate at the interior and exterior tips of the cracks shown in Figs. 7.13(a, b) depict that even with the increase in prescribed electric displacement the energy release rate drops. This confirms the crack arrest. Also as expected, the energy release rate is higher at inner tip that's how the crack opens more at the inner tip and there is a chance of coalesce if the cracks are nearer to each other. However as prescribed mechanical load is increased the ERR also increases, as expected.

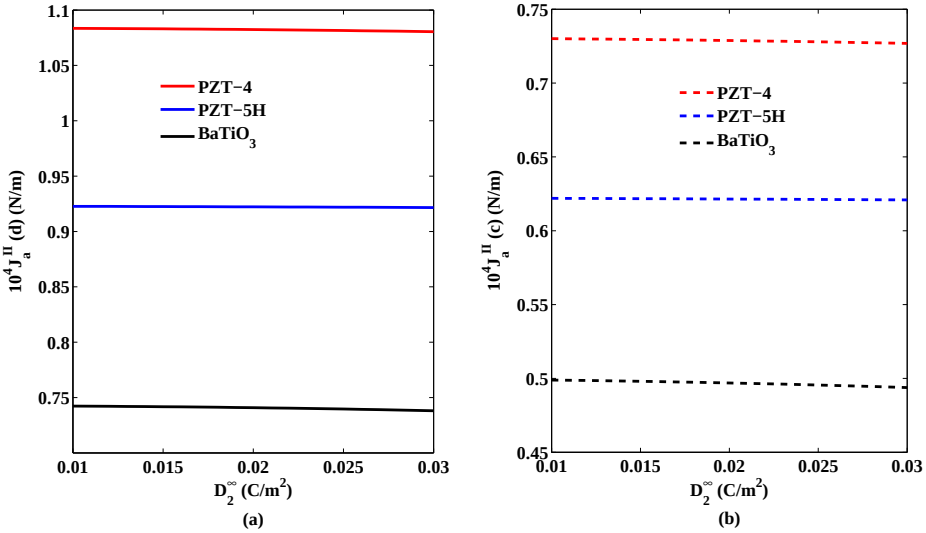

Figure 7.14: ERR versus D_2^∞ for PZT-4, PZT-5H and $BaTiO_3$ ceramics

Figs. 7.14(a, b) show the ERR at the inner and outer tips of the crack versus prescribed electrical load for different ceramics. It is observed that ERR is less for $BaTiO_3$ ceramic and maximum for PZT-4 ceramic. Also the ERR shows a slow reduction rate nevertheless it gives a clue for correctly choosing of the ceramic for appropriate purpose.

7.2.3 Case III: When saturation and yield zones are equal ($|c_1| = |a|$ and $|b| = |d_1|$)

The boundary conditions form (i) to (iv) remain the same as in Case I and boundary condition (v) is replaced by following condition (vii)

(vii) $\mathbf{\Phi}_{,1}^{III+}(x_1) = \mathbf{\Phi}_{,1}^{III-}(x_1) = -\mathbf{V}^{III}, \quad \text{for } d < |x_1| < c,$

where, $\mathbf{V}^{III} = [0, \sigma_{22}^\infty, 0, D_2^\infty]^T$, and superscript III represents that the quantity refers to Case III.

Schematically the configuration of the problem is depicted in Fig. 7.15.

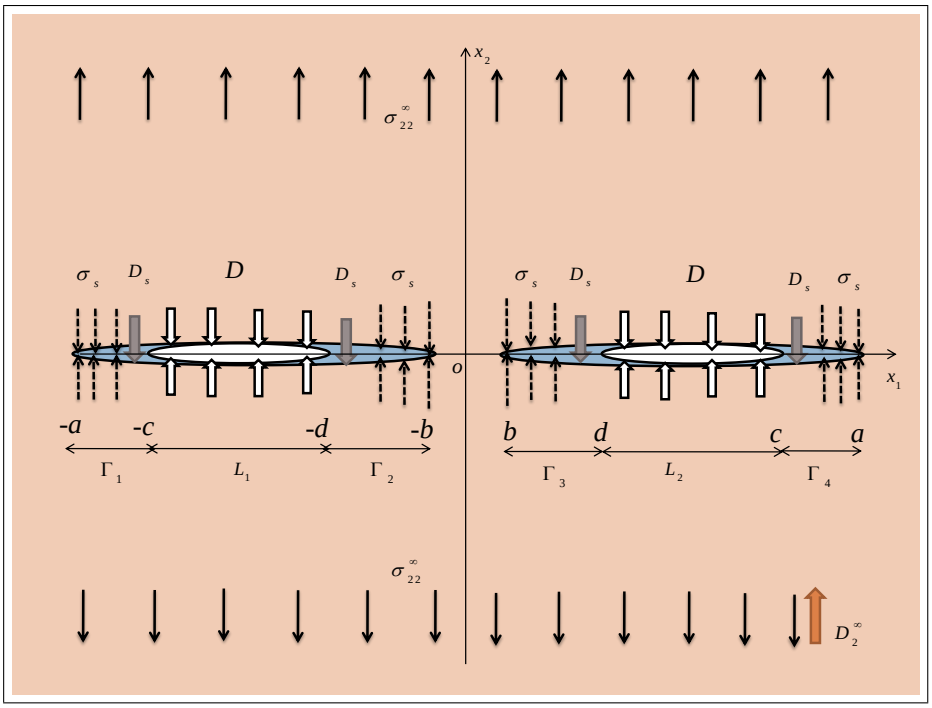

Figure 7.15: Schematic representation of configuration of the problem for Case III, when saturation and yield zones are equal

7.2.3.1 Solution of the Problem

Analogous to Case I the boundary condition (vii) for this case yield the following two dual Hilbert problems for potentials $\Omega_2^{III}(z)$ and $\Omega_4^{III}(z)$

$$\Lambda_{22}[\Omega_2^{III+}(x_1)+\Omega_2^{III-}(x_1)]+\Lambda_{24}[\Omega_4^{III+}(x_1)+\Omega_4^{III-}(x_1)]=-\sigma_{22}^{\infty},\ d<|x_1|<c, \tag{7.2.50}$$

$$\Lambda_{42}[\Omega_2^{III+}(x_1)+\Omega_2^{III-}(x_1)]+\Lambda_{44}[\Omega_4^{III+}(x_1)+\Omega_4^{III-}(x_1)]=D-D_2^{\infty},\ d<|x_1|<c. \tag{7.2.51}$$

The solution of which, carrying out the similar calculation as in Case I, may be written as

$$\begin{aligned}\Omega_2^{III}(z)=&-\frac{\Lambda_{44}\sigma_s+\Lambda_{24}(D-D_s)}{\pi\Sigma X_2(z)}\left\{(z^2-a^2\lambda_2^2)\left(\frac{\pi}{2}-\vartheta_d+\vartheta_c\right)+R_2\right\}\\&+\frac{\Lambda_{44}\sigma_{22}^{\infty}+\Lambda_{24}(D-D_2^{\infty})}{2\Sigma}\left\{\frac{z^2-a^2\lambda_2^2}{X_2(z)}-1\right\}\\&+\frac{\Lambda_{44}\sigma_s+\Lambda_{24}(D-D_s)}{\pi\Sigma}\left(\frac{\pi}{2}-\upsilon_d+\upsilon_c\right),\end{aligned} \tag{7.2.52}$$

$$\Omega_4^{III}(z) = \frac{\Lambda_{42}\sigma_s + \Lambda_{22}(D - D_s)}{\pi\Sigma X_2(z)} \left\{ (z^2 - a^2\lambda_2^2) \left(\frac{\pi}{2} - \vartheta_d + \vartheta_c \right) + R_2 \right\} - \frac{\Lambda_{42}\sigma_{22}^{\infty} + \Lambda_{22}(D - D_2^{\infty})}{2\Sigma} \left\{ \frac{z^2 - a^2\lambda_2^2}{X_2(z)} - 1 \right\} - \frac{\Lambda_{42}\sigma_s + \Lambda_{22}(D - D_s)}{\pi\Sigma} \left(\frac{\pi}{2} - \upsilon_d + \upsilon_c \right). \tag{7.2.53}$$

7.2.3.2 Applications

Expressions for crack opening displacement, crack opening potential drop, energy release rate and developed zones are derived in this section.

Zone size

As in Case II, the stress and electric displacement for this case are obtained using

$$\mathbf{\Phi}_{,1}^{III}(x_1) = \mathbf{B}\mathbf{F}^{III+}(x_1) + \mathbf{B}\mathbf{F}^{III-}(x_1) = \mathbf{\Lambda}[\mathbf{\Omega}^{III+}(x_1) + \mathbf{\Omega}^{III-}(x_1)],\ |x_1| > a. \tag{7.2.54}$$

Comparing second and fourth components and substituting $\Omega_2^{III}(z)$ and $\Omega_4^{III}(z)$ from Equations (7.2.52 and 7.2.53) and simplifying one obtains

$$\sigma_{22}^{III}(x_1) = \frac{2\sigma_s}{\pi} \left(\frac{\pi}{2} - \upsilon_d + \upsilon_c \right) + \sigma_{22}^{\infty} \left\{ \frac{x_1^2 - a^2\lambda_2^2}{X_2(x_1)} - 1 \right\} - \frac{2\sigma_s}{\pi X_2(x_1)} \left\{ (x_1^2 - a^2\lambda_2^2) \left(\frac{\pi}{2} - \vartheta_d + \vartheta_c \right) + R_2 \right\}, \tag{7.2.55}$$

$$D_2^{III}(x_1) = -\frac{2(D - D_s)}{\pi} \left(\frac{\pi}{2} - \upsilon_d + \upsilon_c \right) - (D - D_2^{\infty}) \left\{ \frac{x_1^2 - a^2\lambda_2^2}{X_2(x_1)} - 1 \right\} + \frac{2(D - D_s)}{\pi X_2(x_1)} \left\{ (x_1^2 - a^2\lambda_2^2) \left(\frac{\pi}{2} - \vartheta_d + \vartheta_c \right) + R_2 \right\}. \tag{7.2.56}$$

Applying Dugdale's hypothesis of stresses and electric displacement to remain finite at the tips $x_1 = b$ and $x_1 = a$ of the zones, one obtains non-linear equations to determine b and a from

$$\left(\frac{b^2}{a^2} - \lambda_2^2 \right) \left(\frac{\pi}{2} R - \frac{\pi}{2} + \vartheta_d - \vartheta_c \right) - \frac{R_2}{a^2} = 0, \tag{7.2.57}$$

$$\left(1 - \lambda_2^2\right) \left(\frac{\pi}{2} R - \frac{\pi}{2} + \vartheta_d - \vartheta_c \right) - \frac{R_2}{a^2} = 0. \tag{7.2.58}$$

where, $R = \sigma_{22}^{\infty}/\sigma_s$ or $(D - D_2^{\infty})/(D - D_s)$. The zone lengths are then obtained from $(d - b)$ and $(a - c)$.

Crack opening displacement (COD)

The crack opening displacement for this case is determined using

$$i\Delta\mathbf{u}^{III}_{,1}(x_1) = \mathbf{\Lambda}[\mathbf{\Omega}^{III+}(x_1) - \mathbf{\Omega}^{III-}(x_1)]. \tag{7.2.59}$$

Comparing the second component of the above equation and substituting value of $\Omega^{III}_2(z)$ from Equation (7.2.52) one obtains COD at tips $x_1 = d$ and $x_1 = c$, as

$$\begin{aligned}\Delta u^{III}_2(d) =& -\frac{(\Lambda_{44}\sigma_s + \Lambda_{24}(D - D_s))}{\pi\Sigma}\left\{-d\ln(C) + 2F(\xi_d, k_2)\frac{R_2}{a} + G_1(d,c)\right\}\\ &-\frac{(\Lambda_{44}\sigma_s + \Lambda_{24}(D - D_s))}{\pi\Sigma}\left\{2a\left(\frac{\pi}{2} - \vartheta_d + \vartheta_c\right)R_8 + \frac{2b^2}{a}\sqrt{\frac{a^2-d^2}{d^2-b^2}}R_7\right\}\\ &+\frac{a(\Lambda_{44}\sigma^\infty_{22} + \Lambda_{24}(D - D^\infty_2))}{\Sigma}R_8,\end{aligned} \tag{7.2.60}$$

$$\begin{aligned}\Delta u^{III}_2(c) =& \frac{(\Lambda_{44}\sigma_s + \Lambda_{24}(D - D_s))}{\pi\Sigma}\left\{-c\ln(D) + H_1(c,d) + 2F(\vartheta_c, k_2)\frac{R_2}{a}\right\}\\ &+\frac{(\Lambda_{44}\sigma_s + \Lambda_{24}(D - D_s))}{\pi\Sigma}\left\{2a\left(\frac{\pi}{2} - \vartheta_d + \vartheta_c\right)R_{10} + \frac{2}{a}\sqrt{\frac{c^2-b^2}{a^2-c^2}}R_9\right\}\\ &-\frac{a(\Lambda_{44}\sigma^\infty_{22} + \Lambda_{24}(D - D^\infty_2))}{\Sigma}R_{10}.\end{aligned} \tag{7.2.61}$$

Crack opening potential drop (COP)

COP at the tips $x_1 = d$ and $x_1 = c$ is obtained, comparing fourth component of Equation (7.2.59) and substituting value of $\Omega^{III}_4(x_1)$ from Equation (7.2.53) and simplifying, as

$$\begin{aligned}\Delta u^{III}_4(d) =& \frac{(\Lambda_{42}\sigma_s + \Lambda_{22}(D - D_s))}{\pi\Sigma}\left\{-d\ln(C) + 2F(\xi_d, k_2)\frac{R_2}{a} + G_1(d,c)\right\}\\ &+\frac{(\Lambda_{42}\sigma_s + \Lambda_{22}(D - D_s))}{\pi\Sigma}\left\{2a\left(\frac{\pi}{2} - \vartheta_d + \vartheta_c\right)R_8 + \frac{2b^2}{a}\sqrt{\frac{a^2-d^2}{d^2-b^2}}R_7\right\}\\ &-\frac{a(\Lambda_{42}\sigma^\infty_{22} + \Lambda_{22}(D - D^\infty_2))}{\Sigma}R_8,\end{aligned} \tag{7.2.62}$$

$$\begin{aligned}\Delta u^{III}_4(c) =& -\frac{(\Lambda_{42}\sigma_s + \Lambda_{22}(D - D_s))}{\pi\Sigma}\left\{-c\ln(D) + H_1(c,d) + 2F(\vartheta_c, k_2)\frac{R_2}{a}\right\}\\ &-\frac{(\Lambda_{42}\sigma_s + \Lambda_{22}(D - D_s))}{\pi\Sigma}\left\{2a\left(\frac{\pi}{2} - \vartheta_d + \vartheta_c\right)R_{10} + \frac{2}{a}\sqrt{\frac{c^2-b^2}{a^2-c^2}}R_9\right\}\\ &+\frac{a(\Lambda_{42}\sigma^\infty_{22} + \Lambda_{22}(D - D^\infty_2))}{\Sigma}R_{10}.\end{aligned} \tag{7.2.63}$$

Energy release rate (ERR)

Energy release rate at the interior and exterior tips of the crack is calculated using

$$J_a^{III}(d) = \sigma_s \Delta u_2^{III}(d) + D_s \Delta u_4^{III}(d), \tag{7.2.64}$$

$$J_a^{III}(c) = \sigma_s \Delta u_2^{III}(c) + D_s \Delta u_4^{III}(c). \tag{7.2.65}$$

7.2.3.3 Case III: Results and Discussions

A similar study as in the Case I and Case II is carried out for this Case too.

The COD profile over the interior and exterior yield zones versus zone length to crack length ratio is shown in Figs. 7.16(a, b) for a fixed inter crack distance. The crack opening is reduced as we move from impermeable case to permeable case.

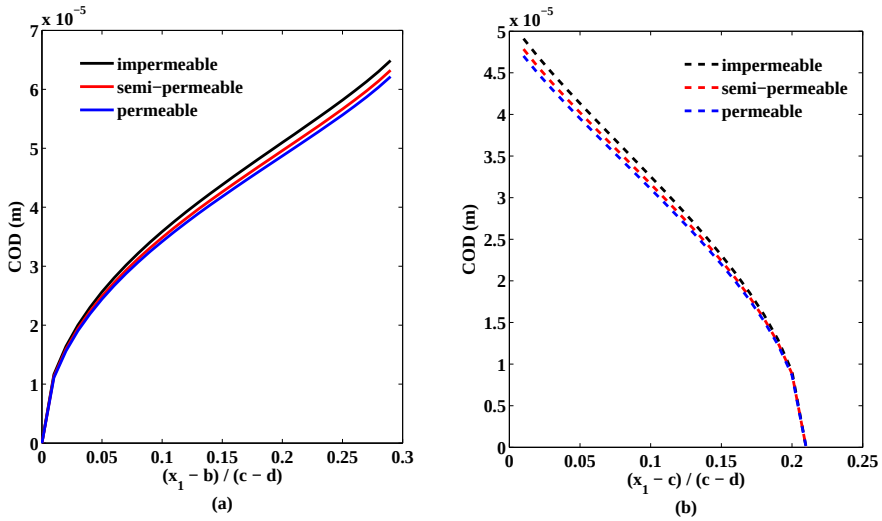

Figure 7.16: COD profile over the interior and exterior yield zones for different electric boundary conditions

Figs. 7.17(a, b) depict the variation of COD at the interior and exterior tips of the cracks versus D_2^{∞} for different prescribed mechanical loads. It is noted that COD is increased as prescribed electrical load increases and it is more at interior crack tip as compared to that at exterior crack tip, as expected. Also COD at both the crack tips increases as mechanical load increases.

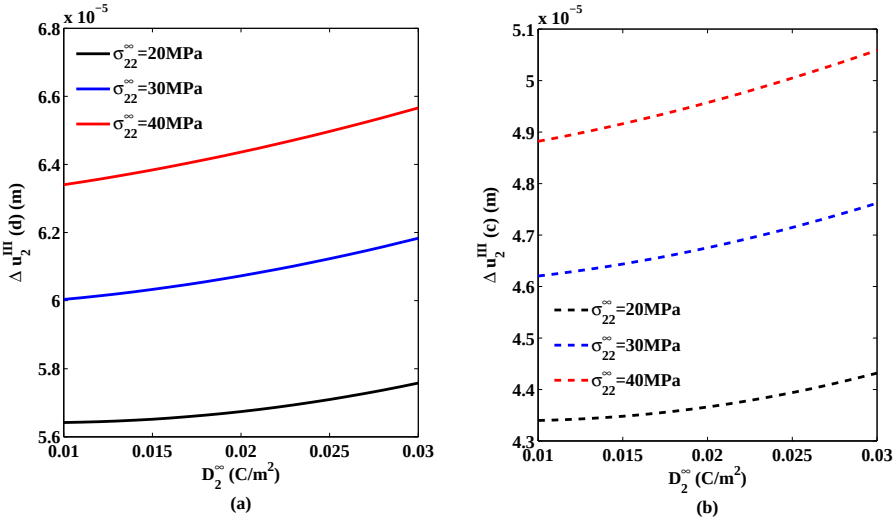

Figure 7.17: COD versus D_2^{∞} for different mechanical loads

Figs. 7.18(a, b) depict the COP drop over interior and exterior saturation zones. It is noted that COP drop is almost 1.5 times more at the interior zone as compared to that at exterior zone. The COP drop decreases as one goes from impermeable to permeable crack.

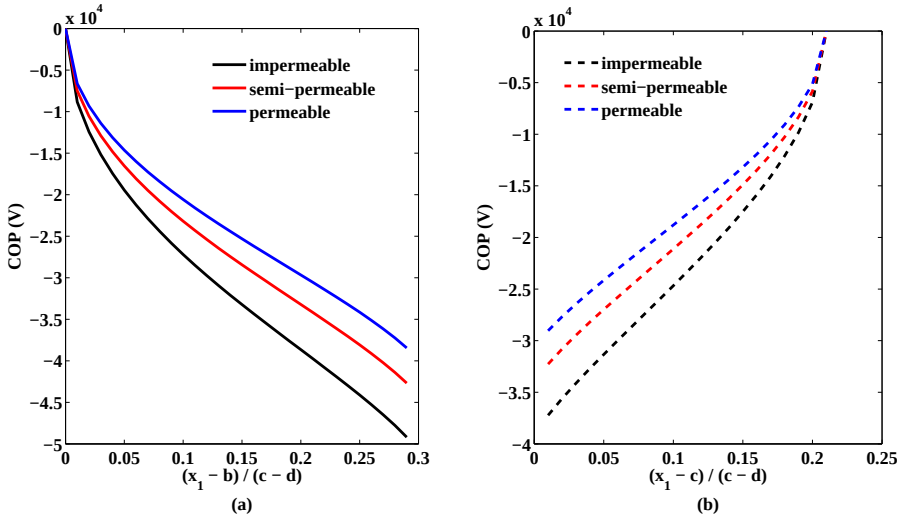

Figure 7.18: COP drop over the interior and exterior saturation zones for different electric boundary conditions

Variation of COP at the inner and outer crack tips of the cracks versus electric displacement for different mechanical loads is shown in Figs. 7.19(a and b). COP decreases with increase in mechanical loading although COP increases with increase in electric loading, as expected.

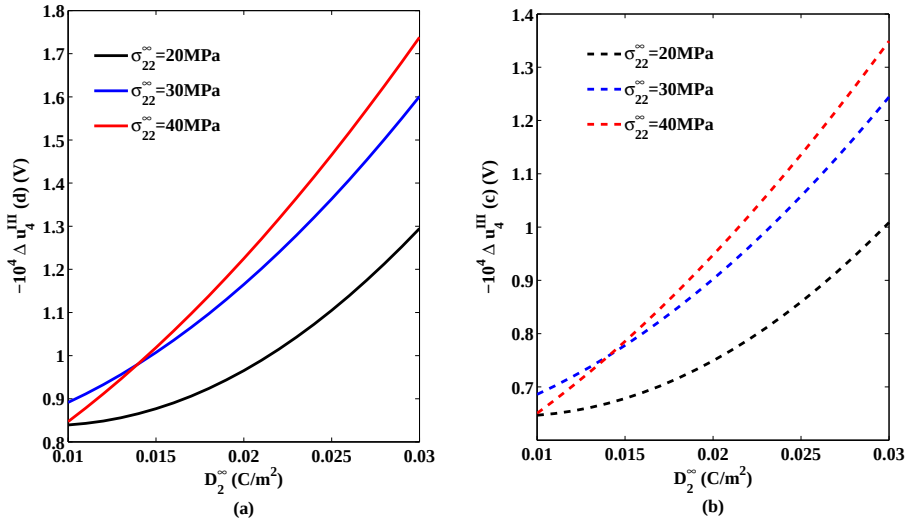

Figure 7.19: COP versus D_2^{∞} for different mechanical loads

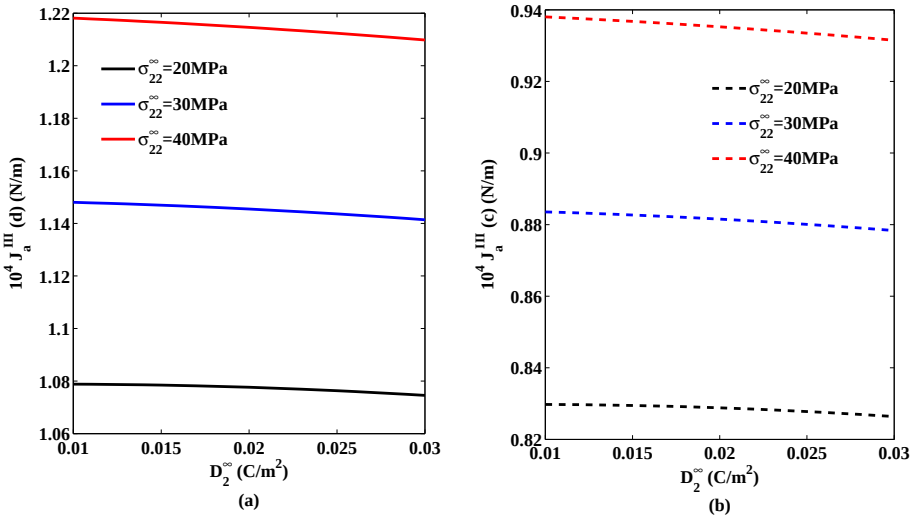

Figure 7.20: ERR versus D_2^{∞} for different mechanical loads

Energy release rate at interior and exterior tips versus prescribed electric load is plotted in Figs. 7.20(a, b). It is observed that energy release rate decreases as prescribed electric load is increased. Also on increasing mechanical loading higher energy release rate is observed.

Figs. 7.21(a, b) depict the energy release rate variation vis-a-vis prescribed electric load for PZT-4, PZT-5H and $BaTiO_3$ ceramics. It is observed that $BaTiO_3$ ceramic has minimum energy release rate and it is maximum for PZT-4 ceramic.

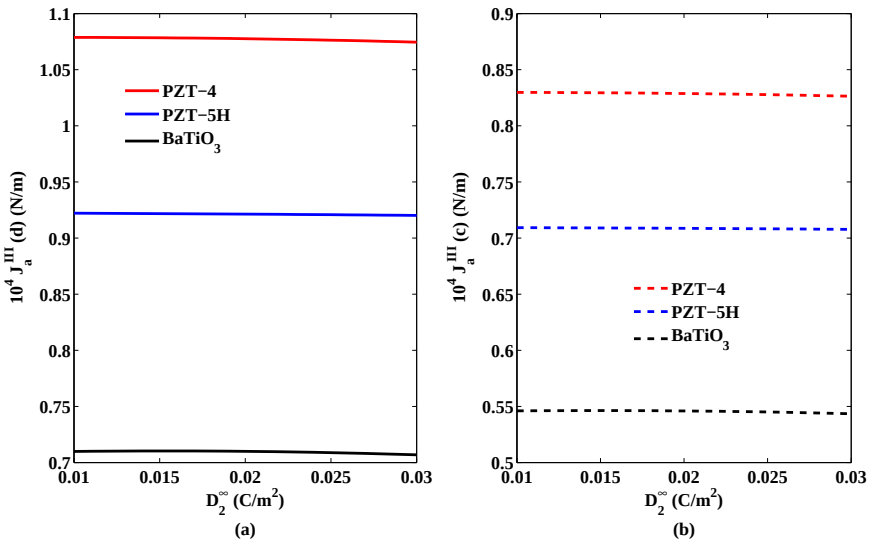

Figure 7.21: ERR versus D_2^∞ for PZT-4, PZT-5H and $BaTiO_3$

7.3 Conclusions

- A strip-electro-mechanical yield model is proposed for a piezoelectric plate weakened by two semi-permeable collinear straight cracks. Three cases are considered when saturation zones are bigger/smaller or equal to developed yield zones.

- Interesting results are seen that the COD is maximum for case when developed zones are equal and little less for the case when saturation zones are smaller and least for the case when saturation zone are bigger. This indicates that crack will open maximum for equal zones and least for case of bigger saturation zone.

- An interesting phenomenon is observed for COP for case when saturation zones are bigger, the COP shows a kink in COP drop at the distance where tip of strip-yield zone crossed. This occurs at both interior and exterior zones.

- ERR for poled piezoceramics PZT-4, PZT-5H and $BaTiO_3$, drawn for prescribed electric displacement load may assist for the correctly choosing of ceramic for specific job. Also less ERR in Case I (when saturation zones are bigger than developed yield zones) affirms the less opening of crack. In Case

III (when saturation and yield zones are equal) ERR is higher as compared to that in Cases I and II, so crack opens more in this case.

Chapter 8

A Study on Influence of Poling Direction for Semi-permeable Strip-electro-mechanical yield Model

It is well-known that a wide range of poled piezoelectric ceramics retain their aligned electric dipole field in the material microstructure below Curie temperature. This electric poling direction affects the material properties and fracture behavior. Numerous studies have demonstrated that crack orientation as well as electric poling direction greatly influences crack growth, which can be enhanced or retarded for mode I, II and III cracks [27, 83, 110–112] in 2D piezoelectric media. Simultaneously, the boundary condition, such as impermeable, permeable, and semi-permeable, on the crack faces also impact the solution as observed in Chapter 3.

Therefore in this chapter, the influence of change in poling direction on a piezoelectric medium cut along two equal collinear straight semi-permeable cracks under mode-I type of electrical and mechanical loads is studied. The cracks yield both electrically and mechanically ahead of the tips of the cracks. Three different situations are investigated when developed electrical saturation zones are bigger/smaller or equal to the developed mechanical yield zones.

An illustrative numerical example is presented to study the effect of change in poling direction on crack opening displacement, crack opening potential drop and energy release rate.

This chapter is published in Acta Mechanica (Springer publication), Vol. 225 (2014), pp. 109-129.

8.1 Fundamental Formulation and Solution Methodology

For a transversely isotropic medium, occupying $ox_1x_2x_3$ orthogonal coordinate system, with x_1ox_3 being considered as plane of isotropy, the constitutive equations may be written as

$$\Xi_{ij} = C_{ijkl}u_{k,j}, \tag{8.1.1}$$

where,

$$\Xi_{ij} = \begin{cases} \sigma_{ij}, & i,j = 1,2,3\ , \\ D_j, & i = 4, \end{cases}$$

and $[C_{ijkl}]$ material constant matrix. And σ_{ij}, D_j, respectively denote stress and electric displacement. $\mathbf{u}_k = [u_1, u_2, u_3, u_4 = \phi]^T$, $u_i (i = 1,2,3)$ denote mechanical displacement and ϕ is the electric potential. Comma in subscript denotes the partial differentiation with respect to the argument following it. Superscript T denotes transpose of the matrix.

For the case when poling direction is oriented at an angle 'θ' with x_1-axis, the constitutive equations can be expressed as

$$\Xi_{ij} = c_{ijkl}u_{k,l}, \tag{8.1.2}$$

where, $c_{ijkl} = \mathbf{m}C_{ijkl}\mathbf{m}^T$, $\mathbf{m} = \begin{pmatrix} \mathbf{m}_1 & \mathbf{0} \\ \mathbf{0} & \mathbf{m}_2 \end{pmatrix}$,

$$[C_{ijkl}] = \begin{pmatrix} c_{11} & c_{13} & c_{12} & 0 & 0 & 0 & 0 & e_{31} & 0 \\ c_{13} & c_{33} & c_{13} & 0 & 0 & 0 & 0 & e_{33} & 0 \\ c_{12} & c_{13} & c_{11} & 0 & 0 & 0 & 0 & e_{31} & 0 \\ 0 & 0 & 0 & c_{44} & 0 & 0 & 0 & 0 & e_{15} \\ 0 & 0 & 0 & 0 & c_{66} & 0 & 0 & 0 & 0 \\ 0 & 0 & 0 & 0 & 0 & c_{44} & e_{15} & 0 & 0 \\ 0 & 0 & 0 & 0 & 0 & e_{15} & -\kappa_{11} & 0 & 0 \\ e_{31} & e_{33} & e_{31} & 0 & 0 & 0 & 0 & -\kappa_{33} & 0 \\ 0 & 0 & 0 & e_{15} & 0 & 0 & 0 & 0 & -\kappa_{11} \end{pmatrix},$$

$$\mathbf{m}_1 = \begin{pmatrix} \sin^2\theta & \cos^2\theta & 0 & 0 & 0 & \sin 2\theta \\ \cos^2\theta & \sin^2\theta & 0 & 0 & 0 & -\sin 2\theta \\ 0 & 0 & 1 & 0 & 0 & 0 \\ 0 & 0 & 0 & \sin\theta & -\cos\theta & 0 \\ 0 & 0 & 0 & \cos\theta & \sin\theta & 0 \\ -\frac{1}{2}\sin 2\theta & \frac{1}{2}\sin 2\theta & 0 & 0 & 0 & -\cos 2\theta \end{pmatrix}, \quad \mathbf{m}_2 = \begin{pmatrix} \sin\theta & \cos\theta & 0 \\ -\cos\theta & \sin\theta & 0 \\ 0 & 0 & 1 \end{pmatrix}.$$

Continuity equations for stress and electric displacement in absence of body force and electric charge may be expressed as

$$\sigma_{ij,j} = 0,\ D_{i,i} = 0,\ i,j = 1,2,3\ (\text{or } x_1, x_2, x_3). \tag{8.1.3}$$

The gradient equations are given as

$$\varepsilon_{ij} = \frac{1}{2}(u_{i,j} + u_{j,i}), \quad E_i = -\phi_i, \tag{8.1.4}$$

The general solution satisfying Equations (8.1.2, 8.1.3 and 8.1.4) according to Stroh formalism, may be written as given by Equations (2.7.6 and 2.7.7).

8.2 Statement of the Problem

A transversely isotropic piezoelectric plate occupies entire x_1ox_2 plane. The poling direction makes an angle 'θ' with x_1-axis. The plate is cut along two equal collinear hairline straight semi-permeable cracks L_1 and L_2. These occupy the respective intervals $[-c,-d]$ and $[d,c]$ on x_1-axis. The crack rims are free of any mechanical load and electrically semi-permeable. The remote boundary of the plate is subjected to in-plane normal, uniform constant tension $\sigma_{22} = \sigma_{22}^{\infty}$ and electrical displacement $D_2 = D_2^{\infty}$, consequently cracks open in self-similar fashion forming a strip-yield and a saturation zone ahead of each tip of the cracks. The saturation zones develop at the cracks tips $-c$, $-d$, d and c, occupy the respective intervals $[-a,-c]$, $[-d,-b]$, $[b,d]$ and $[c,a]$, on x_1-axis. And the strip-yield zone developed at these tips occupy the intervals $[-c_1,-c]$, $[-d,-d_1]$, $[d_1,d]$ and $[c,c_1]$, respectively. To stop the crack from further opening the rims of the developed yield zones are subjected to uniform constant normal cohesive yield point stress $\sigma_{22} = \sigma_s$ and saturation zones rims are

subjected to saturation limit in-plane electric displacement $D_2 = D_s$. Three cases are considered when

Case I: saturation zones are bigger than developed yield zones,

Case II: saturation zones are smaller than developed yield zones,

Case III: saturation and yield zones are equal.

8.3 Mathematical Model and Solution of the Problem

Mathematically the boundary conditions of the problem may be written as

(i) $\sigma_{22}^{+} = \sigma_{22}^{-} = 0, \quad D_2 = D, \qquad \text{on } L = \bigcup_{i=1}^{2} L_i,$

(ii) $\sigma_{22} = \sigma_{22}^{\infty}, \quad D_2 = D_2^{\infty}, \qquad \text{for } |x_2| \to \infty,$

(iii) $\sigma_{22}^{+} = \sigma_{22}^{-} = \sigma_s - \sigma_{22}^{\infty}, \qquad \text{for } \Gamma' = \bigcup_{i=1}^{4} \Gamma_i',$

(iv) $D_2^{+} = D_2^{-} = D_s - D_2^{\infty}, \qquad \text{for } \Gamma = \bigcup_{i=1}^{4} \Gamma_i,$

(v) $\mathbf{\Phi}_{,1}^{j+} = \mathbf{\Phi}_{,1}^{j-} = -\mathbf{V}^j, \qquad \text{for } d < |x_1| < c,$

where, D is the electric flux through the crack regions $(-c, -d)$ and (d, c) determined from the Equation (2.5.3) and $\mathbf{V}^j = [0, \sigma_{22}^{\infty}, 0, D_2^{\infty}]^T$, where superscript j=I, II, III denote that quantity refers to the Case I, Case II and Case III, respectively.
The above boundary conditions and following Hilbert problem give mathematical model.
The continuity of $\mathbf{\Phi}_{,1}$ (defined by Equation (2.7.7)) on x_1-axis yields

$$[\mathbf{B}\mathbf{F}^j(x_1) - \overline{\mathbf{B}}\overline{\mathbf{F}^j}(x_1)]^{+} - [\mathbf{B}\mathbf{F}^j(x_1) - \overline{\mathbf{B}}\overline{\mathbf{F}^j}(x_1)]^{-} = 0. \tag{8.3.1}$$

The solution of which may directly be written using Equation (2.7.31) as

$$\mathbf{B}\mathbf{F}^j(z) = \overline{\mathbf{B}}\overline{\mathbf{F}^j}(z) = \mathbf{h}^j(z) \qquad \text{(say)} \tag{8.3.2}$$

Using principal of superposition, boundary conditions (i) and (v) together with Equations (8.3.2 and 2.7.7) leads to following vector Hilbert problem

$$\mathbf{h}^{j+}(x_1) + \mathbf{h}^{j-}(x_1) = \mathbf{V}^0 - \mathbf{V}^j, \;\; d < |x_1| < c. \tag{8.3.3}$$

where $\mathbf{V}^0 = [0, 0, 0, D]^T$.

Introducing a complex function vector $\mathbf{\Omega}^j(z) = [\Omega_1^j(z), \Omega_2^j(z), \Omega_3^j(z), \Omega_4^j(z)]^T$ as

$$\mathbf{\Omega}^j(z) = \mathbf{H}^R \mathbf{B} \mathbf{F}^j(z), \tag{8.3.4}$$

which on using Equation (8.3.2) gives the relation

$$\mathbf{h}^j(z) = \mathbf{\Lambda} \mathbf{\Omega}^j(z), \tag{8.3.5}$$

where $\mathbf{\Lambda} = [\mathbf{H}^R]^{-1}, \;\; \mathbf{H}^R = 2Re\mathbf{Y}, \;\; \mathbf{Y} = i\mathbf{A}\mathbf{B}^{-1}$.

Consequently Equation's (8.3.3) may be written in component form for $\Omega_2^i(z)$ and $\Omega_4^i(z)$, yield following scalar Hilbert problem

$$\Lambda_{22}[\Omega_2^{j+}(x_1) + \Omega_2^{j-}(x_1)] + \Lambda_{24}[\Omega_4^{j+}(x_1) + \Omega_4^{j-}(x_1)] = -\sigma_{22}^{\infty}, \; d < |x_1| < c, \tag{8.3.6}$$

$$\Lambda_{42}[\Omega_2^{j+}(x_1) + \Omega_2^{j-}(x_1)] + \Lambda_{44}[\Omega_4^{j+}(x_1) + \Omega_4^{j-}(x_1)] = D - D_2^{\infty}, \; d < |x_1| < c. \tag{8.3.7}$$

8.3.1 Solution for Case I: When saturation zones are bigger than developed yield zones ($|b| < |d_1|$ and $|a| > |c_1|$)

Schematically the configuration of the problem is depicted in Fig. 8.1.

Eliminating $\Omega_4^{I+}(x_1) + \Omega_4^{I-}(x_1)$ from Equations (8.3.6 and 8.3.7) and then solved using Equation (2.7.30) together with boundary condition (iii) one obtains

$$\Omega_2^I(z) = \frac{\Lambda_{44}\sigma_s + (D - D_s)\Lambda_{24}}{2\pi i X_1(z)\Sigma} \int_{\Gamma'} \frac{X_1(t)}{t - z} dt + \frac{P_1(z)}{2X_1(z)} - \frac{1}{2} \frac{\Lambda_{44}\sigma_{22}^{\infty} + (D - D_2^{\infty})\Lambda_{24}}{\Lambda_{22}\Lambda_{44} - \Lambda_{24}\Lambda_{42}}, \tag{8.3.8}$$

where

$$P_1(z) = C_0 z^2 + C_1 z + C_2, \; X_1(z) = \sqrt{(z^2 - d_1^2)(z^2 - c_1^2)} \text{ and } \Sigma = \Lambda_{22}\Lambda_{44} - \Lambda_{24}\Lambda_{42}.$$

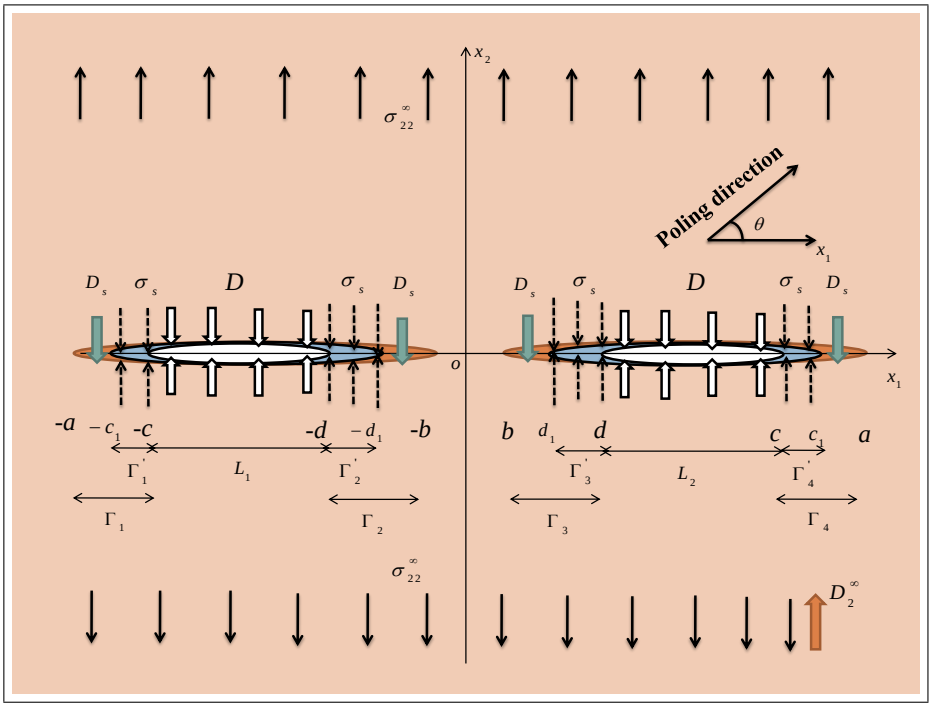

Figure 8.1: Schematic representation of the configuration of problem for Case I, when saturation zones are bigger than developed yield zones

Constant

$$C_0 = \frac{\Lambda_{44}\sigma_{22}^{\infty} + (D - D_2^{\infty})\Lambda_{24}}{\Lambda_{22}\Lambda_{44} - \Lambda_{24}\Lambda_{42}}$$

is determined using condition $\lim_{z\to\infty} \Omega_2^I(z) = 0$. Also C_1 and C_2 are determined from the condition of single-valuedness of displacement around cracks i.e.

$$\int_{C_i'} [\Omega_2^{I+}(x_1) - \Omega_2^{I-}(x_1)]dx_1 = 0,\ i = 1, 2,\ C_1' = [-c_1, -d_1],\ C_2' = [d_1, c_1]. \quad (8.3.9)$$

Finally, evaluating the integral in Equation (8.3.8) and substituting the values of constants C_0, C_1 and C_2, the required potential $\Omega_2^I(z)$, may be written as

$$\begin{aligned}\Omega_2^I(z) = &- \frac{\Lambda_{44}\sigma_s + \Lambda_{24}(D - D_s)}{\pi\Sigma X_1(z)} \left\{(z^2 - c_1^2\lambda_1^2)\left(\frac{\pi}{2} - \psi_d + \psi_c\right) + R_1\right\} \\ &+ \frac{1}{2}\frac{\Lambda_{44}\sigma_{22}^{\infty} + (D - D_2^{\infty})\Lambda_{24}}{\Lambda_{22}\Lambda_{44} - \Lambda_{24}\Lambda_{42}} \left\{\frac{z^2 - c_1^2\lambda_1^2}{X_1(z)} - 1\right\} \\ &+ \frac{\Lambda_{44}\sigma_s + \Lambda_{24}(D - D_s)}{\pi\Sigma}\left(\frac{\pi}{2} - \varphi_d + \varphi_c\right), \end{aligned} \quad (8.3.10)$$

where,

$$k_1^2 = \frac{c_1^2 - d_1^2}{c_1^2},\ \lambda_1^2 = E(k_1)/F(k_1),\ \sin^2\psi_d = \frac{c_1^2 - d^2}{c_1^2 - d_1^2},\ \sin^2\psi_c = \frac{c_1^2 - c^2}{c_1^2 - d_1^2},$$

$$\varphi_d = \tan^{-1}\sqrt{\frac{(d_1^2-z^2)(d^2-c_1^2)}{(c_1^2-z^2)(d_1^2-d^2)}},\ \varphi_c = \tan^{-1}\sqrt{\frac{(d_1^2-z^2)(c^2-c_1^2)}{(c_1^2-z^2)(d_1^2-c^2)}},$$
$$R_1 = dc_1\left\{E(\psi_d,k_1)-\lambda_1^2F(\psi_d,k_1)\right\} - cc_1\left\{E(\psi_c,k_1)-\lambda_1^2F(\psi_c,k_1)\right\}$$
$$- k_1^2c_1^2\left(\sin\psi_d\cos\psi_d - \sin\psi_c\cos\psi_c\right).$$

Analogously to determine $\Omega_4^I(z)$, Equation (8.3.7) is solved using the boundary condition (iv) and Equation (2.7.30), the solution may be written as

$$\Omega_4^I(z) = -\frac{D-D_s}{2\pi i\Lambda_{44}X_2(z)}\int_\Gamma \frac{X_2(t)}{t-z}dt + \frac{P_2(z)}{2\Lambda_{44}X_2(z)} + \frac{D-D_2^\infty}{2\Lambda_{44}} - \frac{\Lambda_{42}}{\Lambda_{44}}\Omega_2^I(z), \quad (8.3.11)$$

where $P_2(z) = A_0z^2 + A_1z + A_2$ and $X_2(z) = \sqrt{(z^2-a^2)(z^2-b^2)}$.
Again constant $A_0 = -D + D_2^\infty$ is determined using condition $\lim_{z\to\infty}\Omega_4^I(z) = 0$. Also A_1 and A_2 are determined from the condition of single-valuedness of displacement around cracks i.e.,

$$\int_{C_i''}[\Omega_4^{I+}(x_1) - \Omega_4^{I-}(x_1)]dx_1 = 0,\ i = 1,2,\ C_1'' = [-a,-b],\ C_2'' = [b,a]. \quad (8.3.12)$$

Finally, evaluating the integral in Equation (8.3.11) and substituting the values of constants A_0, A_1 and A_2, the required potential $\Omega_4^I(z)$, may be written as

$$\Omega_4^I(z) = -\frac{\Lambda_{42}}{\Lambda_{44}}\Omega_2^I(z) - \frac{(D-D_2^\infty)}{2\Lambda_{44}}\left\{\frac{z^2-a^2\lambda_2^2}{X_2(z)} - 1\right\} - \frac{(D-D_s)}{\pi\Lambda_{44}}\left(\frac{\pi}{2} - \upsilon_d + \upsilon_c\right)$$
$$+\frac{(D-D_s)}{\pi\Lambda_{44}X_2(z)}\left\{(z^2-a^2\lambda_2^2)\left(\frac{\pi}{2} - \vartheta_d + \vartheta_c\right) + R_2\right\}, \quad (8.3.13)$$

where,

$$k_2^2 = 1-(b/a)^2,\ \lambda_2^2 = E(k_2)/F(k_2),\ \sin^2\vartheta_d = \frac{a^2-d^2}{a^2-b^2},\ \sin^2\vartheta_c = \frac{a^2-c^2}{a^2-b^2},$$
$$\upsilon_d = \tan^{-1}\sqrt{\frac{(b^2-z^2)}{(a^2-z^2)}\frac{(a^2-d^2)}{(d^2-b^2)}},\ \upsilon_c = \tan^{-1}\sqrt{\frac{(b^2-z^2)}{(a^2-z^2)}\frac{(a^2-c^2)}{(c^2-b^2)}},$$
$$R_2 = da\left\{E(\vartheta_d,k_2) - \lambda_2^2F(\vartheta_d,k_2)\right\} - ca\left\{E(\vartheta_c,k_2) - \lambda_2^2F(\vartheta_c,k_2)\right\}$$
$$- a^2k_2^2\left(\sin\vartheta_d\cos\vartheta_d - \sin\vartheta_c\cos\vartheta_c\right).$$

8.3.1.1 Applications

Expressions for crack opening displacement, crack opening potential drop, energy release rate and developed zones are derived in this section.

Saturation zone

The electric displacement is determined using Equations (2.7.7 and 8.3.5) as

$$\mathbf{\Phi}^{I}_{,1}(x_1) = \mathbf{B}\mathbf{F}^{I+}(x_1) + \mathbf{B}\mathbf{F}^{I-}(x_1) = \mathbf{\Lambda}\mathbf{\Omega}^{I+}(x_1) + \mathbf{\Lambda}\mathbf{\Omega}^{I-}(x_1),\ |x_1| > a. \tag{8.3.14}$$

Taking the fourth component of above equation, we get

$$D_2^I(x_1) = \Lambda_{42}\left[\Omega_2^{I+}(x_1) + \Omega_2^{I-}(x_1)\right] + \Lambda_{44}\left[\Omega_4^{I+}(x_1) + \Omega_4^{I-}(x_1)\right]. \tag{8.3.15}$$

Substituting values of $\Omega_2^I(x_1)$ and $\Omega_4^I(x_1)$ from Equations (8.3.10 and 8.3.13) and simplifying one finally arrives at

$$\begin{aligned} D_2^I(x_1) = &-\frac{2(D-D_s)}{\pi}\left(\frac{\pi}{2} - \upsilon_d + \upsilon_c\right) - (D - D_2^\infty)\left\{\frac{x_1^2 - a^2\lambda_2^2}{X_2(x_1)} - 1\right\} \\ &+\frac{2(D-D_s)}{\pi X_2(x_1)}\left\{(x_1^2 - a^2\lambda_2^2)\left(\frac{\pi}{2} - \vartheta_d + \vartheta_c\right) + R_2\right\}. \end{aligned} \tag{8.3.16}$$

The saturation zones lengths are now obtained by extending Dugdale's hypothesis to the electric displacement to remain finite at every point of the plate. This leads to the determination of two non-linear equations

$$\left(\frac{b^2}{a^2} - \lambda_2^2\right)\left(\frac{\pi}{2}\frac{D - D_2^\infty}{D - D_s} - \frac{\pi}{2} + \vartheta_d - \vartheta_c\right) - \frac{R_2}{a^2} = 0, \tag{8.3.17}$$

$$\left(1 - \lambda_2^2\right)\left(\frac{\pi}{2}\frac{D - D_2^\infty}{D - D_s} - \frac{\pi}{2} + \vartheta_d - \vartheta_c\right) - \frac{R_2}{a^2} = 0, \tag{8.3.18}$$

to determine a and b. Hence saturation zone length at the tip c and d are calculated from $(a - c)$ and $(d - b)$, respectively.

Yield zone

To calculate yield zone length the required stress component is obtained by writing second component of Equation (8.3.14) as

$$\sigma_{22}^I(x_1) = \Lambda_{22}\left[\Omega_2^{I+}(x_1) + \Omega_2^{I-}(x_1)\right] + \Lambda_{24}\left[\Omega_4^{I+}(x_1) + \Omega_4^{I-}(x_1)\right]. \tag{8.3.19}$$

Substituting values from Equations (8.3.10 and 8.3.13) and simplifying, we get

$$\begin{aligned} \sigma_{22}^I(x_1) = &-\frac{2}{\pi X_1(x_1)}\left(\sigma_s + \frac{\Lambda_{24}}{\Lambda_{44}}(D - D_s)\right)\left\{(x_1^2 - c_1^2\lambda_1^2)\left(\frac{\pi}{2} - \psi_d + \psi_c\right) + R_1\right\} \\ &+\left(\sigma_{22}^\infty + \frac{\Lambda_{24}}{\Lambda_{44}}(D - D_2^\infty)\right)\left\{\frac{x_1^2 - c_1^2\lambda_1^2}{X_1(x_1)} - 1\right\} \\ &+\frac{2}{\pi}\left(\sigma_s + \frac{\Lambda_{24}}{\Lambda_{44}}(D - D_s)\right)\left(\frac{\pi}{2} - \varphi_d + \varphi_c\right). \end{aligned} \tag{8.3.20}$$

Using Dugdale's hypothesis that the stress remain finite at every point of the plate consequently at the points $x_1 = d_1$ and $x_1 = c_1$ we get the following transcendental equations

$$\left(\frac{d_1^2}{c_1^2} - \lambda_1^2\right)\left(\frac{\pi}{2}\frac{\Lambda_{44}\sigma_{22}^{\infty} + \Lambda_{24}(D - D_2^{\infty})}{\Lambda_{44}\sigma_s + \Lambda_{24}(D - D_s)} - \frac{\pi}{2} + \psi_d - \psi_c\right) - \frac{R_1}{c_1^2} = 0, \tag{8.3.21}$$

$$\left(1 - \lambda_1^2\right)\left(\frac{\pi}{2}\frac{\Lambda_{44}\sigma_{22}^{\infty} + \Lambda_{24}(D - D_2^{\infty})}{\Lambda_{44}\sigma_s + \Lambda_{24}(D - D_s)} - \frac{\pi}{2} + \psi_d - \psi_c\right) - \frac{R_1}{c_1^2} = 0. \tag{8.3.22}$$

These enable us to determine c_1 and d_1 for prescribed loads. The yield zone lengths are than calculated as $(c_1 - c)$ and $(d - d_1)$.

Crack opening displacement (COD)

The jump displacement vector $\Delta\mathbf{u}_{,1}^I$ is determined as

$$i\Delta\mathbf{u}_{,1}^I(x_1) = i[u_{1,1}^+ - u_{1,1}^-, u_{2,1}^+ - u_{2,1}^-, u_{3,1}^+ - u_{3,1}^-, E_1^- - E_1^+]^T. \tag{8.3.23}$$

The jump displacement component Δu_2^I at the crack tips d and c are obtained by remembering that $\Delta u_2^I = 0$ at the tips $x_1 = \pm d_1, \pm c_1$,

at the inner crack tip $x_1 = d$

$$\begin{aligned}\Delta u_2^I(d) = &- \frac{\Lambda_{44}\sigma_s + \Lambda_{24}(D - D_s)}{\pi\Sigma}\left\{\frac{2d_1^2}{c_1}\sqrt{\frac{c_1^2 - d^2}{d^2 - d_1^2}}R_3 - d\ln(A) + 2F(\tau_d, k_1)\frac{R_1}{c_1}\right\} \\ &- \frac{\Lambda_{44}\sigma_s + \Lambda_{24}(D - D_s)}{\pi\Sigma}\left\{G(d,c) + 2c_1\left(\frac{\pi}{2} - \psi_d + \psi_c\right)R_4\right\} \\ &+ \frac{c_1}{\Sigma}(\Lambda_{44}\sigma_{22}^{\infty} + \Lambda_{24}(D - D_2^{\infty}))R_4,\end{aligned} \tag{8.3.24}$$

at the outer crack tip $x_1 = c$

$$\begin{aligned}\Delta u_2^I(c) = &\frac{\Lambda_{44}\sigma_s + \Lambda_{24}(D - D_s)}{\pi\Sigma}\left\{2c_1\left(\frac{\pi}{2} - \psi_d + \psi_c\right)R_5 + H(c,d) - c\ln(B)\right\} \\ &+ \frac{\Lambda_{44}\sigma_s + \Lambda_{24}(D - D_s)}{\pi\Sigma}\left\{2F(\psi_c, k_1)\frac{R_1}{c_1} + \frac{2}{c_1}\sqrt{\frac{c^2 - d_1^2}{c_1^2 - c^2}}R_6\right\} \\ &- \frac{c_1}{\Sigma}(\Lambda_{44}\sigma_{22}^{\infty} + \Lambda_{24}(D - D_2^{\infty}))R_5,\end{aligned} \tag{8.3.25}$$

where,

$$\ln(A) = \ln\left(\frac{c_1^2 - d^2}{c_1^2 - d_1^2} + \frac{c_1^2(d_1^2 - d^2)}{d^2(c_1^2 - d_1^2)}\right),\ \ln(B) = \ln\left(\frac{(c_1^2 - c^2)(c^2 - d_1^2)}{c^2(c_1^2 - d_1^2)} + 1\right),$$

$$\sin^2\tau_d = c_1^2(d^2 - d_1^2)/\left(d^2(c_1^2 - d_1^2)\right),\ R_3 = \left(F(\tau_d, k_1) - II(\tau_d, \frac{d^2 - d_1^2}{d^2}, k_1)\right),$$

$$R_4 = \left(E(\tau_d, k_1) - \frac{k_1^2 \sin\tau_d \cos\tau_d}{\sqrt{1 - k_1^2 \sin^2\tau_d}} - \lambda_1^2 F(\tau_d, k_1)\right),$$

$$R_5 = \left(E(\psi_c, k_1) - \lambda_1^2 F(\psi_c, k_1)\right),\ R_6 = \left(c_1^2 F(\psi_c, k_1) - c^2 II(\psi_c, \frac{c_1^2 - c^2}{c_1^2}, k_1)\right),$$

$$G(d,c) = d\ln\left(\frac{\sqrt{(d^2 - d_1^2)(c_1^2 - c^2)} + \sqrt{(c_1^2 - d^2)(c^2 - d_1^2)}}{\sqrt{(d^2 - d_1^2)(c_1^2 - c^2)} - \sqrt{(c_1^2 - d^2)(c^2 - d_1^2)}}\right)$$
$$- \frac{2d_1^2}{c_1}\sqrt{\frac{c_1^2 - c^2}{c^2 - d_1^2}} II(\tau_d, \frac{c^2 k_1^2}{c^2 - d_1^2}, k_1),$$

$$H(c,d) = c\ln\left(\frac{\sqrt{(c^2 - d_1^2)(c_1^2 - d^2)} + \sqrt{(c_1^2 - c^2)(d^2 - d_1^2)}}{\sqrt{(c^2 - d_1^2)(c_1^2 - d^2)} - \sqrt{(c_1^2 - c^2)(d^2 - d_1^2)}}\right)$$
$$- \frac{2}{c_1}\sqrt{(d^2 - d_1^2)(c_1^2 - d^2)}\left(F(\psi_c, k_1) + \frac{d^2}{c_1^2 - d^2} II(\psi_c, \frac{c_1^2 - d_1^2}{c_1^2 - d^2}, k_1)\right).$$

Crack opening potential drop (COP)

COP is calculated by taking fourth component from Equation (8.3.23) and substituting from Equation (8.3.13) and integrating, one gets

at the inner crack tip $x_1 = d$

$$\Delta u_4^I(d) = \frac{(D - D_s)}{\pi\Lambda_{44}}\left\{-d\ln(C) + 2F(\xi_d, k_2)\frac{R_2}{a} + G_1(d,c) + \frac{2b^2}{a}\sqrt{\frac{a^2 - d^2}{d^2 - b^2}} R_7\right\}$$
$$+ \frac{2a(D - D_s)}{\pi\Lambda_{44}}\left(\frac{\pi}{2} - \vartheta_d + \vartheta_c\right) R_8 - \frac{a(D - D_2^\infty)}{\Lambda_{44}} R_8 - \frac{\Lambda_{42}}{\Lambda_{44}}\Delta u_2^I(d), \tag{8.3.26}$$

and at the outer crack tip $x_1 = c$

$$\Delta u_4^I(c) = -\frac{(D - D_s)}{\pi\Lambda_{44}}\left\{-c\ln(D) + H_1(c,d) + 2F(\vartheta_c, k_2)\frac{R_2}{a} + \frac{2}{a}\sqrt{\frac{c^2 - b^2}{a^2 - c^2}} R_9\right\}$$
$$- \frac{2a(D - D_s)}{\pi\Lambda_{44}}\left(\frac{\pi}{2} - \vartheta_d + \vartheta_c\right) R_{10} + \frac{a(D - D_2{}^\infty)}{\Lambda_{44}} R_{10} - \frac{\Lambda_{42}}{\Lambda_{44}}\Delta u_2^I(c), \tag{8.3.27}$$

where,

$$\ln(C) = \ln\left(\frac{a^2-d^2}{a^2-b^2} + \frac{a^2(b^2-d^2)}{d^2(a^2-b^2)}\right),\ \ln(D) = \ln\left(\frac{(a^2-c^2)(c^2-b^2)}{c^2(a^2-b^2)} + 1\right),$$

$$\sin^2\xi_d = a^2(d^2-b^2)/\left(d^2(a^2-b^2)\right),\ R_7 = \left(F(\xi_d,k_2) - II(\xi_d, \frac{d^2-b^2}{d^2}, k_2)\right),$$

$$R_8 = \left(E(\xi_d,k_2) - \frac{k_2^2\sin\xi_d\cos\xi_d}{\sqrt{1-k_2^2\sin^2\xi_d}} - \lambda_2^2 F(\xi_d,k_2)\right),$$

$$R_9 = \left(a^2F(\vartheta_c,k_2) - c^2II(\vartheta_c, \frac{a^2-c^2}{a^2}, k_2)\right),\ R_{10} = \left(E(\vartheta_c,k_2) - \lambda_2^2F(\vartheta_c,k_2)\right),$$

$$G_1(d,c) = d\ln\left(\frac{\sqrt{(d^2-b^2)(a^2-c^2)} + \sqrt{(a^2-d^2)(c^2-b^2)}}{\sqrt{(d^2-b^2)(a^2-c^2)} - \sqrt{(a^2-d^2)(c^2-b^2)}}\right)$$
$$- \frac{2b^2}{a}\sqrt{\frac{a^2-c^2}{c^2-b^2}}II(\xi_d, \frac{c^2k_2^2}{c^2-b^2}, k_2),$$

$$H_1(c,d) = c\ln\left(\frac{\sqrt{(c^2-b^2)(a^2-d^2)} + \sqrt{(a^2-c^2)(d^2-b^2)}}{\sqrt{(c^2-b^2)(a^2-d^2)} - \sqrt{(a^2-c^2)(d^2-b^2)}}\right)$$
$$- \frac{2}{a}\sqrt{(d^2-b^2)(a^2-d^2)}\left(F(\vartheta_c,k_2) + \frac{d^2}{a^2-d^2}II(\vartheta_c, \frac{a^2-b^2}{a^2-d^2}, k_2)\right).$$

As for semi-permeable crack model, the electric displacement, D (defined in Equation (2.5.3)) inside the crack gap media is related to the crack opening displacement and the potential drop. Thus the value of electric flux D, is obtained from the quadratic Equation (3.4.4) for two-collinear cracks problem.

Energy release rate (ERR)

Energy release rate is calculated at the interior tip $x_1 = d$ and $x_1 = c$ exterior tip from the formulae

$$J_a^I(d) = \sigma_s\Delta u_2^I(d) + D_s\Delta u_4^I(d), \tag{8.3.28}$$

$$J_a^I(c) = \sigma_s\Delta u_2^I(c) + D_s\Delta u_4^I(c). \tag{8.3.29}$$

8.3.1.2 Case I: Results and Discussions

An illustrative example is presented for a poled PZT-5H ceramic. The material constants are given in Table 2.1.

We assume that the lengths of the collinear cracks, saturation-limit electric displacement and yield stress are $10mm$, $D_s = 0.05C/m^2$ and $\sigma_s = 200MPa$, respectively. And also the prescribed mechanical and electric loads are $\sigma_{22}^\infty = 20MPa$, $D_2^\infty = 0.001C/m^2$, respectively.

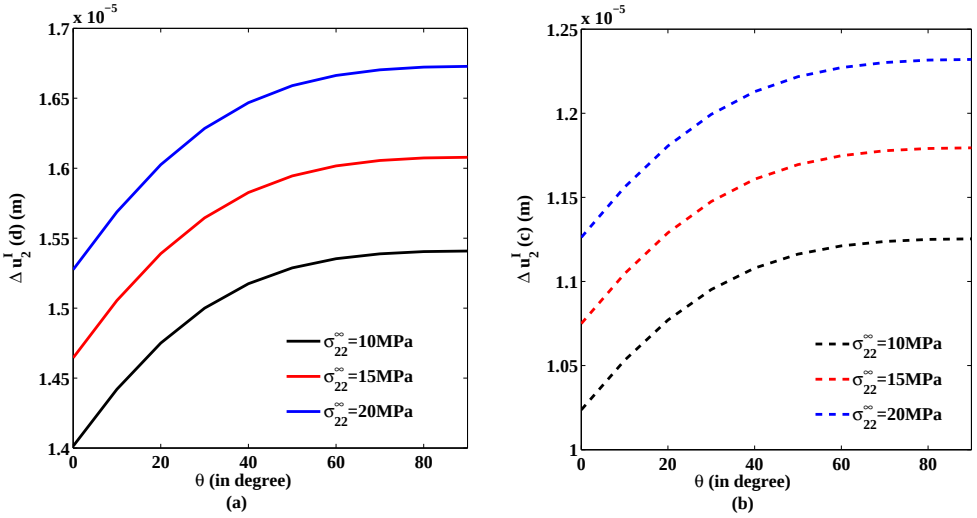

Figure 8.2: Variation of COD versus angle of polarization for different σ_{22}^{∞}

Variation of COD versus increase in angle of polarization 'θ' is plotted in Figs. 8.2(a, b) for a fixed prescribed electric displacement. It is seen that as θ increases, the mechanical COD increases parabolically both at inner and outer crack tips. It is higher at the inner tip of the crack, as expected, although the behavior remains the same at both the tips. Also it may be noted that as the prescribed mechanical load is increased the crack opens more, as expected.

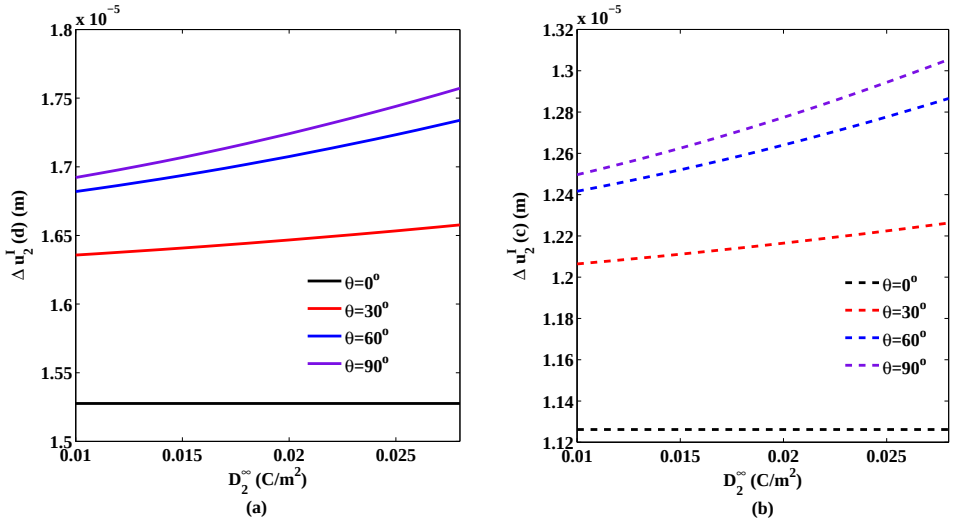

Figure 8.3: Variation of COD versus D_2^{∞} for different angle of polarization

Figs. 8.3(a) and (b), respectively, depict the variation of COD at the interior and exterior tips of the crack versus D_2^{∞} for different angle of polarization. It is noted that COD at each of the tips increases linearly. It is more at inner tip than that at

outer tip. It is also noted as θ is increased the cracks open more.

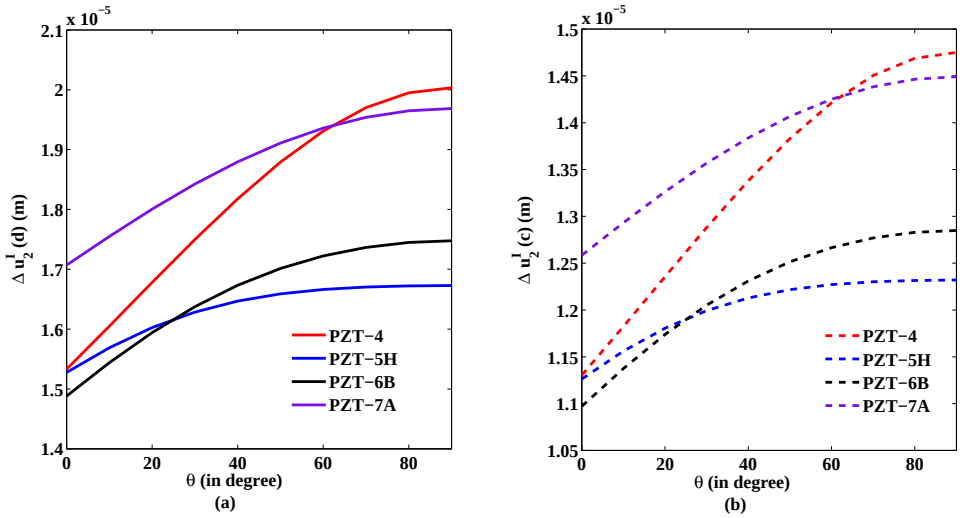

Figure 8.4: Variation of COD versus angle of polarization for different piezoceramics

Figs. 8.4(a, b) show the variation of crack opening for different piezoelectric ceramics against θ. It may be noted that crack opens more at the inner tip than that at the outer tip. Also these variations assist in choosing the correct piezoelectric ceramic, depending on the usage. It may be noted that PZT-5H opens the least and PZT-4 opens more, for higher values of θ and for lower values of θ it opens less than PZT-7A.

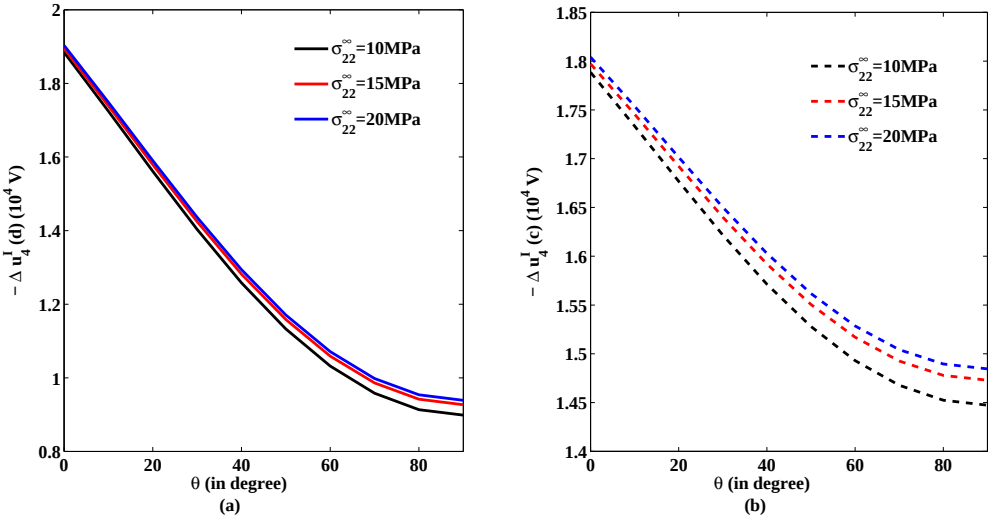

Figure 8.5: COP versus θ for different σ_{22}^{∞}

In Figs. 8.5(a, b) variation of COP vis-a-vis θ is depicted for different σ_{22}^{∞}. It shows

an inverted bell shaped decrease in COP drop as D_2^∞ is increased. At outer tip of crack little variation is seen as σ_{22}^∞ is increased. But very little effect is seen at the inner tip due to increase of σ_{22}^∞.

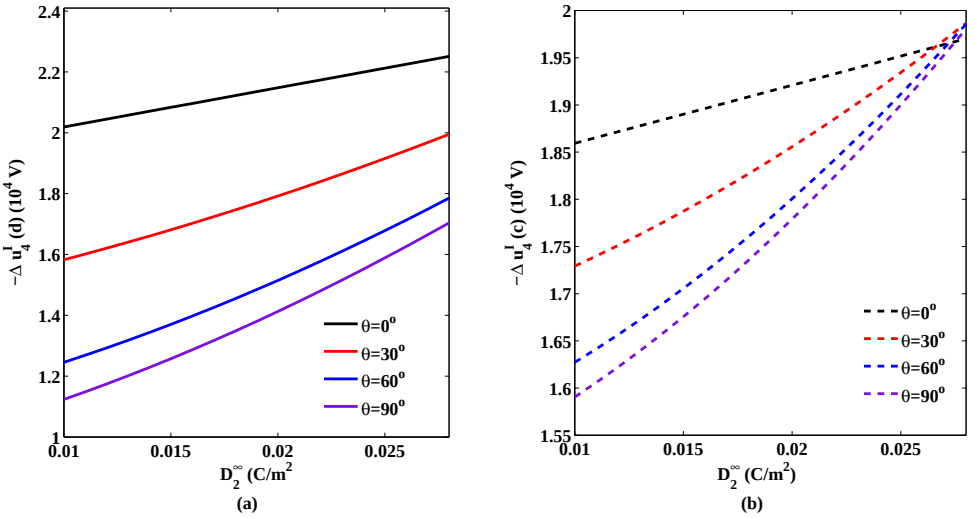

Figure 8.6: COP versus D_2^∞ for different θ

Figs. 8.6(a, b) depict the variation of COP versus D_2^∞ for different polarization angle θ. COP drop is higher at inner tip. The increase is slightly non-linear. An interesting variation is observed at the outer tip of the crack, the COP shows steep slightly non-linearly increase for different polarization angle and becomes independent of polarization for $D_2^\infty = 0.03C/m^2$.

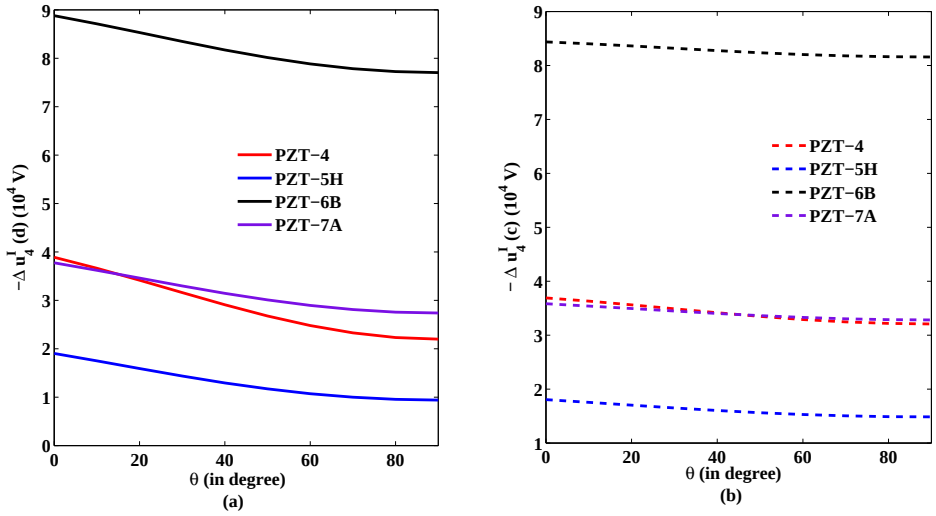

Figure 8.7: COP versus θ for different piezoceramics

Figs. 8.7(a, b) show COP variation vis-a-vis θ for different piezoceramics. At both

the inner and outer crack tips COP has similar variation for PZT-6B and PZT-5H. It is maximum for PZT-6B and minimum for PZT-5H. And for PZT-7A and PZT-4 COP variations are almost equal and more close to that for PZT-5H.

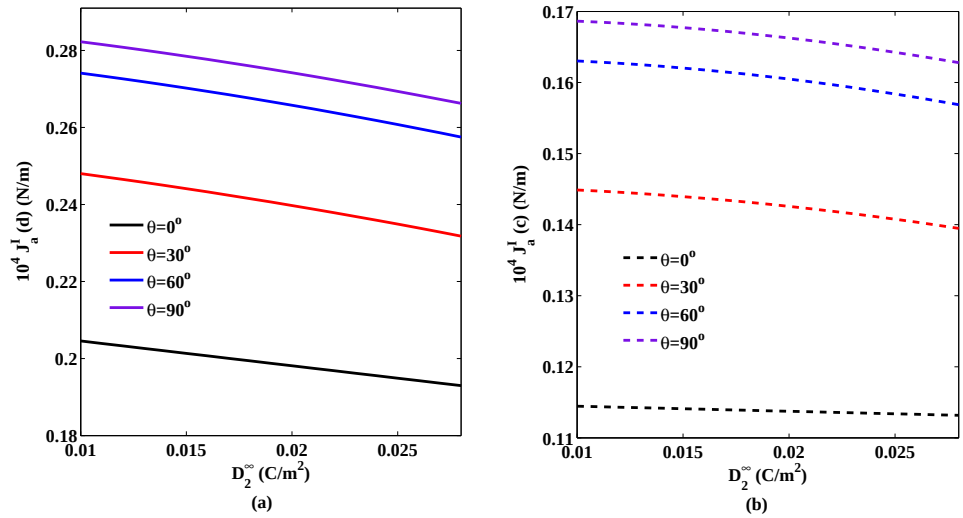

Figure 8.8: ERR versus D_2^∞ for different θ

Energy release rate with respect to prescribed D_2^∞ at inner and outer tip is drawn in Figs. 8.8(a) and (b), respectively. It is seen that the ERR reduces as the prescribed D_2^∞ is increased. Although as polarization angle θ is increased the ERR increases but its decreasing trend continues as D_2^∞ is increased. Also it may be noted from Fig. 8.8 that ERR is higher at inner tip as compared to that at outer tip of the crack, as expected.

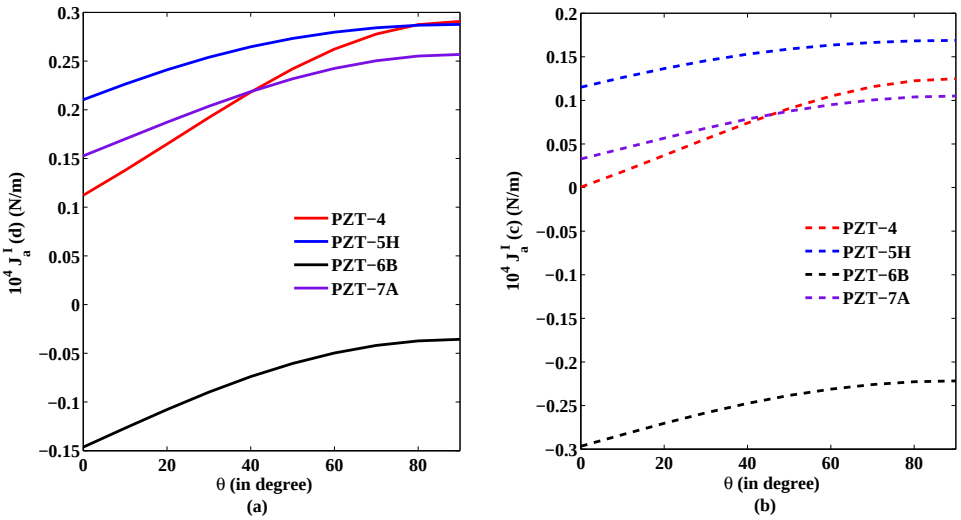

Figure 8.9: ERR versus θ for different piezoceramics

Variation of ERR versus θ for different piezoceramics is shown in Figs. 8.9(a, b). It is seen that as poling angle θ is increased the ERR increases quadratically. PZT-5H ceramic shows the maximum variation as, θ is increased, while PZT-4, PZT-6B and PZT-7A show the similar quadratic variation for ERR.

8.3.2 Solution for Case II: When saturation zones are smaller than the developed yield zones ($|c_1| > |a|$ and $|b| > |d_1|$)

The boundary conditions from (i) to (iv) in subsection (8.3), remain the same as in Case I and the boundary condition (v) is replaced by (vi) as

(vi) $\mathbf{\Phi}_{,1}^{II+}(x_1) = \mathbf{\Phi}_{,1}^{II-}(x_1) = -\mathbf{V}^{II}, \quad \text{for } d < |x_1| < c$

where, $\mathbf{V}^{II} = [0, \sigma_{22}^{\infty}, 0, D_2^{\infty}]^T$, and superscript II represents that the quantity refers to Case II.

Schematically the configuration of the problem is depicted in Fig. 8.10.

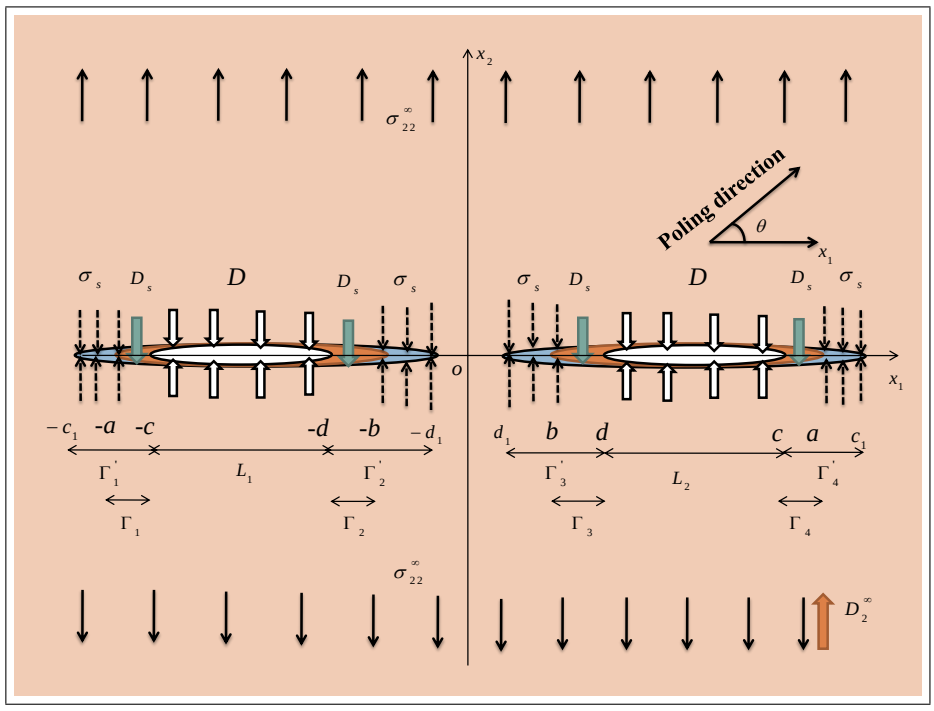

Figure 8.10: Schematic representation of configuration of the problem for Case II, when saturation zones are smaller than the developed yield zones

Carrying out calculations analogous to Case I the boundary condition (vi) for this Case yield the following two dual Hilbert problems for potentials $\Omega_2^{II}(z)$ and $\Omega_4^{II}(z)$

as

$$\Lambda_{22}[\Omega_2^{II+}(x_1)+\Omega_2^{II-}(x_1)]+\Lambda_{24}[\Omega_4^{II+}(x_1)+\Omega_4^{II-}(x_1)]=-\sigma_{22}^{\infty},\ d<|x_1|<c, \tag{8.3.30}$$

$$\Lambda_{42}[\Omega_2^{II+}(x_1)+\Omega_2^{II-}(x_1)]+\Lambda_{44}[\Omega_4^{II+}(x_1)+\Omega_4^{II-}(x_1)]=D-D_2^{\infty},\ d<|x_1|<c. \tag{8.3.31}$$

The solution of which may be written as, carrying out the similar calculation as in Case I, as

$$\begin{aligned}\Omega_4^{II}(z)=&\frac{\Lambda_{42}\sigma_s+\Lambda_{22}(D-D_s)}{\pi\Sigma X_2(z)}\left\{(z^2-a^2\lambda_2^2)\left(\frac{\pi}{2}-\vartheta_d+\vartheta_c\right)+R_2\right\}\\&-\frac{\Lambda_{42}\sigma_{22}^{\infty}+\Lambda_{22}(D-D_2^{\infty})}{2\Sigma}\left\{\frac{z^2-a^2\lambda_2^2}{X_2(z)}-1\right\}\\&-\frac{\Lambda_{42}\sigma_s+\Lambda_{22}(D-D_s)}{\pi\Sigma}\left(\frac{\pi}{2}-\upsilon_d+\upsilon_c\right),\end{aligned} \tag{8.3.32}$$

$$\begin{aligned}\Omega_2^{II}(z)=&-\frac{\Lambda_{42}}{\Lambda_{22}}\Omega_4^{II}(z)+\frac{\sigma_{22}^{\infty}}{2\Lambda_{22}}\left\{\frac{z^2-c_1^2\lambda_1^2}{X_1(z)}-1\right\}+\frac{\sigma_s}{\pi\Lambda_{22}}\left(\frac{\pi}{2}-\varphi_d+\varphi_c\right)\\&-\frac{\sigma_s}{\pi\Lambda_{22}X_1(z)}\left\{(z^2-c_1^2\lambda_1^2)\left(\frac{\pi}{2}-\psi_d+\psi_c\right)+R_1\right\}.\end{aligned} \tag{8.3.33}$$

8.3.2.1 Applications

As in Case I here we obtain the expression for calculations of yield zone, saturation zone length, crack opening displacement, crack opening potential drop and energy release rate.

The stress and electric displacement for this case are obtained using

$$\mathbf{\Phi}_{,1}^{II}(x_1)=\mathbf{BF}^{II+}(x_1)+\mathbf{BF}^{II-}(x_1)=\mathbf{\Lambda\Omega}^{II+}(x_1)+\mathbf{\Lambda\Omega}^{II-}(x_1),\ |x_1|>c_1. \tag{8.3.34}$$

Comparing second and fourth components from above equation, we get

$$\sigma_{22}^{II}(x_1)=\Lambda_{22}[\Omega_2^{II+}(x_1)+\Omega_2^{II-}(x_1)]+\Lambda_{24}[\Omega_4^{II+}(x_1)+\Omega_4^{II-}(x_1)], \tag{8.3.35}$$

$$D_2^{II}(x_1)=\Lambda_{42}[\Omega_2^{II+}(x_1)+\Omega_2^{II-}(x_1)]+\Lambda_{44}[\Omega_4^{II+}(x_1)+\Omega_4^{II-}(x_1)]. \tag{8.3.36}$$

Substituting the values of $\Omega_2^{II}(x_1)$ and $\Omega_4^{II}(x_1)$ from Equations (8.3.33 and 8.3.32) and simplifying one obtains

$$\begin{aligned}\sigma_{22}^{II}(x_1)=&\frac{2\sigma_s}{\pi}\left(\frac{\pi}{2}-\varphi_d+\varphi_c\right)+\sigma_{22}^{\infty}\left\{\frac{x_1^2-c_1^2\lambda_1^2}{X_1(x_1)}-1\right\}\\&-\frac{2\sigma_s}{\pi X_1(x_1)}\left\{(x_1^2-c_1^2\lambda_1^2)\left(\frac{\pi}{2}-\psi_d+\psi_c\right)+R_1\right\},\end{aligned} \tag{8.3.37}$$

$$D_2^{II}(x_1) = \frac{2(\Lambda_{42}\sigma_s + \Lambda_{22}(D - D_s))}{\pi\Lambda_{22}X_2(x_1)}\left\{(x_1^2 - a^2\lambda_2^2)\left(\frac{\pi}{2} - \vartheta_d + \vartheta_c\right) + R_2\right\}$$
$$- \frac{\Lambda_{42}\sigma_{22}^{\infty} + \Lambda_{22}(D - D_2^{\infty})}{\Lambda_{22}}\left\{\frac{x_1^2 - a^2\lambda_2^2}{X_2(x_1)} - 1\right\}$$
$$- \frac{2(\Lambda_{42}\sigma_s + \Lambda_{22}(D - D_s))}{\pi\Lambda_{22}}\left(\frac{\pi}{2} - \upsilon_d + \upsilon_c\right). \tag{8.3.38}$$

Yield zone

Using Dugdale's hypothesis that the stress remains finite at every point of the body, consequently at the tips $x_1 = d_1$ and $x_1 = c_1$ of the yield zones, one obtains non-linear equations to determine d_1 and c_1 from

$$\left(\frac{d_1^2}{c_1^2} - \lambda_1^2\right)\left(\frac{\pi\sigma_{22}^{\infty}}{2\sigma_s} - \frac{\pi}{2} + \psi_d - \psi_c\right) - \frac{R_1}{c_1^2} = 0, \tag{8.3.39}$$
$$\left(1 - \lambda_1^2\right)\left(\frac{\pi\sigma_{22}^{\infty}}{2\sigma_s} - \frac{\pi}{2} + \psi_d - \psi_c\right) - \frac{R_1}{c_1^2} = 0. \tag{8.3.40}$$

Saturation zone

Assuming Dugdale's hypothesis to be true for electric displacement as well hence the condition of finiteness of electrical displacements at every point of the plate yields the following two equations

$$\left(\frac{b^2}{a^2} - \lambda_2^2\right)\left(\frac{\pi}{2}\frac{\Lambda_{42}\sigma_{22}^{\infty} + \Lambda_{22}(D - D_2^{\infty})}{\Lambda_{42}\sigma_s + \Lambda_{22}(D - D_s)} - \frac{\pi}{2} + \vartheta_d - \vartheta_c\right) - \frac{R_2}{a^2} = 0, \tag{8.3.41}$$
$$\left(1 - \lambda_2^2\right)\left(\frac{\pi}{2}\frac{\Lambda_{42}\sigma_{22}^{\infty} + \Lambda_{22}(D - D_2^{\infty})}{\Lambda_{42}\sigma_s + \Lambda_{22}(D - D_s)} - \frac{\pi}{2} + \vartheta_d - \vartheta_c\right) - \frac{R_2}{a^2} = 0. \tag{8.3.42}$$

to determine a and b.

Crack opening potential drop (COP)

The crack opening potential drop for this case is determined using analogous equation to Equation (8.3.23) as

$$i\Delta\mathbf{u}_{,1}^{II}(x_1) = \mathbf{\Lambda}[\mathbf{\Omega}^{II+}(x_1) - \mathbf{\Omega}^{II-}(x_1)]. \tag{8.3.43}$$

Comparing the fourth component of the above equation and substituting value of $\Omega_4^{II}(x_1)$ from Equation (8.3.32) one obtains potential drop at the crack tips $x_1 = d$ and $x_1 = c$ as

$$\Delta u_4^{II}(d) = \frac{\Lambda_{42}\sigma_s + \Lambda_{22}(D - D_s)}{\pi\Sigma}\left\{-d\ln(C) + 2F(\xi_d, k_2)\frac{R_2}{a} + G_1(d, c)\right\}$$
$$+ \frac{\Lambda_{42}\sigma_s + \Lambda_{22}(D - D_s)}{\pi\Sigma}\left\{2a\left(\frac{\pi}{2} - \vartheta_d + \vartheta_c\right)R_8 + \frac{2b^2}{a}\sqrt{\frac{a^2 - d^2}{d^2 - b^2}}R_7\right\}$$
$$- \frac{a(\Lambda_{42}\sigma_{22}^{\infty} + \Lambda_{22}(D - D_2^{\infty}))}{\Sigma}R_8, \tag{8.3.44}$$

$$\Delta u_4^{II}(c) = -\frac{\Lambda_{42}\sigma_s + \Lambda_{22}(D - D_s)}{\pi\Sigma}\left\{-c\ln(D) + H_1(c,d) + 2F(\vartheta_c, k_2)\frac{R_2}{a}\right\}$$
$$-\frac{\Lambda_{42}\sigma_s + \Lambda_{22}(D - D_s)}{\pi\Sigma}\left\{2a\left(\frac{\pi}{2} - \vartheta_d + \vartheta_c\right)R_{10} + \frac{2}{a}\sqrt{\frac{c^2 - b^2}{a^2 - c^2}}R_9\right\}$$
$$+\frac{a(\Lambda_{42}\sigma_{22}^{\infty} + \Lambda_{22}(D - D_2^{\infty}))}{\Sigma}R_{10}. \tag{8.3.45}$$

Crack opening displacement (COD)

The COD at the crack tips $x_1 = d$ and $x_1 = c$ is obtained comparing second component of Equation (8.3.43) and substituting value of $\Omega_2^{II}(x_1)$ from Equation (8.3.33) and simplifying, one obtains

$$\Delta u_2^{II}(d) = -\frac{\sigma_s}{\pi\Lambda_{22}}\left\{-d\ln(A) + \frac{2d_1^2}{c_1}\sqrt{\frac{c_1^2 - d^2}{d^2 - d_1^2}}R_3 + 2F(\tau_d, k_1)\frac{R_1}{c_1} + G(d,c)\right\}$$
$$-\frac{2c_1\sigma_s}{\pi\Lambda_{22}}\left(\frac{\pi}{2} - \psi_d + \psi_c\right)R_4 + \frac{c_1\sigma_{22}^{\infty}}{\Lambda_{22}}R_4 - \frac{\Lambda_{24}}{\Lambda_{22}}\Delta u_4^{II}(d), \tag{8.3.46}$$

$$\Delta u_2^{II}(c) = \frac{\sigma_s}{\pi\Lambda_{22}}\left\{-c\ln(B) + H(c,d) + 2F(\psi_c, k_1)\frac{R_1}{c_1} + \frac{2}{c_1}\sqrt{\frac{c^2 - d_1^2}{c_1^2 - c^2}}R_6\right\}$$
$$+\frac{2c_1\sigma_s}{\pi\Lambda_{22}}\left(\frac{\pi}{2} - \psi_d + \psi_c\right)R_5 - \frac{c_1\sigma_{22}^{\infty}}{\Lambda_{22}}R_5 - \frac{\Lambda_{24}}{\Lambda_{22}}\Delta u_4^{II}(c). \tag{8.3.47}$$

Energy release rate (ERR)

Energy release rate at the interior and exterior tips of the crack is calculated using

$$J_a^{II}(d) = \sigma_s\Delta u_2^{II}(d) + D_s\Delta u_4^{II}(d), \tag{8.3.48}$$
$$J_a^{II}(c) = \sigma_s\Delta u_2^{II}(c) + D_s\Delta u_4^{II}(c). \tag{8.3.49}$$

8.3.2.2 Case II: Results and Discussions

For this Case II too material ceramics are same as in Table 2.1.

We assume that the saturation-limit electric displacement and yield point stress are $D_s = 0.06C/m^2$ and $\sigma_s = 200MPa$, respectively. And also the prescribed mechanical and electric loads are same as in Case I.

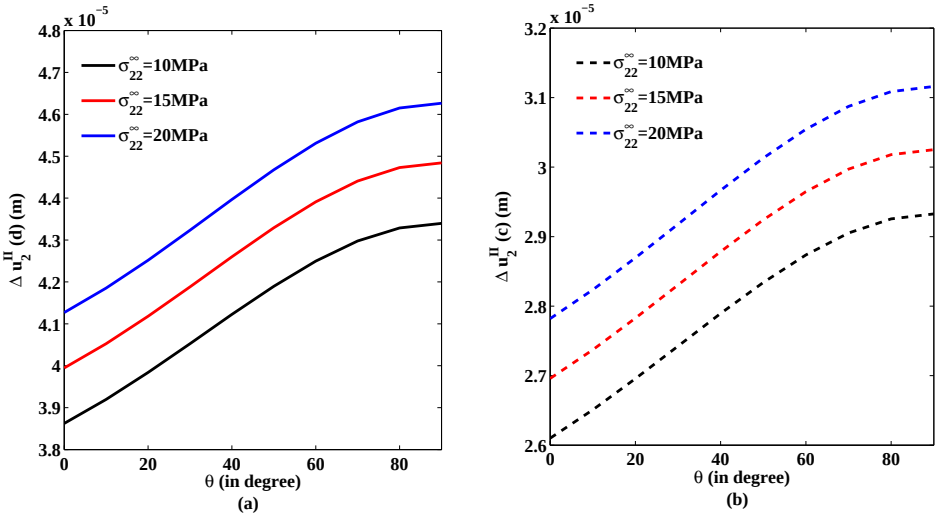

Figure 8.11: COD versus θ for different σ_{22}^{∞}

Figs. 8.11(a, b) depict the variation of COD with respect to θ for different σ_{22}^{∞}. COD shows a linear increase as poling direction angle is changed from 0^0 to 90^0. The COD is maximum when poling direction is perpendicular to crack length. It may be noted from the Figs. 8.11(a, b) that COD is more at the inner tip than that at the outer tip.

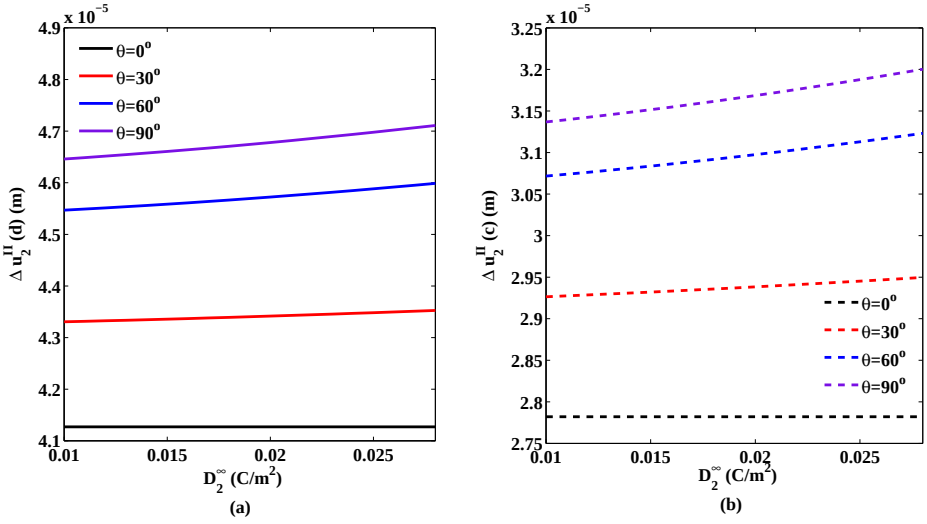

Figure 8.12: COD versus D_2^{∞} for different θ

Figs. 8.12(a) and (b), respectively, depict the variation of COD at the interior and exterior crack tips of the crack versus D_2^{∞} for different angle of polarization. It is noted that COD at both the tips increases linearly. And it is more at inner tip than that at outer tip. It is also noted as θ is increased the cracks open more.

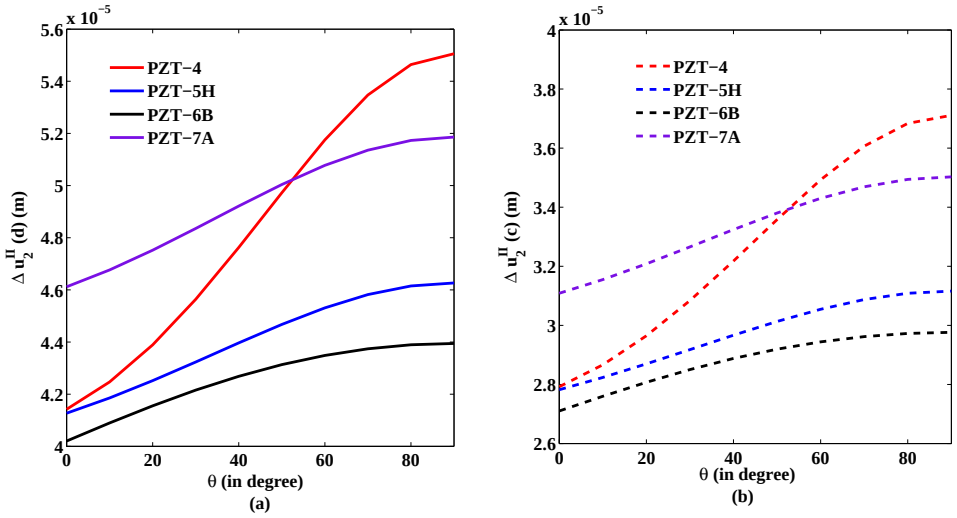

Figure 8.13: COD versus poling angles for different piezoceramics

Figs. 8.13(a, b) depict the crack opening of different piezoelectric ceramics with respect to poling direction for a fixed prescribed mechanical and electric loads. It shows that PZT-6B opens the least. The ceramics PZT-6B, PZT-5H and PZT-7A show a parabolic increase as θ is increased from 0^0 to 90^0 from length of the crack. These ceramics show continuous slight increase but PZT-4 shows a steep parabolic increase. The variation in these Figs. 8.13(a, b) assists the designer to select the correct piezoelectric ceramic.

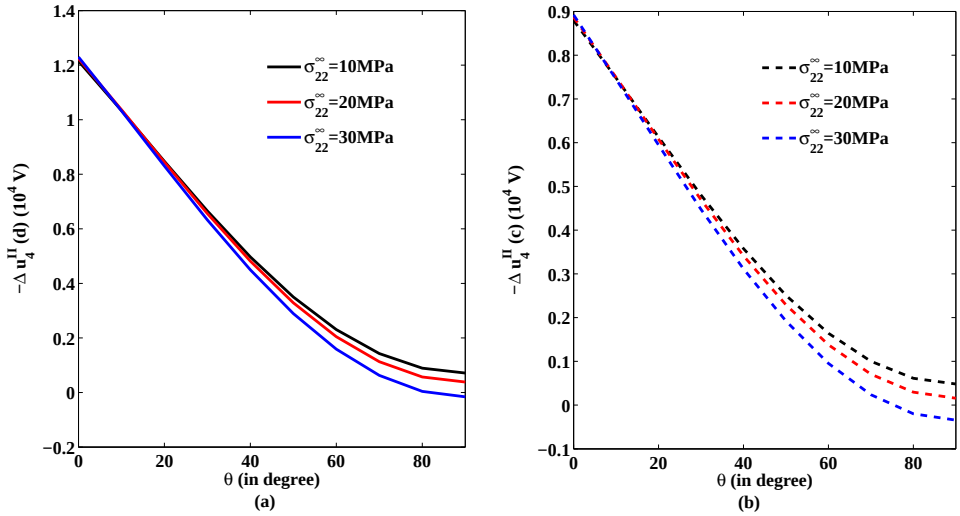

Figure 8.14: COP versus θ for different σ_{22}^{∞}

In Figs. 8.14(a, b) variation of COP vis-a-vis θ is depicted for different σ_{22}^{∞}. It shows an inverted bell shaped decrease in COP drop as σ_{22}^{∞} is increased. At outer tip of

crack little variation is seen as σ_{22}^{∞} is increased. But very little effect is seen at the inner tip due to increase of σ_{22}^{∞}.

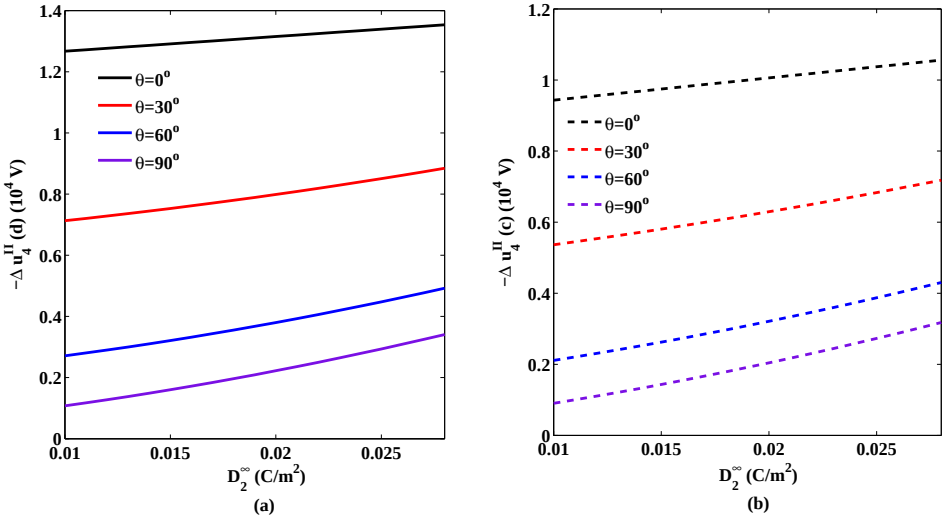

Figure 8.15: COP versus D_2^{∞} for different θ

Figs. 8.15(a, b) depict the variation of COP with respect to prescribed electric loadings. It is seen that the COP drop increases linearly as the prescribed electric load is increased for various values of θ. But as θ is increased from 0^0 to 90^0 the COP drops although the increasing trend is maximum with respect to D_2^{∞}.

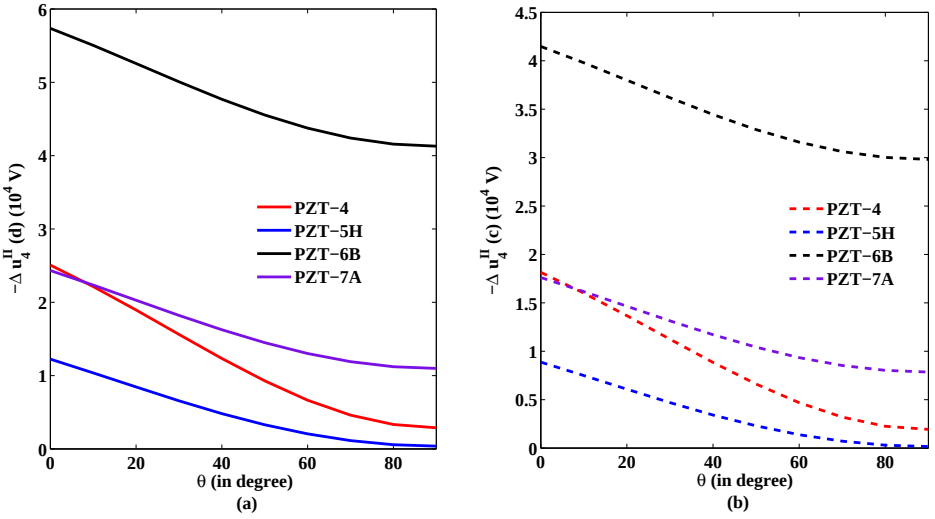

Figure 8.16: COP versus θ for different piezoceramics

For different piezoceramics COP drop is plotted versus θ in Figs. 8.16(a, b). It may be noted that at both inner and outer tips COP drop shows a parabolic variation

as θ is increased. It is observed that COP is highest for PZT-6B and minimum for PZT-5H.

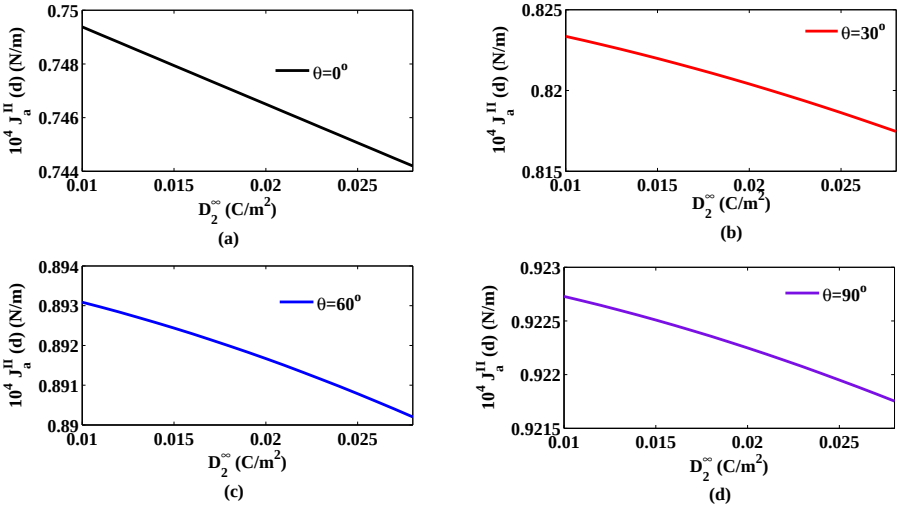

Figure 8.17: ERR at inner tip $x_1 = d$ versus D_2^∞ for different θ

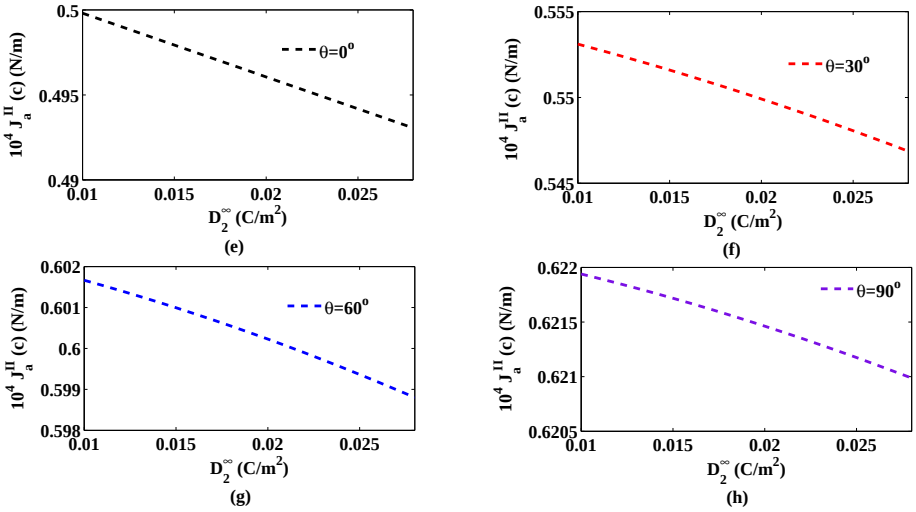

Figure 8.18: ERR at outer tip $x_1 = c$ versus D_2^∞ for different θ

Figs. (8.17, 8.18) (a to h) show the ERR vis-a-vis prescribed electric loads for a fixed prescribed mechanical load ($\sigma_{22}^\infty = 20MPa$). It is observed from all Figs. (8.17, 8.18) (a to h) that ERR decreases in every case. Also it may be noted that ERR is maximum for $\theta = 90^0$ i.e., the poling direction is perpendicular to crack length, and it is minimum when $\theta = 0^0$ i.e., poling direction is along crack length.

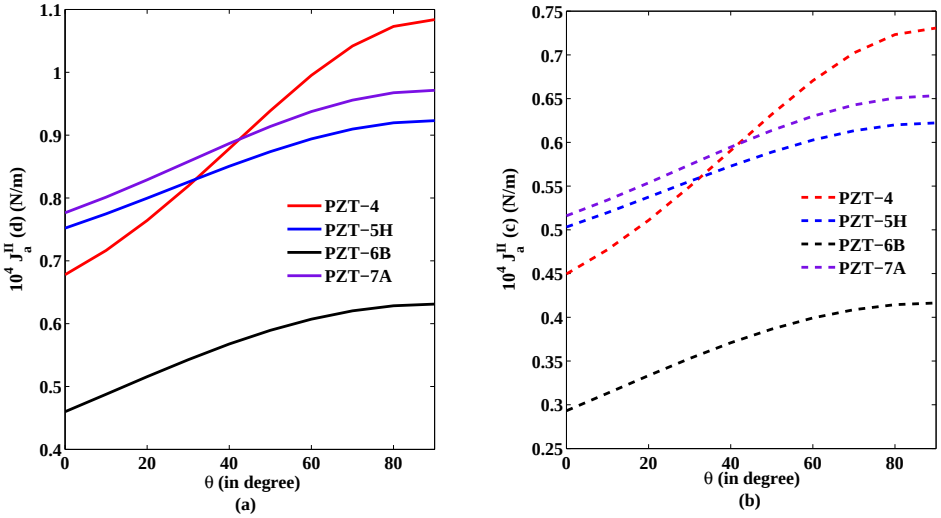

Figure 8.19: ERR versus θ for different piezoceramics

Figs. 8.19(a, b) show the ERR with respect to poling angle, θ, for different piezoceramics. It is seen from both the Figs. 8.19(a, b) that as poling angle is increased the ERR increases quadratically. PZT-4 ceramic shows the maximum variation as, θ is increased, while PZT-6B, PZT-5H and PZT-7A show the similar quadratic variation for ERR.

8.3.3 Solution for Case III: When saturation and yield zones are equal ($|c_1| = |a|$ and $|b| = |d_1|$)

Schematically the configuration of the problem is depicted in Fig. 8.20.

The boundary conditions form (i) to (iv) remain the same as in Case I and boundary condition (v) is replaced by following condition (vii)

(vii) $\mathbf{\Phi}_{,1}^{III+}(x_1) = \mathbf{\Phi}_{,1}^{III-}(x_1) = -\mathbf{V}^{III}, \quad \text{for } d < |x_1| < c$

where, $\mathbf{V}^{III} = [0, \sigma_{22}^{\infty}, 0, D_2^{\infty}]^T$, and superscript III represents that the quantity refers to Case III.

Analogous to Case I the boundary condition (vii) for this case yield the following two dual Hilbert problems for potentials $\Omega_2^{III}(z)$ and $\Omega_4^{III}(z)$ as

$$\Lambda_{22}[\Omega_2^{III+}(x_1) + \Omega_2^{III-}(x_1)] + \Lambda_{24}[\Omega_4^{III+}(x_1) + \Omega_4^{III-}(x_1)] = -\sigma_{22}^{\infty},\ d < |x_1| < c, \tag{8.3.50}$$

$$\Lambda_{42}[\Omega_2^{III+}(x_1) + \Omega_2^{III-}(x_1)] + \Lambda_{44}[\Omega_4^{III+}(x_1) + \Omega_4^{III-}(x_1)] = D - D_2^{\infty},\ d < |x_1| < c. \tag{8.3.51}$$

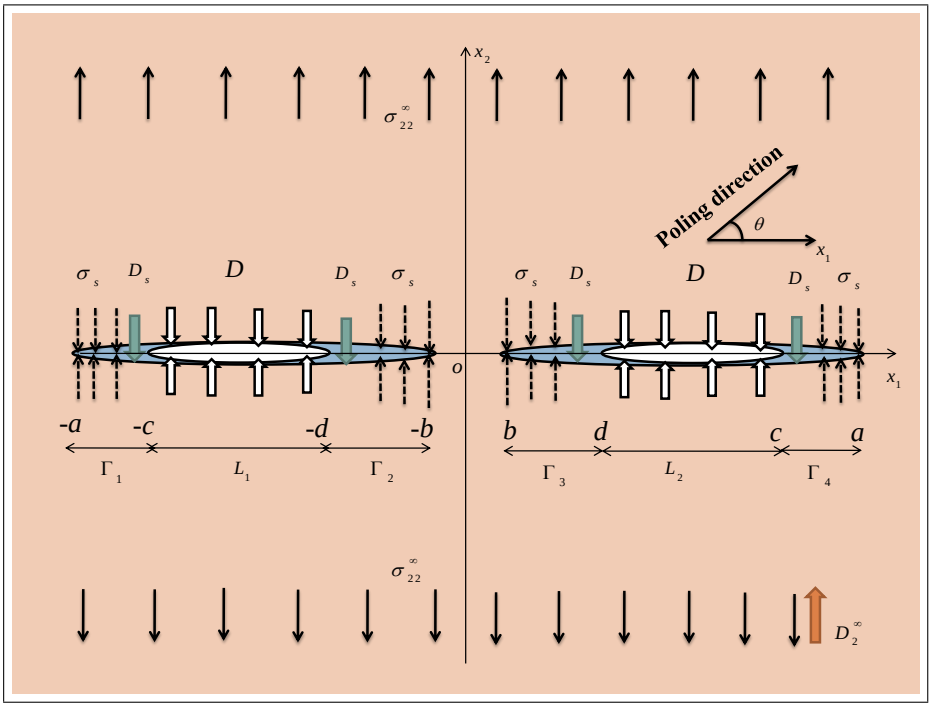

Figure 8.20: Schematic representation of configuration of the problem for Case III, when saturation and yield zones are equal

The solution of which, carrying out the similar calculation as in Case I, may be written as

$$\begin{aligned}\Omega_2^{III}(z) = &-\frac{\Lambda_{44}\sigma_s+\Lambda_{24}(D-D_s)}{\pi\Sigma X_2(z)}\left\{(z^2-a^2\lambda_2^2)\left(\frac{\pi}{2}-\vartheta_d+\vartheta_c\right)+R_2\right\}\\ &+\frac{\Lambda_{44}\sigma_{22}^{\infty}+\Lambda_{24}(D-D_2^{\infty})}{2\Sigma}\left\{\frac{z^2-a^2\lambda_2^2}{X_2(z)}-1\right\}\\ &+\frac{\Lambda_{44}\sigma_s+\Lambda_{24}(D-D_s)}{\pi\Sigma}\left(\frac{\pi}{2}-\upsilon_d+\upsilon_c\right),\end{aligned} \tag{8.3.52}$$

$$\begin{aligned}\Omega_4^{III}(z) = &\frac{\Lambda_{42}\sigma_s+\Lambda_{22}(D-D_s)}{\pi\Sigma X_2(z)}\left\{(z^2-a^2\lambda_2^2)\left(\frac{\pi}{2}-\vartheta_d+\vartheta_c\right)+R_2\right\}\\ &-\frac{\Lambda_{42}\sigma_{22}^{\infty}+\Lambda_{22}(D-D_2^{\infty})}{2\Sigma}\left\{\frac{z^2-a^2\lambda_2^2}{X_2(z)}-1\right\}\\ &-\frac{\Lambda_{42}\sigma_s+\Lambda_{22}(D-D_s)}{\pi\Sigma}\left(\frac{\pi}{2}-\upsilon_d+\upsilon_c\right).\end{aligned} \tag{8.3.53}$$

8.3.3.1 Applications

Expressions for crack opening displacement, crack opening potential drop, energy release rate and developed zones are derived in this section.

Zone size

As in Case II, the stress and electric displacement for this case are obtained using

$$\mathbf{\Phi}^{III}_{,1}(x_1) = \mathbf{B}\mathbf{F}^{III+}(x_1) + \mathbf{B}\mathbf{F}^{III-}(x_1) = \mathbf{\Lambda}[\mathbf{\Omega}^{III+}(x_1) + \mathbf{\Omega}^{III-}(x_1)],\ |x_1| > a. \tag{8.3.54}$$

Comparing second and fourth components and substituting $\Omega^{III}_2(z)$ and $\Omega^{III}_4(z)$ from Equations (8.3.52 and 8.3.53) and simplifying one obtains

$$\begin{aligned}\sigma^{III}_{22}(x_1) =& \frac{2\sigma_s}{\pi}\left(\frac{\pi}{2} - \upsilon_d + \upsilon_c\right) + \sigma^{\infty}_{22}\left\{\frac{x_1^2 - a^2\lambda_2^2}{X_2(x_1)} - 1\right\} \\ &- \frac{2\sigma_s}{\pi X_2(x_1)}\left\{(x_1^2 - a^2\lambda_2^2)\left(\frac{\pi}{2} - \vartheta_d + \vartheta_c\right) + R_2\right\},\end{aligned} \tag{8.3.55}$$

$$\begin{aligned}D^{III}_2(x_1) =& -\frac{2(D - D_s)}{\pi}\left(\frac{\pi}{2} - \upsilon_d + \upsilon_c\right) - (D - D^{\infty}_2)\left\{\frac{x_1^2 - a^2\lambda_2^2}{X_2(x_1)} - 1\right\} \\ &+ \frac{2(D - D_s)}{\pi X_2(x_1)}\left\{(x_1^2 - a^2\lambda_2^2)\left(\frac{\pi}{2} - \vartheta_d + \vartheta_c\right) + R_2\right\}.\end{aligned} \tag{8.3.56}$$

Applying Dugdale's hypothesis of stresses and electric displacement remain finite at the tips $x_1 = b$ and $x_1 = a$ of the zones, one obtains non-linear equations to determine b and a from

$$\left(\frac{b^2}{a^2} - \lambda_2^2\right)\left(\frac{\pi}{2}R - \frac{\pi}{2} + \vartheta_d - \vartheta_c\right) - \frac{R_2}{a^2} = 0, \tag{8.3.57}$$

$$\left(1 - \lambda_2^2\right)\left(\frac{\pi}{2}R - \frac{\pi}{2} + \vartheta_d - \vartheta_c\right) - \frac{R_2}{a^2} = 0. \tag{8.3.58}$$

where, $R = \sigma^{\infty}_{22}/\sigma_s$ or $(D - D^{\infty}_2)/(D - D_s)$.

Crack opening displacement (COD)

The crack opening displacement for this case is determined using

$$i\Delta\mathbf{u}^{III}_{,1}(x_1) = \mathbf{\Lambda}[\mathbf{\Omega}^{III+}(x_1) - \mathbf{\Omega}^{III-}(x_1)]. \tag{8.3.59}$$

Comparing the second component of the above equation and substituting value of $\Omega^{III}_2(z)$ from Equation (8.3.52) one obtains COD at tips $x_1 = d$ and $x_1 = c$, as

$$\begin{aligned}\Delta u^{III}_2(d) =& -\frac{(\Lambda_{44}\sigma_s + \Lambda_{24}(D - D_s))}{\pi\Sigma}\left\{-d\ln(C) + 2F(\xi_d, k_2)\frac{R_2}{a} + G_1(d, c)\right\} \\ &- \frac{(\Lambda_{44}\sigma_s + \Lambda_{24}(D - D_s))}{\pi\Sigma}\left\{2a\left(\frac{\pi}{2} - \vartheta_d + \vartheta_c\right)R_8 + \frac{2b^2}{a}\sqrt{\frac{a^2 - d^2}{d^2 - b^2}}R_7\right\} \\ &+ \frac{a(\Lambda_{44}\sigma^{\infty}_{22} + \Lambda_{24}(D - D^{\infty}_2))}{\Sigma}R_8,\end{aligned} \tag{8.3.60}$$

$$\Delta u_2^{III}(c) = \frac{(\Lambda_{44}\sigma_s + \Lambda_{24}(D - D_s))}{\pi\Sigma}\left\{-c\ln(D) + H_1(c,d) + 2F(\vartheta_c, k_2)\frac{R_2}{a}\right\} + \frac{(\Lambda_{44}\sigma_s + \Lambda_{24}(D - D_s))}{\pi\Sigma}\left\{2a\left(\frac{\pi}{2} - \vartheta_d + \vartheta_c\right)R_{10} + \frac{2}{a}\sqrt{\frac{c^2 - b^2}{a^2 - c^2}}R_9\right\} - \frac{a(\Lambda_{44}\sigma_{22}^{\infty} + \Lambda_{24}(D - D_2^{\infty}))}{\Sigma}R_{10}, \tag{8.3.61}$$

respectively.

Crack opening potential drop (COP)

COP at the tips $x_1 = d$ and $x_1 = c$ are obtained, comparing fourth component of Equation (8.3.59) and substituting value of $\Omega_4^{III}(x_1)$ from Equation (8.3.53) and simplifying, as

$$\Delta u_4^{III}(d) = \frac{(\Lambda_{42}\sigma_s + \Lambda_{22}(D - D_s))}{\pi\Sigma}\left\{-d\ln(C) + 2F(\xi_d, k_2)\frac{R_2}{a} + G_1(d,c)\right\} + \frac{(\Lambda_{42}\sigma_s + \Lambda_{22}(D - D_s))}{\pi\Sigma}\left\{2a\left(\frac{\pi}{2} - \vartheta_d + \vartheta_c\right)R_8 + \frac{2b^2}{a}\sqrt{\frac{a^2 - d^2}{d^2 - b^2}}R_7\right\} - \frac{a(\Lambda_{42}\sigma_{22}^{\infty} + \Lambda_{22}(D - D_2^{\infty}))}{\Sigma}R_8, \tag{8.3.62}$$

$$\Delta u_4^{III}(c) = -\frac{(\Lambda_{42}\sigma_s + \Lambda_{22}(D - D_s))}{\pi\Sigma}\left\{-c\ln(D) + H_1(c,d) + 2F(\vartheta_c, k_2)\frac{R_2}{a}\right\} - \frac{(\Lambda_{42}\sigma_s + \Lambda_{22}(D - D_s))}{\pi\Sigma}\left\{2a\left(\frac{\pi}{2} - \vartheta_d + \vartheta_c\right)R_{10} + \frac{2}{a}\sqrt{\frac{c^2 - b^2}{a^2 - c^2}}R_9\right\} + \frac{a(\Lambda_{42}\sigma_{22}^{\infty} + \Lambda_{22}(D - D_2^{\infty}))}{\Sigma}R_{10}. \tag{8.3.63}$$

Energy release rate (ERR)

Energy release rate at the interior and exterior tips of the crack is calculated using

$$J_a^{III}(d) = \sigma_s\Delta u_2^{III}(d) + D_s\Delta u_4^{III}(d), \tag{8.3.64}$$

$$J_a^{III}(c) = \sigma_s\Delta u_2^{III}(c) + D_s\Delta u_4^{III}(c). \tag{8.3.65}$$

8.3.3.2 Case III: Results and Discussions

A similar study as in the Case I and Case II is carried out for this Case too.

We assume that the saturation-limit electric displacement and yield point stress are $D_s = 0.06C/m^2$ and $\sigma_s = 200MPa$, respectively. And also the prescribed mechanical and electric loads are same as in Case I and Case II.

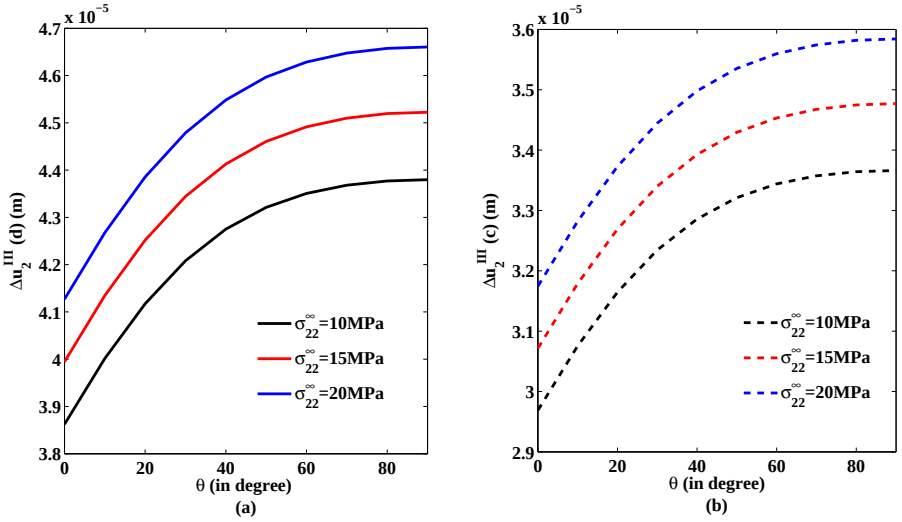

Figure 8.21: COD versus θ for different σ_{22}^{∞}

Figs. 8.21(a, b) respectively, depict the variation of COD at the interior and exterior crack tips versus θ for different σ_{22}^{∞}. COD shows a linear increase as poling direction angle is changed from 0^0 to 90^0 from x_1-axis. Also opening increases at both the crack tips as σ_{22}^{∞} increases.

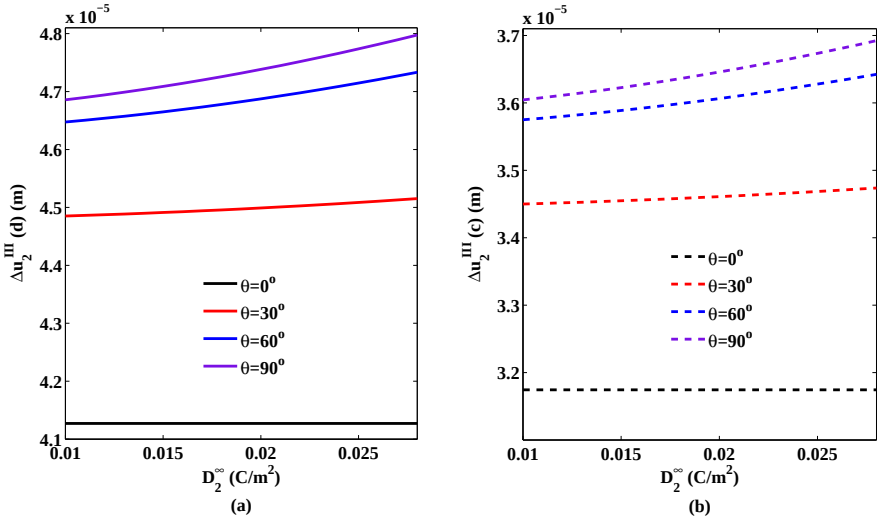

Figure 8.22: COD versus D_2^{∞} for different θ

Figs. 8.22(a, b) show the variation of COD versus D_2^{∞} for different θ. It is observed that COD increases linearly at both the crack tips as D_2^{∞} increases. It is more at inner tip than that at outer tip. It is also noted that θ is increased the cracks open more.

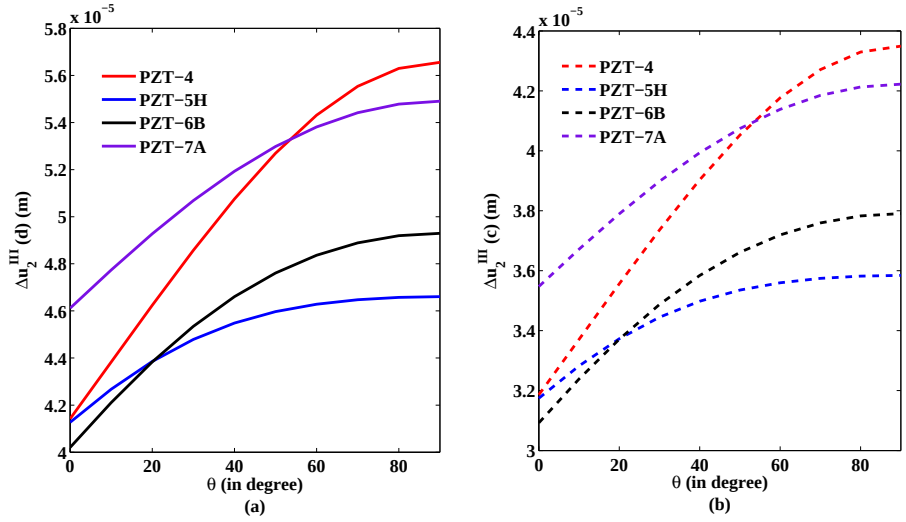

Figure 8.23: COD versus D_2^{∞} for different piezoceramics

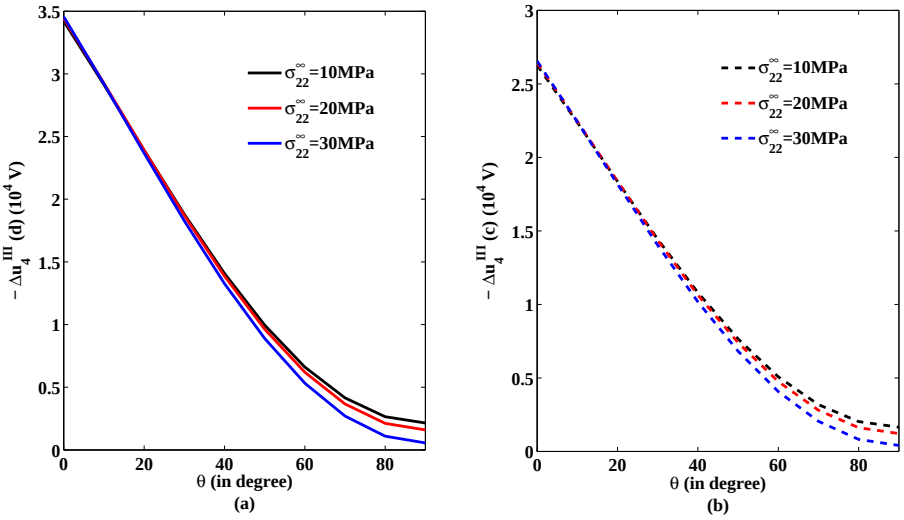

Figure 8.24: COP versus θ for different σ_{22}^{∞}

Variation of COD at the interior and exterior crack tips versus θ for different piezoceramics is shown in Figs. 8.23(a, b). These show the same variation as shown in Figs. 8.21(a, b). It shows that PZT-5H opens the least.

Effect of change in poling direction θ on COP drop is shown in Figs. 8.24(a, b) for different σ_{22}^{∞}. It shows that COP drop increases as θ is increased.

Figs. 8.25(a, b) depict the variation of COP with respect to prescribed electric loadings. It is seen that the COP drop increases linearly as the prescribed electric load is increased for various values of θ.

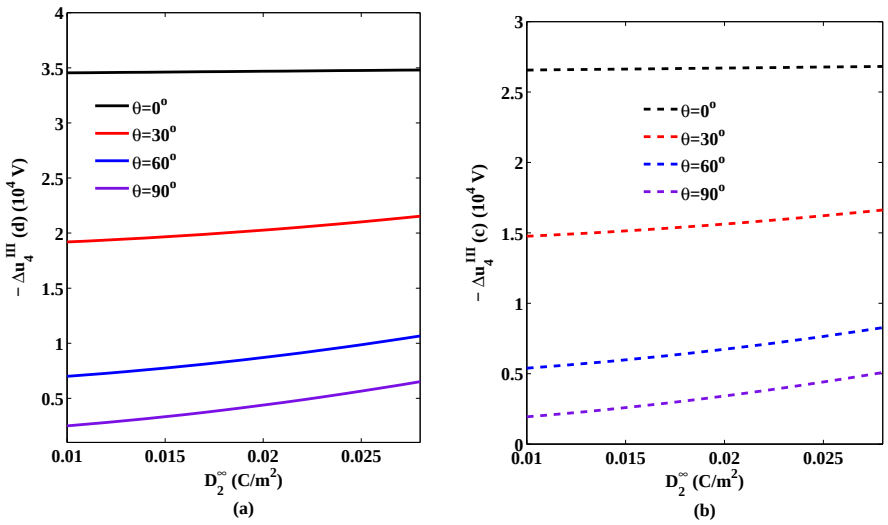

Figure 8.25: COP versus D_2^∞ for different θ

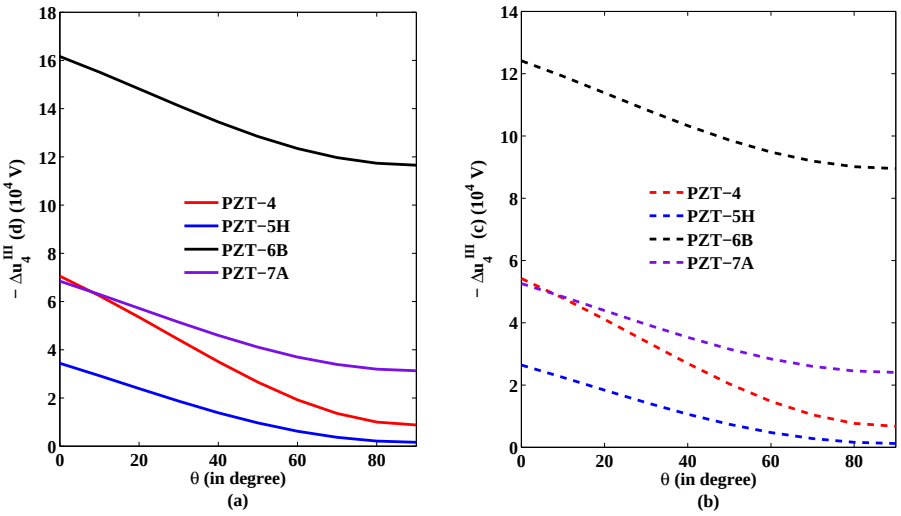

Figure 8.26: COP versus D_2^∞ for different piezoceramics

COP is plotted versus D_2^∞ in Figs. 8.26(a, b) for different piezoceramics. It may be noted that at both inner and outer tips, COP drop shows a parabolic variation as D_2^∞ is increased. It is observed that COP is highest for PZT-6B and minimum for PZT-5H.

Figs. 8.27(a to d) depict the variation of ERR versus prescribed electrical displacement, D_2^∞, for PZT-5H ceramic at the interior tip d. It may be noted that ERR decreases even as D_2^∞ is increased for all poling angles. However the ERR is minimum when poling is along the length of the crack. While it is maximum when

poling direction is perpendicular to crack length. A similar variation is plotted in Figs. 8.28(e to h) at the exterior tip c. It is important to note the ERR is less vis-a-vis that at interior.

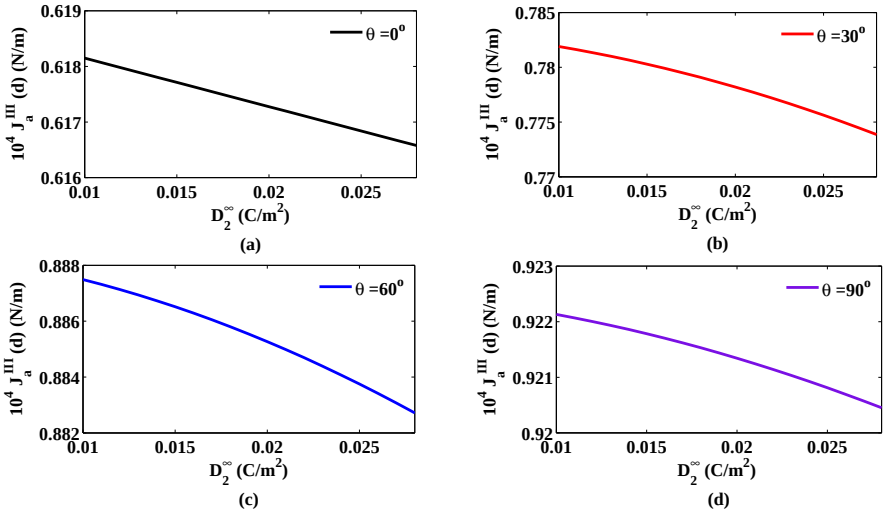

Figure 8.27: ERR at inner tip $x_1 = d$ versus D_2^∞ for different θ

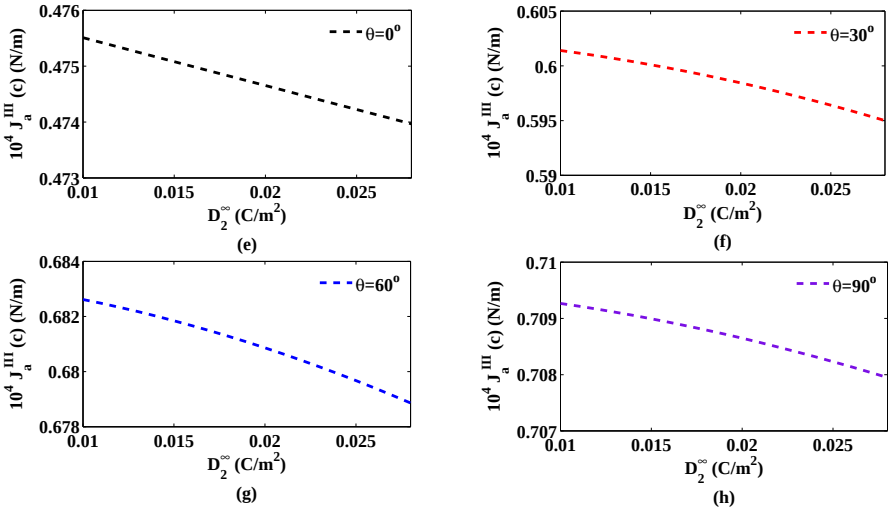

Figure 8.28: ERR at outer tip $x_1 = c$ versus D_2^∞ for different θ

Figs. 8.29(a, b) show the ERR variation with respect to poling direction angle for different poled piezoceramics at the interior and exterior crack tips. This variation is useful for the selection of desired ceramic for the specific work.

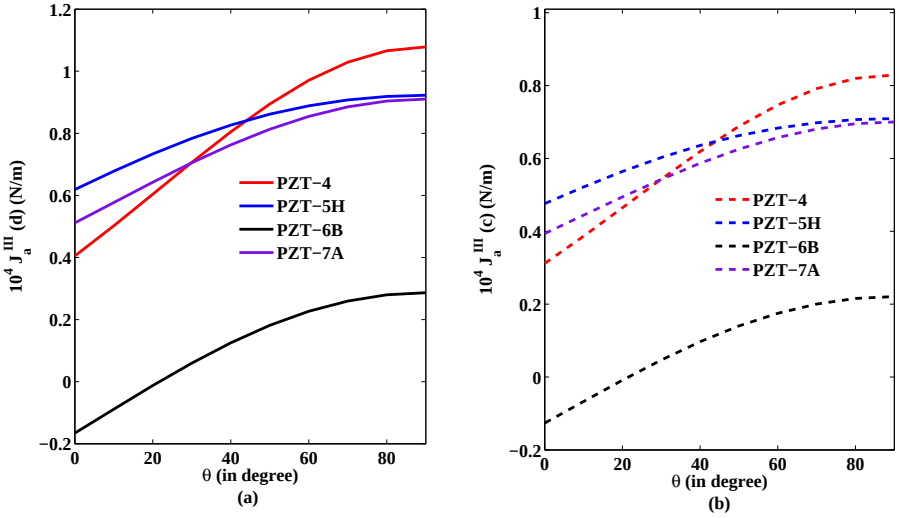

Figure 8.29: ERR versus θ for different piezoceramics

8.4 Conclusions

- Closed form analytical expressions are derived for COD, COP, developed zones and ERR for a piezoelectric plate weakened by two equal collinear semi-permeable cracks.

- An illustrative example presented shows that longer saturation zone vis-a-vis yield zone assists better in crack arrest. Also study presented for COD, COP and ERR for different piezoceramics may assist the designers for correct choice of ceramic for desired purpose for all the cases.

- The interesting phenomenon are observed that COD, COP and ERR are maximum for Case III as compare to Case I and Case II.

- The study shows that poling direction perpendicular to crack length opens the crack maximum. And when poling direction axis moved towards the length of the crack, the crack opening is reduced. Consequently the poling direction may also assist in crack arrest.

Scope of Future Work

Future plan is to investigate the following important topics.

- Strip-electro-elastic yielding model for piezoelectric media weakened by two unequal collinear cracks may be proposed.
- Similar to piezoelectric media a mathematical model solution may be proposed for magnetoelectroelastic (MEE) media weakened by two equal collinear cracks.
- Similar to piezoelectric media a study of arbitrary polarization for magneto-electroelastic (MEE) media weakened by two equal collinear cracks could be done.
- Strip magneto model may be proposed for MEE media weakened by two equal collinear cracks.
- Strip-electro-elastic-magneto yielding model may be proposed for MEE media weakened by two equal collinear cracks.

.

Bibliography

[1] Barenblatt, G. I.: 1962, *The mathematical theory of equilibrium cracks in brittle fracture*, Vol. 7, Academic Press, New York.

[2] Barnett, D. M. and Lothe, J.: 1975, Dislocation and line charges in anisotropic piezoelectric insulators, *Physica Status Solidi (b)* **67**, 105–111.

[3] Beom, H. G.: 2003, Permeable cracks between two dissimilar piezoelectric materials, *International Journal of Solids and Structures* **40**, 6669–6679.

[4] Beom, H. G. and Atluri, S. N.: 2002, Conducting cracks in dissimilar piezoelectric media, *International Journal of Fracture* **118**, 285–301.

[5] Beom, H. G. and Atluri, S. N.: 2003, Effect of electric fields on fracture behavior of ferroelectric ceramics, *Journal of the Mechanics and Physics of Solids* **51**, 1107–1125.

[6] Beom, H. G., Jeong, K. M. and Kim, Y. H.: 2003, Intensity factors for subinterface cracks in dissimilar anisotropic piezoelectric media, *Archive of Applied Mechanics* **73**, 184–198.

[7] Beom, H. G., Jeong, K. M., Park, J. Y., Lin, S. and Kim, G. H.: 2009, Electrical failure of piezoelectric ceramics with a conductive crack under electric fields, *Engineering Fracture Mechanics* **76**, 2399–2407.

[8] Beom, H. G., Kim, Y. H., Cho, C. and Kim, C. B.: 2006, A crack with an electric displacement saturation zone in an electrostrictive material, *Archive of Applied Mechanics* **76**, 19–31.

[9] Bhargava, R. R. and Agrawal, S. C.: 1996, Modified Dugdale model for two

collinear cracks with coalesced interior plastic zone, *19th International Congress of Theoretical and Applied Mechanics, Kyoto, Japan.*

[10] Bhargava, R. R. and Kumar, S.: 2008, Generalised strip yield crack arrest model for a piezoelectric strip with transverse crack, *Asian Journal of Experimental Sciences* **22**, 67–78.

[11] Bhargava, R. R. and Saxena, N.: 2005, Solution for a cracked piezoelectric plate subjected to variable load on plastic zones under mode-I deformation, *Journal of Materials Processing Technology* **164-165**, 1495– 499.

[12] Bhargava, R. R. and Saxena, N.: 2006, Crack arrest model for a piezoelectric plate − A generalised Dugdale model, *Sadhana* **31**, 213–226.

[13] Bhargava, R. R. and Setia, A.: 2008, Modified strip saturation model for a cracked piezoelectric strip, *Archives of Materials Science and Engineering* **30**, 33–36.

[14] Bhargava, R. R. and Setia, A.: 2009, Crack arrest saturation model under combined electrical and mechanical loadings, *Journal of Achivements in Materials and Manufacturing Engineering* **37**, 544–548.

[15] Broek, D.: 1982, *Elementry engineering fracture mechanics*, Martinus Nijhoff publisher.

[16] Chen, B. J., Liew, K. M. and Xiao, Z. M.: 2005, Unified electrical boundary conditions for a crack interacting with a dislocation in piezoelectric media, *International Journal of Solids and Structures* **42**, 5118–5128.

[17] Chen, B. J., Xiao, Z. M. and Liew, K. M.: 2004, A line dislocation interacting with a semi-infinite crack in piezoelectric solid, *International Journal of Engineering Science* **42**, 1–11.

[18] Chen, Y. H. and Ou, Z. C.: 2006, Electrical potential drop across a crack in piezoelectrics, *IUTAM Symposium on Mechanics and Reliability of Actuating Materials.*

[19] Chue, C. H. and Weng, S. M.: 2005, Fracture analysis of piezoelectric materials with an arbitrarily oriented crack using energy density theory, *Computers and Structures* **83**, 1251–1261.

[20] Cui, Z. J., Hu, H. P. and Yang, F.: 2008, Interaction between collinear periodic cracks in an infinite piezoelectric body, *Applied Mathematics and Mechanics (English Edition)* **29**, 863–870.

[21] Das, S., Mukhopadhyay, S. and Prasad, R.: 2011, Stress intensity factor of an edge crack in bonded orthotropic materials, *International Journal of Fracture* **168**, 117–123.

[22] Das, S., Prasad, R. and Mukhopadhyay, S.: 2011, Stress intensity factor of an edge crack in composite media, *International Journal of Fracture* **172**, 201–207.

[23] Deeg, W. F.: 1980, *The analysis of dislocation, crack, and inclusion problems in piezoelectric solids*, PhD thesis, Stanford University, Stanford, CA.

[24] Dugdale, D. S.: 1960, Yielding of steel sheets containing slits, *Journal of the Mechanics and Physics of Solids* **8**, 100–104.

[25] Dunn, M. L.: 1994, The effects of crack face boundary conditions on the fracture mechanics of piezoelectric solids, *Engineering Fracture Mechanics* **48**, 25–39.

[26] Fan, C. Y. and Zhao, M. H.: 2009, Comparison between PS model and DB model in 2D infinite piezoelectric media, *Piezoelectricity, Acoustic Waves, and Device Applications (SPAWDA) and 2009 China Symposium on Frequency Control Technology, Joint Conference of the 2009 Symposium on*.

[27] Fan, C. Y. and Zhao, M. H.: 2010, Influences of poling direction and boundary conditions on cracks in 2D piezoelectric media, *Piezoelectricity, Acoustic Waves and Device Applications (SPAWDA), 2010 Symposium on*.

[28] Fan, C. Y., Zhao, M. H. and Zhou, Y. H.: 2009, Numerical solution of polarization saturation/dielectric breakdown model in 2D finite piezoelectric media, *Journal of the Mechanics and Physics of Solids* **57**, 1527–1544.

[29] Fan, C. Y., Zhao, Y. F., Zhao, M. H. and Ernian, P.: 2012, Analytical solution of a semi-permeable crack in a 2D piezoelectric medium based on the PS model, *Mechanics Research Communications* **40**, 34–40.

[30] Fang, D. N., Soh, A. K. and Liu, J.: 2001, Electromechanical deformation and fracture of piezoelectric/ferroelectric materials, *Acta Mechanica Sinica (English Series)* **17**, 193–213.

[31] Feng, F. X., Lee, K. Y. and Li, Y. D.: 2011, Multiple cracks on the interface between a piezoelectric layer and an orthotropic substrate, *Acta Mechanica* **221**, 297–308.

[32] Fulton, C. C. and Gao, H.: 2001, Effect of local polarization switching on piezoelectric fracture, *Journal of the Mechanics and Physics of Solids* **49**, 927–952.

[33] Gao, C. F. and Balke, H.: 2003, Fracture analysis of circular-arc interface cracks in piezoelectric materials, *International Journal of Solids and Structures* **40**, 3507–3522.

[34] Gao, C. F., Noda, N. and Zhang, T. Y.: 2006, Dielectric breakdown model for a conductive crack and electrode in piezoelectric materials, *International Journal of Engineering Science* **44**, 256–272.

[35] Gao, C. F., Tong, P. and Zhang, T. Y.: 2005, Interaction of a dipole with an interfacial crack in piezoelectric media, *Composites Science and Technology* **65**, 1354–1362.

[36] Gao, C. F. and Wang, M. Z.: 1999a, An easy method for calculating the energy release rate of cracked piezoelectric media, *Mechanics Research Communications* **26**, 433–436.

[37] Gao, C. F. and Wang, M. Z.: 2000, Collinear permeable cracks between dissimilar piezoelectric materials, *International Journal of Solids and Structures* **37**, 4969–4986.

[38] Gao, C. F. and Wang, M. Z.: 2001, Green's functions of an interfacial crack between two dissimilar piezoelectric media, *International Journal of Solids and Structures* **38**, 5323–5334.

[39] Gao, C. F., Zhao, M., Tong, P. and Zhang, T. Y.: 2004, The energy release rate and the J-integral of an electrically insulated crack in a piezoelectric material, *International Journal of Engineering Science* **42**, 2175–2192.

[40] Gao, C. and Fan, W.: 1999, An exact solution of crack problems in piezoelectric materials, *Applied Mathematics and Mechanics (English Edition)* **20**, 51–58.

[41] Gao, C. and Wang, M.: 1999b, Generalized 2D problem of piezoelectric media containing collinear cracks, *Acta Mechanica Sinica (English Series)* **15**, 235–244.

[42] Gao, H. and Barnett, D. M.: 1996, An invariance property of local energy release rate in a strip saturation model of piezoelectric fracture, *International Journal of Fracture* **79**, R25–R29.

[43] Gao, H., Zhang, T. Y. and Tong, P.: 1997, Local and global energy release rates for an electrically yielded crack in a piezoelectric ceramic, *Journal of the Mechanics and Physics of Solids* **45**, 491–510.

[44] Ghosh, M., Chandra, P., Sinha, P. and Shukla, J. B.: 2006, Modelling the spread of bacterial infectious disease with environmental effect in a logistically growing human population, *Nonlinear Analysis: Real World Applications* **7**, 341–363.

[45] Govorukha, V. B., Herrmann, K. P. and Loboda, V. V.: 2008, Electrically permeable crack with contact zones between two piezoelectric materials, *International Applied Mechanics* **44**, 296–303.

[46] Govorukha, V. B. and Loboda, V. V.: 2000, Contact zone models for an interface crack in a piezoelectric material, *Acta Mechanica* **140**, 233–246.

[47] Govorukha, V., Kamlah, M. and Munz, D.: 2004, The interface crack problem for a piezoelectric semi-infinite strip under concentrated electromechanical loading, *Engineering Fracture Mechanics* **71**, 1853–1871.

[48] Griffith, A. A.: 1921, The phenomena of rupture and flow in solids, *Philosophical Transactions of the Royal Society of London* **A221**, 163–198.

[49] Guo, J. H., Liu, P., Lu, Z. X. and Qin, T. Y.: 2011, Anti-plane analysis of semi-infinite crack in piezoelectric strip, *Applied Mathematics and Mechanics (English Edition)* **32**, 75–82.

[50] Hao, T. H. and Shen, Z. Y.: 1994, A new electric boundary condition of electric fracture mechanics and its applications, *Engineering Fracture Mechanics* **47**, 793–802.

[51] Herrmann, K. P., Loboda, V. V. and Govorukha, V. B.: 2001, On contact zone models for an electrically impermeable interface crack in a piezoelectric bimaterial, *International Journal of Fracture* **111**, 203–227.

[52] Huang, G. L. and Wang, X. D.: 2006, On the dynamic behaviour of interfacial cracks between a piezoelectric layer and an elastic substrate, *International Journal of Fracture* **141**, 63–73.

[53] Huang, Z. and Kuang, Z. B.: 2003, A mixed electric boundary value problem for a two-dimensional piezoelectric crack, *International Journal of Solids and Structures* **40**, 1433–1453.

[54] Inglis, C. E.: 1913, Stresses in a plate due to the presence of cracks and sharp conrners, *Transactions of The Institute of Naval Architects* **55**, 219–241.

[55] Irwin, G. R.: 1948, *Fracture Dynamics: Fracturing of metals*, American Society for Metals, Cleveland.

[56] Irwin, G. R.: 1956, Onset of fast crack propagation in high strength steel and aluminum alloys, *Sagamore Research Conference Proceedings*.

[57] Irwin, G. R.: 1957, Analysis of stresses and strains near the end of a crack traversing a plate, *Journal of Applied Mechanics* **24**, 361–364.

[58] Irwin, G. R.: 1961, Plastic zone near a crack and fracture toughness, *Sagamore Research Conference Proceedings*.

[59] Jelitto, H., Felten, F., Hausler, C., Kessler, H., Balke, H. and Schneider, G. A.: 2005, Measurement of energy release rates for cracks in PZT under electromechanical loads, *Journal of the European Ceramic Society* **25**, 2817–2820.

[60] Jelitto, H., Kebler, H., Schneider, G. A. and Balke, H.: 2005, Fracture behavior of poled piezoelectric PZT under mechanical and electrical loads, *Journal of the European Ceramic Society* **25**, 749–757.

[61] Jeong, K. M., Kim, I. O. and Beom, H. G.: 2004, Effect of electric displacement saturation on the stress intensity factor for a crack in a ferroelectric ceramic, *Mechanics Research Communications* **31**, 373–382.

[62] Khan, H. and Sinha, P.: 2011, Analysis of a non-constant gap externally pressurized conical bearing with temperature and pressure dependent viscosity, *International Journal of Surface Science and Engineering* **5**, 205–225.

[63] Kuna, M.: 2010, Fracture mechanics of piezoelectric materials - Where are we right now ?, *Engineering Fracture Mechanics* **77**, 309–326.

[64] Kwon, S. M.: 2003, Electrical nonlinear anti-plane shear crack in a functionally graded piezoelectric strip, *International Journal of Solids and Structures* **40**, 5649–5667.

[65] Kwon, S. M. and Lee, K. Y.: 2000, Analysis of stress and electric fields in a rectangular piezoelectric body with a center crack under anti-plane shear loading, *International Journal of Solids and Structures* **37**, 4859–4869.

[66] Lapusta, Y. and Loboda, V.: 2009, Electro-mechanical yielding for a limited permeable crack in an interlayer between piezoelectric materials, *Mechanics Research Communications* **36**, 183–192.

[67] Li, Q. and Chen, Y. H.: 2007, Solution for a semi-permeable interface crack between two dissimilar piezoelectric material, *ASME Journal of Applied Mechanics* **74**, 833–844.

[68] Li, S.: 2003a, On global energy release rate of a permeable crack in a piezoelectric ceramic, *ASME Journal of Applied Mechanics* **70**, 246–252.

[69] Li, S.: 2003b, On saturation-strip model of a permeable crack in a piezoelectric ceramic, *Acta Mechanica* **165**, 47–71.

[70] Li, X. F.: 2002, Closed-form solution for a piezoelectric strip with two collinear cracks normal to the strip boundaries, *European Journal of Mechanics A/Solids* **21**, 981–989.

[71] Li, X. F. and Lee, K. Y.: 2004, Effects of electric field on crack growth for a penny-shaped dielectric crack in a piezoelectric layer, *Journal of the Mechanics and Physics of Solids* **52**, 2079–2100.

[72] Li, X. F. and Tang, G. J.: 2003, Antiplane interface crack between two bonded dissimilar piezoelectric layers, *European Journal of Mechanics A/Solids* **22**, 231–242.

[73] Li, Y. D. and Lee, K. Y.: 2010, Two collinear unequal cracks in a poled piezoelectric plane: Mode-I case solved by a new approach of real fundamental solutions, *International Journal of Fracture* **165**, 47–60.

[74] Li, Y. D., Lee, K. Y., Feng, F. X. and Pan, J. W.: 2011, Mode-I fracture analysis of a piezoelectric strip based on real fundamental solutions, *European Journal of Mechanics A/Solids* **30**, 158–166.

[75] Liang, J.: 2008, Non-local theory solution of two collinear mode-I cracks in piezoelectric materials, *Applied Mathematical Modelling* **32**, 1126–1142.

[76] Liang, Y. C. and Hwu, C.: 1996, Electromechanical analysis of defects in piezoelectric materials, *Smart Materials and Structures* **5**, 314–320.

[77] Linder, C. and Miehe, C.: 2012, Effect of electric displacement saturation on the hysteretic behavior of ferroelectric ceramics and the initiation and propagation of cracks in piezoelectric ceramics, *Journal of the Mechanics and Physics of Solids* **60**, 882–903.

[78] Loboda, V., Lapusta, Y. and Govorukha, V.: 2008, Mechanical and electrical yielding for an electrically insulated crack in an interlayer between piezoelectric materials, *International Journal of Engineering Science* **46**, 260–272.

[79] Loboda, V., Lapusta, Y. and Sheveleva, A.: 2007, Electro-mechanical pre-fracture zones for an electrically permeable interface crack in a piezoelectric bimaterial, *International Journal of Solids and Structures* **44**, 5538–5553.

[80] Loboda, V., Lapusta, Y. and Sheveleva, A.: 2010, Limited permeable crack in an interlayer between piezoelectric materials with different zones of electrical saturation and mechanical yielding, *International Journal of Solids and Structures* **47**, 1795–1806.

[81] Lu, Z. X., Liu, P. and Guo, J. H.: 2011, Exact solutions of two semi-infinite collinear cracks in piezoelectric strip, *Applied Mathematics and Mechanics (English Edition)* **32**, 1399–1406.

[82] McMeeking, R. M.: 1999, Crack tip energy release rate for a piezoelectric compact tension specimen, *Engineering Fracture Mechanics* **64**, 217–244.

[83] Motola, Y., Sills, L. B. and Fourman, V.: 2009, On fracture testing of piezoelectric ceramics, *International Journal of Fracture* **159**, 167–190.

[84] Mukherjee, S. and Das, S.: 2007, Interaction of three interfacial Griffith cracks between bonded dissimilar orthotropic half planes, *International Journal of Solids and Structures* **44**, 5437–5446.

[85] Muskhelishvili, N. I.: 1975, *Some basic problems of mathematical theory of elasticity*, Noordhoff, Leyden.

[86] Narayanasamy, R., Ramesh, T. and Pandey, K. S.: 2006, Some aspects on strain hardening behaviour in three dimensions of aluminium-iron powder metallurgy composite during cold upsetting, *Materials and Design* **27**, 640–650.

[87] Narayanasamy, R., Ramesh, T. and Pandey, K. S.: 2007, An experimental

investigation on strain hardening behaviour of aluminium - 3.5% alumina powder metallurgy composite preform under various stress states during cold upset forming, *Materials and Design* **28**, 1211–1223.

[88] Narayanasamya, R., Anandakrishnan, V. and Pandey, K. S.: 2008, Effect of geommetric work-hardening and matrix work-hardening on workability and densification of aluminium - 3.5% alumina composite during cold upsetting, *Materials and Design* **29**, 1582–1599.

[89] Narita, F. and Shindo, Y.: 1998, Anti-plane shear crack growth rate of piezoelectric ceramic body with finite width, *Theoretical and Applied Fracture Mechanics* **30**, 127–132.

[90] Narita, F. and Shindo, Y.: 2001, Mode-I crack growth rate for yield strip model of a narrow piezoelectric ceramic, *Theoretical and Applied Fracture Mechanics* **36**, 73–85.

[91] Orowan, E.: 1949, Fracture and strength of solids, *Reports on Progress in Physics* **12**, 185232.

[92] Ou, Z. C. and Chen, Y. H.: 2003, Explicit expressions of eigenvalues and eigenvectors for transversely isotropic piezoelectric materials, *Acta Mechanica* **162**, 213–219.

[93] Ou, Z. C. and Chen, Y. H.: 2005, On approach of crack tip energy release rate for a semi-permeable crack when electromechanical loads become very large, *International Journal of Fracture* **133**, 89–105.

[94] Pak, Y. E.: 1990, Crack extension force in a piezoelectric material, *ASME Journal of Applied Mechanics* **57**, 647–653.

[95] Pak, Y. E.: 1992, Linear electro-elastic fracture mechanics of piezoelectric materials, *International Journal of Fracture* **54**, 79–100.

[96] Pandey, R. K.: 1989, Fracture toughness-microstructure investigation of hyperbarically welded joints in offshore application, *Engineering Fracture Mechanics* **34**, 1119–1129.

[97] Pandey, R. K. and Patel, A. B.: 1984, Mixed-mode fatigue crack growth under biaxial loading, *International Journal of Fatigue* **6**, 119–123.

[98] Park, S. B. and Sun, C. T.: 1995, Effect of electric field on fracture of piezoelectric ceramics, *International Journal of Fracture* **70**, 203–216.

[99] Parton, V. Z.: 1976, Fracture mechanics of piezoelectric materials, *Acta Astronautica* **3**, 671–683.

[100] Prakash, O. and Pandey, R. K.: 1996, Failure analysis of the impellers of a feed pump, *Engineering Failure Analysis* **3**, 45–52.

[101] Qi, H., Fang, D. N. and Yao, Z.: 2001, Analysis of electric boundary condition effects on crack propagation in piezoelectric ceramics, *Acta Mechanica* **17**, 59–70.

[102] Rao, B. N. and Kuna, M.: 2008a, Interaction integrals for fracture analysis of functionally graded magnetoelectroelastic materials, *International Journal of Fracture* **153**, 15–37.

[103] Rao, B. N. and Kuna, M.: 2008b, Interaction integrals for fracture analysis of functionally graded piezoelectric materials, *International Journal of Solids and Structures* **45**, 5237–5257.

[104] Rao, B. N. and Kuna, M.: 2010, Interaction integrals for thermal fracture of functionally graded piezoelectric materials, *Engineering Fracture Mechanics* **77**, 37–50.

[105] Rice, J. R.: 1968, A path independent integral and the approximate analysis of strain concentration by notches and cracks, *Journal of Applied Mechanics* **35**, 379–386.

[106] Ru, C. Q.: 1999, Effect of electrical polarization saturation on stress intensity factors in a piezoelectric ceramic, *International Journal of Solids and Structures* **36**, 869–883.

[107] Ru, C. Q. and Mao, X.: 1999, Conducting cracks in a piezoelectric ceramic of limited electrical polarization, *Journal of the Mechanics and Physics of Solids* **47**, 2125–2146.

[108] Shen, S., Nishioka, T., Kuang, Z. B. and Liu, Z.: 2000, Nonlinear electromechanical interfacial fracture for piezoelectric materials, *Mechanics of Materials* **32**, 57–64.

[109] Shindo, Y., Watanabe, K. and Narita, F.: 2000, Electroelastic analysis of a piezoelectric ceramic strip with a central crack, *International Journal of Engineering Science* **38**, 1–19.

[110] Sih, G. C.: 2002, A field model interpretation of crack initiation and growth behavior in ferroelectric ceramics: change of poling direction and boundary condition, *Theoretical and Applied Fracture Mechanics* **38**, 1–14.

[111] Sih, G. C. and Zuo, J. Z.: 2000, Multiscale behavior of crack initiation and growth in piezoelectric ceramics, *Theoretical and Applied Fracture Mechanics* **34**, 123–141.

[112] Sills, L. B., Motola, Y. and Shemesh, L.: 2008, The M-integral for calculating intensity factors of an impermeable crack in a piezoelectric, *Engineering Fracture Mechanics* **75**, 901–925.

[113] Sinha, P. and Adamu, G.: 2011, THD analysis for finite slider bearing with roughness: special reference to load generation in parallel sliders, *Acta Mechanica* **222**, 1–15.

[114] Sosa, H.: 1991, Plane problems in piezoelectric media with defects, *International Journal of Solids and Structures* **28**, 491–505.

[115] Sosa, H.: 1992, On the fracture mechanics of piezoelectric solids, *International Journal of Solids and Structures* **29**, 2613–2622.

[116] Sosa, H. A. and Pak, Y. E.: 1990, Three-dimensional eigenfunction analysis of a crack in a piezoelectric material, *International Journal of Solids and Structures* **26**, 1–15.

[117] Stroh, A. N.: 1958, Dislocations and cracks in anisotropic elasticity, *Philosophical Magazine* **3**, 625–646.

[118] Suo, Z., Kuo, C. M., Barnett, D. M. and Willis, J. R.: 1992, Fracture mechanics for piezoelectric ceramics, *Journal of the Mechanics and Physics of Solids* **40**, 739–765.

[119] Theocaris, P. S.: 1972, Interaction between collinear asymmetric cracks, *Journal of Strain Analysis* **7**, 186–192.

[120] Tobin, A. C. and Pak, Y. E.: 1993, Effect of electric fields on fracture behavior of PZT ceramics, *Proceedings of SPIE, Smart Structures and Materials*.

[121] Wang, B. L. and Mai, Y. W.: 2002, A piezoelectric material strip with a crack perpendicular to its boundary surfaces, *International Journal of Solids and Structures* **39**, 4501–4524.

[122] Wang, B. L. and Mai, Y. W.: 2003, On the electrical boundary conditions on the crack surfaces in piezoelectric ceramics, *International Journal of Engineering Science* **41**, 633–652.

[123] Wang, B. L. and Zhang, X. H.: 2004, An electrical field based non-linear model in the fracture of piezoelectric ceramics, *International Journal of Solids and Structures* **41**, 4337–4347.

[124] Wang, B. L. and Zhang, X. H.: 2005, Fracture prediction for piezoelectric ceramics based on the electric field saturation concept, *Mechanics Research Communications* **32**, 411–419.

[125] Wang, H. and Singh, R. N.: 1997, Crack propagation in piezoelectric ceramics: Effects of applied electric fields, *Journal of Applied Physics* **81**, 7471–7479.

[126] Wang, T. C.: 2000, Analysis of strip electric saturation model of crack problem in piezoelectric materials, *International Journal of Solids and Structures* **37**, 6031–6049.

[127] Wang, X. D. and Jiang, L. Y.: 2004, The nonlinear fracture behaviour of an arbitrarily oriented dielectric crack in piezoelectric materials, *Acta Mechanica* **172**, 195–210.

[128] Wang, X. D. and Jiang, L. Y.: 2005, Coupled behaviour of interacting dielectric cracks in piezoelectric materials, *International Journal of Fracture* **132**, 115–133.

[129] Wells, A. A.: 1961, Unstable crack propagation in metals: cleavage and fast fracture, *Proceedings of the crack propagation symposium*, Vol. 1, Cranfield, UK.

[130] Wippler, K., Ricoeur, A. and Kuna, M.: 2004, Towards the computation of electrically permeable cracks in piezoelectrics, *Engineering Fracture Mechanics* **71**, 2567–2587.

[131] Xiao, Z. M., Zhang, H. X. and Chen, B. J.: 2007, A piezoelectric screw dislocation interacts with interfacial collinear rigid lines in piezoelectric bimaterials, *International Journal of Solids and Structures* **44**, 255–271.

[132] Xu, W., Wu, X. R. and Wang, H.: 2011, Weight functions and strip yield solution for two equal-length collinear cracks in an infinite sheet, *Engineering Fracture Mechanics* **78**, 2356–2368.

[133] Xu, X. L. and Rajapakse, R. K. N. D.: 2000, A theoretical study of branched cracks in piezoelectrics, *Acta Materialia* **48**, 1865–1882.

[134] Xu, X. L. and Rajapakse, R. K. N. D.: 2001, On a plane crack in piezoelectric solids, *International Journal of Solids and Structures* **38**, 7643–7658.

[135] Xue, C., Yong, H. and Zhou, Y.: 2012, The mechanical crack tip opening displacement fracture criterion in piezoelectric ceramics, *Engineering Fracture Mechanics* **96**, 606–614.

[136] Zhang, N. and Gao, C. F.: 2012, Effects of electrical breakdown on a conducting crack or electrode in electrostrictive solids, *European Journal of Mechanics A/Solids* **32**, 62–68.

[137] Zhang, T. Y.: 2004, Dielectric breakdown model for an electrically impermeable crack in a piezoelectric material, *Computers Materials and Continua* **1**, 107–115.

[138] Zhang, T. Y. and Gao, C. F.: 2004, Fracture behaviors of piezoelectric materials, *Theoretical and Applied Fracture Mechanics* **41**, 339–379.

[139] Zhang, T. Y., Zhao, M. H. and Gao, C. F.: 2005, The strip dielectric breakdown model, *International Journal of Fracture* **132**, 311–327.

[140] Zhong, X. C. and Li, X. F.: 2005, Closed-form solution for two collinear cracks in a piezoelectric strip, *Mechanics Research Communications* **32**, 401–410.

[141] Zhou, Z. G., Chen, J. Y. and Wang, B.: 2000, Analysis of two collinear cracks in a piezoelectric layer bonded to two half spaces subjected to anti-plane shear, *Meccanica* **35**, 443–456.

[142] Zhou, Z. G., Wang, B. and Cao, M. S.: 2003, The behaviour of permeable multi-cracks in a piezoelectric material, *Mechanics Research Communications* **30**, 395–402.

[143] Zhou, Z. G. and Wu, L. Z.: 2007, Basic solutions of two parallel mode-I cracks or four parallel mode-I cracks in the piezoelectric materials, *Engineering Fracture Mechanics* **74**, 1413–1435.